Pei Kang Shen *Editor*

Electrochemical Oxygen Reduction

Fundamental and Applications

Guangxi Science & Technology Publishing House

Springer

Electrochemical Oxygen Reduction

Pei Kang Shen
Editor

Electrochemical Oxygen Reduction

Fundamental and Applications

Guangxi Science & Technology Publishing House

Springer

Editor
Pei Kang Shen
Guangxi University
Nanning, China

ISBN 978-981-33-6076-1 ISBN 978-981-33-6077-8 (eBook)
https://doi.org/10.1007/978-981-33-6077-8

Jointly published with Guangxi Science & Technology Publishing House
The print edition is not for sale in China (Mainland). Customers from China (Mainland) please order the print book from: Guangxi Science & Technology Publishing House.
ISBN of the Co-Publisher's edition: 978-7-5551-1007-1

This Springer imprint is published by the registered company Springer Nature Singapore Pte Ltd.
The registered company address is: 152 Beach Road, #21-01/04 Gateway East, Singapore 189721, Singapore

Foreword

Oxygen Reduction Reaction (ORR) refers to the reduction reaction of oxygen. It includes two-electron reaction and four-electron reaction. Two-electron reaction is to reduce oxygen to H_20_2, and four-electron reaction is to reduce oxygen to H_20. Oxygen reduction is a very important reaction in the chemical field, such as energy conversion and storage of new energy materials (including fuel cells, supercapacitors, lithium secondary batteries, metal-air cells), and corrosion of industrial materials such as steel.

Obviously, when we study oxygen reduction, we also involve the reaction mechanism of materials. Taking fuel cells and other electrochemical processes as examples, oxygen reduction reaction is one of the key steps, and it mainly relies on precious metal catalyst at present (such as Platinum). With the deepening of research, various non-Pt (non-precious metal) catalysts have shown good electrocatalytic activity, such as carbon materials doped with nitrogen. However, there is little research on the working mechanism of this kind of carbon-based catalyst at present, and the relationship between the arrangement of carbon atoms and nitrogen atoms and the catalytic activity is still a mystery, which hinders people from further developing higher performance catalysts that can replace precious metals. Recently, researchers at the University of Tsukuba in Japan published an article in the *American Journal of Science* (Active Sites of Nitrogen-Doped Carbon Materials for Oxygen Regeneration Reaction Clarifying Using Model Catalysts. Science, 2016, 351: 361–365), which clearly stated that the catalytic structure of nitrogen-doped carbon materials was introduced, and the working mechanism of the reaction was put forward. In order to solve this mystery, the team used graphite (highly oriented pyrolytic graphite) model catalyst with definite hexagenics and controllable nitrogen atom doping to simulate potential competition sites and analyze the reaction process. Among them, pyridine nitrogen mainly appears at the edge of materials. By patterning the village bottom to change the number of edges, the team was able to control the existence of pyridine nitrogen and test how it affects the catalytic performance. The results showed that the catalytic sites were related to pyridine nitrogen. Carbon dioxide adsorption experiments further showed that pyridine nitrogen created Lewis base sites. Further analysis shows that the oxygen reduction sites of nitrogen-doped carbon materials are

actually Lewis-basic carbon atoms adjacent to pyridine nitrogen, rather than pyridine nitrogen proton itself.

Professor Nakamura pointed out "Defining the active site of the catalyst and understanding the reaction mechanism make the non-Pt catalyst take a big step forward, and also shift the focus of optimizing the reaction to improve the performance of the catalyst". However, in spite of this, this result cannot be confirmed experimentally. Actually, the recent appearance of environmental spherical aberration electron microscopy can directly detect the selling point of catalyst at the atomic level (Direct atomic-level insight into active sites of a high-performance PGM-free ORR catalyst. Science, 2017, 357: 479–484).

There are many subjects related to the knowledge of oxygen reduction, which are expounded in many electrochemical books, but they are relatively brief. In particular, the knowledge related to the method foundation and test skills is not perfect, which makes readers hard to understand the theory and implement the experiment. Professor Pei Kang Shen studied under the internationally renowned electrochemist Prof. A. C. C. Tseung in his early years, and worked in the field of electrochemistry for a long time, especially the development and innovation of key materials and technology for the conversion and storage of electrochemical energy. He has unique insights and contributions in oxygen reduction mechanism and application, fuel cells, supercapacitors, water splitting, lithium-ion batteries, nano-electrocatalysis, and preparation and application of stereotaxically constructed graphene materials. Professor Pei Kang Shen collected more than 30 years of teaching and practical experience in electrochemistry, and wrote the first edition of monograph with the help of his students. Professor Pei Kang Shen has organized the editors to revise it in this first English edition, adding some necessary updates and some documents. Therefore, the current edition is easier to read, and I hope the new edition will help everyone.

July 2020

Sanping Jiang
John Curtin Distinguished Professor
Curtin University
Perth, Australia

Contents

About the Editor

Dr. Pei Kang Shen is a Professor and Director at the Collaborative Innovation Center of Sustainable Energy Materials in Guangxi University, China. Dr. Shen obtained his B.Sc. degree in Electrochemistry at Xiamen University in 1982, and he continuously carried out his research and teaching at the same university for seven years before he became a visiting researcher in the UK. He received his Ph.D. in Chemistry at Essex University in 1992. From then on, he has been working at different universities both in UK and China. Since 2001, he has been Professor at the Sun Yat-sen University (Guangzhou, China). He is the author of over 400 publications. His research interests include fuel cells and batteries, electrochemistry of nanomaterials and of nanocomposite functional materials, like graphene powders for different applications and electrochemical engineering.

Chapter 1
Introduction

Pei Kang Shen

Abstract This chapter mainly includes the overview of oxygen reduction reaction, the kinetic mechanism of oxygen reduction reaction, including the working principle of proton exchange membrane fuel cell and the kinetic process of proton exchange membrane fuel cell. Through the schematic diagram of proton exchange membrane fuel cell, the working principle, cell structure, function display and equation expression of fuel cell are explained in detail.

Keywords Kinetic mechanism of oxygen reduction reaction · Working principle · Voltage loss diagram · Proton exchange membrane fuel cell · Chemical energy to electric energy

1.1 Overview of Oxygen Reduction Reaction

In our life, oxygen is an indispensable element to maintain the continuous metabolism of matter and energy in human cells. Without oxygen, it is impossible for the organism to obtain the energy needed for all life processes from nutrients. This is because oxygen is the only substance that can accept electrons, but excessive inhalation of oxygen can cause poisoning. Current research suggests that oxygen poisoning is mainly due to excessive active oxygen produced in the body. The most common reactive oxygen species in the body are superoxide anion and hydrogen peroxide. The life process of human body is actually a redox process, therefore, understanding Oxygen Reduction Reaction (ORR) is very helpful to understand the life process.

Oxygen reduction is also a very important process in our life and production. Low-temperature fuel cells, metal-air cells, oxygen sensors and preparation of hydrogen peroxide in the field of energy all involve the reduction process of oxygen. In fact, the high overpotential and complex kinetic mechanism of oxygen reduction seriously restrict the development of new energy sources such as fuel cells. Therefore, the

P. K. Shen (✉)
Collaborative Innovation Center of Sustainable Energy Materials, Guangxi Key Laboratory of Electrochemical Energy Materials, College of Chemistry and Chemical Engineering, Guangxi University, Nanning, Guangxi 530004, China
e-mail: pkshen@gxu.edu.cn

P. K. Shen, *Electrochemical Oxygen Reduction*,
https://doi.org/10.1007/978-981-33-6077-8_1

research on this reaction has been very extensive. In 2012, there were more than 800 research papers in English. However, most people who are engaged in oxygen reduction research are not very clear about the concept of oxygen reduction theory, and there are some test technical problems in experiments. Therefore, many oxygen reduction curves or data we have seen from published literature are not satisfactory, and in many cases, it is not the problem of materials, but the problem of testing methods. At present, commercial Pt/C catalyst is used as a reference for oxygen reduction activity, and the phenomenon that its oxygen reduction activity is lower than 100 mA m-g^{-1} still exists. In addition, it is more common for the limit current value to be lower than 6 mA cm^{-2} or low oxygen reduction onset potential under standard test conditions. Research articles that directly convert data between reference electrodes without giving necessary explanation abound. However, the mass activity of the catalyst can change by 20 mA m-g^{-1} for every 10 mV of potential shift, so the authenticity of the ultra-high activity of the catalyst reported in these literatures is questioned. In addition, the different oxygen reduction test conditions such as scanning speed, rotating speed and catalyst loading scene set by different literatures and research teams will not only affect the test results but also be unfavorable to objectively compare the catalytic activities of different catalysts qualitatively or quantitatively.

Therefore, from the mechanism of oxygen reduction reaction, it is necessary to discuss the measurement technology of oxygen reduction reaction in detail, discuss the key skills of obtaining oxygen reduction polarization curve and analyze the experimental data, so as to obtain the correct experimental method for evaluating oxygen reduction performance and summarize the matters needing attention in the test process, so as to effectively improve the practicability of the experimental test technology.

1.2 Kinetic Mechanism of Oxygen Reduction Reaction

With the rapid development of science and technology, people's quality of life is improving day by day, and the demand for energy is also growing. Rapid increasing industry and population, the gap of available resources on the earth is increasing day by day, and the traditional fossil fuel resources will be exhausted in the near future. According to the survey report of the World Energy Organization, mineral energy such as coal, oil and natural gas will be exhausted in the next 100 ~ 200 years. In addition, a large number of fossil fuels are burned, resulting in CO_2, N_2O, sulfide and other pollutants harmful to the atmosphere and human body, causing serious environmental pollution. Therefore, it is urgent to find an efficient, safe, clean and economical means of energy utilization to solve the urgent task of rational energy utilization. Fuel cell has become the first new energy with great potential.

Fuel cell is an electrochemical device that directly converts the chemical energy generated by the reaction of fuel and oxidant into electrical energy. It is not limited by

Carnot cycle, and the actual working conversion efficiency can reach 40 ~ 60%. Theoretically, as long as oxidant and fuel are continuously supplied, fuel cells can continuously work to generate electric energy. The fuel of fuel cell is mainly hydrogen-rich gas, and the emission of carbon dioxide is about 40% lower than that of heat engine power generation; if the fuel is pure hydrogen, its electrochemical reaction product is only water, which fundamentally reduces the emission of air pollutants such as carbon monoxide, nitride and sulfide. Therefore, fuel cell has become the fourth-generation power generation device after hydropower, thermal power and nuclear power, and is listed as the top ten science and technology in the world in the future.

In 1839, when William Grove studied the water electrolysis reaction, he found that the reverse reaction of the water electrolysis reaction can also occur under certain conditions, and then put forward the first fuel cell model. In 1889, Mond et al., using hydrogen as fuel, oxygen as oxidant and lead as electrode reaction catalyst, successfully prepared a battery device with similar structure to the fuel cell widely used in modern times, and named it "fuel cell." In 1960s, fuel cell was used as an auxiliary power supply on the Apollo spacecraft of NASA. Subsequently, the research of fuel cells entered a rapid development stage, and various power generation devices of fuel cells came out one after another, such as phosphoric acid fuel cells, molten carbonate cells and solid oxide fuel cells. The research focus of fuel cells shifted from aerospace to ground power generation devices.

At present, more than 92% of fuel cell devices are proton exchange membrane fuel cells, and the structural schematic diagram is shown in Fig. 1.1. In 1957, Willard T. Grubb discovered proton exchange membrane fuel cell for the first time, and named it Ion Exchange Resin Membrane Fuel Cell (IEM). Then General Electric Company changed it to proton exchange membrane fuel cell, abbreviated as PEMFC. The first spacecraft Gemini takes proton exchange membrane fuel cell into consideration of

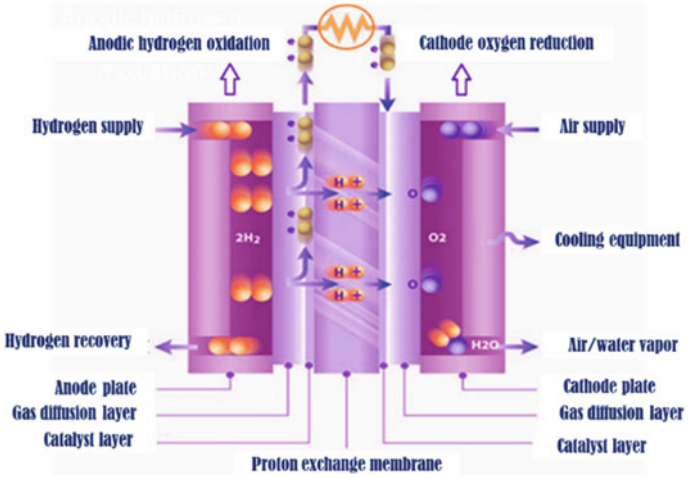

Fig. 1.1 Schematic diagram of PEMFC structure

energy device and uses hydrogen and oxygen produced by solar cell to provide fuel and oxidant. However, the electrode of fuel cell is in poor contact with membrane, resulting in low initial current density. In order to improve this bad contact, the battery is filled with strong acid solution, which also makes the water produced by the reaction not neutral. At high temperature, the first generation PEMFC is very unstable, so Gemini spacecraft changed the membrane material to sulfonated polystyrene. In 1970, DuPont invented Nafion (fully aerated sulfonic acid) membrane, which can keep thermal stability even at temperature higher than 100 °C, and the ionic conductor is difficult to dissociate, with high chemical stability, but it is expensive. So far, only a few teams have been able to produce Nafion membrane with suitable price. The power of proton exchange membrane fuel cell used in Gemini spacecraft is about 50 W ft^{-2}. In the mid-1970s, American General Electric Company transferred fuel cell technology and patents to United Technologies Corporation of America and Siemens Company of Germany. In 1983, Ballard Company of Canada further explored proton exchange membrane fuel cell, including trying new membrane such as Dow chemical membrane, which improved the thermal stability to 120 °C and the pressure to 700 kPa. In 1993, Daimler-Benz Automotive Company of Germany used this fuel cell which only needs to consume water and only generates water for automobiles, which aroused widespread concern in the world and set off a global upsurge of research and development of fuel cell electric vehicles. Up to now, the proton exchange membrane fuel cell has gone deep into aerospace, transportation, communication, military and other fields, which is a hot spot of capital investment by government enterprises in various countries, and also makes great progress in the research and development of fuel cells.

1.2.1 Working Principle of Proton Exchange Membrane Fuel Cells (PEMFCs)

Membrane electrode of fuel cell is composed of three basic units, which are cathode, anode and electrolyte. The cathode and anode are respectively connected with conductive materials. In a common acid fuel cell (as shown in the figure), the cathode and anode catalysts are all platinum, the anode is filled with fuel hydrogen, and the cathode is filled with oxidant oxygen. Platinum particles are supported on carbon carriers with high specific surface area to improve their utilization rate and catalytic activity. At the anode, hydrogen oxidizes to generate hydrogen ions. Protons are transmitted to cathode through proton exchange membrane, but electrons can only be transmitted through external circuit because the membrane cannot transmit electrons. At the cathode, oxygen (usually air) is catalytically reduced under the action of catalyst, and then reacts with protons to generate water. The general reaction equation is as follows.

$$H_2 + 1/2\ O_2 \leftrightarrow\ H_2O \tag{1.1}$$

At a certain temperature, the theoretical output voltage of this reaction under reversible conditions is expressed as follows.

$$E = E^0 + \frac{RT}{\mathrm{nF}} \ln\left[\left(\frac{p_{H_2}}{p^*_{H_2}}\right)^2 \left(\frac{p_{O_2}}{p^*_{O_2}}\right) \right] \tag{1.2}$$

In the formula, p_{H_2}, p_{O_2}, etc. are the partial pressures of hydrogen and oxygen, E^0 is the reversible electrode potential, n represents the number of transferred electrons in the reaction, and for the reaction formula (1.1), the number of transferred electrons is 2, and F is Faraday constant. At room temperature and normal pressure, the theoretical voltage of hydrogen–oxygen fuel cell is 1.229 V. However, in actual use, the actual voltage is much lower than 1.229 V due to the influence of impedance and membrane mass transfer (see the following section for specific analysis).

1.2.2 Dynamic Process of Proton Exchange Membrane Fuel Cell

Formula (1.3) is the contribution of different kinetic processes to the potential loss of PEMFC.

$$E_{\mathrm{cell}} = E - \eta_{\mathrm{HOR}} - \mathrm{i} * R^{effective}_{H^+,\, anode} - \mathrm{i} * \mathrm{R}_{\Omega} - \mathrm{i} * R^{effective}_{H^+,\, cathode} - \eta_{\mathrm{ORR}} - \eta_{\mathrm{mt}} \tag{1.3}$$

In the above formula, E_{cell} is the actual open-circuit potential of a proton exchange membrane fuel cell when the current density is i, E is the theoretical potential under nonequilibrium conditions, η_{HOR} is the overpotential of hydrogen oxidation reaction, $\mathrm{i}*R^{effective}_{H^+,\, anode}$ and $\mathrm{i}*R^{effective}_{H^+,\, cathode}$ are the voltage drop caused by proton conduction in anode and cathode catalyst layers, I * $\mathrm{R}_{\Omega}$is the voltage drop caused by electron conduction and proton transmission on the membrane, η_{ORR} is the overpotential of oxygen reduction reaction, and η_{mt} is the voltage drop caused by mass transfer impedance. Next, by explaining each part of this formula, we will further analyze the causes of voltage drop in PEMFC.

Among the above potential losses, the voltage drop caused by proton and electron conduction resistance may be best understood. The electron conduction resistance and proton conduction resistance R_{Ω} on the membrane can be expressed by the following formula,

$$R_{\Omega} = R_{\mathrm{e}} + R_{\mathrm{mem}} \tag{1.4}$$

R_{e} is the electronic conduction resistance of proton exchange membrane fuel cell, including the resistance of the cell itself and the contact resistance. R_{mem} is the resistance of proton conduction in the membrane. R_{e} can be obtained by directly

testing the voltage drop of the membrane less fuel cell when it is powered on according to Ohm's law. The membrane should be removed during the test, because the results of the in-situ test include not only the inherent electronic conduction resistance R_e of the fuel cell itself, but also the proton conduction resistance R_{mem} on the membrane, so the contributions of both are summarized into R_Ω.

Electronic conduction resistance mainly includes the resistance of electronic conductive material itself (gas channel, gas diffusion layer and catalyst layer) and interface contact resistance (gas channel and gas diffusion layer, diffusion layer and catalyst layer). The gas diffusion layer and catalyst layer are porous media, and the gas flow channel is a circuitous pipeline (almost no electron conduction area), so the electron conduction resistance is related to the internal pressure of the battery and the area of the conductive material.

R_{mem} is the resistance encountered when protons are transferred from anode to cathode, which depends on the conductivity of proton membrane and is related to relative humidity RH and temperature. Although the conductivity of the membrane can be obtained by off-site analysis, in-situ measurement can not only obtain the proton membrane resistance, but also simplify the calculation of the whole potential loss of the fuel cell. The relationship between proton membrane conductivity and membrane resistance is as follows.

$$R_{\text{men}} = \frac{\delta_{\text{men}}}{\kappa_{\text{men}}} \tag{1.5}$$

In which δ_{men} is the thickness of proton membrane and κ_{men} is the conductivity of proton membrane. Like the previous electronic conduction resistance test, it is difficult to separate the proton membrane resistance from the current in-situ test results (AC impedance or current-breaking method). In addition to R_{mem}, the test results also contain a part of electronic conduction resistance R_e. Therefore, the electron conduction resistance R_e and the proton conduction resistance R_{mem} on the membrane are combined into R_Ω, and the whole potential drop of the fuel cell is added.

$$E_{\text{cell}} = E - \text{i} * R_\Omega \tag{1.6}$$

Another function of proton membrane is to prevent hydrogen from diffusing to cathode. Once hydrogen diffuses through the proton membrane and comes into contact with the cathode catalyst layer, it will react with the oxygen of the cathode (parasitic reaction) to generate an additional cathode current. The relationship between this penetration current and hydrogen permeability is as follows.

$$i_x = 2FK_{H_2}(T, RH\%)\frac{p_{H_2}}{\delta_{men}} \tag{1.7}$$

In the formula, i_x is the permeation current and the membrane permeability of hydrogen, which is affected by temperature and humidity RH. p_{H_2} is the partial

pressure of hydrogen. Penetration current i_x is generally about several milliamps, which can be ignored in the high current discharge area, but contributes a lot in the low current discharge area and cannot be ignored. This penetration current is inconsistent with the current mechanism produced by proton penetrating the membrane, so it is classified into the kinetic overpotential equation, and this current cannot be used in ohmic correction of proton membrane or catalyst layer.

The resistance of another proton exchange membrane fuel cell comes from the diffusion of protons in the cathode or anode catalyst layer. Because the reaction kinetics of cathode is very slow, it is difficult for protons to react immediately at the interface between catalyst and proton membrane. Instead, they diffuse into the catalyst layer and react step by step like crossing the proton membrane, and this part of diffusion distance produces resistance. Generally, the catalyst layer is composed of carbon-supported platinum catalyst and proton conductive binder, and the conductivity is lower than that of proton membrane, and the relationship is as follows.

$$\kappa_{\text{eff}} = \kappa_{\text{men}} \cdot \frac{\varepsilon_i}{\tau} \tag{1.8}$$

in the formula, the effective conductivity of κ_{eff} catalyst layer, ε_{i} is the volume fraction of polymer, and τ is the bending degree. The following formula can be obtained by relating the effective diffusion coefficient to the resistance of protons in the catalyst layer.

$$R_{H^+}^{\text{effective}} = \frac{\delta_{cl}}{3 \cdot \kappa_{\text{eff}}} \tag{1.9}$$

$R_{H^+}^{\text{effective}}$ is the resistance when protons are transmitted in the cathode or anode catalyst layer, and δ_{cl} is the thickness of the cathode or anode catalyst layer. The constant 3 in the denominator is obtained on the assumption that the current is evenly distributed in the catalyst layer, and can be compensated according to the utilization rate of the catalyst. Considering the potential loss of this part, the voltage loss formula becomes.

$$E_{\text{cell}} = E - \text{i} * R_{H^+,\,anode}^{effective} - \text{i} * \text{R}\Omega - \text{i} * R_{H^+,\,anode}^{effective} \tag{1.10}$$

The above formula lists the resistance of protons in the anode catalyst layer, because the resistance of this part is generally negligible, mainly because the exchange current density of hydrogen oxidation reaction at the anode is very high, and this reaction can occur at the interface between the electrode and the membrane, without further diffusion of protons.

Finally, the influence of the kinetic process of oxygen reduction and hydrogen oxidation. For oxygen reduction reaction, the exchange current density is of small order of magnitude. Newman put forward the following normalized exchange current density formula,

$$i_{o(T,\,p_{O_2})} = i^*_{o(T)} \left(\frac{p_{o_2}}{p^*_{o_2}}\right)^{\gamma} \left(\frac{a_{H^+}}{a^*_{H^+}}\right)^{\beta} \left(\frac{a_{H_2O}}{a^*_{H_2O}}\right)^{a} \tag{1.11}$$

$i_{o(T,\,p_{O_2})}$ is the exchange current density of oxygen reduction reaction, which is related to temperature, partial pressure of oxygen p_{o_2}, and activity of water a_{H_2O} and proton a_{H^+}. $i^*_{o(T)}$ is the normalized exchange current density at temperature T and oxygen partial pressure $p^*_{o_2} = 101.3$ kPa and $a^*_{H^+} = a^*_{H_2O} = 1$. γ, α, β are the order of reaction kinetics. The exchange current density determines the reaction rate and then affects the overpotential, and the relation is as follows.

$$\eta_{ORR} = b \cdot \log\left(\frac{i + i_x}{10 \cdot (L_{ca} \cdot A_{Pt,el}) \cdot i_{o(T,p_{o_2})}}\right) \tag{1.12}$$

In the formula, η_{ORR} is oxygen reduction overpotential, b is Tafel slope, which is 2.303 RT/a_cF, $L_{ca}$is cathode platinum loading, $A_{Pt,el}$ are effective surface areas of platinum in membrane electrode. Generally speaking, the overpotential of oxygen reduction is very high (in the current density range of <1.0 cm^{-2}, the overpotential exceeds 400 mV), which makes the oxygen reduction process an important factor restricting the performance of the cell.

For the hydrogen oxidation reaction of anode, because the exchange current density is very high and the reaction overpotential is very small, the reaction overpotential has little contribution to the overall pressure drop of PEMFC. Add overpotential of oxygen reduction and hydrogen oxidation to formula (1.10), and get.

$$E_{\mathrm{cell}} = E - \eta_{\mathrm{HOR}} - \mathrm{i} * R^{effective}_{H^+,\,anode} - \mathrm{i} * R_{\Omega} - \mathrm{i} * R^{effective}_{H^+,\,anode} - \eta_{\mathrm{ORR}} \tag{1.13}$$

Except i*R_Ω, all kinds of voltage drops discussed above are related to the kinetic process of hydrogen oxidation reaction and oxygen reduction reaction. However, the design of the flow channel, the performance of the diffusion layer and the structure and design of the components of the proton exchange membrane fuel cell will affect the oxygen transfer. If oxygen cannot reach the reaction area of the catalytic layer smoothly, it is most likely that condensed water affects mass transfer, which will also cause the loss of the overall potential of the cell. According to different materials and test conditions, the mass transfer loss is about 150 mV in high current region. Therefore, the potential contribution of each part of the final proton exchange membrane fuel cell can be summarized in Formula (1.13). The contribution of these losses to each current density region on the polarization curve is shown in Fig. 1.2.

In the figure, iR corresponds to$\eta_{HOR} + i^* R^{effective}_{H^+,\,anode} + i^* R_{\Omega} + i\ ^* R^{effective}_{H^+,\,cathode}$ in formula (3.13). Up to now, it is difficult to quantify or avoid the potential drop caused by mass transfer in proton exchange membrane fuel cells. Other influencing factors have corresponding quantitative analysis methods and optimization methods. As mentioned earlier, the kinetics of hydrogen oxidation is very fast, and the anode overpotential and proton transfer resistance are very small, so the optimization of

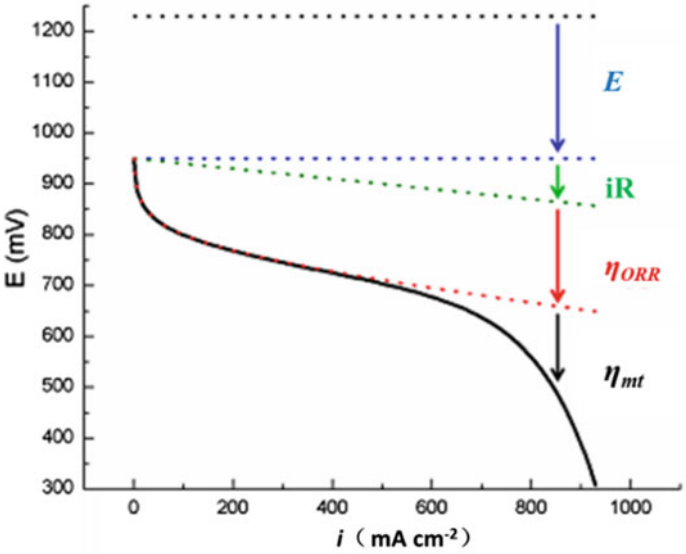

Fig. 1.2 Schematic diagram of PEMFC voltage loss

cell performance is not considered, sometimes even ignored. The film resistance can be improved by reducing the film thickness. The resistance of protons in cathode catalyst layer can also be optimized by reducing the thickness of catalyst layer or platinum loading. At present, reducing the overpotential of oxygen reduction is the most studied. The main methods are to develop new catalysts, increase the exchange current density of oxygen reduction reaction, optimize the performance of catalysts and electrodes, and reduce the overpotential of oxygen reduction. In terms of improving mass transfer loss, the main research direction is to improve the material properties of diffusion layer and catalyst layer, and optimize the interface structure between diffusion layer and catalyst layer. However, the exact location of condensation and the mechanism of water infiltration into diffusion layer and catalytic layer are still unclear, which makes it more difficult to study this part.

Chapter 2
Mechanism of Oxygen Reduction Reaction

Zuzhen Zhao and Pei Kang Shen

Abstract This chapter describes the mechanism and kinetics of oxygen reduction. Therefore, the adsorption of O_2 on transition metals will be discussed in detail below. The adsorption of oxygen molecules on the surface of the catalyst is complicated. It not only has the associative adsorption and dissociative adsorption adsorbed in molecular form but also the oxygen atoms can enter the interior of the metal lattice to form surface oxides. The adsorption of oxygen on a metal catalyst can be regarded as adsorption on metal ions, similar to the case where metal and oxygen are bonded in a transition metal complex. Due to the complexity of the oxygen reduction reaction, the path and mechanism of the reaction are mainly studied by experimental and theoretical calculations. The main difference between the two-electron and the four-electron reaction pathway is the intermediate product. So from the middle product ratio of the reaction and the influencing factors, we know that they are methods of continuous two-electron reactions. Although there have been many studies on the mechanism of oxygen reduction, and many convincing theories have been proposed, there are still many details on the main reaction pathways for oxygen reduction which are not clear enough.

Keywords Oxygen reduction reaction · ORR · H_2O_2 · Multielectron

Oxygen reduction reaction is the basic reaction in electrochemical reaction. It is the cathode reaction of a series of electrochemical cells such as fuel cell, secondary lithium-air cell, metal-air cell, etc. It is also the main conjugate reaction occurring during the process of metal corrosion. The kinetics of the oxygen reduction reaction is slower than that of the anode reaction, and at the same time, the potential on the electrode such as Pt is higher, which makes the active metal or carrier on the

Z. Zhao
Research Institute of Tsinghua University in Shenzhen, Shenzhen, Guangdong, China

P. K. Shen (✉)
Collaborative Innovation Center of Sustainable Energy Materials, Guangxi Key Laboratory of Electrochemical Energy Materials, College of Chemistry and Chemical Engineering, Guangxi University, Nanning, Guangxi 530004, China
e-mail: pkshen@gxu.edu.cn

P. K. Shen, *Electrochemical Oxygen Reduction*,
https://doi.org/10.1007/978-981-33-6077-8_2

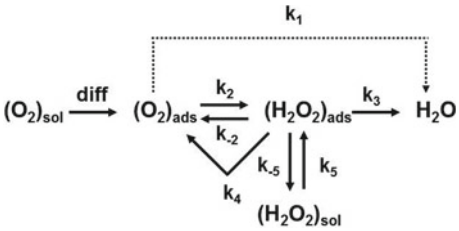

Fig. 2.1 Oxygen reduction pathway

cathode easy to corrode. Both are of the main factors restricting the large-scale application of fuel cells. Understanding the mechanism of oxygen reduction reaction will help to find more cheaper and stable catalysts. Therefore, to understand the kinetic mechanism of oxygen reduction reaction and its intermediate reaction has always been one of the important goals of electrochemical research.

As the process of oxygen reduction reaction is a complex multielectron reaction, the total reaction consists of many basic reactions, involving multiple intermediate products including HO_2^-, H_2O_2, O_2^{2-} and HO− etc. In order to understand the mechanism of the oxygen reduction reaction and the key steps and factors restricting the oxygen reduction reaction, it is necessary to understand the kinetic mechanism and parameters of each step reaction and the intermediate products of the reaction. However, at present, there is no method to observe the process of oxygen reduction reaction in situ, which is mainly inferred by detecting the intermediate products generated in each step of reaction. Therefore, the mechanism of oxygen reduction reaction has not been thoroughly studied. The oxygen reduction reaction pathway is mainly shown in Fig. 2.1 [14].

Oxygen molecules dissolved in the solution diffuse and adsorb to the surface of catalyst atoms (such as Pt). According to the concentration of atoms in the reaction solution and the reaction conditions, a complete or incomplete monoatomic adsorption layer is formed on the surface of the catalyst. There are several pathways for reduction reaction under the electrochemical function.

(I) Direct reduction reaction s(k_1): oxygen atoms adsorbed on the surface of the catalyst directly obtain four electrons and reduce to H_2O, and the reaction mechanism is as follows:

$$O_2 + 4H^+ + 4e^- \rightarrow 2H_2O,\ E^o = 1.229\ \text{V} \tag{2.1}$$

(II) Continuous two-electron reduction reaction: oxygen atoms adsorption on the surface of the catalyst reacts and generate hydrogen peroxide (k_2) through a two-electron reduction pathway, and there are three possible subsequent reactions at this stage, a. hydrogen peroxide is oxidized to regenerate oxygen, b, hydrogen peroxide continues to undergo two-electron reduction to generate water (k_4), or hydrogen peroxide adsorbed on the surface of the catalyst desorbs, dissolves in the solution, and directly becomes the final product hydrogen peroxide (k_5), namely:

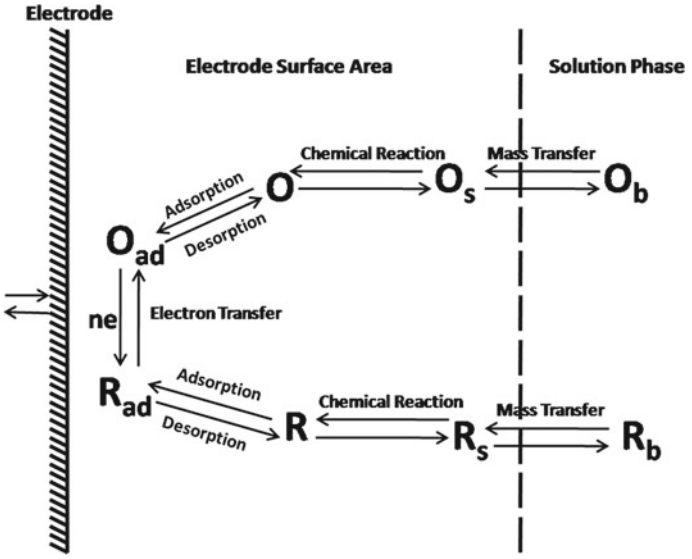

Fig. 2.2 Process of Oxygen Reduction

$$O_2 + 2H^+ + 2\,e^- \rightarrow H_2O_2,\ E^o = 0.67\ V \tag{2.2}$$

$$H_2O_2 + 2H^+ + 2e^- \rightarrow H_2O,\ E^o = 1.77\ V \tag{2.3}$$

There are many factors affecting the final product and intermediate path of oxygen reduction reaction. Oxygen reduction is a gas electrocatalytic reaction occurring at the interface between catalyst and solution, while gas–solid interface heterogeneous catalytic reaction contains three main steps of adsorption, reaction and desorption (Fig. 2.2).

The electrode reaction process refers to the heterogeneous reaction that occurs only at the electrode–electrolyte interface. Unlike the homogeneous reaction, its reaction rate is affected by the kinetic variables such as current and potential, as well as the rate of matter to the electrode and various Surface effect related, its expression is

$$\upsilon = \frac{i}{nFA} = \frac{j}{nF}. \tag{2.4}$$

where i is the current, n is the number of electrons transferred during the reaction, F is the Faraday constant, A is the working area of the electrode, and j is the current density; To get the information of the electrode reaction, you can measure the current as a potential function, iE The curve is obtained.

For an electrode reaction O + ne ⇌ R, the current (or electrode reaction rate) is determined by the rate in the following process: ① substance transfer (transfer of oxide O from the bulk solution to the electrode surface or reduced species R generated from electrode surface transfer to the bulk solution); ② adsorption, dissociation, desorption, protonation process of the oxide O on the surface of the electrode; and adsorption and desorption of the reducing material R on the electrode surface;③ Electron transfer on the surface of the electrode is a chemical reaction kinetics related to the potential applied to the electrode surface, and is also a core part of our electrochemical concerns.

In general, the magnitude of the current during an electrochemical reaction is generally limited by one or more slow reactions, which are referred to as rate-determining steps, where any step in the reaction given by Fig. 2.2 may become a speed-stop step. Below we will discuss in detail the three main processes that affect the reaction rate of the electrode, namely the mass transfer, the adsorption and desorption of molecules on the electrode surface and the kinetics of the electrode reaction.

During the oxygen reduction reaction, oxygen molecules and intermediates dissolved in the solvent participate in the adsorption process, so the mechanism of the adsorption is indistinguishable from the mechanism of the heterogeneous catalytic reaction. According to the adsorption principle, adsorption can be divided into physical adsorption and chemical adsorption, and the adsorption force is also different. The physical adsorption is caused by the inter-force, which is relatively weak and does not affect the molecular structure. The chemical adsorption force is a force formed by a chemical bond between an oxygen atom and a platinum atom, and belongs to a chemical bond force. This force is relatively strong, involving electron rearrangement between the adsorbate molecules and solids, and breaking or formation of chemical bonds. Therefore, the chemical adsorption force has a great influence on the structure of the adsorbed molecules.

The change of the potential energy of the adsorption system during the adsorption process is shown in Fig. 2.3: The energy change of the A molecule near the solid surface is divided into physical adsorption and chemical adsorption [6]. The physical adsorption process is represented by the AYX curve and the chemical adsorption process is represented by the BXZ line. The B position in the figure is the energy state when the molecule dissociates into an atom. D is the dissociation energy. When the molecules are close to the metal surface, the potential energy decreases. When physical adsorption occurs (at the Y point), the heat Qp is released. When the molecule absorbs more energy and reaches the X point, this position is the chemical adsorption state of the dissociated atom (Z point in the figure), and the absorbed energy is called the adsorption activation energy E_a. The intersection X is a transition state that is physically adsorbed to chemical adsorption. From the chemical adsorption state, desorption, and to molecular state, an E_d energy barrier is to be overcome. This part of the energy is called desorption activation energy.

The change in energy from molecular adsorption and desorption is described by the potential energy curve of adsorption. In addition to this, it is necessary to understand the interaction between the molecule and the catalytic surface to understand

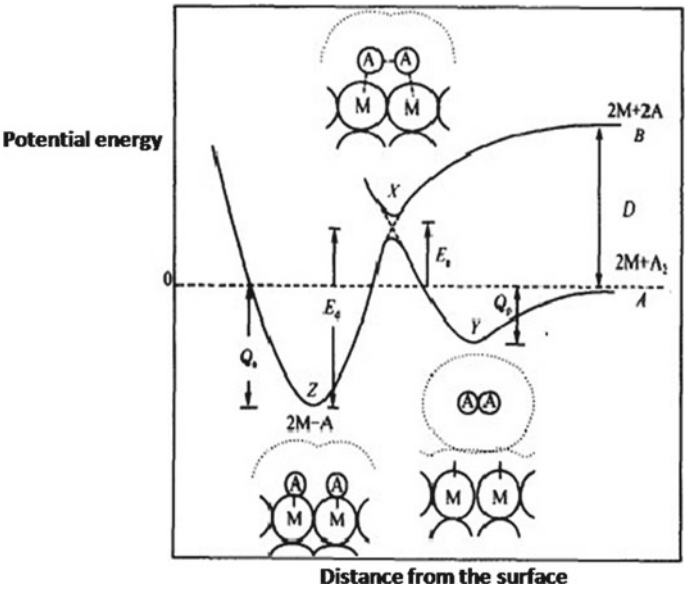

Fig. 2.3 Adsorption energy of molecule A on the surface of metal M

the mechanism of chemical adsorption of the molecule on the solid surface. The d-band model studies the interaction between the catalyst and adsorbed molecules on its surface. For many simple heterogeneous and electrocatalytic reactions, the difference in catalytic performance between different metals is explained to some extent, revealing different active sites the introduction of heterogeneous metal and some other factors have an influence on reactive activity. The energy band model is a simple model that can describe the interaction between atoms, molecules and solids, with particular emphasis on the trend of adsorption energy of small molecules on transition metals and describes the effects of alloys, coordination effects and structures on adsorption energy. To a large extent, the pros and cons of the transition metal catalytic properties depend on the bonding strength between itself and the main intermediate, because the activation energy of the reaction is closely linked to the adsorption energy of the intermediate product. Norskov et al. [11] summarized a series of laws for the dissociation and adsorption of molecules on metal surfaces. The calculation results show that there is a linear relationship between the adsorption energy of the molecule and the dissociation energy barrier, namely Bronsted-Evans-Polanyi (BEP) [8]. This linear relationship indicates that most of the molecules that undergo dissociation adsorption have similar transition states. The best catalyst should have moderate adsorption capacity for the intermediates of the reaction, neither too strong nor too weak. This is the famous Sabatier principle, which is reflected in the periodic table of the typical volcanic curve, as shown in Fig. 2.4. The metal on the left side of the noble metal has strong adsorption capacity, and it is easy to form a stable oxide or nitride; while the metal on the right.

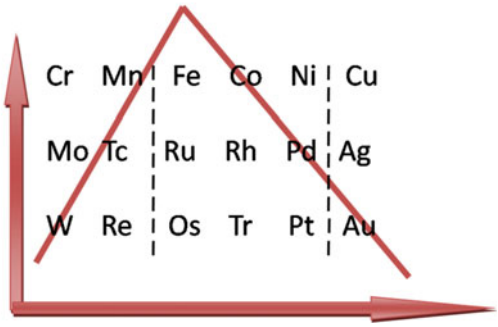

Fig. 2.4 Catalytic activity of transition metals

Side of the noble metal has weak adsorption capacity and stable performance, the reaction barrier is too high, which is not conducive to the catalytic reaction. The strength of metal adsorption is mainly due to the difference in electronic structure between different metals. For example, in the experiment of oxygen reduction, we hope that on the one hand, the M–O bond is easy to form, which is beneficial to the rupture of the O–O bond. On the other hand, the M–OH bond is not too strong, and the OH is easily removed from the surface, leaving more activity. The site is adsorbed by the O_2 molecule, so the catalyst with good oxygen reduction reaction t is the Pt, Pd electrode at present.

This chapter describes the mechanism and kinetics of oxygen reduction. Therefore, the adsorption of O_2 on transition metals will be discussed in detail below. The adsorption of oxygen molecules on the surface of the catalyst is complicated. It not only has the associative adsorption and dissociative adsorption adsorbed in molecular form but also the oxygen atoms can enter the interior of the metal lattice to form surface oxides. The adsorption of oxygen on a metal catalyst can be regarded as adsorption on metal ions, similar to the case where metal and oxygen are bonded in a transition metal complex. Yeager et al. [15] believe that there are three kinds of oxygen molecules adsorption on an electrode as shown in Fig. 2.5.

(i) Griftiths mode: the oxygen molecule acts laterally with a transition metal atom, the orbital in the oxygen molecule interacts with the hollow dz_2 orbital of the central atom; and the at least partially filled dxx or dyz orbital of the central atom feeds back to the oxygen molecular orbital. And this strong interactions can weaken the O–O bond and even cause dissociative adsorption of O_2 (double-position adsorption), which is beneficial to the direct four-electron reduction reaction of O_2. On the surface of clean Pt, the activation of oxygen is likely to proceed according to this mode.

(ii) Pauling mode: one side of the oxygen molecule points to the transition metal atom and interacts with the dz_2 orbital of the central atom through the orbit. In this way, only one atom in the oxygen molecule is strongly activated, which is

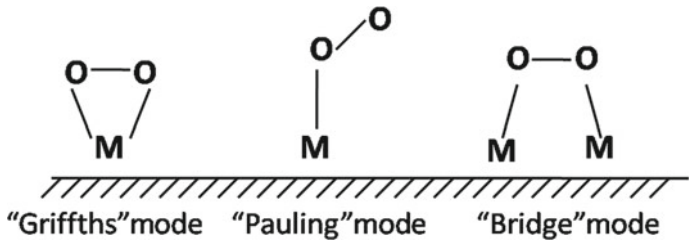

Fig. 2.5 Adsorption of oxygen molecules on the catalyst surface

not conducive to breaking the O–O bond. Two-electron reaction, the reduction of oxygen on most electrode materials may be according to the mode

(iii) Birdge mode: If the nature and spatial position of the central atom are appropriate, the oxygen molecule can also be activated by two central atoms simultaneously to promote the activation of two oxygen atoms in the molecule. This mode is obviously beneficial to the oxygen four-electronic reaction. In principle, Griffth mode and Pauling mode belong to "single site adsorption," while bridge mode is "dual site adsorption." Research results show that if there is a small amount of underpotential deposition (UPD) on the surface of Pt, adsorption of Ag atoms, which has a significant inhibitory effect on oxygen reduction, indicating that oxygen molecules may be mainly adsorbed on Pt by bridge "double position."

For organic catalysts containing functional groups, the catalytic reduction of oxygen is achieved by the conversion of the corresponding redoxant of the organic catalyst, as shown in Fig. 2.6.

The following chapter will analyze the oxygen reduction mechanism by analyzing the two main reaction pathways of oxygen reduction. At present, the main method for studying the mechanism of oxygen reduction is to observe the intermediate product by changing influencing factors during the reaction for inferring the reaction mechanism. It is known from the intermediate reactants HO_2^-, H_2O_2, O_2^{2-}, HO^-, etc. that the reaction mechanism of secondary electrons is definitely there. But at present, most of the intermediate products are further reduced due to the means of detecting H_2O_2, resulting in whether there is a direct four-electron reaction. If the latter is practical, the main factors affecting the ratio between the two pathways of oxygen reduction and their mechanisms are the main problems of the study.

2.1 Mechanism of Two-Electron and Four-Electron Reduction Reaction

Due to the complexity of the oxygen reduction reaction, the path and mechanism of the reaction are mainly studied by experimental and theoretical calculations. The main difference between the two-electron and the four-electron reaction pathway is

the intermediate product. So from the middle product ratio of the reaction and the influencing factors, we know that they are methods of continuous two-electron reactions. Although there have been many studies on the mechanism of oxygen reduction, and many convincing theories have been proposed, there are still many details on the main reaction pathways for oxygen reduction which are not clear enough. The oxygen reduction reaction produces a small amount of H_2O_2 on the electrocatalysts single-crystal Pt and Pt particle for the outside H_{upd} (hydrogen under potential deposition) potential range, and this is evidence that the four-electron reaction is considered to be the main reaction pathway for oxygen reduction. Some theories suggest that the dissociated oxygen is adsorbed on the Pt electrode, and then the adsorbed oxygen atoms are directly reduced. While some others believe that this reaction process must undergo two-step continuous two-electron reaction process. At the same time, whether the intermediate product H_2O_2 during the oxygen reduction reaction produced by electrochemical reduction or chemical adsorption is also inconclusive. Therefore, the control reaction theory of oxygen reduction reaction has been in dispute. One theory that is currently widely accepted is that the process in which O_2 first acquires electrons is a controlled reaction of the oxygen reduction reaction. However, there are many other theories that hold different views. The control reaction is to destroy the O–O double bond by the double-site mechanism, or the process of O_2 initial adsorption on the surface of the electrocatalyst, or the process of desorbing O or OH from the surface of the electrocatalyst. Among them, Wang et al. believe that OH_{ads} desorption in the potential interval of OH_{ads} adsorption is a control step. While in the interval where Pt has no product adsorption, O_2 acquired electrons is a control step. These theories all indicate that the multielectron oxygen reduction is a complex multistep reaction, and there are many reaction paths depending on the morphology of the electrode and the difference of electrode potential.

Studying the mechanism of the two-electron reaction need first considers the formation and detection of H_2O_2 products. At present, rotating ring plate electrode and rotating disk electrode for detecting H_2O_2 are commonly used. The third chapter will introduce the oxygen reduction research technology in detail, which will be briefly introduced here.

Usually, the current on the planar electrode is not uniform and the mass transfer rate in the aqueous solution is also relatively small. Which these bring many problems to electrochemical manufacture and electrochemical theoretical research. Uneven current density distribution in electrochemical devices means that the production potential of each part of the electrode surface cannot be fully utilized and may cause uneven distribution of reaction products. When the electrode reaction is studied in the laboratory, this means that the polarization of electrode surfaces is different throughout, making data processing complicated. The most common is the rotating electrode. The mathematical processing of the liquid phase mass transfer kinetics on the surface of the rotating electrode is relatively simple, and the uniform current distribution on the electrode surface is the basic experimental method in electrochemical research.

The electrode is a disk electrode and a ring disk electrode that rotates around an axis perpendicular to the disk surface through its center. As shown in Fig. 2.7,

the liquid below the electrode rises at the center of the disk and is thrown around when approaching the disk. Therefore, the center of the disk corresponds to the surface of the electrode which is farther away from the center of the disk, and the relative tangential liquid flow rate due to the rotation of the disk also increases in proportion. The current calculation on the disk when the concentration polarization is not considered can be expressed by the following Eq. (2.5).

$$I_d = 0.62nFD_o^{2/3}v^{-1/6}\omega^{1/2}c_o^0 \tag{2.5}$$

where I_d is the current collected by the disk, n is the number of electrons transferred in the reaction, F is the Faraday constant, D_o is the saturation concentration of oxygen

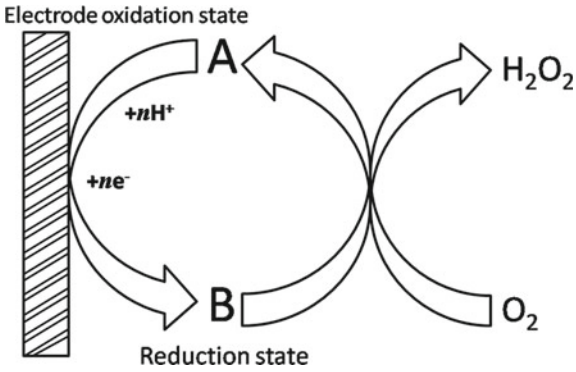

Fig. 2.6 Adsorption pathways of oxygen molecules on the catalyst surface

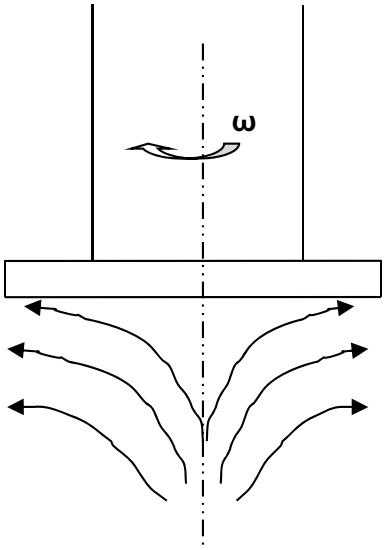

Fig. 2.7 The structure of the rotating disk electrode

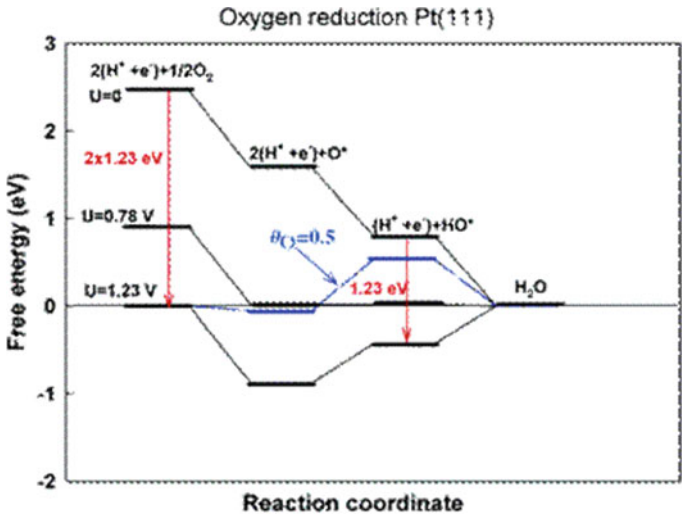

Fig. 2.8 Free energy variation of oxygen at different potentials and low initial oxygen blanket concentration (θ_o) reduction on Pt(111) plane

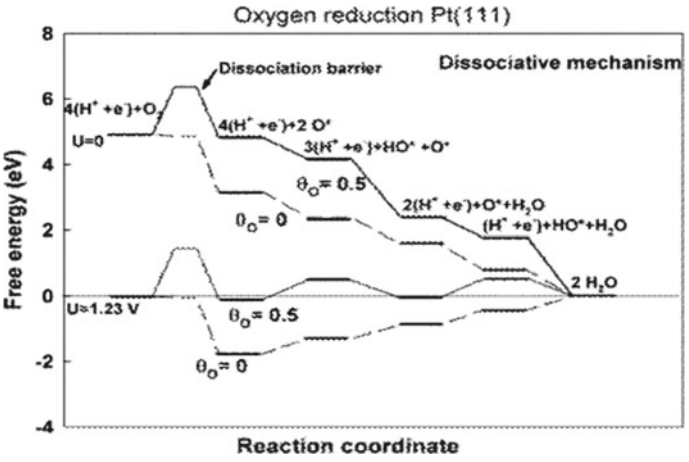

Fig. 2.9 Free energy variation of oxygen at different potentials and different initial oxygen blanket concentration (θ_o) reduction on Pt(111) plane

in the electrolyte, v is the viscosity, and ω is the rotational speed of the rotating disk. Equation (2.5) is used to calculate the oxygen reduction limit current density.

On the rotating ring disk electrode, O_2 is reduced to an intermediate product on the disk of the rotating electrode, and the intermediate product is thrown to the periphery due to the centrifugal force. The mechanism of the oxygen reduction reaction is

studied by adding a certain voltage to the peripheral metal ring for oxidizing these intermediate products.

The current of the two-electron reaction (I_{2e-}) is given by:

$$I_{2e-} = \frac{I_R}{N}. \tag{2.6}$$

where I_R is the current collected on the ring electrode and N is the current collection efficiency of the ring disk electrode.

The current (I_D) on the rotating disk can be composed by the sum of the two-electron reaction current and the four-electron reaction current.

$$I_{\mathrm{D}} = \mathrm{I}_{2e\text{-}} + \mathrm{I}_{4e\text{-}} \tag{2.7}$$

The following formula calculates the average number of electrons involved in the ORR reaction.

$$\frac{I_{\mathrm{D}}}{n_{e-}} = \frac{\mathrm{I}_{2e\text{-}}}{2} + \frac{\mathrm{I}_{4e\text{-}}}{4} \tag{2.8}$$

where n_{e-} represents the average number of electrons participating in the ORR reaction, which is obtained by equation,

$$\mathrm{n}_{e-} = \frac{4I_D}{I_D + I_R/N} \tag{2.9}$$

Generally, the value of n is between 2 and 4. When $n_{e\text{-}}$ is 4, it indicates that the reaction is completely a four-electron reaction process, and there is no secondary electron reaction; when $n_{e\text{-}} < 4$, it indicates that H_2O_2 is formed, and the reaction is two-electron reaction and four-electron reaction. when $n_{e\text{-}}$ is 2, indicating that all of the oxygen molecules are reduced by the secondary electron reaction path. Calculating the ratio of the two-reaction path can be calculated by calculating the ratio of the generated H_2O_2.

$$\mathrm{x}_{H_2O_2} = \frac{2I_R/N}{I_D + I_R/N} \tag{2.10}$$

When all oxygen passes through the two-electron reaction path, the value of x is 1, and if all are directly reduced by the four-electron reaction process, the value of x is 0, usually the value of x is between the two. The value reflects the path and mechanism of ORR reaction.

2.1.1 Starting Step of Oxygen Reduction

There are two theories about the initial step of oxygen reduction being the key for the reaction [11]. The adsorption mode of oxygen molecules is divided into two kinds of reaction pathways, dissociative and associative. The reaction mechanism of dissociative is O_2 double bond. First, the O–O bond is broken into a free O atom, and the O atom is adsorbed onto the surface of the catalyst metal, and hydrogen protons and electrons are obtained by the reaction to further react to form water.

$$O_2 + * \rightarrow O_2* \tag{2.11}$$

$$O_2 * + (H^+ + e^-) \rightarrow HO_2* \tag{2.12}$$

$$HO_2 * + (H^+ + e^-) \rightarrow H_2O + O* \tag{2.13}$$

$$O * + (H^+ + e^-) \rightarrow HO* \tag{2.14}$$

$$HO * + (H^+ + e^-) \rightarrow H_2O + * \tag{2.15}$$

The reaction mechanism of the oxygen molecules combination is that the adsorbed oxygen molecules with proton first produce of HO_2* and then the HO_2* further reduces to form water (i.e., as shown in Eqs. 2.11–2.13). From Eqs. 2.11 to 2.13, we know the process that oxygen molecule adsorbed on the catalyst surface first obtains an electron and a hydrogen atom to form HO_2*, and then continue to obtain an electron and a hydrogen atom to form $H_2O + O*$. This step produces H_2O_2 and free oxygen atom adsorbed on the surface of the catalyst. The free oxygen atom obtains an electron and a hydrogen atom to form HO* , and HO* continues to reduce to form water (as in Eqs. 2.14 and 2.15). The latter two steps reaction are the same as the combined reaction, and the difference between the two is whether the front reaction is obtained by adsorption reduction or oxygen molecules separated into free oxygen atoms directly.

Figure 2.8 shows the opposite reaction process by theoretical calculations. At a voltage below 0.78 V, H_2O separates into OH or O, and above 0.78 V while H_2O will be dissociated. At this potential, H_2O is dissociated while electrons/H are transferred to oxygen atoms adsorbed on the surface of the electrode. OH activation leads to a slower process of oxygen reduction. This is also the reason why the oxygen reduction potential or the dissociation initiation potential of H_2O is high. This process is consistent with the results of a large number of experiments. H_2O/OH^- can be formed only when oxygen is adsorbed on the platinum electrode and there is nothing with strong adsorption on the surface of the electrode. Conversely, when there is a strong anion or hydrogen adsorption on the surface of the electrode, the amount of generated hydrogen peroxide will increase as the coverage of adsorbed chemical

material increases, which indicates that oxygen reduction is more likely to generate H_2O_2 than H_2O.

Therefore, through the results of thermodynamic calculations, both ways are achievable. In an electrochemical environment, it takes 498 kJ/mol to break the O–O bond, which requires that the bond energy M–O between the metal and the oxygen atom must be greater than 250 kJ/mol. But by transferring an electron to generate O_2^-, then separating O_2^- only require 98.7 kJ/mol, and the associative mechanism is the main pathway under the action of electric field. By conclusion, Neurock et al. [11] believe that the initial step of the oxygen reduction reaction should be that the oxygen molecule adsorbed on the surface of the electrode first gets an electron and then combines with the hydrogen proton diffused on the surface of the electrode to form HO_2*.

On the other hand, when $^{18}O_2$, $^{16}O^{18}O$ and $^{16}O_2$ are used as reactants, no isotope exchange effect is observed in the product H_2O_2/HO_2^-, so oxygen molecules are more likely to form O_2^- as an intermediate product. This result also supports the path of oxygen reduction through the combination of oxygen molecule.

2.1.2 Control Factor of Oxygen Reduction Reaction

Although the rate-determining step of the oxygen reduction reaction has been in dispute. Currently, the control reaction process in which O_2 first acquires electrons is widely accepted. However, there are many other theories that hold different views. The control reaction is to destroy the O–O double bond by the double-active site mechanism, or the process of O_2 initial adsorption to the surface of the electrocatalyst, and the desorbing process of O or OH from the surface of the electrocatalyst. Among them, Wang et al. [13] consider that the OH_{ads} desorption in the potential interval of OH_{ads} adsorption is a control step, while in the interval where Pt has no product adsorption, O_2 acquiring electron is a control step. These theories all indicate that the oxygen reduction multielectron reaction is a complex multistep reaction, and there are many reaction paths depending on the morphology of electrode and the electrode potential.

A large number of studies have shown that oxygen reduction reaction conditions are the key factors affecting the mechanism of oxygen reduction reaction. They mainly include different catalyst metals or metal compounds, different carrier materials, catalyst surface state, electrode structure and oxygen concentration.

This book will analyze the effects of catalysts and carrier materials in Chap. 4. For details, please refer to Chap. 4. Currently, for commercial catalyst systems, Pt metal particles (Pt/C) supported on high surface area carbon materials as catalysts still exhibit the best activity and stability in both experimental and industrial applications. Therefore, in this section, the Pt/C catalyst is taken as an example to discuss the surface state and the electrode structure of the Pt metal for study of ORR mechanism.

The important influencing factors on the Pt/C electrocatalyst are first the oxygen concentration Po_2 adsorbed on the surface, and the rate of the ORR reaction is linear

with the oxygen partial pressure. These indicating that the double bond of O_2 will be destroyed after the control step of the ORR. Second, the concentration of H^+ is also an important influence factor. While the electrode potential is higher than 0.8 V, the slope of the Tafel curve is from $-120\ mV^{-1}$ to $-60\ mV^{-1}$.

The reaction rate of the ORR on the Pt/C electrocatalyst can be expressed by the following formula [4, 9].

$$j_k = -k_0 n F P_{O_2} [H^+](1-\theta)\exp(-\frac{\Delta G_\theta}{RT})\exp(-\frac{a_c F E}{RT}) \tag{2.15}$$

K_0 is the reaction constant of the control step, n is the number of electrons participating in the reaction, F is the Faraday constant, P_{O2} is the oxygen pressure, (1-θ) is the ratio of the Pt surface without covered by the oxide, and ΔG_θ is the free energy of oxygen adsorption, E Indicates the electrode potential.

Since the exchange current density is very low, the activity of oxygen reduction is determined by the reaction current density of a specific voltage (generally 0.9 V) in the power control region as catalytic activity (SA, A cm^{-2}), or for the dispersed catalyst material determined by catalytic activity (MA, A g^{-2}).

The intermediate product of the ORR reaction was calculated by this method, but research showed that the particle size of the catalyst and the spacing between the particles have a great influence on the detection of the oxygen reduction intermediate. Chen and Kucernak et al. developed a novel method to study the mechanism of oxygen reduction [4]. They used carbon fiber with implanted submicron Pt (40 nm) to prepare microelectrodes. For single Pt particle, the transmission radius is hemispherical, the distance equaling to the radius of the particle. Therefore, for a 36-nm particle, the diffusion coefficient is 10 cm s^{-1}. If a rotating disk electrode is used to achieve the same diffusion coefficient, the rotational speed should reach 4.6*108 r min^{-1} which is obviously unachievable. Under this condition, the Pt particles can be regarded as a polycrystalline Pt disk. However, it was found that the number of electrons involved in the transfer reaction decreased from 4 to 3.5 by using a diffusion-enhanced method. It shows that only 75% of the oxygen molecules are reduced to water, and the remaining oxygen molecules are only reduced to hydrogen peroxide. This shows that the traditional four-electron reaction proposed by the small amount of hydrogen peroxide molecules obtained by the RRDE test prevails because the slow rate of H_2O_2 causes the H_2O_2 escaping from the catalyst surface, readsorption to the Pt surface and further reduced to the water.

This important experiment led us to find that many of the conclusions of the RRDE test need to be reconsidered, especially regarding the mechanism of the oxygen reduction reaction, whether it is the direct four-electron reaction or the two-electron reaction, or the two reaction pathways ratio calculation in the total reaction. H_2O_2 molecule is more difficult to escape from the catalytic layer surface due to the experimental conditions using the high specific surface area carbon-supported Pt nanoparticle as a catalyst compared to the polycrystalline Pt disk surface. After H_2O_2 molecule is produced, it is readsorbed to the adjacent Pt metal surface or the porous carbon material surface, thereby further reduced to the final product water, resulting

in a very small amount of H_2O_2 detected on the ring. This is also direct evidence that the four-electron reaction is considered to be the main pathway for oxygen reduction, but from the current point of view, the two-electron continuous reaction is greatly underestimated, and which may be the main pathway. The same conclusion was also used by Inaba [5] to reduce the loading of the PDE/C on the RRDE surface. They found that H_2O_2 molecule can be greatly increased by carrying a very low Pt/C electrocatalyst on the RRDE. The catalytic activity of oxygen reduction on the Pt particles of the cube was improved, but after repeated cyclic voltammetry scanning in 0.05–1.4 V versus RHE for a period of time, the activity of oxygen reduction was significantly decreased and the production of H_2O_2 molecules was increased. The main reason is that the Pt (100) plane on the Pt particles surface is changed to polycrystalline Pt. This conclusion can clearly indicate that the particle size and surface state of the catalyst have an important influence on the catalytic principle of oxygen reduction.

A large amount of work has shown that the decrease in the particle size of the Pt catalyst leads to lower activity of the ORR [7, 10], that is, "negative particle size function." That discovered when H_3PO_4 was used as an electrolyte. Later, this discipline was also applied to acidic electrolytes such as H_2SO_4 and $HClO_4$. When the Pt particle is less than 4–5 nm, SA will decrease with the decrease of the Pt particle size.SA will reach the maximum value on Pt particles of 3–4 nm and reduce the Pt particle size, SA will decrease the ratio of active sites on the surface of the large Pt particles decreases which is the reason why increasing particle size also leads to decrease of SA. Therefore, reducing the Pt particles continuously does not necessarily increase the activity of the catalyst.

The effect of Pt different crystal plane on the catalytic activity of ORR is obvious. There are some regular patterns in different electrolytes [1]: sulfuric acid, Pt(110) > (100) > (111); perchloric acid, Pt(100) > (110) > (111); and alkaline potassium hydroxide Pt(100) > (110) > (111). These all indicate that the Pt(111) crystal plane has the lowest catalytic activity in different electrolytes. The reason for this law is that the different anions included $HSO4^-$ have the strongest adsorption on the Pt(111) crystal plane, resulting in a decrease in the active catalytic position.

In addition to the adsorption of anions in the above solution, another factor that may explain the decrease in the particle size of the Pt catalyst leading to lower activity of the ORR is the adsorption of oxygen-containing molecules on the Pt particle surface [10]. As the atomic proportion of the low coordination number on the surface of the metal particles increases, surface free energy increasing makes it easier to adsorb atoms and other molecules. O_2 forms strong chemical adsorption on the surface of Pt particles below 3 nm. In solution, OH_{ads} are more readily adsorbed on the surface of smaller Pt particles. The reduction of the active sites on the surface of the Pt catalyst by these oxygen atoms or oxygen-containing groups is also one of the reasons why smaller Pt particle leads to a decrease in ORR performance.

In addition, the decrease of O_2 diffusion coefficient on the Pt particles surface is also one of the possible factors for the effect of Pt particle reduction on the catalyst activity decrease [4]. Since the Pt particles reduce the diffusion coefficient of O_2 and its intermediates on the surface of Pt, leading to the catalytic performance is lowered.

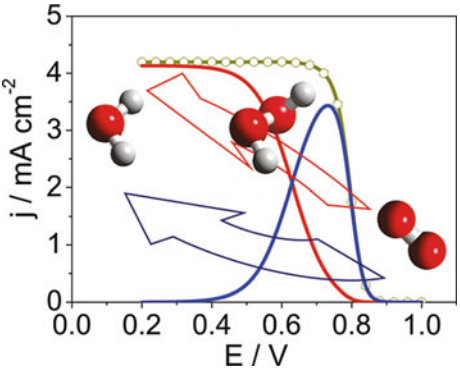

Fig. 2.10 Reaction mechanism diagram of oxygen on different potentials and Pt particles (blue indicating direct four-electron reaction and red indicating continuous two-electron reaction)

The oxygen reduction reaction is a complex multielectron reaction, and the control steps and reaction mechanism are yet to be further studied. Some mechanism models have been proposed for reactions. For example, Ruvinskiy and Savinova et al. [12] attempted to establish an ORR model using experimental and theoretical calculations of 3D porous electrodes. It is proposed that the oxygen reduction is a complex reaction of four-electron reaction and two-electron continuous reaction, and the control condition of the reaction controls by the reaction potential, as shown in the Fig. 2.10

(I) Below 0.8 V, the four-electron reaction pathway is inhibited by ORR mainly through the continuous two-electron reaction pathway.
(II) H_2O_2 is reduced by chemical decomposition rather than direct electrochemical reduction to form water.
(III) At a potential between 0.8 V and the initial potential of ORR, the four-electron reaction is the main reaction pathway.

References

1. Wroblowa HS, Yen Chi P, Razumney G (1976) Electroreduction of oxygen: A new mechanistic criterion. J Electroanal Chem Interfac 69:195–201
2. Kaiji Z. et al.: Catalysis basis (2005)
3. Nørskov JK (2004) Origin of the overpotential for oxygen reduction at a fuel-cell cathode. J Phys Chem B 108:17886–17892
4. Logadottir A (2001) The brønsted–evans–polanyi relation and the volcano plot for ammonia synthesis over transition metal catalysts. J Catal 197:229–231
5. Yeager E (1984) Electrocatalysts for O_2 reduction. Electrochim Acta 29:1527–1537
6. Wang JX, Zhang J, Adzic RR (2007) Double-trap kinetic equation for the oxygen reduction reaction on Pt(111) in acidic media. J Phys Chem A 111:12702–12710
7. Bard AJ (2002) Electrochemical methods: fundamentals and applications, student solutions manual, 2nd edn.
8. Adžić RR, Wang JX (1998) Configuration and site of O_2 adsorption on the Pt(111) electrode surface. J Phys Chem B 102:8988–8993

9. Chen S, Kucernak A (2004) Electrocatalysis under conditions of high mass transport rate: Oxygen reduction on single submicrometer-sized pt particles supported on carbon. J Phys Chem B 108:3262–3276
10. Maillard F, Pronkin S, Savinova ER (2008) Size effects in electrocatalysis of fuel cell reactions on supported metal nanoparticles. In: Fuel cell catalysis. Wiley Inc., pp 507–566
11. Inaba M (2006) Controlled growth and shape formation of platinum nanoparticles and their electrochemical properties. Electrochim Acta 52:1632–1638
12. Kinoshita K (1990) Particle size effects for oxygen reduction on highly dispersed platinum in acid electrolytes. J Electrochem Soc 137:845–848
13. Mukerjee S, McBreen J (1998) Effect of particle size on the electrocatalysis by carbon-supported pt electrocatalysts: An in situ xas investigation. J Electroanal Chem 448:163–171
14. 14El-Deab MS, Sotomura T, Ohsaka T (2005) Morphological selection of gold nanoparticles electrodeposited on various substrates. J Electrochem Soc 152:C730–C737
15. Ruvinskiy PS (2011) Using ordered carbon nanomaterials for shedding light on the mechanism of the cathodic oxygen reduction reaction. Langmuir 27:9018–9027

Chapter 3
The Measurements of the Oxygen Reduction Reaction

Juhong Cheng, Xiaojun Lin, and Pei Kang Shen

Abstract The oxygen reduction reaction is a typical electrocatalytic reaction, which is very sensitive to the surface state of the electrode and the type of adsorbate, and is the object of many basic researches. In this chapter, we mainly start from the oxygen reduction reaction mechanism, discuss the measurement technology of the oxygen reduction reaction in detail, discuss the key techniques for obtaining the oxygen reduction polarization curve, and analyze the experimental data.

Keywords Oxygen reduction reaction · Cyclic voltammetry · Rotating ring disk electrode · Reference electrode · Working electrode · Electrochemical specific surface area

3.1 Oxygen Reduction Reaction Mechanism and Testing Method

As described in 1.2.2, the kinetics of the oxygen reduction reaction limits the overall performance of the fuel cell. In addition, this reaction also plays an important role in the corrosion system. Oxygen reduction is also a typical electrocatalytic reaction, sensitive to the surface state of the electrode and the type of adsorbate, so it is also the object of many basic researches. These basic researches focus on the effects of different electrode materials, crystal faces, surface atom modifications, electrolyte types, and contaminating ions on reaction kinetics and reaction progress.

J. Cheng
Hunan Aerospace TianLu Advanced Matirial Testing Co., Ltd., Ningxiang High-Tech Zone, Changsha, China

X. Lin
Southern University of Science and Technology, Shenzhen, Guangdong, China

P. K. Shen (✉)
Collaborative Innovation Center of Sustainable Energy Materials, Guangxi Key Laboratory of Electrochemical Energy Materials, College of Chemistry and Chemical Engineering, Guangxi University, Nanning, Guangxi 530004, China
e-mail: pkshen@gxu.edu.cn

P. K. Shen, *Electrochemical Oxygen Reduction*,
https://doi.org/10.1007/978-981-33-6077-8_3

Research on the electrochemical behavior of oxygen has been around for a long time, and there are many research teams and review articles. Although the reduction of molecular oxygen is a crucial step, the oxygen reduction reaction is an extremely complex four-electron reaction, and unstable intermediates are easily formed in the reaction, such as hydrogen peroxide generation by two-electron reaction (H_2O_2), thereby reducing energy conversion efficiency. The intermediate, H_2O_2, will damage the membrane in fuel cells by combining transition metal cations, like iron ion, to proceed with a Fenton reaction as follows.

$$M^{2+} + H_2O_2 \rightarrow M^{3+} + {}^{\bullet}OH + OH^- \tag{3.1}$$

$$M^{3+} + H_2O_2 \rightarrow M^{2+} + {}^{\bullet}OOH + H^+ \tag{3.2}$$

where M^{2+} is the transition metal cation. These metal ions will react with hydrogen peroxide and produce-free radicals to attack the weak sites in a membrane. In a perfluorinated sulfonic acid membrane electrode, the weak polymer end groups or the side chain cleavage are the potential sources of carboxylic acid end groups. Once the carboxylic acid end groups are formed, it will be attacked by free radicals in an unzipping reaction:

$$\sim CF_2COOH + 2OH^- \rightarrow COOH + CO_2 + 2HF \tag{3.3}$$

If the structure of the membrane is damaged, the pinhole formation, fragmentation and short circuit of the system become possible. The following is a brief introduction to the common reaction mechanism of oxygen reduction in fuel cell systems.

3.1.1 Oxygen Reduction Reaction Mechanism

In the acidic solution, the total reaction formula of the four-electron reaction in which oxygen is reduced to water is expressed as follows.

$$O_2 + 4H^+ + 4e^- \rightarrow 2H_2OE = 1.229\ \text{V}\ vs.\ \text{SHE}25\,^{\circ}\text{C} \tag{3.4}$$

The overall reaction equation in an alkaline solution is,

$$O_2 + 2H_2O + 4e^- \rightarrow 4OH^-E = 0.40\ \text{V}\ vs.\ \text{SHE}25\,^{\circ}\text{C} \tag{3.5}$$

1.229 and 0.40 V are theoretical equilibrium potentials, calculated from thermodynamic data.

The Gibbs free energy generated by the standard mole of 1 mol of liquid water is −237.142 kJ mol^{-1}, the Faraday constant is 96485 C mol^{-1}, the number of transferred electrons is 2, and the conversion formula of Gibbs free energy and electrode potential is obtained.

$$E = -\frac{\Delta G}{\mathrm{nF}} \tag{3.6}$$

It can be calculated that the theoretical equilibrium potential for generating 1 mol of liquid water at 298 K is 1.229 V. It can be seen from the Gibbs free energy of this reaction that the reaction is thermodynamically spontaneous, but because the reaction rate is extremely slow and limited by the reaction kinetics, an external catalyst is needed to improve its kinetics performance.

In addition, the entire process of this reaction involves many intermediates, electron transfer processes, and reaction steps. Figure 3.1 shows the chemical potential of different oxygen reduction intermediates in an acidic solution. As can be seen from this figure, there are many possible reaction processes during the reaction, but the actual situation is much more complicated than that described in this figure, because different intermediates will interact with the electrode surface, including the intermediate product adsorbed on the surface of the electrode, the surrounding adsorbed material, and the ions in the electrolyte solution, etc., so the chemical potential of the intermediate product is affected by the system test conditions. At present, the simplification steps of the oxygen reduction reaction approved by most research teams are direct four-electron reaction and indirect two-electron reaction. The difference between the two is whether there is an intermediate product hydrogen peroxide. As seen in Fig. 3.1, the direct four-electron reaction requires the surface of the electrode

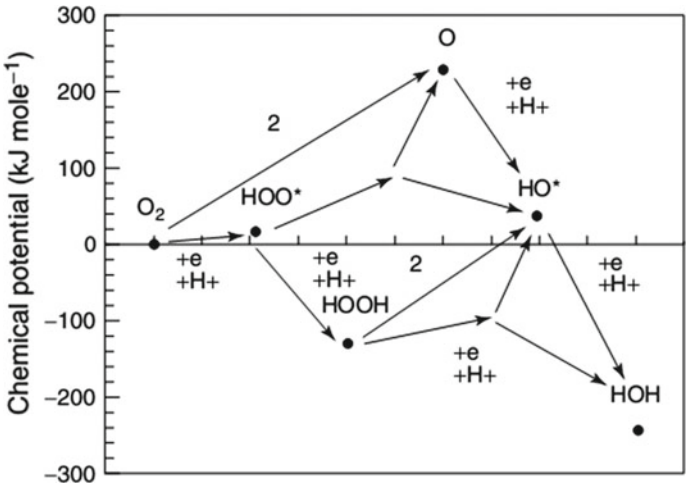

Fig. 3.1 Chemical potential of different oxygen reduction intermediates in an acidic solution

to have a chemical potential for the complete reduction of the intermediate species, which can only be achieved on a few metal surfaces, such as the (100) crystal planes of platinum, palladium, silver and gold. Most materials, including carbon, mercury, other crystal faces of gold, and oxide-modified metals, are indirect two-electron reactions. The direct four-electron reaction and indirect two-electron reaction in acidic and alkaline solutions are briefly described below.

In an acidic aqueous solution, the reduction reaction of oxygen on a metal such as platinum is carried out by a direct four-electron reaction, taking metal Pt as an example, that is,

$$2Pt + O_2 \rightarrow 2Pt\text{-}O \tag{3.7}$$

$$2Pt\text{-}O + 2H^+ + 2e^- \rightarrow 2Pt\text{-}OH \tag{3.8}$$

$$2Pt\text{-}OH + 2H^+ + 2e^- \rightarrow Pt + 2H_2O \tag{3.9}$$

The overall response is still of formula (3.4).

In addition, if the oxygen molecule is reduced by an indirect two-electron reaction, two electrons are reduced to H_2O_2.

$$O_2 + 2H^+ + 2e^- \rightarrow H_2O_2 E = 0.68\ \text{V}\ (vs.\ \text{SHE}\ 25\ ^\circ\text{C}) \tag{3.10}$$

Due to the instability of the intermediate H_2O_2, the catalytic decomposition reaction is easily carried out and further reduced to water.

$$H_2O_2 + 2H^+ + 2e^- \rightarrow 2H_2O \quad E = 1.78\ \text{V}(vs.\ \text{SHE}\ 25\ ^\circ\text{C}) \tag{3.11}$$

The process (3.11) also yields two electrons, but the potential of the reaction is much higher than the process (3.4), resulting in increased energy consumption for energy conversion. From the perspective of output voltage and energy conversion, the number of electron transfer in the four-electron process is double that of the two-electron process, that is, the energy is converted to twice. This is why oxygen reduction is a direct four-electron process. Especially in the energy conversion process, the four-electron oxygen reduction reaction is a requirement for maximizing energy conversion.

In an alkaline solution, the reaction mechanism of O_2 can generally be expressed as follows.

If O_2 is directly reacted to water by direct four-electron processes, the total reaction equation is as shown in (3.4); if an indirect two-electron process occurs, the following processes may occur.

O_2 first occurs in a single electron reaction to generate O_2^-

$$O_2 + e^- \rightarrow O_2^- \tag{3.12}$$

$O_2{}^-$ is protonated to $HO_2{}^-$ by a water molecule, which is also a single electron reaction.

$$O_2^- + H_2O \rightarrow HO_2^- + OH \tag{3.13}$$

$$OH + e^- \rightarrow OH^- \tag{3.14}$$

Then the total response of the two-electronic processes is.

$$O_2 + H_2O + 2e^- \rightarrow HO_{2-} + OH^- \tag{3.15}$$

$HO_{2\text{-}}$ formed by two electron processes through O_2 has two further reaction pathways.

The first is catalytic decomposition of the electrode surface to adsorbed oxygen.

$$2HO_2^- \rightarrow 2OH^- + O_2 \tag{3.16}$$

The second is electrochemical reduction to OH^-.

$$HO_2^- + H_2O + 2e^- \rightarrow 3OH^- \tag{3.17}$$

In fuel cells, in order to obtain maximum output power and reduce corrosion of carbon carriers or other materials due to peroxides, optimization studies of oxygen reduction catalysts are directed to achieving a direct four-electron reaction of the catalyst. The two-electron reaction is mainly used to study the preparation of hydrogen peroxide.

3.1.2 Oxygen Reduction Reaction Test Means

The current techniques for studying the state of adsorption of particles on metal surfaces are basically not used to detect the mechanism of oxygen reduction in situ, mainly because these techniques basically require working under ultra-high vacuum conditions, but almost no electrochemical system is capable of working under vacuum. For example, electron or optoelectronic-based technologies, including EELS, AES, XPS, and UPS, cannot be used in situ to determine electrode reactions because the electrolyte solution will volatilize. Similarly, TPD also requires work to test the desorption of adsorbate under vacuum conditions. Infrared Reflectance Absorption Spectroscopy (IRAS) can be used for in situ testing, but the oxygen stretching IR cross-section is too small and the strong adsorption of the electrolyte

makes this test technique difficult to perform accurate analysis. X-ray absorption spectroscopy techniques such as extended X-ray absorption fine structure spectroscopy (EXAFS) and near-edge X-ray absorbing fine structure spectroscopy (NEXAFS) can also be used for oxygen reduction mechanism studies, but the information about the reaction mechanism that can be obtained is very limited [1–4]. Strasser et al. used Synchrotron radiation X-ray diffraction to study the structural properties of PtCo particles [5, 6]. Wieckowski et al. improved the NMR method to make it suitable for electrochemical working conditions, and used this method to study the oxygen reduction reaction [7].

The earliest mechanism for studying the mechanism of oxygen reduction in situ is the fixed electrode method proposed by Damjanovic et al., but the fixed electrode method was greatly affected by the mass transfer of the solution. The current in situ study of oxygen reduction kinetics mainly uses the rotating disk electrode method (see 3.2.2 for detailed analysis). Rotating disk electrode is a fluid dynamic electrode that increases liquid flow by convection and improves mass transfer. This electrode can be used to study the progress of electrochemical reactions in steady state, transient, constant voltage or constant current conditions. The voltage and current data obtained by rotating the disk electrode are plotted as a Koutecký-Levich curve with the reciprocal of the current and the reciprocal of the square of the electrode speed, the intercept of the curve is the limiting current density. The limiting current density is proportional to the electrochemical reaction rate and can therefore be used to compare the kinetic mechanisms of different reactions. Since the rotating disk electrode cannot obtain the information of the oxygen reduction reaction intermediate product, a rotating ring disk electrode has been researched on the basis of the rotating disk electrode for studying the intermediate products in the reaction process, such as H_2O_2in the oxygen reduction reaction. And this method is used to study the factors affecting oxygen reduction, such as the influence of different electrolyte solutions, including H_3PO_4, H_2SO_4, $HClO_4$, trifluoromethanesulfonic acid (TFMSA) and the like. In addition, the commonly used catalyst active material platinum and the proton membrane Nafion for PEMFC were slurried to form a catalyst electrode for oxidative kinetics studies.

3.2 Research Method of Electrochemical Oxygen Reduction Reaction

3.2.1 Cyclic Voltammetry

There are many experimental methods for testing the polarization curves of electrochemical systems. According to the types of independent variables, they can be simply divided into constant current method (control current method) and constant potential method (control potential method). The constant current method records the change relationship (polarization curve) between the corresponding electrode

potential and current density by controlling a given current density. The apparatus used in this method is simple and easy to control, but is not suitable for electrodes that vary greatly in current density or electrode surface state. The constant potential method is a technique for controlling the potential of a given electrode and measuring the relationship between the potential of the electrode and the current density. It is also the most widely used method.

According to the relationship between electrode process and time, the test method can be divided into steady-state method and transient method. The steady-state method means the current potential curve of the measuring electrode in a steady state, in this case, the current density and the electrode potential are independent of time and do not change with time. The transient method is a curve showing the current potential change of the electrode process when the steady state is not reached, and the influence of the time factor on the electrode reaction is considered. The following mainly introduces the basic working principle of the constant potential method for measuring cyclic voltammetry.

The first use of cyclic voltammetry for scientific research dates back to about 80 years ago—Electrochemical studies by Heyrovsky et al. In their research, linear scanning and cyclic voltammetry have been used for polarographic analysis. The working electrode of this test is mercury, the counter electrode and the reference electrode are both large-area calomel electrodes, and the potential region of interest is negative compared with the calomel electrode, so the cyclic voltammetry curve appears in the first quadrant. The study did not use the mathematical analysis of reversible and irreversible reaction electron transfer proposed by Matsuda and Ayabe in 1955 to determine the positive sweep potential. Moreover, there is no electronic potentiostat (invented in 1954), and the calomel electrode serves as both the counter electrode and the reference electrode, so it is necessary to correct the voltage drop caused by the solution resistance between the working electrode and the calomel electrode. After extensive application of potentiostats, cyclic voltammetry and linear voltammetry began to be applied to the three-electrode test system (Fig. 3.2). The

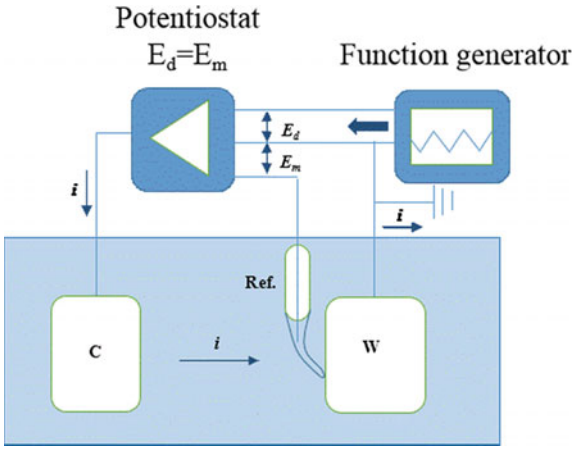

Fig. 3.2 Basic circuit diagram of the potentiostat. (W, C, and Ref. are the working electrode, the counter electrode, and the reference electrode, respectively; Ed is the driving potential difference, and Em is the test potential difference)

electrode potential can be controlled by applying a driving potential difference Ed between the reference electrode and the working electrode. In addition, by adding the Luggin capillary and shortening the distance between the Luggin capillary and the working electrode, most electrochemical tests do not require solution resistance correction for iR drop. Therefore, this potential scanning technique is applicable to most metal electrodes. Moreover, the scanning rate and the potential scanning interval of the cyclic voltammetry curve are controlled, and the electrochemical process of the metal or alloy surface is highly reproducible. Today, this potential scanning method has been widely used in the research of various electrode processes.

Figure 3.2 shows a simplified potentiostat test circuit. The most important electronic device is the potential comparison circuit, which has the following two functions. The first is to make the control potential Ed (obtainable by the function generator) equal to the effective potential difference Em between the working electrode and the reference electrode. Since the response times of the balanced potentials, Ed and Em are in the order of microseconds, the input voltage allowed by the output current can oscillate beyond 10 kHz. Another function is to convert the current signal between the working electrode and the counter electrode into a voltage signal through a resistor R. In order to ensure that the output current signal is only from the counter electrode and the working electrode, the reference electrode needs to be connected to a very high resistance R. The voltage drop of the resistor R and the potential Ed are plotted as images by an x/y recorder or as digital signals.

The potentiostat has three interfaces that can be connected to the working electrode, the reference electrode and the counter electrode. Therefore, as long as an external fixed resistor is used, the potentiostat can also be used for constant current testing. The working electrode and the reference electrode are disconnected from the potentiostat, and the input terminals of the potentiostat are connected to the fixed resistor Rg. Then, the input terminal of the reference electrode is connected to the working electrode, and the potential of the working electrode is referenced by the reference electrode. If the output potential of the constant voltage meter is Ed, the current flowing through the working electrode will be Ed/Rg. The potential on the working electrode is changed by controlling this current. Both the galvanostatic method and the potentiostatic method can be used to test the current potential curve of a specified potential region. However, for an electrode reaction with a negative resistance value (voltage increase current decreases), stabilizing one current value may result in two voltage values and two oscillations at the same time.

In a cyclic voltammetric scan, the scan rate changes the scan direction at a set reversal point. The generally selected reversal point can present the oxidation and reduction reactions that may occur in the electrode process on the scan curves in different directions, such as the oxygen process in the forward scan and the hydrogen process in the negative scan. The linear scan curve is a one-way (forward or negative) sweep volt-ampere curve over a specified potential interval. For the surface reaction process of most metals or alloys, when the scanning rate is 50–500 mVs^{-1}, the surface state of the metal or alloy is basically unchanged after undergoing a complete cyclic voltammetry scanning process, thus ensuring the test repeatability. Platinum, gold and palladium, the test results are highly reproducible. Electrochemical testing of

other electrode materials is very sensitive to the purity of the electrolyte solution. When the sweep speed is lower than 5–10 mV s^{-1}, the surface is prone to passivation. In the case of rapid scanning, impurities adsorbed on the surface may be removed by oxidation or reduction, but may also cause the electrode reaction of interest to be suppressed.

3.2.2 Rotating Circular (Ring) Disk Electrode

3.2.2.1 Rotating Circle (Ring) Disk Electrode Overview

Molecular oxygen reduction reaction is usually measured by the rotating disk electrode (RDE) or the rotating ring-disk electrode (RRDE) which is an inimitable electrode system that can give a quantitative analysis by solving the fluid dynamics and convective diffusion equation.

It has long been observed that in the stirred solution, there is a limiting current and a diffusion current of the steady state polarization curve. The current of the fixed electrode in the agitated state measured by cyclic voltammetry is much larger than that observed in the natural convection state and is less affected by the potential scanning speed. However, to keep the convection state constant, it is difficult to achieve by simply stirring the solution. In contrast, the electrode rotates to stabilize the convective mass transfer on the electrode surface. As early as 1900s, Nernst et al. used the rotating electrode to determine the current–potential curves of the reduction reactions of elements such as sulfur, bromine and so on, but they did not realize the importance of the electrode shape. Moreover, Kolthoff et al. did many electrochemical studies with a rotating cylindrical electrode but just putting a Pt wire into the glass tube. However, it is very difficult to analyze the current values in those reactions carried out in a rotating cylindrical electrode, because the fluid flow on the electrode surface are very complex. In 1942, Levich et al. proposed a formula for the limiting diffusion current density in a rotating disk electrode and founded a new electrochemistry system which is easier to reproduce the results and can do quantitative analysis called as rotating disk electrode system. Compared with the previous rotating electrode, its superiority is that the results can be analyzed via the calculation of fluid mechanics.

Since the flow of the solution on the rotating disk electrode is laminar, the cylindrical polar coordinate is used to solve the differential equation under steady state, and the following limit current i_d can be derived.

$$i_d = 0.62nFAD_0^{2/3}\omega^{1/2}v^{-1/6}C_0 \tag{3.18}$$

where ω is the angular velocity, v is the dynamic viscosity ($cm^2\ s^{-1}$), C_0 is the concentration ($mol{\cdot}L^{-1}$), A is the surface area (cm^2) of the electrode, and D_0 is the diffusion coefficient ($cm\ s^{-1}$).

Further deriving the above formula, the thickness of the effective diffusion layer in the liquid phase near the rotating disk electrode can be obtained.

$$\delta = 1.61 D_o^{1/2} v^{1/6} \omega^{-1/2} \tag{3.19}$$

From (3.19), we can see that the effective diffusion layer thickness δ is easy to control and calculate, and has nothing to do with the radius of the disk electrode, that is, it has the same value at every point on the surface of the disk. When the rotation speed is constant, since the state of the substance transport on the electrode is kept constant, it can obtain a stable convection state as compared with the simple solution stirring.

In addition, when the electrode reaction is reversible, the following formula holds.

$$\mathrm{E} = \mathrm{E}_{1/2} \pm \left(\frac{\mathrm{RT}}{\mathrm{nF}}\right) \ln\left(\frac{i_d - i}{i}\right) \tag{3.20}$$

Therefore, the current–potential curve is measured using a rotating disk electrode, and the reproducible data can be obtained in the same manner as the current–potential curve measured by polarographic analysis.

The nature of the current versus potential curves measured by RDEs has been derived in many electrochemistry textbooks and articles. Compared with the stationary electrode, the rotating disk electrode has the following advantages: (1) the concentration polarization is stable and the effect from concentration polarization can be eliminated to a lower degree, (2) the polarization curve is in a good stability, (3) it can be used to measure fast electrochemical reactions, (4) some important dynamic parameters such as diffusion coefficient, the number of electron transferred, the concentration of reactants and so on can be obtained by Levich equation and Koutecký-Levich equation, (5) the rate of mass transport of reactants can be controlled by adjusting the rotating rate ω, (6) incidental vibrations of RDE apparatus have little influence on the current response. Therefore, the rotating disk electrode has become an indispensable tool to study various electrochemical reactions on the electrode.

A common equation for analyzing the cyclic volt–ampere curve of a rotating disk electrode is the Levich equation [Eq. (3.18)] and the Koutecký-Levich (KL) equation as shown below.

$$\frac{1}{i} = \frac{1}{nFA_g k_f C_A} + \frac{1}{0.62nFA_g D_A^{2/3} \omega^{1/2} v^{-1/6} C_A} \tag{3.21}$$

where A_g is the geometric area of the electrode (cm^2), ω is the angular velocity (s^{-1}), v is the dynamic viscosity ($\mathrm{cm}^2\ \mathrm{s}^{-1}$), and k_f is the nonuniform rate constant of the electron transfer ($\mathrm{cm\ s}^{-1}$), C_A, D_A indicates the concentration of species A ($\mathrm{mol\ dm}^{-3}$) and diffusion coefficient ($\mathrm{cm}^2\ \mathrm{s}^{-1}$).

From Eq. (3.21), the plot of $1/i$ versus $1/\omega^{1/2}$ should be linear at a fixed overpotential, where the slop and intercept are proportional to the $1/n$ and $1/k_f$, respectively. Thus, the electron transferred number n and the heterogeneous rate constant k_f can be obtained. If the electrode area is $A_g = 0.2475$ cm^2, the dynamic viscosity $\upsilon = 1.009 \times 10^{-2}$ cm^2 s^{-1}, the diffusion coefficient of O_2 is $D_{02} = 1.93 \times 10^{-5}$ cm^2 s^{-1}, and the concentration of dissolved O_2 is $CO_2 = 1.26 \times 10^{-3}$ mol·L^{-1}, the electrode reaction is a four-electron reaction, and the slope value is 8.657 mA^{-1} s$^{-1/2}$.

Additionally, the reaction mechanism on the surface of electrode can be developed by using the Koutecký-Levich plots in different overpotential. The nature of $1/i$ versus $1/\omega^{1/2}$ plots in various reaction mechanisms could be found in Ref. [8]. It can predict the reaction mechanism from Koutecký-Levich plots, which is extremely significant in the development of the novel ORR catalysts. Particularly, for those new catalysts such as non-Pt catalysts, Koutecký-Levich plots provide a simple electrochemical method to study the kinetic processes.

In order to further study the intermediates of the reaction, a rotating ring disk electrode was developed. The rotating disk electrode is composed of a disc and an outer insulating layer, and the rotating ring disk electrode has a ring of rings around the periphery of the disk. The disk and the ring are insulated, and the disk or ring surrounds the center of the circle. The central axis rotates and is adjusted and measured by the rotating system (see Fig. 3.5 for its construction). The difference between the steady-state technique of the rotating ring disk electrode and the steady-state technique of the rotating disk electrode is that while measuring the polarization curve of the disk electrode, the ring electrode can be controlled at a fixed potential for detecting the generated on the disk electrode, reaction intermediate. Therefore, rotating the ring disk electrode is one of the important tools for studying or detecting the unstable intermediate products generated during the electrode process and studying the reaction mechanism of the electrode. Since two working electrodes need to be controlled simultaneously during the measurement process, the rotating ring disk electrode needs to be measured using a dual potentiostat or two potentiostats.

The rotating ring-disk electrode has the same solution flowing course as the rotating disk electrode. The bulk solution flows from the disk electrode to the ring electrode, resulting in the transmission of electrolyte which connects the ring electrode with the disk electrode so that the chemical species generated on the disk electrode can be detected on the ring electrode. For example, when there is a red body (Red) in the bulk solution, rotating up the electrode, Red will transfer from the bulk solution to the surface of disk electrode and reacts on the disk as follows.

$$\text{Red} - \text{ne-} \rightarrow \text{Ox} \tag{3.22}$$

The reduced (Ox) product produced on the disk electrode will transfer to the electrode in the direction of flowing. Therefore, if the ring electrode is fixed at a potential for Ox to be oxidized, the reaction is shown below.

$$\text{Ox} + \text{ne-} \rightarrow \text{Red'} \tag{3.23}$$

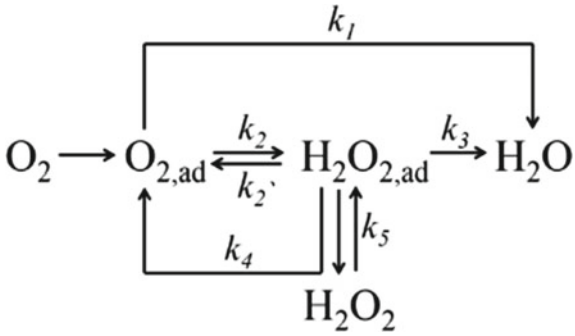

Fig. 3.3 Diagram of the oxygen reduction mechanism proposed by Damjanovic et al.

The oxidant (Ox) can be detected according to the reduction reaction formula. It can be seen that by rotating the ring disk electrode method, we can obtain information about the product or intermediate of the electrode reaction.

The mechanism of the oxygen reduction reaction is currently the most commonly used direct four-electron and indirect two-electron reactions proposed by Damjanovic et al. The mechanism diagram is shown below (Fig. 3.3).

The oxygen molecules adsorbed on the surface of the electrode can directly form water by a four-electron process (rate constant k_1), or H_2O_2 can be generated by a two-electron reduction reaction (rate constant k_2). The H_2O_2 produced can be reduced to water (rate constant k_3), either directly desorbed (rate constant k_5) or oxidized to oxygen molecules (rate constant k_2'). In addition, a part of H_2O_2 can participate in the catalytic reaction of the electrode and further catalytic decomposition (rate constant k_4). This complex process provides a thorough analysis with rotating ring disk electrodes. Reference [9] details how the oxygen reduction mechanism is analyzed by the relationship between the ring current and the disk current and the rotational speed. From the usual considerations, the following additional conditions are introduced to illustrate how to determine the rate constant of each reaction step of oxygen reduction by ring current, disk current and rotation speed.

If an oxygen reduction reaction occurs on the disk electrode and the oxidation potential of H_2O_2 is set to a potential for diffusion control, it is assumed that all reactions are first-order reactions, and O_2 and H_2O_2 are in adsorption–desorption equilibrium. Then, the relationship between the ring current I_R and the disk current I_D can be expressed by the following two equations.

$$\frac{I_D}{I_R} = \frac{1}{N}\left\{\frac{2k_1 + k_2}{k_2} + \left[\frac{(2k_1 + k_2)(k_3 + k_2' + k_4)}{k_2} + (k_3 - k_2')\right]\frac{r_{H_2O_2}}{D_{H_2O_2}\sqrt{\omega}}\right\} \tag{3.24}$$

$$\frac{I_{dO_2} - I_D}{I_R} = \frac{1}{N}\left\{1 + 2\frac{(k_1 + k_2' + k_4)}{k_2}\frac{D_{O_2} r_{H_2O_2}}{D_{H_2O_2} r_{O_2}} + \frac{2D_{O_2}\sqrt{\omega}}{k_2 r_{O_2}}\right\} \tag{3.25}$$

In the formula $I_{d\ O_2} = 4Fr_{O_2}C\sqrt{\omega}$, is the limiting current of the four-electron reaction of oxygen molecules, r = 0.62D2/3v−1/6, D is the diffusion coefficient, v is the dynamic viscosity coefficient, and ω is the electrode rotation speed.

Taking $\frac{I_D}{I_R}$ or $\frac{I_{d\ O_2}-I_D}{I_R}$ as the X axis and ω(−1/2) as the y axis, the above two equations can be drawn as two straight lines. The two slopes and the two intercepts of the two lines can list four equations with five rate constants as variables. However, an equation is still needed to completely solve these five variables. Other additional conditions can be introduced. For example, it is assumed that the change in potential does not affect the catalytic decomposition of hydrogen peroxide (k_4), or that k_2 and $k_{2'}$ are linked by the standard equilibrium potential of the O_2/H_2O_2 pair.

Therefore, the determination steps of the oxygen reduction reaction can be studied by analyzing the ratio of the ring current to the disk current at a fixed potential, I_D/I_R, $(I_d-I_R)/I_R$, and the rotational speed ω (−1/2), and solve the rate constant for each reaction step.

3.2.2.2 Film Rotating Round (Ring) Disk Electrode

The simplest catalyst activity test method is membrane electrode test, but due to the mass transfer of the oxygen reduction reactant to the membrane electrode, the incomplete utilization of the electrocatalyst and the influence of water during the reaction, it is difficult to obtain the intrinsic electrocatalysis of the high specific surface area catalyst performance. The rotating ring (ring) disk electrode can eliminate the mass transfer effect, obtain the catalytic kinetic limit, and can quantitatively analyze the intermediate products of the reaction, and then analyze the reaction mechanism.

In 2001, the research team of Schmidt and Gasteiger proposed using a thin-film rotating disk electrode method (TF-RDE) to simulate a fuel cell membrane electrode test to study the kinetic limit of the catalyst without mass transfer and no ohmic drop. This method is based on predecessors, dating back to 1976 by Stonehart and Ross, who used a rotating thin-layer electrode (RTLE) to directly test the electrochemical rate constant of a high specific surface area catalyst. The preparation method of coating the porous catalyst on the surface of the rotating disk electrode at that time was similar to the preparation of a gas diffusion electrode of Teflon platinum thin-film electrode (PTFE). Therefore, the treatment analysis method of the rotating thin layer electrode is similar to the Teflon platinum thin-film electrode model, and is established on the full penetration model, that is, the void of the porous film layer is also sufficiently wetted. In order to explain the mass transfer efficiency of the porous catalyst layer, the model introduces an effective mass transfer coefficient Ɛ, which is the ratio of the measured current density to the net current density without any mass transfer, and is affected by the exchange current density, the diffusivity of the reactant in the porous liquid region of the porous layer, the ratio of the active material of the catalytic layer, and the thickness of the catalytic layer. For slow reaction or thin catalytic layer electrodes, the effective mass transfer coefficient Ɛ is approximately equal to 1, and the Ɛ of each region of the catalytic layer is substantially the same,

that is, the concentration of the reactants is the same whether it is the porous layer on the surface of the electrode or the internal catalytic layer. This means that the current distribution of the catalytic layer is uniform. In other words, in the complete catalytic layer, the utilization of the electron conductor and the ionic conductor can reach 100%. Conversely, for fast reaction or thick film, the effective mass transfer coefficient $\mathfrak{E}$ is close to zero, and the internal catalytic layer has almost no reactive species, resulting in a decrease in the utilization rate of the catalytic layer.

In 1987, Tanaka et al. further expanded the RTLE process and tested the oxygen reduction performance of high specific surface area catalyst Fe-phthalocyanine. They applied a slurry of catalyst and Teflon to the disk electrode cavity of a rotating disk electrode with a thickness of about 100 μm, and called this technique a porous thin-layer coating technique (TPC-RDE). Although the film resistance is large enough to affect the correctness of the test for the 100 μm film, they only use RTLE to compare the similarities and differences of several catalytic systems, and do not discuss the dynamic properties of the system, or the thickness. The effect of the film on mass transfer. Subsequently, Perez et al. used the same method to study the oxygen reduction performance of carbon-supported platinum catalysts. To explain the effect of the porous membrane catalytic layer with a thickness of 100 μm on mass transfer, they cited the PTFE full permeability model to calculate the oxygen reduction kinetic parameters. However, only about 10–50% of the catalyst solids produced by Perez et al. can be wetted, resulting in incomplete electron and ion conduction of the catalyst. Similar to the TPC-RDE model, Gloaguen et al. further reduced the thickness of the film. The thin active disk electrode layer (TAL–RDE) made of the catalyst/Nafion slurry coated on the platinum carbon rotating disk electrode was about 1–7 μm, and study the oxygen reduction performance of the Pt/C electrode to verify the effectiveness of the electrode using the full penetration model. In this model, a thin active layer can be seen as a superposition of an ionic conductor (Nafion) and an electron conductor (catalyst). This means that the solubility and diffusion coefficient of the reactants in the Nafion membrane and the solubility and diffusion coefficient of the material in the solution are fully considered. Perez et al. found that the kinetic parameters can only be obtained directly from the mass transfer correction formula in catalyst samples with a film thickness of less than 1 μm. The thicker membrane mass transfer dynamics corrections are related to the applied model and additional corrections need to be considered. Moreover, the accuracy of these kinetic parameters is affected by the accuracy of the physical property data of the catalyst/Nafion layer. However, compared to TPC-RDE, TAL-RDE is 100% wetted and all catalyst layers are involved in electron and ion conduction. In 1987, Alonso-Vante and Tributsch used a rotating thin-layer electrode to study the oxygen reduction performance of Mo4.2Ru1.8Se8 catalyst. They also deposited a mixture of catalyst/Nafion on the glassy carbon rotating disk electrode, but did not give details. Preparation information and film thickness data. Similarly, Tamizhmani, Gojkovic, Claude et al. used a similar method to study the oxygen reduction performance of different catalysts. However, their film is thicker, the ratio of Nafion to catalyst is high, and the loading of the catalyst is also large, which also leads to an increase in the material diffusion resistance of the film, which affects the correction of the dynamic current

density (mathematical simulation). Calculations and experiments have shown that the reduction in film thickness is beneficial to simplify the correction of the kinetic current).

Based on previous research results, in 2001, Paulus, Schmidt and Gasteiger proposed the film rotation (ring) disk electrode method [TF–R(R)DE]. They prepared a 20 wt % Pt/Vulcan XC 72 catalyst with Nafion as a catalyst slurry and applied it to a polished glassy carbon electrode with a loading of 28 μg Pt cm^{-2}. According to the mass of Nafion and electrode area estimates, the Nafion film thickness is about 0.1–0.2 μm. Although the film thickness is submicron, it is enough to allow the catalyst particles to adhere to the surface of the glassy carbon substrate. The optical microscope shows the catalyst/Nafion layer. The total thickness is approximately 1 μm. The cyclic voltammogram of this electrode is similar to the polycrystalline Pt electrode. In addition, if the error of the dispersion of the high-resolution lens is calculated and the error of the active area is calculated by the electrochemical method, the surface platinum concentration calculated by the hydrogen underpotential deposition method is $n_{Pt,s} = 4.2 \times 10^{-8}$ mol_{Pt} cm^{-2}, this is very close to $n_{Pt,s} = 3.7 \times 10^{-8}$ mol_{Pt} cm^{-2} calculated from the dispersion of platinum and the dispersion of the grain size of the platinum particles, which means that the utilization rate of the Pt/Vulcan catalyst is basically 100%. [10] In addition, the hydrogen desorption and desorption of different platinum-loaded catalysts are linear with the platinum loading, which also demonstrates the effectiveness of the method. The repeatability of this method was also confirmed by comparing the amount of electricity in the hydrogen desorption zone of the electrode with a platinum loading of 7 μg $_{Pt}$ cm^{-2} and 14 μg $_{Pt}$ cm^{-2}.

Further discussing the mass transfer effect of the film thickness, Lawson D. R et al. added the influence of the film impedance to the Koutecký-Levich equation, fully considering the influence of the mass transfer diffusion resistance on the experiment. The corrected formula is as follows [11].

$$\begin{aligned} \frac{1}{j} &= \frac{1}{j_k} + \frac{1}{j_d} + \frac{1}{j_f} \\ &= \frac{1}{j_k} + \frac{1}{Bc_0\omega^{1/2}} + \frac{L}{nFc_fD_f} \end{aligned} \tag{3.26}$$

where j_k and j_d are the net kinetic current density and the diffusion limit current density, respectively, j_f is the limiting current density of the Nafion membrane, B is the Levich constant, c_0 is the concentration of the reactant in the solution, and c_f is the reactant in the membrane. The concentration, D_f is the diffusion coefficient of the reactant in the film, and L is the thickness of the film. On the smooth electrode, j_f does not exist, and the measured current density is only related to j_k and j_d. If the film thickness can be reduced such that j_f is much larger than j_k and j_d, then the film resistance is negligible. Paulus et al. mapped the Koutecký-Levich curves with different platinum loadings and different film thicknesses. The KL curve intercepts and film thicknesses of different film thicknesses were plotted to obtain the Nafion

film limiting current density j_f when the Nafion film thickness was $\leq$0.3 μm. For 40 mA.cm^{-2}, when the net kinetic current is less than 4 mA.cm^{-2}, which is less than 10% of the limiting current density j_f of the Nafion membrane, its effect on the measured current is negligible. When the same calculation method calculates 333 K, the limit current density j_f of the Nafion membrane is 70 mA cm^{-2}. As long as the net kinetic current is less than 7 mA.cm^{-2}, the effect on the measured current is negligible. This also means that the maximum mass activity obtained from the experiment is 1 A.mg-1, which is very close to the maximum mass activity of the actual PEMFC. In addition, the research team verified the effectiveness of this method in hydrogen reduction and oxygen oxidation, and introduced TF-RRDE. The collection coefficient of the method and the influence of film thickness were discussed. The results show that the method is suitable for testing oxygen reduction and high reproducibility of intermediate materials, and the data deviation is within the experimental allowable range.

The TF-R(R)DE method is simple, the catalyst film is completely wetted, the participation rate of electron conduction and ion conduction is 100%, the amount of catalyst required is very small, and the current correction is simple and easy, and the kinetics of the catalyst can be directly quantitative analysis of the limits. Therefore, this method has been widely applied to the electrochemical kinetic performance analysis of catalysts since Schmidt and Gasteiger proposed and verified feasibility.

3.3 Electrochemical Reduction Test

The oxygen reduction test first requires a suitable electrolytic cell. The electrolytic cell for measuring the oxygen reduction reaction of the rotating circular (ring) disk electrode is composed of a glass tank, a working electrode, a counter electrode and a reference electrode. Here the working electrode is a rotating circular (ring) disk electrode.

3.3.1 Reference Electrode

The measurement of the oxygen reduction reaction requires a stable reference electrode, the reference electrode does not contaminate the electrolyte and itself cannot be contaminated by the electrolyte. Reference electrodes commonly used in electrochemical testing include standard hydrogen electrodes (SHE), saturated calomel electrodes (SCE), silver/silver chloride electrodes (Ag/AgCl), mercury/mercury oxide electrodes (Hg/HgO), and Reversible hydrogen electrode (RHE).

The measurement of the oxygen reduction reaction requires a stable reference electrode, which should not contaminate the electrolyte and itself should not be

contaminated by the electrolyte. Reference electrodes commonly used in electrochemical testing include standard hydrogen electrodes (SHE), saturated calomel electrodes (SCE), silver/silver chloride electrodes (Ag/AgCl), mercury/mercury oxide electrodes (Hg/HgO), and Reversible hydrogen electrode (RHE).

The standard hydrogen electrode referred to as "SHE" is a hydrogen electrode that is reversible under standard conditions. A primary standard reference electrode for measuring the hydrogen electrode potential of various reversible electrodes. The platinum-plated platinum sheet was immersed in a solution containing hydrogen ions, and a platinum-plated platinum sheet was continuously impinged with a stream of pure hydrogen, and the hydrogen gas escaped from the upper portion. The siphon and other electrodes on one side can form a battery. The following reversible electrode reactions were carried out when hydrogen was adsorbed on platinum black and contacted with an aqueous solution:

$$1/2\mathrm{H_2g} \rightleftharpoons \mathrm{H^+}\left(a_{\mathrm{H}}^{+}\right) + \mathrm{e^-} \tag{3.27}$$

According to the Nernst equation, the electrode potential (E_{H^+}/H_2) is related to hydrogen ion activity (a_{H^+}), hydrogen pressure, temperature, etc.

$$E_{H^+,H_2} = E^{\theta}_{H^+,H_2} + \frac{RT}{F}\log\frac{\mathrm{a}_{H^+}}{(P_{H_2})^{1/2}} \tag{3.28}$$

If the temperature is constant, $a_{\mathrm{H}}{}^{+} = 1$, $P_{H_2}\mathrm{P_{H2}} = 101.325$ Pa, specify the electrode potential of the hydrogen electrode

$$E_{\mathrm{H^+,H_2}} = 0$$

This electrode is then referred to as a "standard hydrogen electrode." The hydrogen electrode is very sensitive when it is applied. To obtain a stable electrode potential, it must meet strict experimental conditions. The reversible hydrogen electrode is derived from a standard hydrogen electrode, the difference being that the electrolyte solution of the reversible hydrogen electrode is identical to the electrolyte solution of the test system.

If a silver chloride is plated on the silver wire and then immersed in a solution of chloride, it is a silver–silver chloride electrode. Ag–AgCl electrode structure system is Ag | AgCl(s) | KCl, the electrode reaction is.

$$\mathrm{AgCl\ (s)} + \mathrm{e^-} \rightleftharpoons \mathrm{Ag(s)} + \mathrm{Cl^-(l)} \tag{3.29}$$

Like the calomel electrode, the electrode potential depends on the chloride ion activity in the solution, i.e.,

$$E = E^{\theta}_{\mathrm{Ag/AgCl}} - \frac{2.303RT}{F}\log \mathrm{a}_{Cl^-} \tag{3.30}$$

The detailed preparation method of the Ag/AgCl electrode is a thermal decomposition method and an electroplating method, wherein the electroplating method is simple, and the process is as follows: First, the silver wire is taken and the surface oil is first washed with acetone, and if silver is plated on the silver wire, it is required first elute with ammonia water and then rinse carefully with distilled water. Then, the silver electrode was used as the anode, the platinum wire was used as the cathode, and a layer of silver chloride was electroplated in a 1 mol·L^{-1} hydrochloric acid solution for 30 min (current density of 2 mA.cm^{-2}), and finally rinsed with distilled water. The electrode produced is purple-brown and this electrode can be applied directly without a liquid junction.

If platinum wire is used as the substrate, silver plating should first be applied to the platinum wire. Platinum wire silver plating method: First, prepare a silver plating solution ($AgNO_3$ 3 g, KCl 60 g, concentrated ammonia water 7 mL, add water to make 100 mL solution), then a platinum wire to be plated as a cathode, another platinum wire as an anode, and a series of about 2000 Ω variable resistor, voltage is set to 4 V, electroplate at 0.5 mA.cm^{-2} current density for 0.5 h. Wash the silver-plated electrode and then plate a layer of silver chloride in the same manner as above.

In 0.1 mol·L^{-1} KCl solution, the electrode potential of Ag/AgCl electrode is equal to 0.2880 V (SHE, 25 °C). The electrode potential of silver–silver chloride electrode is stable, reproducible, simple in structure and convenient to use. It is also relatively stable in seawater, so it is widely used for ship cathodic protection in addition to its application in the laboratory.

The calomel electrode is one of the most widely used reference electrodes in the laboratory. It consists of metallic mercury and mercurous chloride (Hg_2Cl_2) and potassium chloride solution.

Hg | Hg_2Cl_2 (saturated), KCl (X mol·$L^{-1)}$ (X represents the molar concentration of KCl in solution.)

$$\mathrm{HgCls} + 2\,e^- \rightleftharpoons 2\mathrm{Hgl} + 2\,\mathrm{Cl}^- \tag{3.31}$$

$$E = E^{\theta}_{\mathrm{Hg_2Cl_2/Hg}} - \frac{2.303RT}{F} \log a_{\mathrm{Cl}^-} \tag{3.32}$$

A platinum wire is sealed in the inner glass tube, the platinum wire is inserted into pure mercury (thickness 0.5 to 1 cm), a paste of mercurous chloride and mercury is placed underneath, and potassium chloride is placed in the outer glass tube. The solution constitutes the calomel electrode. The contact portion of the lower end of the electrode with the solution to be tested is a porous substance such as a sintered ceramic core or a glass sand core or a capillary channel. When the temperature is fixed, the electrode potential of the calomel electrode is determined by the chloride ion activity. When the chloride ion activity is constant, the electrode potential is also constant, regardless of the pH of the solution to be tested. Different concentrations of potassium chloride solution can make its potential have different constant values. At 25 °C, different concentrations of potassium chloride solution can have different potentials

Table 3.1 Calomel electrode potential corresponding to different concentrations of potassium chloride solution (SHE, 25 °C)

KCl solution concentration ($mol \cdot L^{-1}$)	0.1	1.0	4.2 (saturation solution)
Electrode potential (V)	+0.3365	+0.2828	+0.2438

for their potentials. At 25 °C, the electrode potentials of the calomel electrodes of different concentrations of potassium chloride solution are based on standard hydrogen electrodes as follows (Table 3.1).

The saturated calomel electrode is very stable, easy to prepare and store, and easy to use. However, the results obtained with 0.1 or 1.0 $mol \cdot L^{-1}$ calomel electrodes are better. Because they can reach equilibrium potential quickly, and their potential is less dependent on temperature change, while the saturated reference electrode is affected by temperature. Larger.

The mercury–mercury oxide electrode is a commonly used reference electrode for alkaline solution systems. The electrode reaction is.

$$HgO + H_2O + 2\,e^- \rightleftharpoons Hg + 2\,OH^- \tag{3.33}$$

The standard electrode potential is 0.1100 V.

When using a standard hydrogen electrode, a saturated calomel electrode or a silver/silver chloride electrode as the reference electrode, the system needs to be pH corrected and temperature corrected because the standard electrode potential is specified at a certain temperature and pH. In a strong electrolyte solution, for every 1 pH increase, the potential should move 59 mV in the negative direction. For example, the measurement range set for an acidic solution (pH = 0) is 0–1 V (potential difference is 1 V). When the pH is 7, the measurement range should be corrected to −0.413–0.587 V. Only with such correction can the desired curve appear in the measurement range. The potential of the reference electrode is typically measured at 25 °C. When the temperature changes, temperature correction is also performed. The temperature correction formula is as follows (in the case of SHE),

$$E_{SHE,T\neq 298K} = E_{SHE,298K} + (T - 298)\left(\frac{\partial E}{\partial T}\right)_P \tag{3.34}$$

In the above formula, $E_{SHE,298}$ K is the electrode potential at 298 K or the standard electrode potential of the electrode, and $E_{SHE,T\neq 298}$ K is the electrode potential at the actual test temperature.$\left(\frac{\partial E}{\partial T}\right)_P$ is a temperature gradient at constant pressure and can be obtained from the electrochemical manual or reference electrode instructions.

In addition, if the working electrode is a Pt electrode and the reference electrode is a chloride ion electrode such as a saturated calomel electrode (SCE), a salt bridge is required. Because the chloride ions diffused into the solution are highly adsorbed on the Pt electrode, thereby affecting the oxygen reduction performance of the Pt electrode. However, when the test period is long, the salt bridge cannot effectively

prevent the chloride ions on the reference electrode from diffusing to the test electrode. Mayrhofer et al. used an ion-conducting membrane (Nafion®) instead of a salt bridge to study the effect of a saturated calomel electrode on the oxygen reduction of a platinum electrode after using an ion-conducting membrane. The results show that the oxygen reduction test is stable for up to 290 min using a system of three conductive films, independent of free chloride ions. The Nafion® ion-conducting membrane consists of a polytetrafluoroethylene skeleton and a side chain containing a sulfonate group. The sulfonate group is hydrophilic, and the polytetrafluoroethylene skeleton is hydrophobic, and the membrane allows water and cations to diffuse through. It rejects negative ions that are electrically equivalent to sulfate groups, such as chlorine, thereby preventing the passage of chloride ions.

If a reversible hydrogen electrode (RHE) is used as the reference electrode (see the U-shaped portion of Fig. 3.4), it is convenient to use. The solution in the reference electrode is the same as the test system, so pH calibration and temperature correction are not required. The measurement range of the instrument does not need to be changed regardless of the pH of the test solution. Moreover, since the electrolyte solution of the reversible hydrogen electrode is identical to the electrolyte solution of the electrolytic cell, the reference electrode does not introduce chloride ions, so there is no problem that the chloride ions contaminate the electrode, so that it is not necessary to use a salt bridge or a barrier film, so that the measurement system is simple.

The reversible hydrogen electrode can be prepared on site to ensure the purity and freshness of the electrode system. Figure 3.4 shows the electrolytic cell and reference electrode we designed. In Fig. 3.4, A and B are electrodes, C is a piston, D is a fixed (oxygen) inlet, E is a socket for the counter electrode, G is opened for insertion

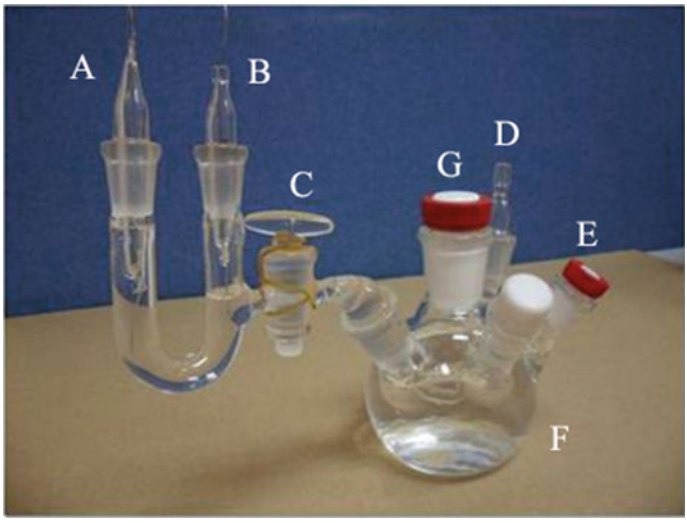

Fig. 3.4 Electrolyzer and reference electrode for rotating the ring electrode

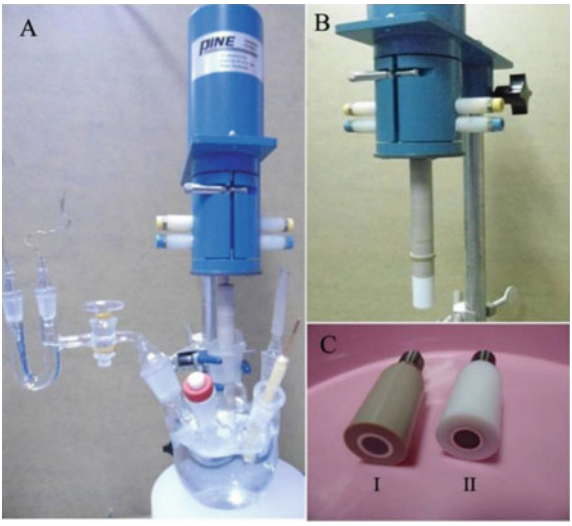

Fig. 3.5 Rotating ring disk electrode assembly. **a** Rotating ring disk electrode integral device, **b** Research electrode and rotating shaft connection and **c** Rotating ring disk electrode

into the working electrode, and F is the main body of the electrolytic cell storage liquid. According to this design, the piston C is first opened during use, and the same solution as the electrolyte solution in the electrolytic cell is filled with the reference electrode glass tubes A and B to communicate with the solution in the electrolytic cell, and then the piston C is closed in time. The two platinum or platinum black electrodes of A and B are respectively connected to a potentiostat or a regulated power supply, the positive electrode is connected to the A electrode, and the negative electrode is connected to the B electrode. Then, the electrolysis of hydrogen is started. At this time, the piston of the A electrode can be pulled apart to make the oxygen generated during the preparation run out and maintain the internal pressure balance. According to the electrochemical reaction, the electrode A generates oxygen and the electrode B generates hydrogen. When the position of the hydrogen-discharging solution produced by electrolysis is about half of the platinum electrode exposed, the electrolysis can be stopped to prevent the hydrogen from discharging the solution below the platinum electrode. Close the piston of electrode A to keep the hydrogen in a stable position. Finally, the piston C is opened, and the electrolyte in the U-tube is electrically connected to the electrolytic cell through the Lujin capillary.

Regarding the conversion between the potential of the non-RHE reference electrode and the RHE reference electrode, Gregory et al. [12, 13] calculated by the Nernst equation and the Davis equation, it is recommended to use the following conversion formula.

In 0.05 mol·L^{-1} H_2SO_4 solution.

$$E_{SHE} = E_{RHE(0.05\text{mol L}^{-1}\,H_2SO_4)} + 0.075\ \ V \tag{3.35}$$

In 0.1 mol·L^{-1} H_2SO_4 solution.

$$E_{SHE} = E_{RHE(0.1\text{mol L}^{-1}\,H_2SO_4)} + 0.060\ \text{V} \tag{3.36}$$

In 0.5 mol·L^{-1} H_2SO_4 solution.

$$E_{SHE} = E_{RHE(0.5\ \text{mol L}^{-1}\,H_2SO_4)} + 0.021\ \text{V} \tag{3.37}$$

In order to test the feasibility and rigor of the above conversion formula, we will express the detailed derivation process of the above formula as follows.

The Nernst equation of the electrode potential of the reversible hydrogen electrode can be expressed as follows.

$$E_{RHE} = E_{SHE} + \frac{RT}{F} \ln a(H^+) \tag{3.38}$$

where $\alpha(H^+)$ is the activity of H^+,$\alpha(H^+) = \frac{\gamma_+ c_+}{c^\Theta}$, γ_+ is the activity coefficient of H^+, c_+ is the molar concentration of H^+,$c^\Theta = 1$ mol·L^{-1}.

In theory, the reversible hydrogen electrode can be corrected using the Nernst equation of the hydrogen electrode. In the calculation, since γ_+ cannot be directly measured, the average activity coefficient $\gamma_\pm$ of the ions can only be measured experimentally, so in the calculation, the positive and negative ions are considered to have the same activity, and the average activity $\alpha_\pm$ is substituted for α (H^+).

When c ($H2SO_4$) = 0.1 mol·L^{-1}, the average activity coefficient $\gamma_\pm = 0.265$ [14], at 298 K.

$$\begin{aligned} E_{RHE} &= E_{SHE} + \frac{RT}{F} \ln a(H^+) \\ &= E_{SHE} + 0.0257 \ln(0.0265 \times \sqrt[3]{4}) \\ &= E_{SHE} - 0.081\ V \end{aligned} \tag{3.39}$$

If calculated directly in molar concentration.

$$\begin{aligned} E_{RHE} &= E_{SHE} + \frac{RT}{F} \ln c(H^+) \\ &= E_{SHE} + 0.0257 \ln 0.1 \\ &= E_{SHE} - 0.059\ V \end{aligned} \tag{3.40}$$

When c (H_2SO_4) = 0.05 mol·L^{-1}, the average activity coefficient $\gamma_\pm = 0.340$ [14], at 298 K.

$$\begin{aligned} E_{RHE} &= E_{SHE} + \frac{RT}{F} \ln a(H^+) \\ &= E_{SHE} + 0.0257 \ln (0.017 \times \sqrt[3]{4}) \\ &= E_{SHE} - 0.093\ V \end{aligned} \tag{3.41}$$

If calculated directly in molar concentration.

$$\begin{aligned} E_{RHE} &= E_{SHE} + \frac{RT}{F} \ln c(H^+) \\ &= E_{SHE} + 0.0257 \ln 0.05 \\ &= E_{SHE} - 0.077\ V \end{aligned} \tag{3.42}$$

Comparing the calculated results with the conversion formula of Gregory Jerkiewicz et al., it can be found that Gregory et al. calculated the molarity directly instead of the activity, and did not perform the activity correction, so the calculation method is not rigorous. In addition, although the concentration is corrected for activity, there is a great uncertainty in the method because the activity coefficients of different solutions are difficult to measure accurately. Therefore, the general reference electrode potential and the reversible hydrogen electrode potential conversion need to know the activity coefficient at a certain acid concentration, which is actually difficult to achieve. Therefore, it can be said that it is generally not directly convertible.

Liang et al. [15, 16] recommended the use of experimental methods to convert the reference electrode potential. The reference electrode actually used in the experimental procedure was a saturated calomel electrode (SCE). When the reference electrode is corrected, the working electrode and the counter electrode of the three-electrode system are replaced with Pt wires, and the reference electrode is still a saturated calomel electrode. The electrolyte passes through high purity hydrogen to saturation. The linear scanning speed was set to 0.1 $mV.s^{-1}$, and the potential value corresponding to the current at the transition of the hydrogenation and reduction reaction was taken as the thermodynamic potential of hydrogen relative to the saturated calomel electrode. At 0.1 $mol{\cdot}L^{-1}$ $HClO_4$, the thermodynamic potential is -0.304 V, and the correction formula is $E_{RHE} = E_{SCE} + 0.304$ V; at 0.1 $mol{\cdot}L^{-1}$ KOH, the thermodynamic potential is -0.998 V, the correction formula is $E_{RHE} = E_{SCE} + 0.998$ V.

3.3.2 Working Electrode

A rotating circular (ring) disk electrode is used as the working electrode, and is composed of an outer protective material and a central disk (disc plus platinum ring) electrode. The material of the disc can be differently selected according to different testing needs. Currently, a platinum disc (platinum disc) electrode or a glassy carbon disc (platinum disc) electrode is commonly used. The platinum disk (platinum disk) electrode is relatively simple to use, only need to pay attention to the temperature and speed limit. In the study of new catalysts, in order to avoid the influence of platinum, a glassy carbon disk electrode is generally used as a base conductive material, and the surface thereof may be coated with different catalyst layers. In the following, a

glassy carbon disk (platinum disk) electrode will be taken as an example to describe the selection of the electrode and the preparation and coating of the catalyst layer.

Rotating disc (ring disc) electrodes operating under different test conditions require special manufacture. Rotating disc (ring disc) electrodes manufactured by Pine Instrument Company of the USA are of various types and are composed of different materials. The glassy carbon ring electrode used for the oxygen reduction test of the electrocatalytic system is composed of a glassy carbon disk electrode and a platinum ring electrode. Ordinary rotating ring electrodes can be used at temperatures not higher than 30 °C and rotating at speeds not higher than 3,000 rpm. The electrode working under high temperature conditions needs special production. The key point is that the electrode does not seep at high temperature. This is because the connecting wire in the electrode is a special metal material. Once the liquid is exuded, the working electrode will become the metal. Electrode, not the electrode we want to measure. Therefore, in order for the electrode to be liquid-free during operation, we need a special protective material which is equivalent to the coefficient of thermal expansion between the electrodes. Typical rotating ring electrodes manufactured by Pine Instruments of the USA are AFE6R2/GC-Pt (see Fig. 3.5(c)I) for high temperature use and AFE7R9/GC-Pt for ambient temperature (see Fig. 3.5(c)II). The insulating material at room temperature is Teflon, and the high temperature insulating material is PEEK.

The device for rotating the ring electrode is shown in Fig. 3.5. It consists of an electric rotating system, an electrolytic cell system, a constant temperature system (which maintains a constant oxygen solubility), and an electrochemical test instrument. Figure 3.5a shows the overall assembly drawing, Fig. 3.5b shows the study electrode mounting, and Fig. 3.5c shows the ring disk electrode. When using, connect the electrode to the rotating shaft Fig. 3.5b, and finally insert it into the electrolytic cell.

In the new catalyst study, when the experimental instrument is ready, the catalytic layer is prepared on the surface of the glassy carbon electrode. The following describes the method for preparing the catalytic layer in our laboratory, as follows.

First, a small amount of catalyst sample was accurately weighed by an electronic balance, dispersed in distilled water, ultrasonically shaken for 15 min, and then centrifuged for 30 min until the catalyst and moisture layers were removed, and the water was removed. This step was to clean the catalyst and reduce the influence of impurities. The catalyst was then dispersed in water/alcohol, and a certain amount of a 5% Nafion suspension solution (manufactured by DuPont, USA) was added, and ultrasonically dispersed to prepare an ink-like slurry. The slurry should be well dispersed and cannot be agglomerated or precipitated. A proper amount of slurry was accurately transferred with a 25.0 μl micro-syringe, uniformly coated on the surface of the electrode, and baked to dryness under an infrared lamp to form a uniform thin layer of catalyst on the surface of the electrode. The general usage is $10 \mu g_{Pt}$ cm^{-2}–$40\ \mu g_{Pt}\ cm^{-2}$.

It has been reported in the literature [7, 8] that the Pt/C layer with a glassy carbon surface of less than 0.1 μm does not affect the distribution of oxygen on the electrode. Intrinsically hydrophobic catalysts, as well as alcohol or high temperature treated

samples, may need to increase the ratio of alcohol (ethanol or isopropanol) to water for better dispersion. Increasing the ratio of isopropanol to water and multiple ultrasonic oscillations can obtain a slurry with a good dispersion state, thereby improving the dispersibility and electrocatalytic activity of the catalytic layer. The hydrophilic catalyst is well dispersed in a mixed liquid of Nafion solution and water.

The catalyst-coated electrode is first wetted with an electrolyte solution to have no bubbles on its surface. After the electrode is mounted, adjust the distance between the electrode surface and the Lujin capillary (about 2 times the diameter of the Lujin capillary), and try to rotate the electrode two to three times to remove the air bubbles on the electrode surface. The potentiostat was turned on, stabilized at 1600 rpm, and activated at 50–200 $mV.s^{-1}$, and activated until a stable curve was obtained.

3.3.3 Effect of Electrolyte Concentration on the Measurement of Oxygen Reduction Performance of Pt/C Catalyst

At present, most research teams use the rotating ring-disk electrode (RRDE) to study the hydrogenation and oxygen reduction performance of the catalyst. The advantage of this test method is that it can deduct the effect of mass transfer on the measured current, thus reflecting intrinsic properties of the catalyst. In order to ultimately compare the results of RRDE with actual fuel cell membrane electrode (MEA) testing, factors affecting RRDE test results and activity characterization need to be noted. These factors include the determination of the active area, the effects of ion adsorption, the mass transfer effects of the Nafion membrane, and the effects of electrolytes. The first three factors have been studied accordingly. However, in the treatment of electrolytes, it is most commonly used to measure the resistance of the solution by AC impedance method, or to think that the solution is completely conductive, and the solution resistance is negligible. From an electrochemical point of view, the ionic strength of the electrolyte solution will greatly affect the results of the oxygen reduction test. The easiest way to reduce the resistance of the solution and increase the conductance of the solution is to add a certain concentration of strong electrolyte to the solution to increase the number of conductive ions per unit volume of solution. In the study of this book, try to introduce different concentrations of strong electrolyte salt sodium perchlorate in 0.1 M $HClO_4$ to reduce the solution resistance, and study its effect on the oxygen reduction performance of commercial Pt/C catalyst under the oxygen reduction standard test.

3.3.3.1 Electrochemical Characterization

Figure 3.6 is a cyclic voltammetric scan of a commercial Pt/C catalyst in different electrolyte solutions. It can be seen that the addition of different concentrations of

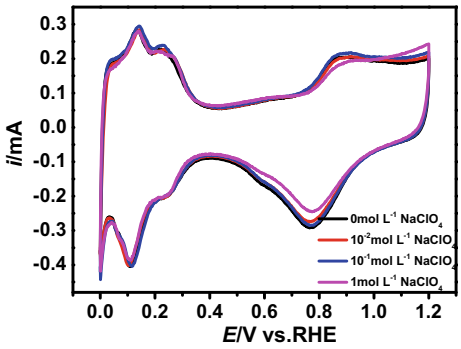

Fig. 3.6 Cyclic voltammetry scan of a commercial Pt/C catalyst in different concentrations of electrolyte solution

sodium perchlorate in 0.1 mol·L^{-1} $HClO_4$ does not affect the potential of hydrogen underpotential precipitation. Moreover, the addition of different concentrations of sodium perchlorate does not affect the peak, peak current and peak area of hydrogen absorption and desorption, indicating that the adsorption of perchlorate on the Pt active point does not increase with the increase of perchlorate ion concentration. Therefore, it is feasible to understand the effect of solution resistance on the oxygen reduction performance of commercial Pt/C catalyst by adding sodium perchlorate. However, the redox peak potential and current density of oxygen are affected by the concentration of the added salt, indicating that the addition of different concentrations of sodium perchlorate will affect the cathodic reduction activity of Pt, and the oxygen reduction reaction is still the rate-determining step of the cathodic reaction.

3.3.3.2 Analysis of Oxygen Reduction Performance

Figure 3.7 is a graph showing the effect of 0.1 M $HClO_4$ solution with different concentrations of sodium perchlorate on the oxygen reduction performance of commercial Pt/C catalysts. It can be seen from Fig. 3.6a that as the concentration of the added salt increases, the measured current density value of the disk electrode at 0.9 V decreases in turn, when the concentration of sodium perchlorate added reaches 1 mol·L^{-1}. The peak potential of the oxygen reduction curve is significantly negatively shifted to 30 mV. In addition, between 0.7 and 0.9 V, the ring current also increases as the concentration of the added salt increases. From the oxygen reduction electron transfer number n and the hydrogen peroxide production amount in Fig. 3.7b, c, it can be seen that in the 0.7–0.9 V region, as the sodium perchlorate concentration increases, the oxygen reduction electron transfer number n decreases. The amount of hydrogen peroxide produced increases. It can be concluded that the addition of sodium perchlorate in 0.1 mol·L^{-1} $HClO_4$ solution has a significant effect on the oxygen reduction performance of commercial Pt/C catalysts, and the cathode reduction of oxygen increases with the concentration of sodium perchlorate added. The reaction became difficult, especially in the electrolyte solution to which 1 mol·L^{-1} $NaClO_4$ was added, the four-electron reduction reaction of partial

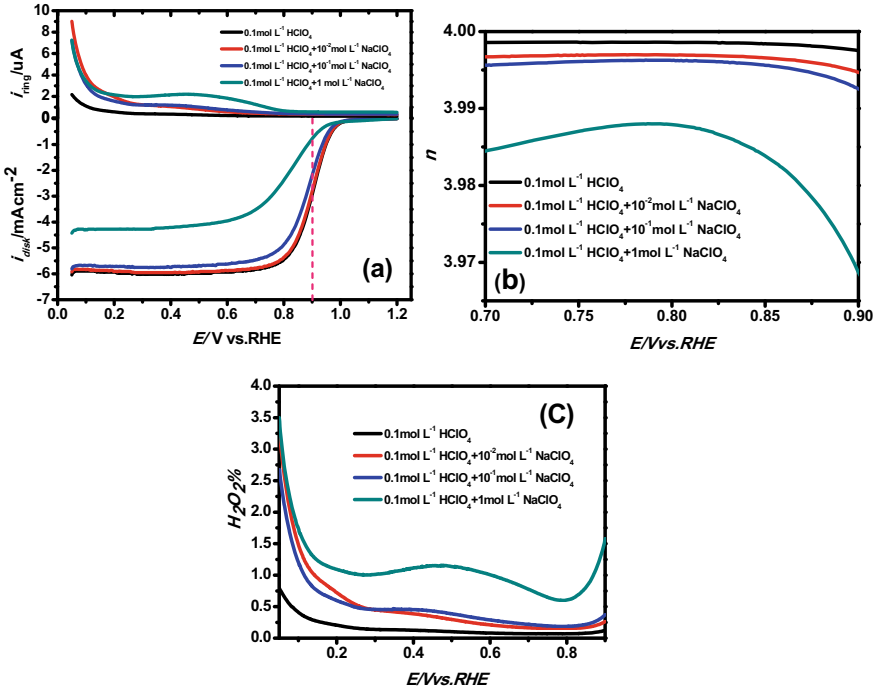

Fig. 3.7 Effect of acidic electrolyte solutions with different concentrations of sodium perchlorate on the oxygen reduction performance of commercial Pt/C catalysts (47.6% Pt, TKK, Japan). **a** Oxygen reduction curve, **b** Number of transferred electrons, and **c** Amount of hydrogen peroxide generation

oxygen was suppressed, and the oxygen reduction performance of the commercial Pt/C catalyst was the worst.

In addition, the value of the limiting current density of the disk electrode in Fig. 3.7a decreases as the concentration of sodium perchlorate added increases. According to the Levich Limit Current Density equation (as shown in Eq. (3.43)), factors affecting the limiting current density are aerobic solubility, electrode speed, temperature, and dynamic viscosity of the solution. It can be seen from Table 3.2

Table 3.2 Concentration of saturated dissolved oxygen in acidic electrolyte solutions with different sodium perchlorate concentrations (25 °C)

Electrolyte solutions	Concentration of saturated dissolved oxygen ($mg.L^{-1}$)
0.1 mol L^{-1} $HClO_4$	20.17
0.1 mol L^{-1} $HClO_4$ + 10^{-2} mol L^{-1} $NaClO_4$	20.25
0.1 mol L^{-1} $HClO_4$ + 10^{-1} mol L^{-1} $NaClO_4$	20.19
0.1 mol L^{-1} $HClO_4$ + 1 mol L^{-1} $NaClO_4$	20.25

that the addition of different concentrations of $NaClO_4$ to 0.1 mol·L^{-1} $HClO_4$ has little effect on the concentration of saturated dissolved oxygen at 25 °C. Therefore, in the case of a certain speed and temperature, the possible cause of the decrease in the limit current density is that the dynamic viscosity of the solution increases as the salt concentration increases, resulting in a decrease in the limit current density value.

$$i_d = 0.62nFD_0^{2/3}\omega^{1/2}v^{-1/6}C_0 \tag{3.43}$$

where ω is the angular velocity, v is the dynamic viscosity ($cm^2.s^{-1}$), C_0 is the concentration (mol·L^{-1}), and D_0 is the diffusion coefficient ($cm.s^{-1}$).

3.3.3.3 Analysis of Oxygen Reduction Activity

Figure 3.8 is a graph showing the effect of a 0.1 M $HClO_4$ electrolyte solution with different concentrations of sodium perchlorate on the kinetic current (a) and mass activity (b) of a commercial Pt/C catalyst. As can be seen from Fig. 3.8, the addition of low concentrations of sodium perchlorate does not have a large effect on its kinetic current and mass activity, and at 0.9 V as the concentration of sodium perchlorate added increases. The kinetic current and mass activity test values were significantly reduced, especially when the sodium perchlorate added was 1 M, the kinetic current and mass activity were minimal, and the mass activity of the commercial Pt/C catalyst was measured at this time. Only 17% of the 0.1 mol·L^{-1} $HClO_4$ solution without salt indicates that the reduction reaction of oxygen at the active point of the catalyst becomes difficult, which is consistent with the deterioration of the oxygen reduction performance of the catalyst in the high concentration salt in the previous part. The 4 electron process was suppressed, making the tested catalyst activity worse.

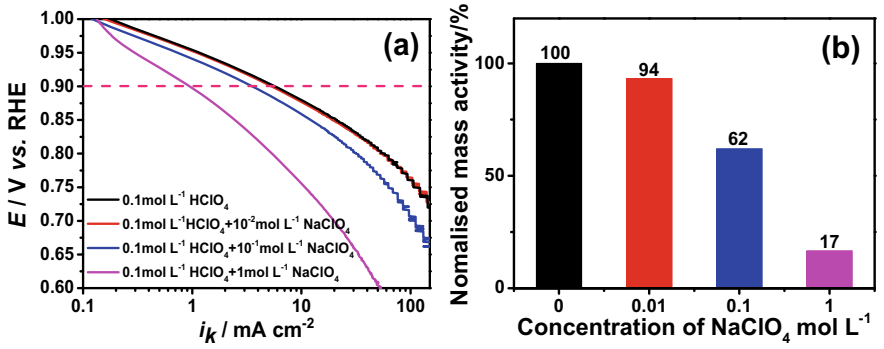

Fig. 3.8 Effect of different sodium perchlorate concentrations of acidic electrolyte solution on mass activity and kinetic current of commercial Pt/C catalysts (47.6% Pt, TKK, Japan). **a** Kinetic current curve and **b** Normalized mass activity

The results showed that different concentrations of sodium perchlorate were added to 0.1 mol·L^{-1} $HClO_4$, and the oxygen reduction mass activity of the commercial Pt/C catalyst was worse than that without time. Moreover, when the concentration of sodium perchlorate added was 1 mol·L^{-1}. The oxygen reduction of the commercial Pt/C catalyst has a negative shift of about 30 mV, and the kinetics of oxygen reduction was hindered. It is indicated that reducing the resistance of the solution by introducing a strong electrolyte salt will affect the test results, and the high concentration of salt will hinder the correct characterization of the oxygen reduction performance of the catalyst. The current possible explanation is that increasing the concentration of salt actually increases the concentration of ions. On the one hand, these ions affect the mass transfer of oxygen on the one hand, and may adsorb on the surface of the electrode on the other hand, affecting the adsorption and reduction of oxygen, and finally, the data that led to the measurement of oxygen reduction performance deteriorated, which is why the conventional oxygen reduction test was carried out in 0.1 mol·L^{-1} $HClO_4$. The following section will discuss in detail the other important factors affecting the oxygen reduction test.

3.3.4 Electrode Film-Forming Technology

In the rotating disk electrode test, the film formation quality and film formation uniformity of the electrode will greatly affect the oxygen reduction activity of the catalyst.

There are two ways to dry the catalyst film. One is the static drying method, that is, the dispersed catalyst slurry is dropped on the surface of the electrode, and then dried in the air or by other auxiliary drying means in a static state, thereby rotating the circle. A uniform film is obtained on the surface of the disk electrode; the other method is a spin-drying method, that is, the dispersed catalyst slurry is dropped on the surface of the electrode, and then the electrode is dried at a certain rotation speed to obtain a catalyst with uniform adhesion film.

3.3.4.1 Static Drying Method

Figure 3.9 is a catalyst film obtained by a static drying method, here taking 19.7% of a Pt/C catalyst as an example (E-TECK). It can be seen from the figure that the catalyst film obtained by the static drying method has the following problems: (1) the film-forming quality of the edge portion of the catalyst film is relatively uniform, and the film quality of the intermediate portion is poor; (2) the center of the electrode is formed. The film thickness is thin, and the edge portion is not completely formed, and the electrode is not completely covered; (3) the film-forming quality of the electrode surface is uniform, but the edge portion is preferentially dried due to faster diffusion, and the center portion of the electrode is finally dried, if when the obtained catalyst

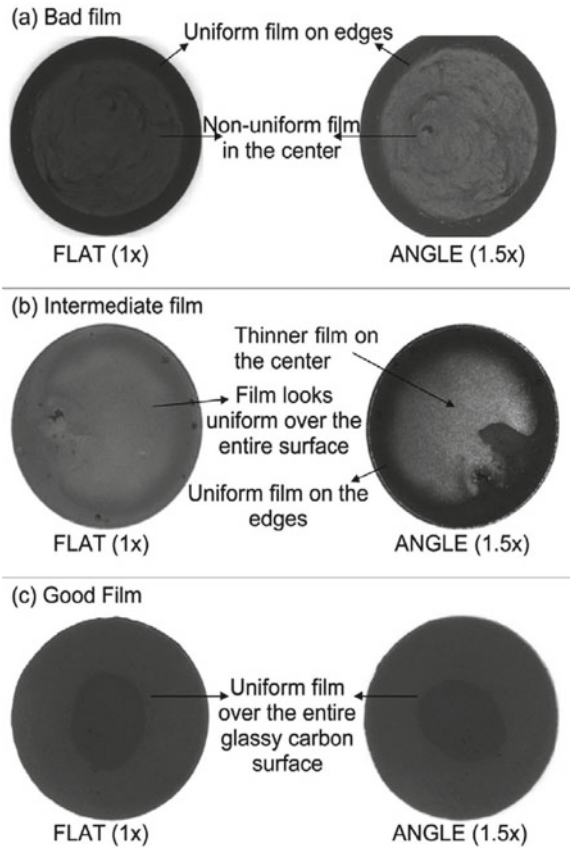

Fig. 3.9 Catalyst film obtained by static drying method. Reprinted from ref. [17], copyright©2010 American Chemical Society, with permission from American Chemical Society

slurry is dispersed very uniformly, it is possible to obtain a catalyst film having a relatively uniform surface dispersion state.

Figure 3.10a is a CV curve of a Pt/C catalyst of different film-forming qualities. It can be seen from the figure that due to the difference in film formation quality, the CV curves obtained by the same catalyst under the same test conditions are greatly different. Whether it is the size of the absorption and desorption peak of hydrogen or the formation position of Pt–OH, the difference is different. As can be seen from Fig. 3.10b, the oxygen reduction polarization curves are quite different. For electrodes with better film formation quality, the slope of the polarization region is larger. In the diffusion control region, the electrode with better film formation quality can obtain a larger limiting current. This is because the electrode with good film formation quality is more conducive to the uniform diffusion of oxygen and electrolyte on its surface.

It can be seen from Fig. 3.11 that the catalyst film obtained by the static drying method has better film formation uniformity at the edge portion, and the thickness of the central portion is significantly thicker, and some central regions are not completely

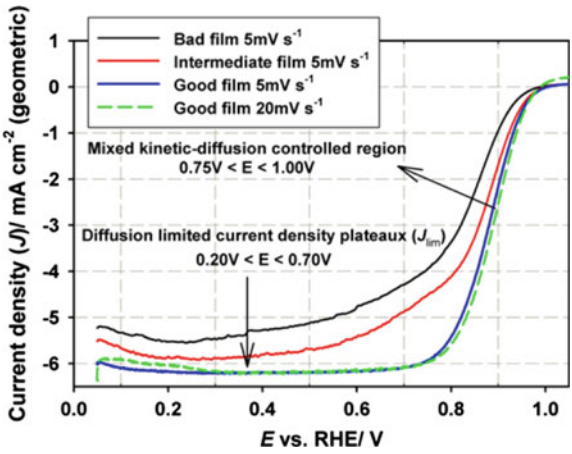

Fig. 3.10 Cyclic voltammogram of the Pt/C catalyst with different filming qualities in 0.1 M $HClO_4$ solution (left) and oxygen reduction polarization curve (right). Reprinted from ref. [17], copyright©2010American Chemical Society., with permission from American Chemical Society

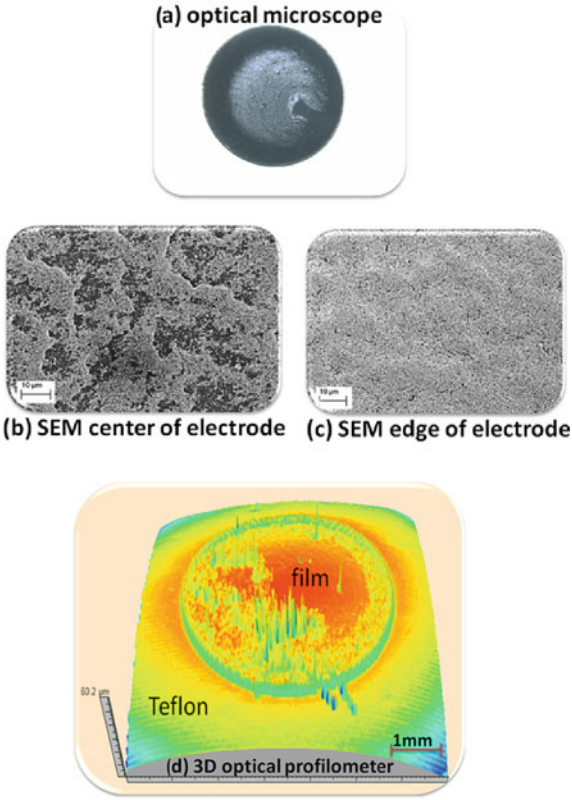

Fig. 3.11 **a** Catalyst film under an optical microscope. **b** SEM photograph of the center of the electrode. **c** SEM photograph of the edge of the electrode. **d** 3D optical photograph of the catalyst film. Reprinted from ref. [18], copyright©2011 Elsevier B.V., with permission from Elsevier

covered, which will affect the electrochemical active area of the catalyst and the magnitude of the oxygen reduction limit current. In addition, since the calculation of the electrochemical active area and the oxygen reduction mass activity is calculated based on the geometrical area of the electrode, it is assumed here that the catalyst film uniformly covers the surface of the electrode, and the actual situation is that the catalyst film obtained by the static drying method is It is not uniform coverage, so the calculation results of the electrochemical active area and the oxygen reduction mass activity are more deviated than the actual values.

3.3.4.2 Rotary Drying Method

In view of the problem of uneven film formation quality in the static drying method, Garsany et al. developed a spin-drying method [18, 19]. The specific method of operation is to invert the rotating disk device, and the electrode on which the catalyst slurry is dropped is turned upward to be rotated to obtain a dried catalyst film. The speed of rotation will cause the catalyst slurry to splash out of the rotating disk electrode. If the rotation speed is too slow, it will not be uniformly dried, and the rotation speed is generally controlled at 700 rpm.

It can be seen from Fig. 3.12 that the film formed by the spin-drying method has a good film-forming quality, and the film-forming quality is relatively uniform regardless of the center of the rotating disk electrode or the edge portion. This is because under the conditions of spin drying, the catalyst slurry can be evenly spread on the surface of the rotating disk electrode, which is more favorable for the solvent in the catalyst slurry to be uniformly volatilized.

It can be seen from Fig. 3.13 that the electrochemical activity areas of the catalysts obtained by the static drying method and the rotary drying method are relatively uniform, but the oxygen reduction activities are quite different. This is because the catalyst film obtained by the spin-drying method is relatively uniform, and thus the electrode is less affected by the surface effect, which is more advantageous for the electrolyte and oxygen to diffuse on the surface of the catalyst. Moreover, the spin-drying method is more reproducible (see Fig. 3.14) and is therefore more suitable for studying the electrocatalytic activity of the catalyst.

3.4 Oxygen Reduction Reaction Test Considerations

The factors that need to be noted during the test are as follows.

The effect of different anions. Markovic et al. found that the reduction of oxygen is greatly inhibited in sulfur- and chlorine-containing acidic electrolyte solutions, which is more pronounced in chlorine-containing electrolyte solutions. Schmidt et al. found that the presence of Cl^- in the electrolyte solution does not change the decisive step of the cathode reduction reaction of commercial Pt/C catalysts, but the

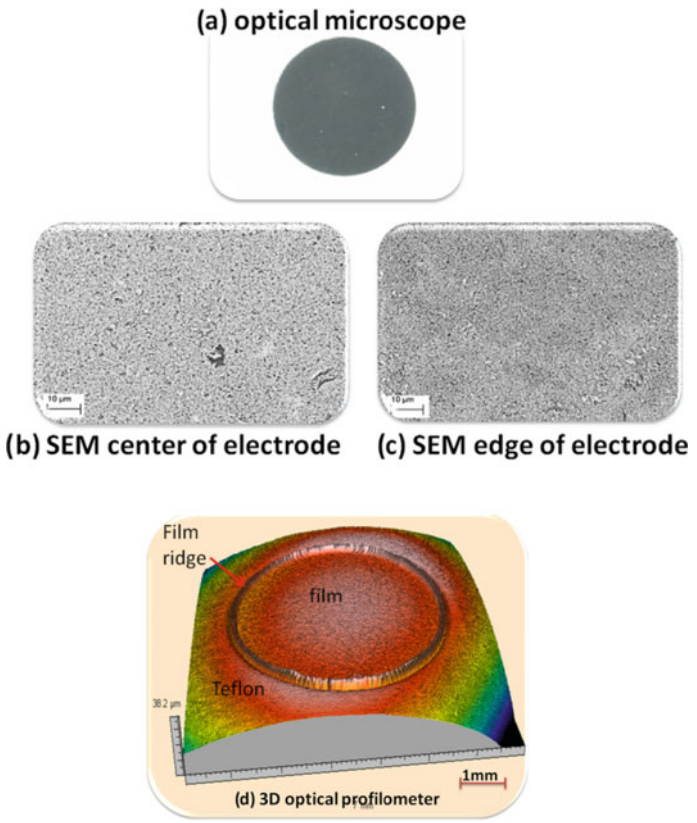

Fig. 3.12 **a** Catalyst film under an optical microscope. **b** SEM photograph of the center portion of the electrode, **c** SEM photograph of the edge of the electrode, **d** 3D optical photograph of the catalyst film. Reprinted from ref. [18], copyright©2011 Elsevier B.V., with permission from Elsevier

formation of H_2O_2 is at the electrode potential >0.2 V, with Cl^- in the $HClO_4$ solution. As the concentration increases, the four-electron reaction process of oxygen is significantly suppressed. We also studied it using polycrystalline Pt disk electrodes. The polycrystalline Pt disk electrode has high activity, low electrode resistance, and is very sensitive to impurities in the solution. It can be used to test the effect of ions on the oxygen reduction reaction in the solution, and more objective results can be obtained. From the practical point of view, we studied the oxygen reduction performance of commercial Pt/C catalysts (Japan TKK, 47.6% Pt) in different acidic electrolyte solutions. The results show that the oxygen reduction performance of commercial Pt/C catalysts is strongly dependent on the type of electrolyte solution. The results show that the oxygen reduction performance of commercial Pt/C catalysts is strongly dependent on the type of electrolyte solution. The oxygen reduction performance of commercial Pt/C catalysts in high concentration acid solutions or in different kinds of inorganic acid solutions is not as good as 0.1 mol·L^{-1} $HClO_4$

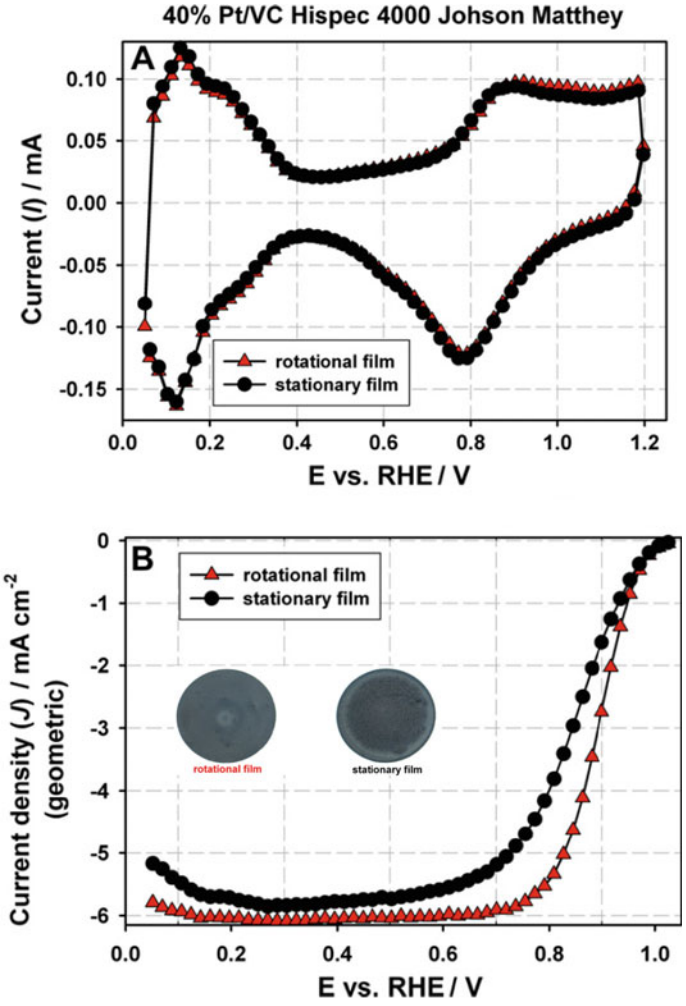

Fig. 3.13 **a** CV curve and **b** oxygen reduction polarization curve of 40% Pt/VC (JM) catalyst obtained by static drying method and spin-drying method, 0.1 M $HClO_4$, 20 mV.s^{-1}, 30°C.Reprinted from ref. [18], copyright©2011 Elsevier B.V., with permission from Elsevier

solution. From Fig. 3.17, we can see that in the solution containing different anionic acids, the oxygen reduction activity ClO_4^- > NO_3^- > SO_4^{2-} > Cl^-, the oxygen reduction overpotential is the largest in the acid solution containing chloride ions. Therefore, during the experimental operation, impurity ions such as Cl^- should be excluded as much as possible. In addition, increasing the ionic strength also reduces the oxygen reduction performance, increases the concentration of sulfuric acid, and deteriorates the performance of oxygen reduction (Fig. 3.15a blue line). Yannick et al. performed oxygen reduction tests on Pt/C catalysts with electrolytes of 0.1 mol·L^{-1}

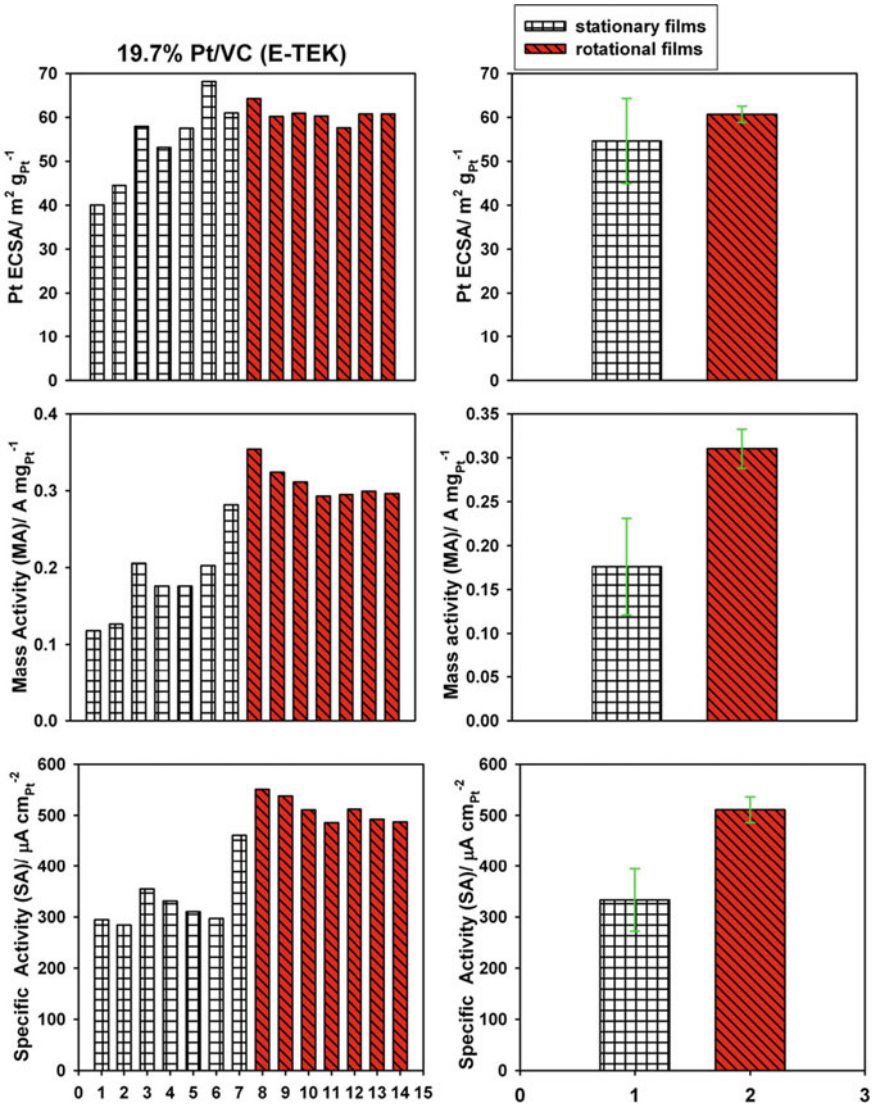

Fig. 3.14 Left: Electrochemical active area and oxygen reduction activity of 40% Pt/VC (JM) catalyst obtained by different drying methods; right panel: difference between electrochemical active area and oxygen reduction activity. Reprinted from ref. [18], copyright©2011 Elsevier B.V., with permission from Elsevier

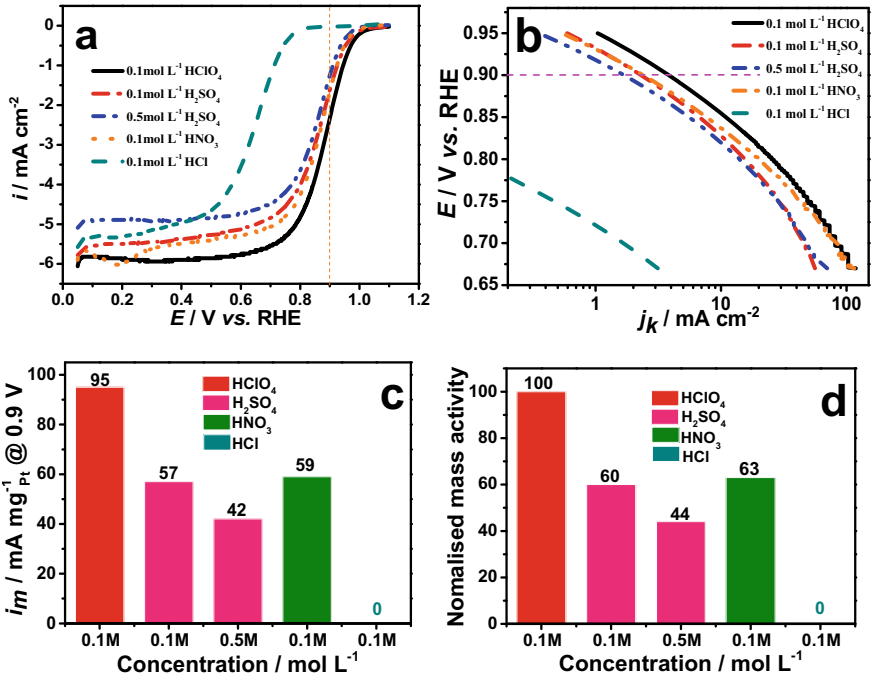

Fig. 3.15 Effect of different acidic electrolyte solutions on the oxygen reduction performance of commercial Pt/C catalysts (Japan TKK, 47.6% Pt). **a** oxygen reduction curve, **b** kinetic current curve, **c** mass activity and **d** normalized mass activity. Oxygen-saturated solution, electrode speed 1600 rpm, potential sweep speed 5 mV.s^{-1}, temperature 25 °C, Pt load 40 μg.cm^{-2}

$HClO_4$, 0.05 mol·L^{-1} H_2SO_4 and 0.5 mol·L^{-1} H_2SO_4 at 1600 rpm and 20 mV.s^{-1}. The results showed that the catalyst had the highest oxygen reduction activity in 0.1 mol·L^{-1} $HClO_4$, and the mass activity in 0.1 mol·L^{-1} $HClO_4$ was 80% higher than that in 0.5 mol·L^{-1} H_2SO_4. In addition, Marković and Schmidt et al. also found that in different electrolyte solutions, oxygen reduced the activity of ClO_4^- > HSO_4^-. Figure 3.15b shows the kinetic current for each catalyst. Based on this result, we can obtain mass activity at 0.9 V (Fig. 3.15c). Based on the activity in 0.1 mol·L^{-1} $HClO_4$, we have a normalized graph comparison (Fig. 3.15d). It can be seen that the commercial Pt/C catalyst is 0.1 mol·L^{-1} H_2SO_4 and 0.5 mol·L^{-1}. The mass activity in the H2SO_4 electrolyte solution was only 60 and 44% in the 0.1 mol·L^{-1} $HClO_4$ solution.

In the choice of electrolyte solution, mainly determined by the performance of the working electrode and the research system, the generally selected electrolyte solution is required to contain no ions that can be adsorbed on the working electrode. For a platinum electrode or a platinum-based catalyst, a perchloric acid solution is an electrolyte solution which does not substantially contain ions which adsorb ions with platinum, and thus is widely used. For most carbon-based materials, whether it

is the use of perchloric acid or sulfuric acid, there is basically no impact on the test. As for the catalyst containing ruthenium, since ruthenium catalyzes the reduction of perchloric acid to form a large amount of strongly adsorbed chloride ions, the electrolyte solution is not suitable for the perchloric acid solution for the oxygen reduction test of the catalyst.

The effect of ionic strength. The commonly used electrolyte solution is a 0.1 mol·L^{-1} $HClO_4$ solution. From an electrochemical point of view, the ionic strength of the electrolyte solution will greatly affect the results of the oxygen reduction test. However, from the literature, our research also found that increasing the concentration of perchloric acid, the performance of oxygen reduction of polycrystalline platinum disk electrode deteriorated. Figure 3.18 shows the results of oxygen reduction of commercial Pt/C catalysts in different perchloric acid concentration solutions. It can be seen that as the concentration of perchloric acid increases (the ionic strength increases), the relative performance of oxygen reduction decreases (Fig. 3.16), and this phenomenon of decreased ionic strength increase performance requires further investigation.

The electrolyte solution used each time should be freshly prepared. An electrolyte solution that is not freshly prepared may have problems. Garsany et al. found that the oxygen reduction performance of the same catalyst in an electrolyte solution used for more than 2 days was significantly worse than that in a freshly prepared electrolyte solution, especially at a low sweep speed of 5 mV.s^{-1}.

The effect of scanning speed. Under the same test conditions, the sweep speed increases, and the limit current increases due to the decrease in the thickness of the effective diffusion layer, which is consistent with the results of the Koutecký-Levich equation.

The test temperature should be constant. The experiment is preferably carried out in a constant temperature water bath, and the change in temperature affects the saturation solubility of the oxygen and the kinetics of the electrode. Although an

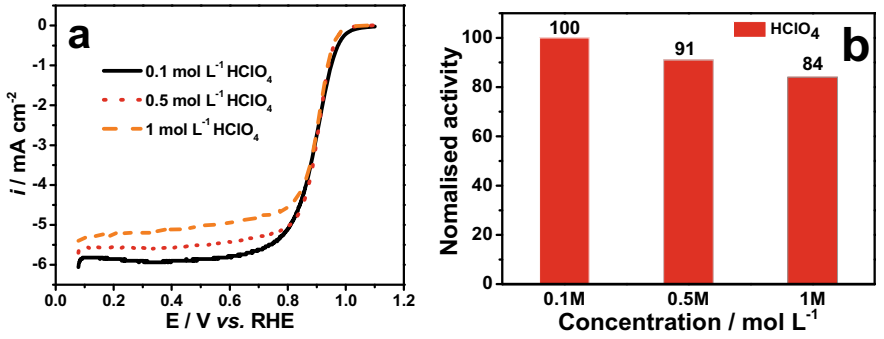

Fig. 3.16 Effect of different concentrations of perchloric acid electrolyte solution on oxygen reduction performance of commercial Pt/C catalyst (Japan TKK, 47.6% Pt). **a** Oxygen reduction curve, **b** Mass activity normalized to 0.1 mol·L^{-1} $HClO_4$ solution. Oxygen-saturated solution, electrode speed 1600 rpm, potential sweep 5 mV.s^{-1}, temperature 25 °C, Pt load 40 μg.cm^{-2}

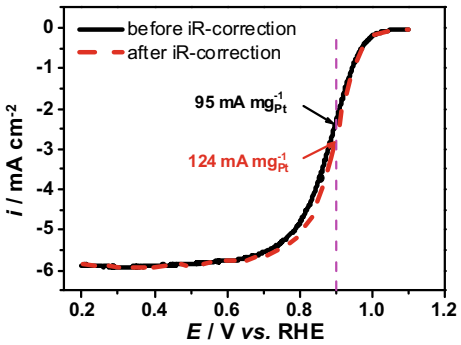

Fig. 3.17 Comparison of the oxygen reduction curve of 47.6% Pt/C commercial catalyst of TKK Company of Japan in 0.1 mol·L^{-1} $HClO_4$ aqueous solution before and after solution resistance correction. Sweep speed 5 mV.s^{-1}, 1600 rpm, 25 °C, platinum loading 40 μg.cm^{-2}

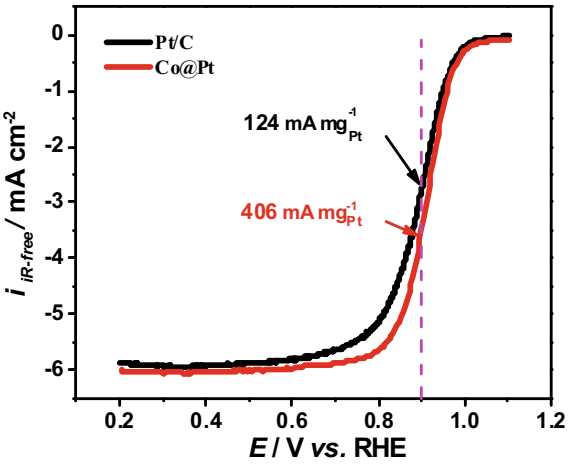

Fig. 3.18 Oxygen reduction curve of 47.6% Pt/C commercial catalyst (black line) and Co@Pt catalyst (red line) of Japan TKK Company in 0.1 mol·L^{-1} $HClO_4$ aqueous solution. The sweep rate is 5 mV.s^{-1}, 1600 rpm, 25 °C, platinum loading, Pt/C 40 μg.cm^{-2}, and Co@Pt 20 μg.cm^{-2}

increase in temperature can improve the kinetics of oxygen reduction, an increase in temperature also reduces the dissolved concentration of oxygen. Therefore, to investigate the effect of temperature on oxygen reduction must take into account the effect of oxygen concentration. Our study found that the oxygen reduction performance measured at 60 °C was not better than the data measured at 25 °C, mainly because the oxygen concentration could not be controlled under normal pressure. Moreover, previous studies have found that at 60 °C, $HClO_4$ will decompose and produce a small amount of chloride ions enough to contaminate the Pt electrode, thus affecting the test results.

The test process should maintain a stable oxygen concentration. Before the experiment, we must pass oxygen for about 30 min, and then measure. Generally, it is necessary to reenergize for about 30 min of oxygen every time to ensure that there is saturated dissolved oxygen in the solution.

The usual conditions for measuring oxygen reduction are the instrument's rotational speed of 1600 rpm, 25 °C, 0.1 mol·L^{-1} $HClO_4$, and a potential sweep rate

of 5 $mV.s^{-1}$. The potential range is set to 0.05 V–1.1 V relative to the reversible hydrogen electrode. The onset potential is determined by the potential of the underpotential hydrogen evolution of the electrode (see next section). The terminal potential is dependent on the initial potential of the oxygen reduction on the electrode. The starting potential of a typical catalyst is around 1 V. If the initial potential of the electrode oxygen reduction is positive, the terminal potential can be increased.

Correction of the oxygen reduction curve solution resistance. The solution resistance has a great influence on the objectivity of the oxygen reduction curve test. If the solution resistance is 10 Ω and the measured current is 1 mA at 0.9 V versus RHE, then the oxygen reduction curve has a 10 mV shift. Although the amount of movement is small, it will calculate the oxygen reduction activity. Have a great impact. Our study found that the mass activity of the commercial Pt/C catalyst after calibration can be increased by about 30%. As can be seen from Fig. 3.17, the change in mass activity values before and after solution resistance correction at 0.9 V versus RHE.

Based on the above measurement conditions, we determined the oxygen reduction curves of commercial Pt/C catalysts and our laboratory-made catalysts (Co@Pt) (Fig. 3.18). The mass activity of the commercial Pt/C catalyst at 0.9 V was 124 $mA.mg^{-1}{}_{Pt}$, and the mass activity of the Co@Pt catalyst was $mA.mg^{-1}{}_{Pt}$.

3.5 Analysis of Electrochemical Reduction Curve of Oxygen

3.5.1 Overview of Electrochemical Reduction Curves of Oxygen

Figure 3.19 shows the oxygen reduction curve sweeped out using the rotating ring disk electrode. The curve consists of an electrochemical polarization region, a concentration polarization region, and a concentration polarization and electrochemical polarization mixing control region, respectively. Electrochemical polarization refers to the phenomenon of electrode polarization caused by the slow reaction of the electrode and the reaction speed of the electrode lags behind the mass transfer rate of the solution. This region is mainly used to analyze the dynamic principle of the working electrode, and to solve the electrode overpotential, exchange current density, etc. Kinetic parameters. Concentration polarization refers to the electrode reaction process, and the diffusion rate of liquid phase mass transfer lags behind the electrode reaction rate, thereby generating electrode polarization. From the concentration polarization region, we can get the limiting current and investigate the factors related to the test conditions through the limiting current.

For concentrated polarization regions, if the cathode electrode reacts to.

$$O + en- \rightarrow R \tag{3.44}$$

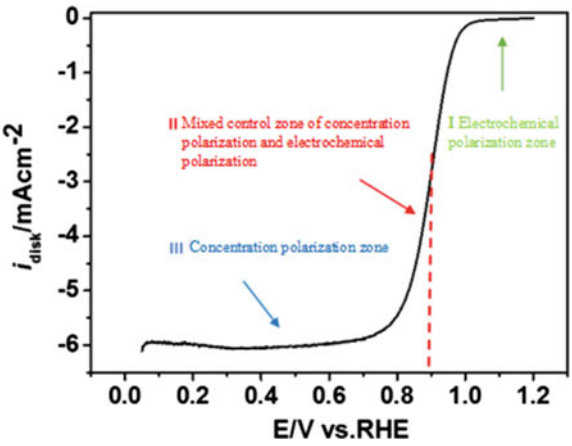

Fig. 3.19 Schematic diagram of the linear volt–ampere curve of oxygen reduction

When the electrode reaction reaches a steady state, according to Fick's first law, the electrode current density can be expressed as follows.

$$i = nFD_0 \frac{a_O^0 - a_O^s}{\delta} \tag{3.45}$$

where $a_o{}^s$ is the activity of substance O on the electrode surface, $a_o{}^0$ is the activity of substance O in the bulk solution, δ is the thickness of the diffusion layer, and D_0 is the diffusion coefficient of substance O.

If the reaction is controlled only by mass transfer (Zone III), the activity of substance O on the electrode surface tends to 0, $a_o{}^s \rightarrow 0$, so the limiting current density can be expressed as follows.

$$i_d = nFD_0 \frac{a_O^0}{\delta} \tag{3.46}$$

For the oxygen reduction reaction, the above formula can be expressed as follows.

$$i_d = \frac{nFD_0C_0}{\delta} \tag{3.47}$$

where D_O is the diffusion coefficient of oxygen and C_0 is the concentration of oxygen in the solution.

It can be seen from the above formula that if the catalyst film is uniform and the thickness is moderate, the limiting current is affected by the temperature, the electrolyte solution and the rotational speed. As the temperature increases, the diffusion coefficient of oxygen molecules increases, but the solubility of oxygen in solution decreases with increasing temperature. Therefore, the effect of temperature on the oxygen reduction limit current is the balance between the two, Paulus et al. The

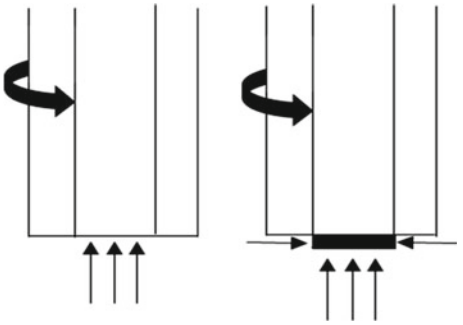

Fig. 3.20 Schematic diagram of the mass transfer effect on the side of the disc electrode film. **a** Thin-film electrode without any side mass transfer; **b** Thick film with side mass transfer

oxygen reduction limit current is the smallest at 80 °C, the maximum at 40 °C, and the limit current at 20 °C is between 80 and 40 °C. In different electrolyte solutions, the diffusion coefficient and solubility of oxygen are different, which affects the value of the limiting current. In addition, as the rotational speed increases, the thickness of the diffusion layer decreases, and the limiting current increases.

For a common thin-film electrode, such as a commercial Pt/C catalyst electrode, the limit current value tends to be 6 $mA.cm^{-2}$ at a sweep rate of 25 °C, 1600 rpm, and 5 $mV.s^{-1}$. For nonplatinum catalysts, the limit current values measured under the same conditions often exceed 6 $mA.cm^{-2}$. This may be because when preparing a nonplatinum catalyst film, the amount of catalyst used in the test tends to be relatively large, and the thickness of the formed catalyst film has exceeded 0.1 μm. At this time, the contribution of side mass transfer to the limiting current of the film electrode is not negligible. Considering the contribution of this part, the limit current value measured under the same conditions will be greater than 6 $mA.cm^{-2}$. The approximate derivation process is as follows (Fig. 3.20).

If the nonplatinum catalyst film layer is uniform, the liquid flow near the electrode is laminar, the catalyst film is simplified to a cylinder, and assuming that the catalyst layer thickness is 0.5 mm and the electrode geometric area A_{geo} is 0.2475 cm^2, the true area of the steady state is involved.

$$\text{Areal} = A_{geo} + A_{side} = 0.2475 + 0.05 * 2 * 3.14 * 0.25 = 0.326\ cm^2 \quad (3.48)$$

According to the Levich limit current equation, at 25 °C, 1600 rpm.

$$i_d = 0.62nFD_0^{2/3}\omega^{1/2}v^{-1/6}C_0 \quad A_{real} = 6 * 0.326 = 1.956\ mA \quad (3.49)$$

$$i_d/A_{geo} = 7.9 mA.cm^{-2} \quad (3.50)$$

From the above brief deduction, it is known that the limit current value is amplified in consideration of the influence of side mass transfer. In addition, when the rotating shaft is bent, causing the electrode to sweep through a larger solution area, the phenomenon of limiting current amplification also occurs.

In summary, the limiting current can be used to detect whether the film is uniform, whether the experimental conditions are properly set, and whether the solution is pure.

From the oxygen reduction curve, in addition to the limit current i_d, we can also obtain oxygen reduction parameters such as half-wave potential and initial potential. Thereby, the oxygen reduction performance of the catalyst can be roughly evaluated. Of course, the steeper the oxygen reduction curve, the better the electrical properties of the catalyst.

3.5.2 Mass Activity and Specific Activity

The mass activity i_m (mass activity) and specific activity i_s (specific activity) of the catalyst are two different normalization criteria, that is, the activity is normalized to the active material loading or the active area of the catalyst, so that the objective evaluation can be different. Catalytic activity of the catalyst. Taking metal platinum as an example, its calculation formula is as follows.

$$i_m\ (\text{A mg}_{\text{Pt}}^{-1}) = \frac{i_k\ (\text{mA})}{\text{L}_{\text{Pt}}\ (\mu g)} \tag{3.51}$$

$$i_s\ (\mu A\ \text{cm}_{\text{Pt}}^{-2}) = \frac{i_k\ (\text{A})}{(Q_{H-adsorption}\ (C)/210\ (\mu C\ \text{cm}_{\text{Pt}}^{-2}))} \tag{3.52}$$

where i_k represents the kinetic current, $Q_{H\text{-}adsorption}$ represents the amount of hydrogen absorbed, and L_{Pt} represents the loading of Pt.

It can be seen from the above equation that in order to obtain mass activity and specific activity, it is first necessary to obtain a kinetic current i_k. The kinetic current, also called the net kinetic current, is the current value after removing the mass transfer effect. Below we will derive the kinetic current and further explore how to obtain the kinetic current i_k by correcting the measured current. The derivation process of the kinetic current is as follows.

On the rotating disk electrode, the convection–diffusion equation of the substance j is as shown in (3.57).

$$\frac{\partial C_j}{\partial t} = D_j \nabla^2 C_j - v \nabla C_j \tag{3.53}$$

Among them $\nabla C_j = i\frac{\partial C_j}{\partial x} + j\frac{\partial C_j}{\partial y} + k\frac{\partial C_j}{\partial z}$, D_j is the diffusion coefficient of substance j, the unit is$\text{cm}^2.\text{s}^{-1}$, vector v represents the motion of the solution, and its cylindrical coordinate form can be expressed as follows.

$$v = iu_x + ju_y + ku_z \tag{3.54}$$

Where *i, j, k* are unit vectors, and u_x, u_y, and u_z are the flow rates of the solution in the x, y, and z directions, respectively. In order to solve the convection–diffusion equation of the material on the rotating disk electrode and obtain the concentration distribution of the substance on the surface of the electrode, it is necessary to discuss its velocity distribution *v*. By solving the hydrodynamic Eq. (3.55) under steady-state conditions, Von Karman and Cochran obtained the velocity distribution of the fluid near the rotating disk electrode as shown in Eq. (3.56).

$$\begin{aligned}
&\frac{v_\varphi}{r}\frac{\partial v_r}{\partial \varphi}+v_r\frac{\partial v_r}{\partial r}-\frac{v_\varphi^2}{r}+v_y\frac{\partial v_r}{\partial y}=-\frac{1}{\rho}\frac{\partial \rho}{\partial r}+v(\Delta v_r-\frac{v_r}{r^2}-\frac{2}{r^2}\frac{\partial v_\varphi}{\partial \varphi})\\
&\frac{v_\varphi}{r}\frac{\partial v_\varphi}{\partial \varphi}+v_r\frac{\partial v_\varphi}{\partial r}+\frac{v_r v_\varphi}{r}+v_y\frac{\partial v_\varphi}{\partial y}=-\frac{1}{\rho r}\frac{\partial \rho}{\partial r}+v(\Delta v_\varphi+\frac{2}{r^2}\frac{\partial v_r}{\partial \varphi}-\frac{v_\varphi}{r^2})\\
&\frac{v_\varphi}{r}\frac{\partial v_y}{\partial \varphi}+v_r\frac{\partial v_y}{\partial r}+v_y\frac{\partial v_y}{\partial y}=-\frac{1}{\rho}\frac{\partial \rho}{\partial y}+v\Delta v_y\\
&\frac{1}{r}\frac{\partial v_\varphi}{\partial \varphi}+\frac{\partial v_r}{\partial r}+\frac{v_r}{r}+\frac{\partial v_y}{\partial y}=0
\end{aligned} \tag{3.55}$$

Among them, v_φ, v_r, v_y respectively angular velocity, the linear velocity, and the axial velocity are respectively expressed as follows.

$$\begin{aligned}
v_r &= r\omega(a\gamma-\frac{\gamma^2}{2}-\frac{1}{3}b\gamma^3+..)\\
v_\varphi &= r\omega(1+b\gamma+\frac{1}{3}\alpha\gamma^3+..)\\
v_y &= (\omega v)^{\frac{1}{2}}(-a\gamma^2+\frac{\gamma^3}{3}+\frac{b\gamma^4}{6}..)
\end{aligned} \tag{3.56}$$

Here, a = 0.51023 and b = −0.6159, $\gamma = (\omega/v)^{1/2}y$, ω is the angular velocity of rotation, the unit is s^{-1}, *v* is the kinematic viscosity, the unit is $cm^2.s^{-1}$. The research on rotating disk electrodes is concerned with the speeds v_r and v_y.

Near the surface of the disc, y → 0 (or γ → 0), so

$$\mathrm{vy} = (\omega\mathrm{v})1/2\left(-\alpha\gamma^2\right) = -0.51\omega 3/2\mathrm{v} - 1/2\,\mathrm{y}^2. \tag{3.57}$$

In steady state, the concentration near the electrode is not a function of time, so the convection–diffusion Eq. (3.53) can be written as:

$$v_r\frac{\partial C}{\partial r}+\frac{v_\varphi}{r}\frac{\partial C}{\partial \varphi}+v_y\frac{\partial C}{\partial y}=D_O\left(\frac{\partial^2 C}{\partial y^2}+\frac{\partial^2 C}{\partial r^2}+\frac{1}{r}\frac{\partial^2 C}{\partial r}+\frac{1}{r^2}\frac{\partial^2 C}{\partial \varphi^2}\right) \tag{3.58}$$

Under limiting current conditions, the boundary conditions are:

$$\begin{aligned}
&y=0 \quad C=0\\
&y\to\infty \quad C=C_0
\end{aligned} \tag{3.59}$$

Moreover, C_0 is the concentration of the solution body, regardless of φ, and v_y is independent of r. So (3.58) can be written as:

$$v_y \frac{\partial C}{\partial y} = D_O \frac{\partial^2 C}{\partial y^2} \tag{3.60}$$

Bring (3.57) into (3.60): so

$$\frac{\partial^2 C}{\partial y^2} = \frac{-y^2}{B} \frac{\partial C}{\partial y} \tag{3.61}$$

Among them $B = D_0 \omega^{(-3/2)} v^{(1/2)}/0.51$.

By integrating (3.61) with the upper and lower limits of the integral of (3.60), you can get.

$$C_0 = (\frac{\partial C}{\partial y})_{y=0} (D_0 \omega^{-3/2} v^{1/2}/0.51)^{1/3} \tag{3.62}$$

And because of the current.

$$i = nFAD_0 (\frac{\partial C}{\partial y})_{y=0} \tag{3.63}$$

Here n is the number of electrons involved in the electrode reaction, F is the Faraday constant, and A is the electrode area. So by combining (3.62) and (3.63), you can get the Levich limit current equation.

$$i_d = 0.62nFAD_0^{2/3} \omega^{1/2} v^{-1/6} C_0 \tag{3.64}$$

Under nonlimiting current conditions, only the integral limit of the (3.60)-type integration process needs to be changed.

$$i = 0.62nFAD_0^{2/3} \omega^{1/2} v^{-1/6} \nu C_0 - C_{y=0} \nu \tag{3.65}$$

So $i = i_d \frac{(C_0 - C_{y=0})}{C_0}$ or

$$C_{y=0} = C_0 (1 - \frac{i}{i_d}) \tag{3.66}$$

For a completely irreversible reaction, the disk current can be expressed as:

$$i = FAk_f(E) C_{y=0} \tag{3.67}$$

where $k_f(E) = k^0 \exp\{-af\left(E - E^{\ominus}\right)\}$, $f = F/RT$ k0 is the standard rate constant and α is the transfer coefficient. When there is no exact measurement, α is generally considered to be equal to 0.5.

Substituting (3.66 into (3.67) gives:

$$i = FAk_f(E)C_0(1 - \frac{i}{i_d}) \tag{3.68}$$

Order $i_k = FAk_f(E)C_0$, you can get the Koutecký-Levich equation:

$$\frac{1}{i} = \frac{1}{i_k} + \frac{1}{i_d} \tag{3.69}$$

Where i_k represents the current without any mass transfer, called the kinetic current; i_d is the limiting current; i is the measured current at any potential.

(3.69) can be transformed into:

$$i_k = \frac{i_d \times i}{i_d - i} \tag{3.70}$$

By measuring the oxygen reduction polarization curve, we can obtain the measured current i and the limit current i_d, and substitute it into the above deformation expression to obtain the kinetic current i_k.

After the kinetic current i_k is obtained, the i_k is removed from the mass of the catalyst platinum or its relative electrochemical specific surface area, and two key parameters characterizing the activity of the oxygen reduction catalyst, mass activity im and specific activity is further solved.

The measured current value at 0.9 V versus RHE is generally selected for dynamic correction, and the kinetic current i_k, mass activity i_m and specific activity is calculated. The main reason is that if the important kinetic parameters of the exchange current density are used for correction, since this parameter can only be obtained by extrapolating the measured current, the extrapolation of the extrapolation method causes a large error in the exchange current density, resulting in significant experimental error. In addition, if the activity standard is set at 0.9 V versus RHE, one can guarantee the maximum output of power, because the fuel cell generally operates at less than 0.9 V versus RHE; both can minimize the test error, which is Because at lower potentials, the current is affected by Ohmic drop and oxygen mass transfer, while at higher potentials, the test on the rotating ring disk electrode is affected by the electric double layer, and the fuel cell stack is infiltrated by hydrogen influences. Moreover, the simulation test results of the rotating disk electrode at 0.9 V versus RHE have a high degree of fit with the actual test results of the fuel cell. H. A. Gasteiger et al. reported that the oxygen reduction activity on the rotating disk electrode of the Pt/C catalyst at 0.9 V versus RHE was consistent with that measured by

the fuel cell stack, while at 0.8 V versus RHE there was a bias. Therefore, in combination with various factors, most literature and fuel cell activity standards use 0.9 V versus RHE as the dynamic correction standard and activity comparison standard.

From the above derivation process and the Levich limit current equation, the factors affecting the limit current value include the number of electrons involved in the electrode reaction, the electrode area, the angular velocity of the electrode, the dynamic viscosity of the electrolyte solution, and the diffusion ability and solubility of oxygen molecules. From the current measurement of the limit current in most of the literature, the limit current measured at 1600 rpm for different catalysts is 6 mA.cm^{-2} at 298 K, which also proves that for the speed, temperature, electrolyte type and the oxygen reduction test system of the same concentration has a constant current value as long as the catalyst layer is sufficiently uniform and the thickness is moderate, regardless of the type of the catalyst and the grain size.

If $i_d \rightarrow 6$ mA.cm^{-2}, $L_{Pt} = 20$ μg.cm^{-2}, the relationship between i and i_m can be obtained.

$$i_m(\text{A mg}_{\text{Pt}}^{-1}) \rightarrow \frac{3i(\text{mA cm}^{-2})}{60 - 10i(\text{mA cm}^{-2})} \tag{3.71}$$

The graph of Fig. 3.21 can be obtained by plotting the above formula. When the measured current i at 0.9 V infinitely approaches the limiting current of 6 mA.cm^{-2}, the mass activity i_m increases rapidly.

The mass activity of the catalyst released by the U.S. Department of Energy at 0.9 $V_{iR\text{-free}}$ versus RHE will reach 0.44A.mg$_{Pt}^{-1}$ by 2017. Although most of the current research is focused on improving oxygen reduction activity, there are still many problems to be solved. If only from the point of view of mass activity calculation and oxygen reduction curve analysis, the method of increasing oxygen reduction activity is to increase the measured current of 0.9 $V_{iR\text{-free}}$ versus RHE while ensuring

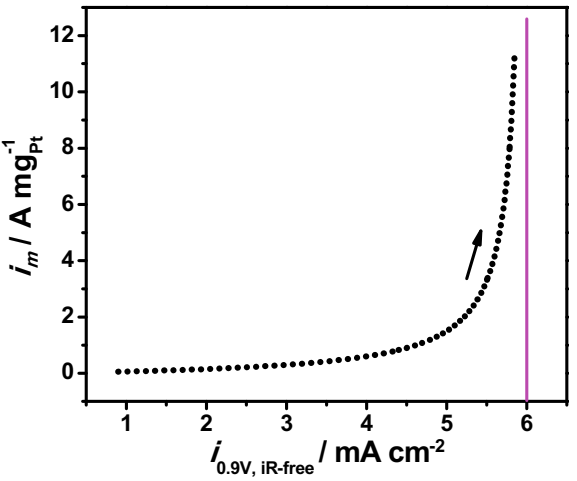

Fig. 3.21 The relationship between i_m and i. $i_d \rightarrow$ 6 mA.cm^{-2}, $L_{Pt} =$ 20 μg.cm^{-2}

the limiting current. From this perspective, the current optimization methods can be simply classified into three categories. The first is to increase the peak potential of oxygen reduction and inhibit the oxidation of Pt. The main methods are Pt-based alloys and ionic liquids. Second, the slope of the curve of the concentration polarization and the electrochemical polarization mixing control region is increased, that is, the internal resistance of the catalyst is lowered or the conductivity of the catalyst is improved. Qu et al. [20] reported that the internal resistance of nitrogen-doped graphene is very small, although the oxygen reduction catalytic activity of this material is still smaller than Pt, especially in the low overpotential region, but it is also a potential material for optimizing oxygen reduction activity. The third method is to reduce the loading of Pt or increase the utilization rate of Pt. The main methods include dealloying, increasing the proportion of Pt(111) crystal plane, increasing the active area, and preparing various special nanostructured catalysts.

Although there are many reports on high-activity oxygen reduction catalysts, Pt-based catalysts are still put into practical use, mainly Pt/C catalysts. The research focuses on the following aspects.

(i) Rotating ring disk electrode test. The effectiveness of the catalyst oxygen reduction still needs further exploration, especially the oxygen reduction simulation test of nonprecious metal catalysts. In many of the literatures already reported, the rotating ring disk electrode test results of most of the new catalysts are highly reproducible and almost identical to actual cell stack test results. However, with the further exploration of catalysts, especially the discovery of nonprecious metal catalysts, it is still unknown whether the rotary ring electrode oxygen reduction simulation test is still valid.
(ii) The relationship between the active substances, the relationship between the carrier and the doping elements, and the activeness of the substances still require more experimental exploration, such as environmental spherical aberration correction electron microscopy and DFT simulation calculations.
(iii) Exploring new forms of catalysts, such as simulated enzyme catalysts, which have lower oxygen reduction over potentials than Pt(111) planes, and even lower than the currently reported Pt_3Ni alloys with the highest activity. It also includes the preparation of self-assembled nanostructured catalysts and the like.
(iv) The high activity catalysts simulated by the simulation should be tested on actual stacks to investigate their activity and stability.
(v) Reduce the cost of an efficient synthetic process for commercialization purposes.

3.6 Electrochemical Determination of Specific Surface Area

The specific activity of the catalyst is required, first of all, to know its electrochemical specific surface area. Ref. [21] details the principle and method of specific surface area measurement. Here we only mention the most commonly used electrochemical test methods.

3.6.1 Overview of Commonly Used Electrochemical Measurements of Specific Surface Area

The electrochemical methods currently used to measure the electrochemical specific surface area of catalysts having a high specific surface area include measuring the integrated charge of the hydrogen desorption zone, the desorption of the saturated adsorbed CO, and the desorption of the underlying potential of the single layer of Cu.

Measuring the desorption amount of saturated adsorbed CO The basic principle of determining the active area is to use CO as a detection molecule, which can occupy all active sites of electrocatalytic activity of the catalyst, and obtain the active area of the catalyst by monitoring the change of the oxidative desorption electric quantity. For organic electrochemical reactions, CO is very easy to achieve CO adsorption because it is an intermediate substance for many reactions. As early as 1962, Gilman began to study the adsorption behavior of CO on the electrode [22], and found that the adsorption of CO is controlled by diffusion and there are at least two bonding states on the polycrystalline platinum electrode. Adsorption of CO can be used to measure the active area of a metal or alloy, but the bonding mode of adsorbed CO is very complicated, such as linear adsorption, bridge adsorption and flat adsorption, and the bonding mode is closely related to metal surface state and defect density. At lower potentials, CO adsorbs strongly on the surface of Pt and other metals. When the adsorption of CO on the surface of the electrode reaches saturated adsorption, it is electrochemically oxidatively desorbed. In this process, oxidative desorption is complete with a single layer of CO. The amount of active point exchanged between the molecule and the electrode is calculated. This part of the oxidative desorption is usually included in the cyclic voltammetry curve, the amount of electricity required for oxidation of the CO, the charge of the electric double layer, the oxidation of the active material, and the oxidation of the remaining adsorbed ions. In the calculation, it is necessary to deduct the electric charge of the electric double layer, the oxidation of the active material, and the oxidation amount of the remaining adsorbed ions, and extract the desorption amount purely for CO oxidation. The electric charge deduction of the electric double layer is generally considered to be the same as that of the electric double layer in the CO oxidation desorption region and the electric double layer region, thereby simplifying the calculation. A more rigorous subtraction method can be found in the literature 23, which proposes two CO double-layer electric charge deduction models, which respectively compare or exclude the influence of the electric quantity caused by the Pt(111) surface special adsorption state on the coverage calculation. The deduction of the oxidative charge of the active material and the remaining adsorbed ions are complicated, which also limits the application of CO in determining the active area. In addition to the complex background current subtraction, the saturated adsorption state of CO is difficult to determine, and there is also a CO coverage problem, such as incomplete coverage or lamination coverage, and measurement results may have large errors. It is generally believed that the

saturation coverage of CO on the Pt electrode is between 0.63 and 0.68 mL, and the power density required for CO oxidation of the single layer of CO is 420 $\mu C.cm^{-2}$.

The basic principle of characterizing the active area by the underpotential deposition of a single layer of Cu is similar to measuring the CO oxidative desorption. Here, the probe atom is Cu, and at the Nernst equilibrium potential, the probe atom begins to deposit on the surface of the substrate. For the catalyst containing metal Ru, the adsorption of CO and H on its surface is accompanied by a large ion adsorption, resulting in a large error, and the adsorption of Cu does not have this problem. However, the main disadvantage of this method is that the metal ions strongly influence the reaction of the catalyst and are not conducive to the cleaning of the electrolytic cell after the reaction.

The electrochemical specific surface area is calculated by the integrated electric quantity of the hydrogen desorption zone. The biggest advantage is that this method is simple and easy and can be directly obtained by integrating the CV curve. In the following, metal platinum is taken as an example to discuss in detail how to calculate the electrochemical specific surface area of the catalyst by measuring the integrated electric quantity in the hydrogen desorption zone and give considerations for using the method.

3.6.2 Integrated Power of Hydrogen Adsorption Zone

Different research teams have different selection tendencies in the choice of hydrogen adsorption or desorption of electricity to characterize the active area. Theoretically, the amount of hydrogen absorbed and desorbed should be the same, but the underpotential reduction of hydrogen easily causes the oxidation of hydrogen, which interferes with the amount of electricity in the hydrogen desorption zone. In addition, setting the upper limit potential of different catalyst oxidation will affect the desorption peak of hydrogen. Considering these factors comprehensively, this paper adopts the method of measuring the electricity in the hydrogen adsorption zone.

For metal Pt, when cyclic scanning is performed in an acidic aqueous solution, a hydrogen atom adsorption peak appears in the potential region of +0.4 ~0.05 V (vs. SHE), and the specific surface area of the electrode can be calculated by the amount of the adsorption peak. As shown in (3.75).

$$\mathrm{ECSA_{Pt}}\ (\mathrm{m^2}\ g_{Pt}^{-1}) = \left(\frac{Q_{H-adsorption}\ (C)}{210\ (\mu C\ cm_{Pt}^{-2}) L_{Pt}\ (mg_{Pt}\ cm^{-2}) A_g\ (cm^2)} \right) \times 10^5 \tag{3.72}$$

Where $Q_{\text{H-adsorption}}$ represents the amount of hydrogen adsorbed, L_{Pt} represents the loading of Pt, and Ag represents the geometric area of the glassy carbon electrode carrying Pt. In the formula, 210 $\mu C.cm^{-2}$ is the electric charge density when Pt

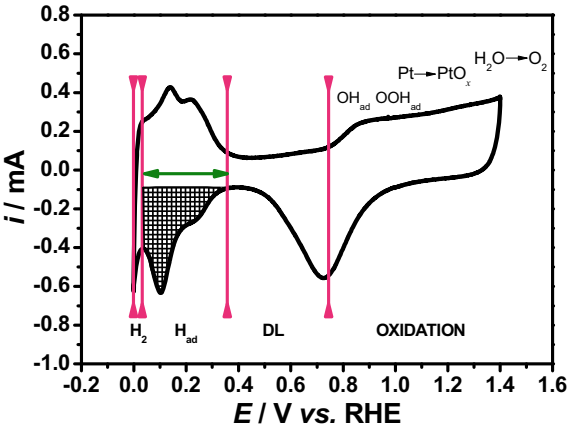

Fig. 3.22 Scanning potential curve of Pt/C electrode in 0.1 mol·L^{-1} $HClO_4$ solution (potential sweep speed 50 mV.s^{-1}. The shaded area is the area of hydrogen adsorption)

is adsorbed on a single layer of H atoms, which is the average value of the three low-index crystal surface charge densities of Pt.

The amount of hydrogen adsorbed by $Q_{H\text{-adsorption}}$ can be obtained by integrating the hydrogen adsorption region on the cyclic voltammetry curve. Figure 3.22 is the cyclic voltammetry curve of a commercial catalyst in 0.1 mol·L^{-1} $HClO_4$ solution. The upper curve of the abscissa in the figure is the forward scan (from low to high) curve, and the lower is the negative scan curve.

The cyclic voltammetry curve can be divided into four different regions. The first region is an underpotential reduction (hydrogen evolution) region (H_{UPD}) of a hydrogen atom. In 1935, Frumkin and Slygin first studied the underpotential reduction of hydrogen on the Pt electrode. In an acidic solution, the oxidation and reduction mechanism of the surface H of the polycrystalline Pt electrode is generally considered to be initiated by the adsorption of H molecules, involving the decomposition of H molecules into adsorbed H atoms and the recombination of H ions into H molecules, which are generally considered to be as follows.

$$H_2 \rightarrow H_{ad} + H_{ad} \tag{3.73}$$

$$H_2 \rightarrow H^+ + H_{ad} + e^- \tag{3.74}$$

$$H_{ad} \leftrightarrow H^+ + e^- \tag{3.75}$$

It can be seen from the above equation that H_{ad} is an intermediate medium for H oxidation or reduction reaction, so the reaction kinetics of H is closely related to the state of H_{ad} on the surface of Pt, that is to say, its coverage has a greater influence on it. The electrode potential varies with the hydrogen atom coverage of the electrode surface $\Theta_{H,\,UPD}$ satisfies the following formula:

$$\frac{\theta_{H,UPD}}{1-\theta_{H,UPD}} = K \exp -(g\theta_{H,UPD}) \times \exp -(EF/RT) \tag{3.76}$$

g is a constant characterizing the two-dimensional lateral growth of the H adsorbed layer.

The underpotential hydrogen evolution process will occur at around 0.05 V depending on the electrode material, not at 0 V. The oxidation of free hydrogen in this process may result in a large desorption of the measured adsorbed hydrogen. Due to the existence of such an underpotential hydrogen evolution process, it is necessary to avoid this region during the oxygen reduction test to avoid the influence of the precipitated hydrogen on the result. This area is typically 0–0.05 V (vs. RHE).

The second region is mainly the absorption and desorption (H_{ad}) of hydrogen, and the amount of electricity passing through this potential region is mainly used to change the amount of hydrogen absorption and desorption.

$$Pt + H_3O^+ + e^- \rightarrow Pt - H_{ad} + H_2O \tag{3.77}$$

If H_{ad} is assumed to be a single layer of adsorption on the surface of a smooth Pt electrode, the amount of hydrogen adsorbed to a single layer of hydrogen is 210 $\mu C.cm^{-2}$. The crystal structure of Pt has a great influence on the precipitation and reduction potential of this region H. The characteristics of the absorption and desorption peaks of hydrogen on different crystal faces are also completely different. On a cyclic voltammogram of 0.5 $mol{\cdot}L^{-1}$ $H2SO_4$solution, for Pt(100), when E < 0.25 V has a larger plateau, E = 0.25 V has a butterfly peak, the latter is in solution The sulfate/hydrogen sulfate ion participates in the adsorption/desorption process. On Pt(111), there are one small and two current spikes at E = 0.1 V and 0.42 V, respectively. The former corresponds to the adsorption of hydrogen on the short-range ordered (111) position, and the latter corresponds to the hydrogen in the long-range order (111) adsorption on the site. On the Pt (110), only the peak at 0.12 V appears. The different adsorption and desorption peaks of hydrogen on the three basic crystal faces have become the criterion for in situ detection of different crystal plane structures.

In the third region, there are few hydrogen atoms adsorbed in the potential range, and the charged electric quantity is mainly used for charging the electric double layer, so it is called "double electric layer region." Since the electric double layer can quickly reach equilibrium, the electric double layer capacitance is independent of the scanning rate and is affected by the electrode potential. The charging current density of the electric double layer can be expressed by the following formula.

$$j_c = C_d \frac{d\varphi}{dt} \tag{3.78}$$

In the formula, C_d is an electric double layer differential capacitance, and $d\phi/dt$ is a rate of change of the electrode potential with time, that is, a scanning rate.

The absorption and desorption of hydroxide and oxygen began to appear in the fourth region. As the potential increases, the adsorbed oxygen atoms and hydroxide ions formed on the surface of the electrode combine with platinum to form oxides (PtO_x) and hydroxides, and even oxygen evolution occurs.

In an acidic solution, Conway et al. believe that at 1.18 V (vs. RHE), the platinum surface is filled with a single layer of PtOH.

$$Pt + H_2O \rightarrow Pt - OH + H_+ + e^- \tag{3.79}$$

Subsequently, PtOH is further reacted to form PtO. Gregory and Jerkewic et al. proposed a potential for forming a single layer of PtO of 1.4 V (vs. RHE).

In an alkaline solution, hydroxide adsorption occurs at about 0.55 V, and the reaction equation is as follows:

$$Pt + OH^- \rightarrow Pt{-}OH + e^- \tag{3.80}$$

PtO is formed at about 0.8 V.

$$Pt{-}OH + OH^- \rightarrow Pt{-}O + H_2O + e^- \tag{3.81}$$

Therefore, this area is called the "oxygen zone." If the reverse phase of the oxygen adsorption zone is reached, as the potential becomes negative, oxygen desorption (reduction), electric double layer charging, and hydrogen adsorption process will occur in sequence.

The hydrogen adsorption zone of the second region is integrated, and the result is the amount of electricity in the zone. Since the region contains the charging of the electric double layer, the result obtained by subtracting this part of the charging power is the hydrogen adsorption amount, and the calculation formula of the adsorption amount of the hydrogen adsorption region is as shown in (3.82).

$$Q_{H-adsorption} = \frac{\int_{E_L}^{E_h} (I - I_{DL}) dE}{v} \tag{3.82}$$

In the above formula,v is the scanning speed, I is the adsorption region current, I_{DL} is the electric double layer charging current, the lower integration limit E_L is the potential at the end of the hydrogen underpotential deposition, generally between 0.03 and 0.05 V, and the upper limit of integration E_h is hydrogen. The end of the adsorption zone determines or the initial potential of the adsorbed hydrogen, typically between 0.45 and 0.5 V.

Taking the shaded portion of Fig. 3.22 as an example, the result is the hydrogen adsorption energy $Q_{H\text{-adsorption}}$, and the hydrogen adsorption energy $Q_{H\text{-adsorption}}$ is substituted into (3.82) to obtain the electrochemical specific surface area. The detailed calculation process is as follows.

$$Q_{H-adsorption} = \frac{\int_{E_L}^{E_h} (I - I_{DL})dE}{v} = \frac{\int_{0.037}^{0.394} (I + 8.869 \times 10^{-5})dE}{0.05}$$
$$= 1.52 \times 10^{-3} C \tag{3.83}$$

$$\mathrm{ECSA_{Pt}(m^2\ g_{Pt}^{-1})} = \left(\frac{Q_{H-adsorption}(C)}{210(\mu C\ \mathrm{cm_{Pt}^{-2}}) L_{Pt}(\mathrm{mg_{Pt}\ cm^{-2}}) A_g(\mathrm{cm^2})} \right) \times 10^5$$
$$= \frac{152 \times 10^{-5}}{210 \times 11.9 \times 10^{-3}} \times 10^5$$
$$= 61$$

The catalyst was obtained to have an electrochemical specific surface area of 61 $m^2.g^{-1}$. It should be noted here that since the deduction of the electric quantity of the electric double layer is manual operation, it is recommended to calculate the integral area of the hydrogen adsorption area of three or more CV curves, and take the average value in order to minimize the human error.

Characterization of active regions using electrochemically adsorbed hydrogen species requires attention to the following points:

(i) For most catalysts, the cyclic voltammetry curve is 0–1.4 V versus RHE can generally be divided into four regions. The main difference is the peak current value of each region and the potential of each region. Scope (Fig. 3.16).

(ii) The adsorption capacity of the single layer of hydrogen adsorbed $Q_{H\text{-adsorption}}$ is calculated or tested by the action of the active substance and hydrogen used. The above value of 210 $\mu C.cm^{-2}$ is polycrystalline platinum and three low-index Miller. The average value of the surface hydrogen adsorption amount is the hydrogen adsorption amount which is only considered to be the (100) plane.

(iii) This method is based on the assumption that hydrogen adsorption and its coverage are independent of the surface structure and alloying of the catalyst. However, many studies have found that an increase in the weak bonding mode between hydrogen and the catalyst reduces the amount of hydrogen adsorbed. For example, multilayer adsorption or submonolayer adsorption of hydrogen due to synergy between metals results in a large error in characterizing the electrochemically active area of the platinum-based alloy by hydrogen adsorption. In addition, whether the hydrogen is full of monolayer adsorption at the active site, whether the catalyst and hydrogen are one-to-one adsorption (i.e., pure monolayer adsorption), and the active point contribution of each polycrystalline surface also make the method have greater uncertainty.

(iv) The use of this method requires careful consideration. For example, for a metal-containing Pd catalyst, this method is not suitable because the hydrogen atom not only adsorbs on the metal surface but also penetrates into the gap of the palladium to become a gap atom, that is, palladium absorbs hydrogen atoms. In addition to important metals such as gold, enamel and enamel, this method is not applicable. However, for precious metal ruthenium, measuring the desorption

power of hydrogen to characterize the active area may be the only effective method to characterize the active area of the metal.

In summary, hydrogen desorption and desorption characterizes the active area due to its own premise, which makes it more uncertain, but its operation is simple and can be detected in situ, so it is still a valuable test method.

After obtaining the electrochemical specific surface area, if the net kinetic current i_k is known, the specific activity is further determined. For the activity of the catalyst to be characterized by specific activity, it is necessary to pay attention to the fact that, from the formula, to increase the specific activity, since the increase of the net kinetic current is generally difficult to keep up with the increase of the active area, there are two options, which are greatly reduced. The active area or the net kinetic current is greatly increased. Since the active area can be made very large under normal circumstances, and the increase of the net kinetic current is very small, in many cases, the experimental result is to increase the specific surface area several times, but the specific activity does not increase or even decrease. However, as far as we know, in general, the larger the specific surface area, the higher the utilization rate of the noble metal in the catalyst, and the increase of the specific surface area is advantageous for increasing the utilization rate of the active material of the catalyst and thereby improving the catalytic activity of the oxygen reduction. However, using this activity standard, the most common case is to reduce the active area or the catalyst utilization is beneficial to increase the specific activity, thereby optimizing the oxygen reduction catalytic activity, which is contrary to our research common knowledge. The U.S. Department of Energy has been aware of this problem and has removed the activity standard for activity than the latest DOE indicator.

References

1. Teliska A, O'Grady WE, Ramaker DE (2005) Determination of O and OH adsorption sites and coverage in situ on Pt electrodes from Pt L23 X-ray absorption spectroscopy. J Phys Chem B 109:8076
2. Murthi VS, Urian RC, Mukerjee S (2004) Oxygen reduction kinetics in low and medium temperature acid environment: correlation of water activation and surface properties in supported Pt and Pt alloy electrocatalysts. J Phys Chem B 108:11011
3. Roth C, Benker N, Buhrmester T et al (2005) Determination of O[H] and CO coverage and adsorption sites on PtRu electrodes in an operating PEM fuel cell. J Am Chem Soc 127:14607
4. Teliska M, Murthi VS, Mukerjee S et al (2005) Correlation of water activation, surface properties, and oxygen reduction reactivity of supported Pt–M/C bimetallic electrocatalysts using XAS. J Electrochem Soc 152:A2159
5. Koh S, Leisch J, Toney MF et al (2007) Structure-activity-stability relationships of Pt−Co alloy electrocatalysts in gas-diffusion electrode layers. J Phys Chem C 111:3744
6. Koh S, Toney MF, Strasser P (2007) Activity–stability relationships of ordered and disordered alloy phases of Pt3Co electrocatalysts for the oxygen reduction reaction (ORR). Electrochim Acta 52:2765
7. Yano H, Inukai J, Uchida H et al (2006) Particle-size effect of nanoscale platinum catalysts in oxygen reduction reaction: an electrochemical and 195Pt EC-NMR study. Phys Chem Chem Phys 8:4932

8. Treimer S, Tang A, Johnson DC (2002) A consideration of the application of Koutecký-Levich plots in the diagnoses of charge-transfer mechanisms at rotated disk electrodes. Electroanalysis 14:165
9. Wroblowa HS, Pan YC, Razumney G (1976) Electroreduction of oxygen: A new mechanistic criterion. J Electroanal Chem 69:195
10. Schmidt TJ, Gasteiger HA, Stäbc GD et al (1998) Characterization of high-surface-area electrocatalysts using a rotating disk electrode configuration. J Electrochem Soc 145:2354
11. Lawson DR, Whiteley LD, Martin CR et al (1988) Oxygen reduction at Nafion film-coated platinum electrodes: transport and kinetics. J Electrochem Soc 135:2247
12. Jerkiewicz G, Zolfaghari A (1996) Determination of the energy of the metal-underpotential-deposited hydrogen bond for rhodium electrodes. J Phys Chem 100:8454
13. Zolfaghari A, Jerkiewicz G (1999) Temperature-dependent research on Pt(111) and Pt(100) electrodes in aqueous H_2SO_4. J Electroanal Chem 467:177
14. Xiancai Fu et al (2006) Physical chemistry (Volume II). Higher Education Press, Beijing
15. Liang Y, Li Y, Wang H et al (2011) Co3O4, nanocrystals on graphene as a synergistic catalyst for oxygen reduction reaction. Nat Mater 10:780
16. Li Y, Zhou W, Wang H et al (2012) An oxygen reduction electrocatalyst based on carbon nanotube—nanographene complexes. Nat Nanotech 7:394
17. Garsany Y, Baturina OA, Swider-Lyons KE, Kocha SS (2010) Experimental methods for quantifying the activity of platinum electrocatalysts for the oxygen reduction reaction. Anal Chem 82:6321–6328
18. Garsany Y, Singer IL, Swider-Lyons KE (2011) Impact of film drying procedures on RDE characterization of Pt/VC electrocatalysts. J Electroanal Chem 662:396–406
19. Garsany Y, Ge J, St-Pierre J, Rocheleau R, Swider-Lyons KE (2014) Analytical procedure for accurate comparison of rotating diskelectrode results for the oxygen reduction activity of Pt/C. J Electrochem Soc 161:F628–F640
20. Qu L, Liu Y, Baek JB et al (2010) Nitrogen-Doped graphene as efficient metal-free electrocatalyst for oxygen reduction in fuel cells. ACS Nano 4:1321–1326
21. Chikazawa M, Takei T (2006) Surface characterization of powder particles-surface properties and powder properties. In: Masuda H, Higashitani K, Yoshida H (eds) Powder Technology Handbook, 3rd edn. CRC Press, p 325
22. Gilman S (1962) A study of the adsorption of carbon monoxide and oxygen on platinum significance of the "polarization curve." J Phys Chem 66:2657
23. Orts JM, Fernández-Vega A, Feliu JM et al (1992) Electrochemical behaviour of CO layers formed by solution dosing at open circuit on Pt (111) voltammetric determination of CO coverages at full hydrogen adsorption blocking in various acid media. J Electroana Chem 327:261

Chapter 4
Catalyst Materials for Oxygen Reduction Reaction

Yunyong Li, Chunyong He, and Pei Kang Shen

4.1 Catalyst Support Material: Carbon Materials Such as Graphene with Three-Dimensional Structure

In order to prepare an oxygen reduction electrocatalyst with high catalytic performance, the catalyst is usually loaded on a carrier material with high specific area during the preparation process, this is because the catalyst carrier material can perform the functions of supporting and dispersing of active components, mass transfer, electricity, and heat conduction, and even some catalyst carrier materials also have the function of cocatalyst [1]. Therefore, the catalyst carrier material has great influence on the activity and stability of the catalyst. As a catalyst carrier material, the following conditions should be met [1, 2]: (1) high specific surface area is conducive to highly uniform dispersion of the catalyst; (2) low combustible reaction under dry and humid conditions; (3) high electrochemical stability; (4) high conductivity; (5) easy catalyst loading; (6) excellent anti-corrosion performance to prevent the corrosion of electrolyte.

Catalyst support materials can generally be divided into two types [3]: carbon support materials and non-carbon support materials. Carbon carrier materials mainly include carbon black, mesoporous carbon, carbon nanotubes, carbon nanofibers, graphene, etc. Non-carbon carrier materials mainly include oxides, carbides, nitrides, etc.

Y. Li
Guangdong University of Technology, Guangzhou, Guangdong, China

C. He
Spallation Neutron Source Science Center, Dongguan, Guangdong, China

P. K. Shen (✉)
Collaborative Innovation Center of Sustainable Energy Materials, Guangxi Key Laboratory of Electrochemical Energy Materials, College of Chemistry and Chemical Engineering, Guangxi University, Nanning 530004, Guangxi, China
e-mail: pkshen@gxu.edu.cn

P. K. Shen, *Electrochemical Oxygen Reduction*,
https://doi.org/10.1007/978-981-33-6077-8_4

4.1.1 Carbon Carrier Materials

Carbon referent carrier materials [6–9] due to their high specific surface area, good electrical conductivity, electrochemical stability, low cost, easy processing, and other characteristics.

4.1.1.1 Carbon Black

Carbon black is currently the most commonly used carrier material for fuel cell catalysts [10–14], including acetylene black, VulcanXC-72, Bleak Pearl 2000, etc. All these carbon materials have good conductivity. Acetylene black has a small specific surface area, but because there are no micropores, it will not hinder mass transfer of reactants. Although Bleak Pearl 2000 has a high specific surface area, there are too many micropores, resulting in uneven distribution of active substances and ineffective utilization of active sites on the inner surface of the catalyst. VulcanXC-72 produced by Cabot Company is a carbon black material graphitized by amorphous activated carbon, with a specific surface area of about 250m^2 g^{-1}, good electrical conductivity, and good pore structure (mesopore area accounts for about 53% of the specific surface area). Therefore, it is currently the most used catalyst carrier in fuel cell electrocatalysts [15].

4.1.1.2 Carbon Nanotube

Carbon nanotubes (CNTs), also known as bucky tubes, are seamless and hollow tube structures composed of honeycomb-shaped hexagonal carbon. According to the thickness of the tube wall, CNTs can be divided into two types: one is single-walled carbon nanotubes (SWCNTs); the other is multi-walled carbon nanotubes (MWCNTs). Compared with Vulcan XC-72, firstly, CNTs have a unique hollow structure, good electrical conductivity and thermal stability, stable chemical properties, large specific surface area, a and special interaction between delocalized π electrons and catalyst metal d electrons, so as to enable electrocatalyst to have higher catalytic activity [2, 16]. Secondly, CNTs are purer and contain less impurities, while Vulcan XC-72 contains a certain amount of organic sulfur impurities, which will have a certain toxic effect on Pt catalyst, thus affecting its electrocatalytic activity. Thirdly, CNTs have a complete planar structure and few cracks, which makes it easy to form a three-phase interface in the catalytic process of metal particles deposited on its surface, thus facilitating the catalysis of metal catalysts. Therefore, when CNTs are used as the carrier material for oxygen reduction catalysis, if the metal catalyst deposited on the surface of CNTs can form an orderly catalytic layer, it is conducive to electron conduction and mass transfer, thus achieving a higher catalytic performance [1, 17]. However, due to the high curvature and chemical inertness of CNTs, its surface is not easily loaded with metal catalytic particles. Even if loaded,

the nanoparticles loaded on its surface have large size and poor dispersibility, thus greatly reducing the catalytic activity of the electrocatalyst [1]. In order to uniformly support metal catalyst nanoparticles on CNTs surface, there are usually two treatment methods, one is covalent method, i.e., chemical oxidation of CNTs surface with some strong acid or strong oxidant. This method will reduce the conductivity and stability of CNTs. Another non-covalent method is to modify its surface with some surfactants or polymers to form a large number of uniform surface groups on its surface, so that the metal catalyst nanoparticles can be loaded on it in a large number and uniformly. The advantage of this method is that the original physical and chemical properties of CNTs can be maintained, but the stability and electrochemical activity of the prepared catalyst are directly affected by the surfactant or polymer structure. Zhang et al. [18] modified positively charged poly (allylamine hydrochloride, PAH) on the surface of CNTs, then adsorbed negatively charged $PtCl_6^{2-}$ on the surface of CNTs through electrostatic action, and then $PtCl_6^{2-}$ was then reduced in situ with ethylene glycol, so that Pt nanoparticles were uniformly loaded on the surface of CNTs, thus obtaining Pt/PAH-CNTs catalyst, which showed high electrochemical activity area. More importantly, in 0.5 mol·L^{-1} H_2SO_4 solution, the catalytic activity of Pt/PAH-CNTs catalyst for oxygen reduction is 1.85 times that of Pt/COOH-CNTs (acid-treated CNTs), which is mainly due to the high Pt electrocatalytic activity area and good conductivity of Pt/PAH-CNTs catalyst. Pt nanoparticles were deposited on the surface of graphitized CNT by a similar non-covalent method, and the prepared electrocatalyst showed high oxygen reduction electrocatalytic activity and stability.

4.1.1.3 Mesoporous Carbon

Mesoporous carbon (MPC) is a kind of porous carbon material which pore diameter is mainly distributed in 2–50 nm. According to its internal structure and preparation method, it can be divided into two types [19]: one is ordered mesoporous carbon (OMC) and the other is disordered mesoporous carbon (DOMC). Although DOMC is rich in mesopores, the mesopores it contains are disordered and connected irregularly, so compared with OMC, DOMC has relatively poor conductivity and relatively wide pore size distribution. OMC, as a catalyst carrier material, is more conducive to improving the catalytic activity of the catalyst because of its large specific surface area, high conductivity, and easy mass transfer. MPC has been widely studied as a carrier material for oxygen reduction catalysts. Compared with traditional carbon materials, MPC has more advantages as a carrier material for oxygen reduction catalysts because of its single three-dimensional interconnected mesopores. In addition, Pt [20, 21] or Pt alloy [22, 23] supported by MPC all exhibit good electrocatalytic performance for oxygen reduction, which is mainly attributed to the good dispersibility of metal catalyst, the high conductivity of MPC, and its characteristic of special pore structure and easy mass transfer [24]. As is known to all, a high-performance oxygen reduction electrocatalyst needs an effective reaction region on a nanometer scale, such as a three-phase interface. In this region, when the electrochemical reaction is carried out, it is easy to transport materials (reactants and

products), protons and electrons. For traditional carbon carriers (such as Vulcan XC-72), they are rich in micropores and have deep chapping, which makes it difficult to form a three-phase interface. When Pt is deposited on its surface, the utilization rate of Pt decreases, which is due to the fact that reactants and proton-conducting polyelectrolytes (such as Nafion) are not easy to enter micropores. However, carbon carriers with pore sizes larger than 50 nm have low specific surface area and large internal resistance [23]. Therefore, the performance of carbon-supported catalyst is affected by the pore structure, pore size, and conductivity of MPC. Wang et al. [25] reported that N-doped NiFe/3D MPC was used for high-performance ORR/OER catalysts. Under the condition of 0.1 M KOH, the $\eta 10$ of OER was 340 mV and the half-wave potential of ORR was 0.862 V, which was due to the chemical interaction between the nanodots and the substrate, and the increase of catalytic sites exposed to electrolyte at nNiFe LDH nanodots.

4.1.1.4 Carbon Nanofiber

Carbon nanofibers (CNFs) are fibrous nanocarbon materials formed by crimping multi-layer graphite sheets, which have high strength, light weight, good thermal conductivity, and high electrical conductivity [26, 27]. According to its microstructural characteristics, it can be divided into fishbone, flat plate, ribbon, and tubular [28]. The diameter is generally 10 to 500 nm, and the length is distributed in the range of 0.5 to 100 m. It is a one-dimensional carbon material between carbon nanotubes and common carbon fibers. It has high crystallinity, good electrical and thermal conductivity. Carbon nanofibers have the characteristics of low density, high specific modulus, high specific strength, high electrical conductivity, and thermal stability of ordinary carbon fibers grown by chemical vapor deposition; it also has the advantages of small number of defects, large aspect ratio, large specific surface area, compact structure, etc. [29]. It is a high-performance fiber, which not only has the inherent characteristics of carbon materials, but also has the flexibility and processability of textile fibers, so it has a good application prospect in catalyst carrier materials [30, 31].

As a new type of carbon material, CNFs have good electrochemical catalytic activity. Compared with other catalyst carriers, CNFs have many advantages [32], mainly as follows:

(1) Carbon nanofibers have a large specific surface area, usually 50 ~ 300m^2 g^{-1}, which enables metal catalyst particles to be better positioned on the surface of carbon nanofibers, thus facilitating the loading and dispersion of metal catalyst. At the same time, carbon nanofibers contain almost no micropores, and their pore volume is mainly composed of mesopores formed by hollow parts of carbon nanofibers and macropores and mesopores formed by intertwining and stacking of carbon fibers. The mesoporous structure is favorable for reducing the resistance of reactants or products to migrate out of the surface of the catalyst, thereby alleviating the diffusion problem caused by catalytic reaction, and is

especially suitable for liquid phase reaction systems containing macromolecular substances to participate in the reaction.

(2) Carbon nanofibers have the characteristic of inactive surface chemistry, which enables them to exist stably under strong acidic and alkaline conditions. At the same time, carbon nanofibers have certain stability in air at normal temperature.

(3) Carbon nanofibers have unique electronic characteristics. CNFs graphite sheet has delocalized π electrons, which makes it to have good conductivity similar to graphite. However, because the graphite layer of CNFs is continuously curled in space, the electronic characteristics of CNFs are obviously different from that of complete graphite, and the distribution and density of electron clouds are also slightly different. The surface structure of CNFs synthesized by vapor deposition inevitably introduces defects and carbon nanofiber end atoms, which have higher energy and can further affect their electronic properties. Research shows that curling of CNTs graphite sheet can cause further hybridization between sp^2 orbit of carbon and d orbit of Ni and other catalysts, and its acting force is far greater than that between catalyst and graphite [33]. Therefore, when CNTs are used as catalyst carrier, They are more conducive to the positioning and loading of metal catalyst on its surface, to make the catalyst more evenly dispersed on the surface of CNTs, and to improve the activity of the catalyst.

(4) Carbon nanofibers have good mechanical stability. Almost every carbon atom in CNFs forms a stable covalent bond with the surrounding three carbon atoms. The structure is tight, both ends are closed, and there is no unbroken lone pair. This structure makes CNFs have good mechanical stability. At the same time, large π bonds formed between carbon atoms have higher binding energy, which greatly improves the stretching ability of CNFs. Some studies have shown that the surface structure of CNFs hardly changes after ultrasonic dispersion, while for activated carbon, many fragments can be obviously found.

(5) Carbon nanofibers have good thermal conductivity. The unique structure of CNFs makes its thermal conductivity have great difference between the direction perpendicular to the axis and the direction parallel to the axis. Its thermal conductivity along the axis direction is almost comparable to that of diamond. However, the thermal conductivity perpendicular to the axial direction is very poor and hardly has thermal conductivity.

(6) Adjustability of carbon nanofiber surface structure. The microstructure of CNFs obtained by different preparation methods is different. Therefore, by changing the preparation method and preparing different CNFs for appropriate systems, it is beneficial to improve their loading capacity or catalytic capacity.

4.1.1.5 Graphene

Simply put, graphene is a single-layer graphite sheet with only one carbon atom thick, and carbon and carbon atoms are closely arranged in a sp^2 heterozygous manner into a honeycomb six-membered ring structure (Fig. 4.1a). The distance between carbon and carbon atoms is about 0.142 nm. There are three σ bonds in each lattice of

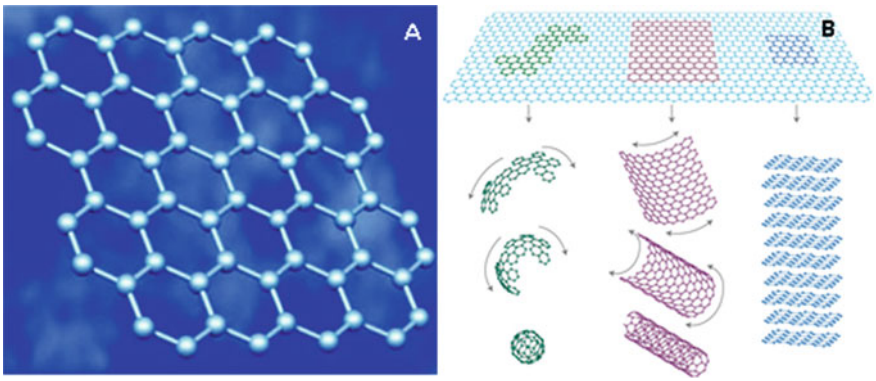

Fig. 4.1 Structural diagram of graphene (**a**) and its relationship with nano-carbon material family (**b**) [36]

graphene plane, which firmly connect carbon atoms and carbon atoms to form a very stable hexagonal structure, thus making the structure of graphene very stable. However, the joints between carbon atoms are very soft. When acted by external force, the carbon atoms will not break, only need to bend in plane to adapt to external force, thus greatly improving the stability of its own structure. In addition, the p orbitals of each carbon atom in the graphene plane have an unbound electron, and a large π delocalization bond perpendicular to the upper surface of the carbon atom crystal plane can be formed between them. The bond can move freely on the graphene crystal plane, thus making graphene have super-strong conductivity [34, 35]. Graphene is the thinnest two-dimensional material in the world, its thickness is only 0.34 nm. Graphene is also the basic structural component unit of all nanocarbon materials [36] (see Fig. 4.1b). If graphene is wrapped up, it is zero-dimensional fullerene; if it is rolled up, it is one-dimensional carbon nanotubes; if it is stacked up, it is three-dimensional graphene.

Graphene has many excellent properties [37–39], such as optical, thermal, mechanical and electrical physical and chemical properties. Graphene is by far the thinnest and hardest material in the world and also the material with the lowest resistivity (only 10^{-6} Ω·cm). At the same time, it also has the characteristics of super large specific surface area (its theoretical value can reach 2630 $m^2\ g^{-1}$) [40], good thermal stability, stable chemical properties, and good flexibility [41]. Therefore, in the fields of nano devices [42], field emission [43, 44], energy storage and conversion [45–48], chemical and biological sensors [49, 50], nano composite materials [51, 52], and biological nanotechnology [53, 54], it has a wide range of potential application values [55].

With the wide application of graphene nanomaterials, the macro-scale preparation of graphene is becoming more and more important [56–58]. At present, graphene can be prepared by two methods: "Top-down" and "Bottom-up" methods [55]. The "Top-down" method for preparing graphene refers to the method of peeling off the graphite layer (Fig. 4.2). It mainly includes mechanical stripping, chemical stripping, solvent

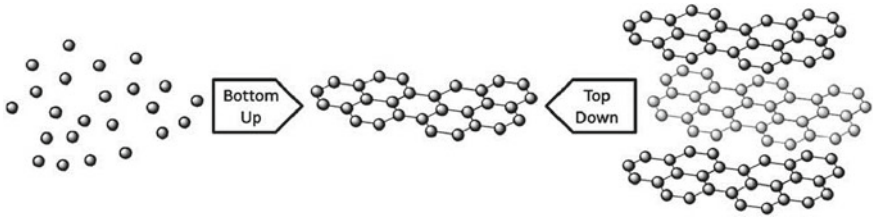

Fig. 4.2 schematic diagram of "top-down" and "Bottom-up" synthetic graphene [55]

stripping, carbon nanotube cutting, etc. The "Top-down" preparation method has simple equipment and can be prepared in large quantities. However, when graphene is synthesized by this method, special physical or chemical processes are required to destroy van der Waals forces between graphite layers to form graphene sheets, and the structure of graphene will be more or less destroyed during the processing process, so that some characteristics of graphene will be changed, thus the quality of prepared graphene is not high. In addition, due to the high activity of the stripped graphene, they will reunite through the action of π-π bonds, resulting in low yield of high-quality graphene. However, the "Bottom-up" method for preparing graphene refers to the method of recombining carbon source small molecules (Fig. 4.2). It mainly includes epitaxial growth method, chemical vapor deposition method, and other preparation methods. The method can prepare high-quality graphene, but the operation is complicated, and special treatment needs to be carried out under high-temperature conditions. Therefore, high-end large-scale instruments and equipment are needed, so that the synthesis cost is high, and actual large-scale production is difficult. To sum up, although the above two preparation methods have their own characteristics, there are more or less some problems when applied to actual large-scale production. Therefore, the large-scale preparation of graphene is still the bottleneck restricting its wide application.

Recent studies have shown that graphene sheets can be used as catalyst materials for low-temperature fuel cells [59]. Highly dispersed noble metal catalysts, mainly platinum and platinum-based catalysts, with carbon black as the main conductive medium as the carrier, can be used as electrode materials for catalytic oxidation–reduction reactions and applied to various fuel cells. Graphene, which combines many excellent properties such as high specific surface area (theoretical value 2630 $m^2\ g^{-1}$), high conductivity, unique planar structure of graphite substrate and potential low manufacturing cost, has become the most promising candidate carrier material for low-temperature fuel cells. Compared with CNTs, graphene not only has similar stable physical properties, but also has higher specific surface area. In addition, the large-scale production cost of graphene is much lower than that of carbon nanotubes. Therefore, the synthesis of fuel cell catalysts supported by graphene has attracted extensive attention [60, 61].

Graphene-supported platinum catalysts (Pt-Graphene nanosheets, Pt-GNs) have first attracted the attention of researchers [60, 62–64]. The preparation methods of

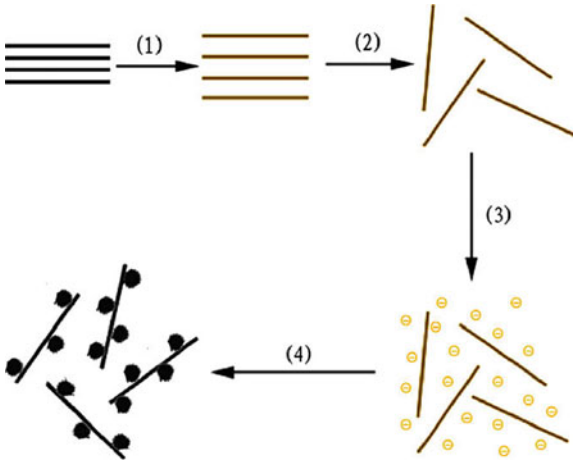

Fig. 4.3 Synthesis diagram of Pt-GNS catalyst [65]

Pt-GNs catalysts are usually Graphene Oxide (GO) and noble metal precursors. The presence of noble metal nano-ions can not only catalyze the reduction of graphene oxide, but also prevent the aggregation of reduced graphite dilute (rGO). Generally speaking, this kind of catalyst can be obtained by depositing metal precursors on the surface of graphene oxide first and then reducing them together at the same time. Figure 4.3 shows the preparation process of Pt-GNs catalyst. Firstly, the mixture of GO and H_2PtCl_6 is reduced with $NaBH_4$, and the final sample is obtained after freeze drying [65].

Subsequently, researchers found that graphene doped with heteroatoms (N, P, S, B) has oxygen reduction catalytic capability [66, 67]. Nitrogen, boron, and other heteroatoms can be introduced through subsequent treatment of graphene, which is called doping [68]. The most typical method of doping treatment is to heat the graphene and corresponding heteroatom precursor components in inert gas at high temperature. This method can prepare heteroatom-doped graphene on a large scale. Through doping treatment, the electronic structure of graphene has changed, which greatly increases its application range, especially as an oxygen reduction catalyst.

Nitrogen-doped graphene (N-Graphene) is currently the most widely studied non-noble metal catalyst [69]. The physical and chemical properties of N-Graphene and undoped pure graphene are very different. Since the doped nitrogen atoms will affect the spin density and electron cloud distribution of adjacent carbon atoms, inducing them to generate "active centers," these active regions can directly participate in the catalytic oxygen reduction reaction [70]. Liming Dai et al. [71] prepared N-Graphene by vapor deposition, which showed good catalytic activity for oxygen reduction (Fig. 4.4). Graphene doped with single elements of boron, phosphorus, sulfur, and iodine, and graphene doped with binary elements of sulfur, nitrogen, sulfur and phosphorus, boron and nitrogen all show good catalytic activity for oxygen reduction.

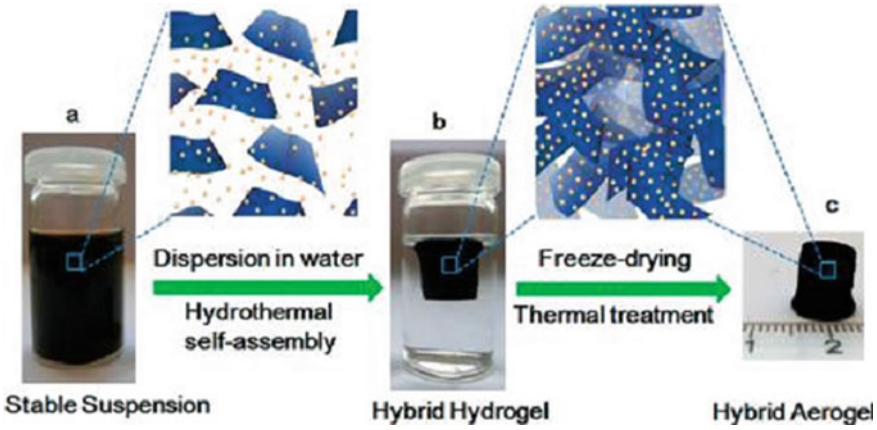

Fig. 4.4 Schematic diagram of preparation process of Fe_3O_4/n-Gas [83]

Graphene is a newly discovered nano material with many functions. It has a bright application prospect. The application research of graphene in electrocatalysts still needs continuous exploration.

4.1.1.6 Graphene with Stereoscopic Structure

Graphene has attracted much attention due to its unique physical and chemical properties, [37–39] especially the research on graphene-based devices [72, 73]. At present, most researches mainly focus on the preparation and properties of two-dimensional graphene materials. However, the size for two-dimensional materials is very small, which greatly limits their processing and application. In addition, due to the strong van der Waals force or dangling bond force between the two-dimensional graphene, the prepared graphene is easy to agglomerate or stack, thus restricting the large-scale production and actual use of graphene [74–77]. Three-dimensional graphene is a structure which can effectively prevent agglomeration or stacking between two-dimensional graphene [78, 79]. It not only maintains the intrinsic characteristics of graphene, but also has unique self-supporting structure and porosity [80, 81]. In addition, it can also provide large specific surface area, high mechanical strength and fast electron and ion transport. Therefore, three-dimensional graphene is considered as an important direction for the development of graphene materials in the future [80–82]. At present, there are mainly two methods for synthesizing three-dimensional graphene [80]: one is a self-assembly method, which is a process of reassembling precursors derived from graphene oxide or reducing graphene through hydrothermal, vacuum filtration, templates and other technologies, including solution self-assembly, template self-assembly, solvothermal self-assembly, and organic aerogel self-assembly. The other is a metal-catalyzed synthesis method, which is mainly a process of removing a template or a catalyst by directly catalyzing a

carbon source on a porous metal or nanoparticle surface by chemical vapor deposition (CVD) or heat treatment to form a three-dimensional structured graphene. It is mainly synthesized by stereo porous metal catalysis or metal nanoparticle catalysis.

Recent studies have shown that three-dimensional graphene is also an excellent catalyst material for oxygen reduction. Compared with two-dimensional graphene, three-dimensional graphene not only maintains the intrinsic characteristics of graphene, but also has unique self-supporting structure and porosity, which can provide good three-dimensional electron transmission path and rapid mass transfer. In addition, the three-dimensional graphene can also provide large specific surface area, high mechanical strength, uniform dispersion of a large number of catalyst nanoparticles, and high electrochemical stability [83, 84].

Three-dimensional graphene as a catalyst carrier for platinum loading has first attracted attention [84]. Wang et al. [84] prepared Pt/3D graphene catalyst by depositing platinum catalyst on the surface of three-dimensional graphene synthesized by CVD method. Compared with the carbon fiber carrier, the platinum catalyst supported by the carrier has higher catalytic performance and service life. In addition, non-noble metals supported by graphene with three-dimensional structure have also attracted attention. Wu et al. [1] prepared a Fe_3O_4/N-GAs non-noble metal catalyst by uniformly depositing Fe_3O_4 on the surface of nitrogen-doped cubic graphene gel (N-GAS). The preparation process is shown in Fig. 4.4. Firstly, GO solution, iron acetate, and polypyrrole are ultrasonically dispersed to form a uniform and stable suspension, and then the suspension is put into a hydrothermal reaction autoclave and heated for 12 h at 180 °C to obtain a three-dimensional gel-like compound, and then the solid gel-like compound is freeze-dried, and heat-treated for 3 h at 600 °C under nitrogen to finally obtain the sample. The preparation process promotes Fe_3O_4 nanoparticles to be deposited on the surface of graphene and is accompanied by a nitrogen-doping process. Compared with the catalyst in which nanoparticles are deposited on nitrogen-doped two-dimensional graphene and carbon black, the Fe_3O_4/N-GAs catalyst has a more positive peaking potential and a higher current density for oxygen reduction tests under alkaline conditions. This further proves that the three-dimensional graphene can improve the electrocatalytic performance of the oxygen reduction catalyst. In addition, the three-dimensional graphene is not only used as a catalyst carrier to support platinum and non-noble metal catalysts, but also used as a non-metal catalyst itself. For example, doped graphene with N, P, S, B mono-, binary, or multi-component structure, which is used as an oxygen reduction catalyst, exhibits catalytic activity close to or even better than commercial Pt/C under acidic or alkaline conditions, while its stability and lifetime are far better than commercial Pt/C [85–89].

Professor Shen Peikang's research group of Guangxi University proposed a new polymer pyrolysis method to prepare self-doped three-dimensional porous graphene (3D HPG) with adjustable porosity and specific surface area [45]. The preparation process is shown in Fig. 4.5. Firstly, the pretreated polymer is exchanged with metal ions (such as Ni^{2+}), then the dried polymer exchanged with metal ions is added into KOH/ethanol solution, evenly stirred, heated, and evaporated to dryness until a pasty mixed solution is formed, then the pasty mixed solution is dried and pulverized at

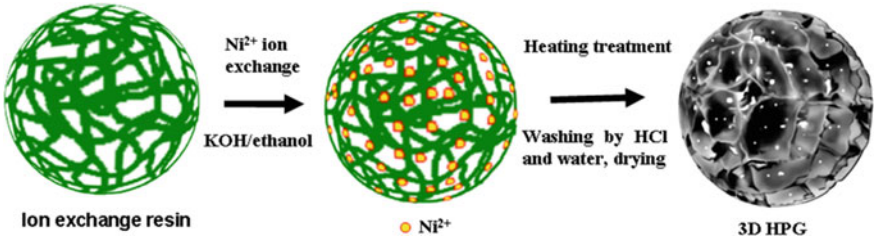

Fig. 4.5 Synthesis diagram of 3D porous graphene (3D HPG) [45]

70 °C, finally, the pulverized product is placed in a tube furnace, subjected to high-temperature heat treatment under nitrogen atmosphere, and the heat-treated product is repeatedly treated with hydrochloric acid and deionized water and dried to obtain the sample. The method is simple to prepare and easy to scale up. The prepared 3D HPG material can not only be used as a catalyst carrier to support noble metal catalysts and non-noble metal catalysts [90], but also can be used as a non-metal catalyst [91]. The oxygen reduction catalyst prepared by the method exhibits catalytic activity close to or even better than commercial Pt/C under acidic or alkaline conditions, and its stability and service life are far better than commercial Pt/C. For example, 3D HPG with appropriate specific surface area prepared by the method is used as a carrier to support a binary platinum silver metal catalyst to prepare an oxygen reduction catalyst with low platinum.

Figure 4.6 shows the morphology of 3D HPG supported binary platinum silver metal catalyst (PtAg/3D HPG). PtAg bimetallic nanoparticles are uniformly distributed in 3D HPG, and the morphology of 3D HPG is not changed, thus facilitating electron transfer and oxygen transport in the electrocatalytic process of oxygen

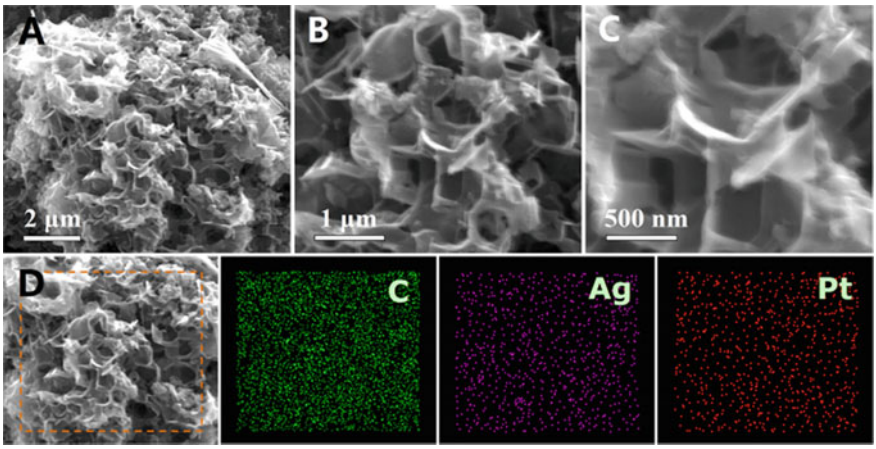

Fig. 4.6 SEM micrographs (**a**–**c**) and **d** SEM–EDS elemental surface scanning images of PtAg/3D HPG catalyst at different rates. Green: carbon; Purple: silver; Red: platinum

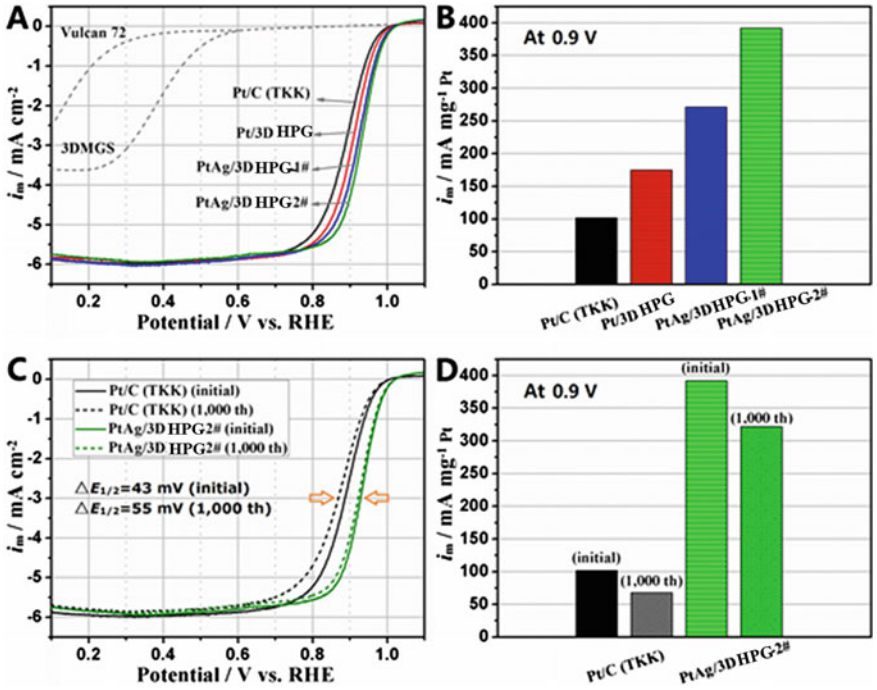

Fig. 4.7 Oxygen reduction curves (**a**) and mass activity at 0.9 V (**b**) of each catalyst sample (Pt/c (TKK), Pt/3D HPG, AgPt/3D HPG-1# and AgPt/3D HPG-2#). Performance comparison after 1000 CV cycles: oxygen reduction curve (**c**) and mass activity at 0.9 V (**d**). ORR condition: the electrolyte is 0.1 mol·L^{-1} $HClO_4$ solution saturated with oxygen; Speed is 1600 rpm; Scanning rate is 5 mv s^{-1}; The temperature is 30 °C. CV condition: the electrolyte is 0.1 mol·L^{-1} $HClO_4$ solution saturated with nitrogen; the scanning rate is 50 mv s^{-1}; the temperature is 30 °C

reduction. The experimental results confirm that the catalyst exhibits significantly better electrocatalytic performance than commercial Pt/C in acidic medium, i.e., the mass activity of platinum in the catalyst is 3.5 times that of commercial Pt/C at 0.9 V, and the stability is also far better than commercial Pt/C (see Fig. 4.7).

4.1.2 Non-Carbon Carrier Materials

Although carbon material has its unique advantages as the support of oxygen reduction electrocatalyst, due to the long-term operation of PEM fuel cell, carbon support will inevitably be oxidized to generate CO_2, resulting in metal electrocatalyst peeling off from carbon support material and agglomeration, resulting in a sharp decline in the performance of fuel cell [92]. Therefore, many non-carbon support materials, such as oxides, carbides, or nitrides of conductors or semiconductors, have been widely studied as support materials for oxygen reduction electrocatalysts [93–96].

The use of these materials not only reduces the amount of noble metal electrocatalyst, but also improves the activity and stability of the catalyst.

4.1.2.1 Oxide

Metal oxides as electrocatalyst support materials can greatly improve the catalytic activity and stability of electrocatalysts [97–100]. Popov et al. [101] used an electrode prepared with Pt/TiO_2 as an electrocatalyst, and obtained a performance matching that of commercial Pt/C. This is mainly due to the good mass transfer effect of Pt/TiO_2 electrocatalysts at high current densities. The Pt/TiO_2 electrocatalyst also exhibits a high stability, which is mainly due to the strong metal interface force formed between the Pt nanoparticles and TiO_2 in the Pt/TiO_2 electrocatalyst. Adzic et al. [102] first prepared niobium oxide by aerogel method, and then deposited monodispersed Pt nanoparticles on the carbon-supported niobium oxide surface to form $Pt/NbO_2/C$ composites. The composite exhibits oxygen reduction performance, and its mass specific activity is three times that of Pt/C. This is mainly due to the reduced OH adsorption, which is caused by the side repulsion between PtOH and the surface sites of the oxide. Sun et al. [103] deposited Pt nanoparticles on the surface of carbon paper directly grown SnO_2 nanowires by electrochemical deposition. The performance of the oxygen reduction electrocatalyst prepared by this method is higher than that of standard Pt/C catalysts. Kulesza et al. [104] reported that carbon-supported RuSex nanoparticles were coated with a layer of WO_3 film, and then the oxygen reduction electrocatalytic performance was enhanced under acidic conditions. The coated WO_3 thin film is favorable for the decomposition of the intermediate H_2O_2, so that the entire reduction process is mainly performed by a four-electron process.

4.1.2.2 Carbide

Since the discovery of transition metal carbides with platinum-like electrocatalytic properties in the 1870s [105], carbides have received widespread attention [106–109]. This is due to the fact that transition metal carbides, especially tungsten carbides, have similar Fermi levels and electron cloud densities to platinum. Therefore, the carbide itself has certain oxygen reduction electrocatalytic performance, and as a catalyst support material, it can also improve catalytic activity through synergy [106–109]. In addition, carbides also have a variety of chemical properties, so they are more interesting to researchers as electrocatalysts. Tungsten carbide is one of the most studied materials in carbide, because it still has high stability, good conductivity, and high activity under acidic conditions. Therefore, tungsten carbide is also widely used as an electrocatalytic support material to synergistically enhance the oxygen reduction performance of the catalyst [106–110]. For example, Shen et al. [109] directly deposited platinum nanoparticles on the surface of carbon-supported tungsten carbide to form a Pt-WC/C catalyst, and its oxygen reduction electrocatalytic performance was far better than that obtained by direct physical mixing of WC and

Pt/C performance. Its superior performance is mainly due to the fact that Pt is evenly distributed on the tungsten carbide surface of the carbon support, which results in the formation of more electrochemically active areas. In addition, tungsten carbide has a synergistic effect not only with platinum, but also with other metal catalysts (such as Au, Pd, etc.). For example, Shen et al. [108] prepared AuPd-WC/C catalysts by depositing AuPd alloys onto WC by alternating microwave method. This electrocatalyst exhibits much better electrocatalytic performance for oxygen reduction than commercial Pt/C catalysts. In addition, tungsten carbide also shows good long-term stable performance [111, 112]. Tungsten carbides mainly exist in two forms of WC and W_2C, while W_2C is thermodynamically unstable at room temperature, but WC thermodynamics is very stable [113]. In order to confirm that WC also has good stability under electrocatalytic conditions, Zellner et al. [114] tested the prepared WC film in 0.5 mol·L^{-1} H_2SO_4 medium. The results confirm that the WC film exhibits a stable electrochemical performance at a potential below 0.6 V. There is an unstable region for W_2C, which is mainly caused by the oxidation of W_2C in the air during the electrocatalytic process to produce the intermediate product W_xO_y [2]. Chhina et al. [115] used a multi-potential step method (constant 20 s at 1.8 V and 60 s at 0.6 V for one cycle) to perform accelerated aging tests on Pt/WC and WC. After 30 cycles, Stability is only reduced by 20 and 10%, respectively; however, commercial Pt/C decays completely after only 10 turns. For the WC stability test, a small amount of WO_x will be generated, which is a short-bandwidth semiconductor material and has a certain electron conductivity. Therefore, when the WC is oxidized, the structure of the carrier is partially changed, and the Pt load on the WC surface becomes Pt load on the WO_x-coated WC surface [115]. This mechanism is not like a carbon support, which will be oxidized to CO or CO_2, which will cause Pt to fall off and agglomerate from the surface of the support, which will greatly reduce the effective utilization area of Pt, which will cause the oxygen reduction performance of the catalyst to decrease sharply [111]. Although carbides have so many advantages, for carbides, as catalyst supports, further improvements are needed [115]. For example, the specific surface area of WC is very low, so it is necessary to further increase the effective utilization area of Pt by reducing the size of Pt nanoparticles (e.g., the size of Pt nanoparticles is optimized from 30 to 3 nm) to achieve higher mass activity [115].

4.1.2.3 Nitride

Nitrides, especially transition metal nitrides, have been widely used in coatings, such as cutting tools and refractory materials, due to their unique physical and chemical properties, such as strong hardness and good wear resistance. Because transition metal nitrides have an electronic structure similar to that of precious metals [116], they are considered as alternatives in various heterogeneous catalysis such as isomerization reactions [117], hydrodesulfurization reactions, hydrogenation reactions, etc. Best candidate for platinum catalyst [116]. Recently, as nitrides are considered to have better electrical conductivity, thermal and electrochemical stability, corrosion resistance, and good synergistic effects, they have also been widely used as oxygen

reduction electrocatalyst carriers [118, 119]. At present, CrN [120], TiN [[121], $Ti_xNb_{1-x}N$ [122, 123], VN [124], etc. as catalyst support materials loaded with Pt or Pd have excellent catalytic performance and stability. For traditional carbon-supported catalysts. Kumar et al. [125] reported that Nafion-modified Pt nanoparticles were immobilized on the surface of TiN to form a Pt-TiN catalyst. The catalyst was tested for oxygen reduction in a 0.5 mol·L^{-1} H_3PO_4 solution, showing a ratio of commercial Pt/C catalyst. Better electrochemical stability, durability, and higher electrocatalytic performance. Pan et al. [126] reported that the Pt/TiN NTs catalyst prepared by depositing Pt nanoparticles on the surface of TiN nanotubes (TiN NTs) has far better catalytic activity and stability than commercial Pt/C catalysts. Yang et al. [120] reported that Pt nanoparticles were supported on the surface of mesoporous CrN prepared by the solid–solid separation method, and the oxygen reduction and charging catalytic performance of the prepared catalyst was far superior to that of commercial Pt/C catalyst. Although the above-mentioned nitrides have such advantages as catalyst support materials, the nitrides face high synthesis temperatures (mostly more than 1500 °C, even more than 2000 °C), small specific surface area, large particle diameter, and dense active sites which causes problems such as low current density, so in the future development, further research is needed by reducing the synthesis temperature, increasing the specific surface area, and reducing the size of the nanoparticles [118, 127, 128].

4.2 Novel Platinum-Based Catalyst

Membrane electrode assembly (MEA) is the core component of proton exchange membrane fuel cells (PEMFCs), while cathode and anode catalysts in MEA are key to determining MEA performance. From a catalytic point of view, Pt-based catalysts are currently the best performing catalysts and used as catalysts for commercial PEMFCs. Due to the high price of Pt and the scarcity of the earth's reserves, the commercial process of PEMFCs is greatly restricted. In particular, the cathode in MEA has a slower kinetics of oxygen reduction reaction (ORR), resulting in more requirement on catalyst performance. High requirements push up costs. At present, the cost of catalysts accounts for 40–60% of the entire PEMFCs stack. Therefore, the development of high-performance, low-cost ORR electrocatalysts has important significance in the development of advanced, efficient, and low-cost PEMFCs, has a crucial role to the large-scale commercialization of fuel cells. Current strategies to reduce the cost of ORR catalysts include (1) reducing the use of Pt by optimizing the utilization of Pt catalysts, (2) reducing the amount of Pt used by increasing the intrinsic properties of Pt catalysts, and (3) developing inexpensive alternative catalyst to Pt. The third strategy can theoretically solve the problem that the catalyst is subject to Pt, but as far as the current research is concerned, these non-Pt catalysts have a big gap on catalytic performance and practical application requirements. Therefore, there is still a long distance on the commercialization of their applications.

In order to achieve a reduction in the amount of Pt, there are currently several ways to (1) increase the utilization of catalyst and the number of active sites. The method generally improves the utilization of the catalyst by reducing the particle size of the Pt catalysts and increasing the Pt dispersion, thereby greatly increasing the ratio of surface atoms to bulk atoms [129–131]; (2) increasing the intrinsic activity of the catalyst, which is usually alloyed by introducing the second element or more elements (PtM/N (M/N = Pd, Fe, Co, Ni, Cu, Cr, Y, etc.) to form alloys [132–137]; (3) synergistic effect, introduce a second substance or load Pt on other carriers that can synergize with Pt, such as loading Pt on some nano-carbides, transition metal oxides, graphenes, etc.; there is a certain electronic effect between Pt and its carrier, which produces a synergistic effect, thereby increasing the ORR activity of Pt [138–140]; (4) constructing special nanostructures, due to nano-scale effects, special nano-structures will change in their electronic structure and properties, which will be beneficial to the improvement of ORR catalytic activity, such as nanowires, nanotubes, nanoframes, nanocages, nanodenrites, and polyhedrons with high crystal face index [141–143]. In the actual synthesis of high-performance Pt-based ORR catalysts, one or more of the above-mentioned pathways are usually included. For example, the prepared PtFe nanowires belong to both the alloying of pathway 2 and the special nanostructure of pathway 4.

4.2.1 Pt Atom Cluster

For spherical particles, the smaller the particle size, the larger the specific surface area and the more atoms are exposed to the outside. For example, the size of Pt particles is reduced from 15 nm to about 3 nm, and the electrochemical active area (ECSA) is increased from 5 to 80 $m^2\ g^{-1}{}_{Pt}$, and the ratio of the number of surface atoms to the total number of atoms is increased from 3 to 13%. This greatly increases the effective utilization of precious metal Pt, which is called the size effect of Pt nanoparticles.

JOO et al. [144] prepared Pt nanoparticles with sizes of 2.7 to 6.7 nm and loading of 60wt% on ordered mesoporous carbon (OMC) by continuous impregnation reduction. The size of the particles was reduced by temperature and frequency to control. Their experimental results show that the ORR performance of 3.3 nm Pt is best in 0.1 M $HClO_4$ medium, as shown in Fig. 4.8. This is consistent with the results reported in some other literatures [145, 146]. The case where the ORR activity of Pt with size of below 3 nm decreases as the Pt particle becomes smaller is called a “negative particle size effect”. This effect can be attributed to the following three possible reasons: (1) The orientation of the crystal plane orientation of the surface of Pt nanoparticles below 3 nm varies with the decrease of the particle size, while the ORR activity of each crystal plane of Pt is different: Pt (100) < Pt(111) < Pt(110) [147, 148]; (2) The crystallinity of Pt particles decreases with the decrease of crystal grains, and the coordination of Pt atoms in the surface layer changes greatly; (3) Inhibition of anions adsorbed on different crystal plane orientations and the crystal plane orientation of the surface of the Pt nanoparticle vary with the particle size.

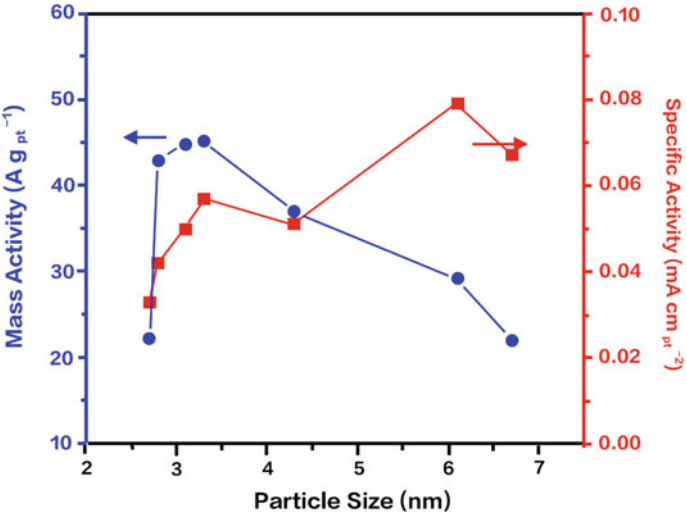

Fig. 4.8 Curve of ORR mass and area activity of Pt/OMC catalyst versus Pt nanoparticle size. Reprinted with permission. [144] Copyright (2012) American Chemical Society

However, the above studies on the effect of Pt particle size are basically studied in the range of 2–10 nm, and the actual research on the size effect of Pt nanoparticles below 2 nm (especially below 1 nm) (which can be called Pt clusters) is rare, because it is difficult to prepare Pt nanoparticles below 2 nm by using the methods to prepare 2–10 nm Pt nanoparticles. It is difficult to systematically study them under different preparation methods. In addition, the structure of the Pt clusters undergoes significant changes as the particles decrease, and the effect of this change on the ORR performance of Pt can no longer be explained by the previous size effect.

Imaoka et al. [149] prepared Pt_{12} and Pt_{13} nanoclusters by using four-generation dendritic phenylazomethine with a tetraphenylmethane core (DPA-TPM) and fourth-generation dendritic phenylazomethine with a triphenylpyridylmethane core (DPA-PyTPP) as templates, as shown in Fig. 4.9. They found that when Pt_{13} removes a Pt atom and turns it into Pt_{12}, its ORR mass activity change to more than two times. They used the extended X-ray absorption fine structure and electrospray ionization time-of-flight mass (ESI-TOF-mass) to analyze the structure of Pt_{12} and Pt_{13} clusters. Pt_{13} clusters have a well-defined dodecahedral atomic coordination, while the Pt_{12} clusters have coordination distortions, as evidenced by density functional theory.

Nesselberger et al. [150] prepared three Pt clusters under vacuum conditions by precise regulation: Pt_{20} ($Ø = 0.6$ nm), Pt_{46} ($Ø = 0.8$ nm), and $Pt_{>46}$ ($Ø = 2.3$ nm). They compared these three Pt clusters with Pt/C with a size of 3 nm and 5 nm. They found that the mass activity at 0.85 V (vs. RHE) of the five catalysts is Pt/C(5 nm) < Pt/C(3 nm) < Pt_{46} < Pt_{20} < $Pt_{>46}$. Among them, $Pt_{>46}$ is the highest, reaching nearly 8 A $mg^{-1}{}_{Pt}$, which is nearly 10 times higher than that of 5 nm Pt/C, and nearly 7 times higher than 3 nm Pt/C, as shown in Fig. 4.10.

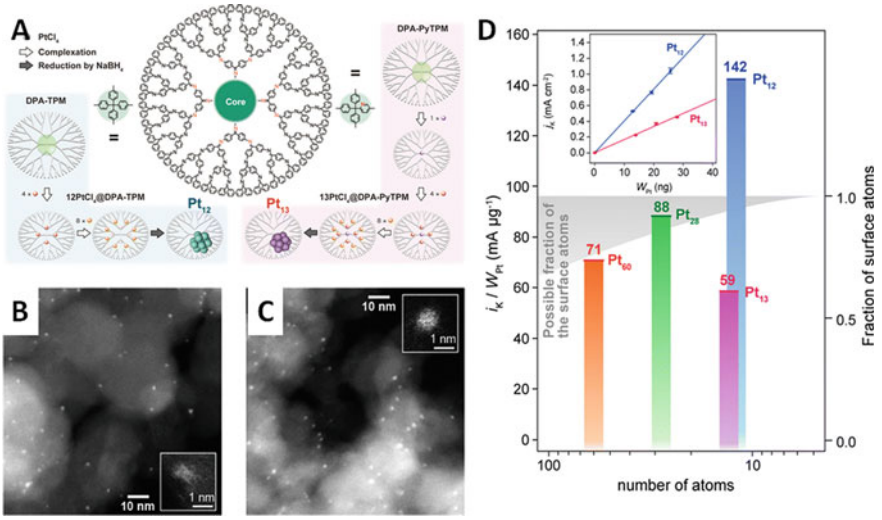

Fig. 4.9 **a** Schematic diagram of the selective preparation of Pt12 and Pt13 clusters using DPA-TPM and DPA-PyTPM as templates, **b** HAADF-STEM images of Pt12 and **c** Pt13 clusters supported on mesoporous carbon, The loading is 1 wt % Pt, the inset is a magnified image of the cluster, **d** the ORR mass specific activity of the Pt12 and Pt13 clusters, the inset is the kinetic current density of the Pt12 and Pt13 clusters at different loadings calculated according to Koutecky–Levich [149]. Reprinted with permission. [149] Copyright (2011) American Chemical Society

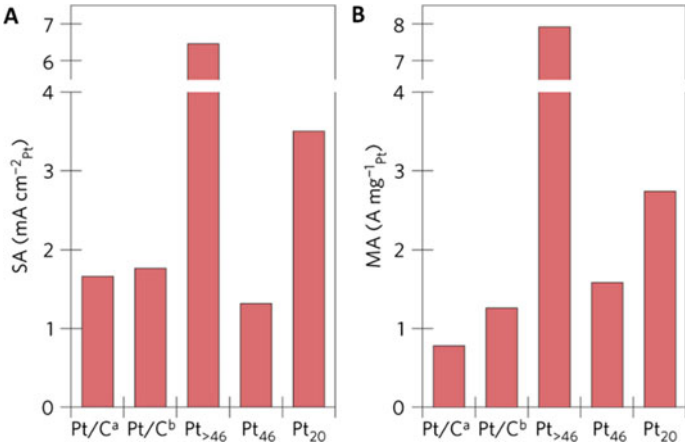

Fig. 4.10 **a** Specific activity and **b** mass activity of Pt/C (5 nm), Pt/C (3 nm), $Pt_{>46}$ (2.3 nm), Pt_{46} (0.8 nm) and Pt_{20} (0.6 nm). [150] Reprinted with permission. [150] Copyright (2002) Springer

4.2.2 Pt-Based Alloy ORR Catalysts

By reducing the Pt particle size to achieve an improvement in the ORR performance of Pt, which subjects to the "negative size effect," it does not meet the PEMFC's requirement for a significant reduction in the amount of Pt. Furthermore, the smaller the Pt particles (less than 2 nm), the more difficult it is to prepare by a simple method. Another way to effectively increase the ORR activity of Pt is to change the structure and electronic properties of Pt by alloying, thereby achieving the purpose of enhancing ORR activity.

At a voltage of 0.8–0.9 V, which is also the voltage during normal operation of PEMFC, oxygen is adsorbed on the surface layer of the catalyst, followed by the cleavage of the O–O bond and the generation of hydroxyl groups adsorbed on the surface. The hydroxyl groups adsorbed on the surface then react with a proton to produce water. This is the basic reaction process of ORR on the surface of Pt, and also the basis for the design of Pt-based alloy on ORR [151]. Based on this, researchers have studied a series of bimetallic Pt-based alloy catalysts for different metals (such as Ni, Co, Fe, Ti, Y, Au, Pd, Rh, Ir, Ru, etc.) [132, 152–156]. The research results show that the ORR activity of these bimetallic Pt-based ORR catalysts is directly related to the electronic structure on their surface, especially the d-band center of the surface Pt atom is related to the oxygen binding energy (BE_O) [157]. Figure 4.11

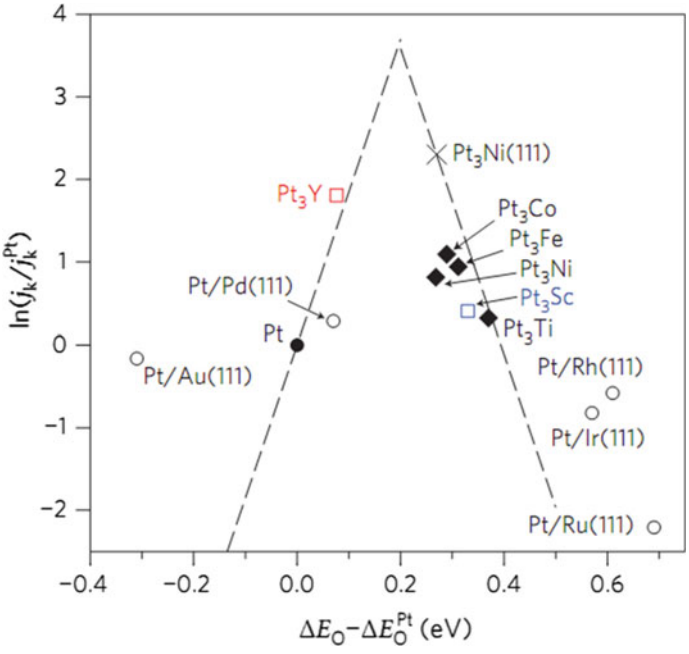

Fig. 4.11 Relationship between ORR activity and oxygen adsorption energy of bimetallic Pt-based ORR catalysts [132]. Reprinted with permission. [132] Copyright (2009) Springer

shows the relationship between the ORR activity and oxygen adsorption energy of bimetallic Pt-based ORR catalysts reported in the literature, similar to the volcano diagram [132].

Lim et al. [153] first prepared truncated octahedral Pd nanoparticles with a size of 9 nm by using ascorbic acid, and then prepared nano-dendritic Pd–Pt bimetallic alloys (Pd–Pt dendrites) with a size of 23 nm by using truncated octahedral Pd nanoparticles as seeds. At room temperature, the mass activity of Pd–Pt dendrites in 0.1 M $HClO_4$ medium at 0.9 V (vs. RHE) is 204 mA $mg^{-1}{}_{Pd+Pt}$, which is 2.1 times, and 4.3 times of commercial Pt/C (95 mA $mg^{-1}{}_{Pt}$) and carrier-free Pt black (48 mA $mg^{-1}{}_{Pt}$). If only the mass specific activity of Pt is counted, the mass activity of such dendritic Pd–Pt dendrites can reach 241 mA $mg^{-1}{}_{Pt}$, which is 2.5 times that of commercial Pt/C. At a temperature of 60 °C, the mass specific activity of Pd–Pt dendrites can reach 433 mA $mg^{-1}{}_{Pt}$, which is still better than commercial Pt/C (204 mA $mg^{-1}{}_{Pt}$) and carrier-free Pt black (78 mA $mg^{-1}{}_{Pt}$), which is very close to the goal set by the US Department of Energy (at 80 °C, the specific mass activity at 0.9 V (vs. RHE) reaches 440 mA $mg^{-1}{}_{Pt}$).

It can be predicted from Fig. 4.12 that the surface of $Pt_3Ni(111)$ has the best ORR activity. Stamenkovic et al. [159] synthesized $Pt_3Ni(hkl)$ alloy surface under ultra-high vacuum (UHV) experimental conditions, and compared it with Pt(hkl). They found that compared with the Pt(111) surface, the H_{upd} formation potential of the $Pt_3Ni(111)$ surface was significantly negatively shifted by approximately 0.15 V, and the OH_{ad} formation potential was positively shifted by approximately 0.1 V. This is consistent with its corresponding adsorption on-set potential. In addition, compared

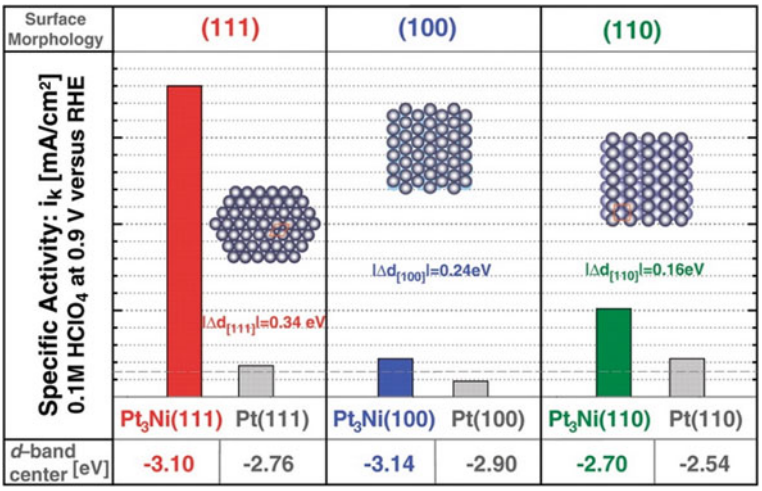

Fig. 4.12 Comparison of kinetic current densities and d-band center of different $Pt_3Ni(hkl)$ and Pt(hkl) surfaces at 0.9 V (vs. RHE) at 333 K in 0.1 M $HClO_4$ and different $Pt_3Ni(hkl)$ and Pt(hkl) [159]. Reprinted with permission. [159] Copyright (2007) American Association for the Advancement of Science

with the Pt(111) surface, the local coverage of H_{upd} and OH_{ad} (Θ_{Hupd} and Θ_{OHad}) on the $Pt_3Ni(111)$ surface has decreased by 50%, which is also reflected in the decrease in the d-band center on the Pt surface (The d-band center on the $Pt_3Ni(111)$ surface is 0.34 eV lower than the Pt(111) surface). A similar situation also occurred on the surfaces of other two crystal planes. The Θ_{Hupd} on the surface of $Pt_3Ni(100)$ was more than 25% lower than that of Pt(100), and the d-band center decreased by 0.24 eV. The Θ_{Hupd} on the surface of $Pt_3Ni(110)$ was more than 20% lower than Pt (110), and the d-band center decreased by 0.16 eV. Figure 4.12 shows a comparison of the ORR activities of different single crystal planes of Pt_3Ni and Pt. For Pt_3Ni, the order of activity is $Pt_3Ni(100) < Pt_3Ni(110) < < < Pt_3Ni(111)$, where the activity of the Pt3Ni (111) plane is orders of magnitude higher than the other two single crystal planes. For Pt, the order of ORR activity of different crystal planes is $Pt(100) \ll Pt(111) < Pt(110)$. The ORR activity on the surface of $Pt_3Ni(111)$ is 10 times higher than that of Pt (111) and 90 times higher than that of commercial Pt/C surface. This is related to its different electronic structure (d-band center) and an increase in active sites for oxygen adsorption.

Although the theoretical and experimental research on Pt bimetallic alloy catalysts has been very rich and in-depth, it is still difficult to predict which specific bimetallic catalyst has the best ORR performance. The ORR performance of bimetallic catalysts depends on two key factors: first, the formation of heteroatomic bonds will change the electronic environment of Pt, and the change in Pt electronic structure are caused by the change in Pt coordination; Second, the geometry structure of the bimetal is different from Pt, for example, a change in the metal-to-metal bond length will cause a strain effect, thereby changing the electronic structure of the metal by the orbital overlap [156]. Strasser et al. [161] treated PtCu alloys with different Pt: Cu components at high temperature (800 °C and 900 °C), and then dealloyed to obtain an alloy with a thin Pt shell layer. They used K-edge X-ray emission spectra (XES) and X-ray absorption spectra (XAS) to study the position and the specific atom occupation state of O 2p and Pt 5d, to obtain the corresponding compressive strain, as shown in Fig. 4.13. By testing its ORR performance, the relationship between compressive strain and ORR activity of PtCu alloys with different components was obtained. They used DFT to theoretically study the relationship between compressive strain and ORR activity of PtCu alloys with different compositions, and obtained a result similar to the volcanic map, but their experiments did not find the apex of the volcanic map. Research in this area is still in its infancy, and a lot of research needs to be followed up by researchers.

Although the ORR performance will increase to varying degrees when the second metal alloy with Pt, adding elements which promote ORR performance significantly such as Fe, Co, and Ni to the Pt lattice is not stable under acidic conditions when running in PEMFC, and will gradually dissolve in the electrolyte during the catalysis process, which will damage the proton exchange membrane [162, 163]. As mentioned earlier, in the ORR reaction, the adsorption of the reactants on the Pt bimetallic surface should not be too strong or too weak, and an appropriate amount of adsorption energy is the most favorable for the occurrence of ORR. Figure 4.14 lists the relationship between the adsorption energy, activity, and stability of the reactants for different

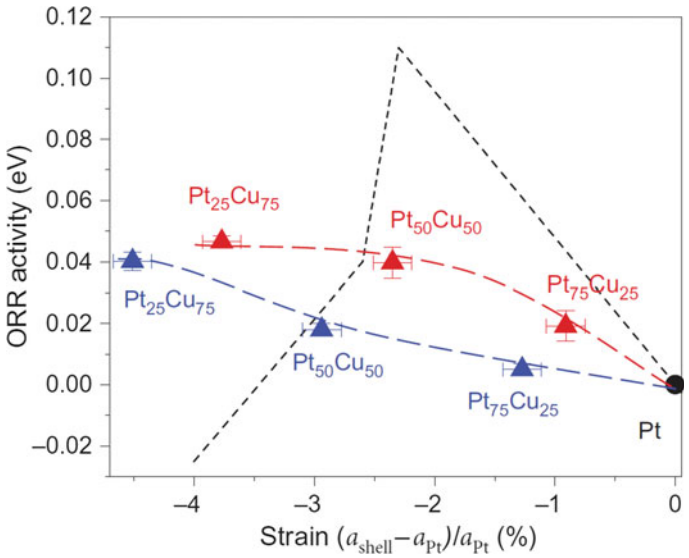

Fig. 4.13 Relationship between ORR performance (kT ln ($j_{s,\,alloy}$ / $j_{s,\,Pt}$) and compressive strain of ORR catalysts with different Pt/Cu composition. The result of the relationship between the compressive strain and ORR activity of the PtCu alloy calculated by DFT theory [161]. Reprinted with permission. [161] Copyright (2010) Springer

alloy catalysts [164]. It can be seen from the figure that although PtCo and PtNi have high ORR activity, their stability cannot meet the requirements of practical applications. It is worth noting that Pt_3Y and Pt_3Sc show high ORR activity and high stability. Greeley et al. [132] prepared bimetallic alloy ORR catalysts (Pt_3Sc and Pt_3Y) by sputtering, and tested their ORR performance, as shown in Fig. 4.15. They found that in the mixed control region, the half-wave potential of Pt_3Sc (the potential at which the current reaches half of the limit diffusion current) is about 20 mV positively shifted from Pt/C, and the ORR performance of the Pt_3Y catalyst is better, which is about 60 mV positively shifted from Pt/C. This result shows that the addition of Sc and Y can significantly improve the ORR performance of Pt-based catalysts. At 0.9 V (vs. RHE), the specific activity of Pt_3Sc is 50% higher than Pt/C, and Pt_3Y is 6 times higher than Pt/C. At 0.87 V (vs. RHE), the specific activity of Pt3Sc is increased by 80%, while Pt_3Y is an order of magnitude higher than Pt/C. Below 0.87 V, the performance is improved even more, which is very close to the best ORR catalyst PtNi (111) mentioned earlier [159]. They further studied the stability of Pt_3Sc and Pt_3Y. After 90 min of ORR cycle testing, their ORR performance curve hardly changed, which shows that their stability is very good. Since then, Yoo et al. [165] also formed PtLa bimetallic alloy catalysts using La in the same group of La-based metals, which also showed good ORR activity and stability. Hernandez-Fernandez et al. [186] prepared a Pt_xY bimetallic alloy ORR catalyst with a size of 4–9 nm by using a magnetron sputter gas-aggregation method, and the mass activity

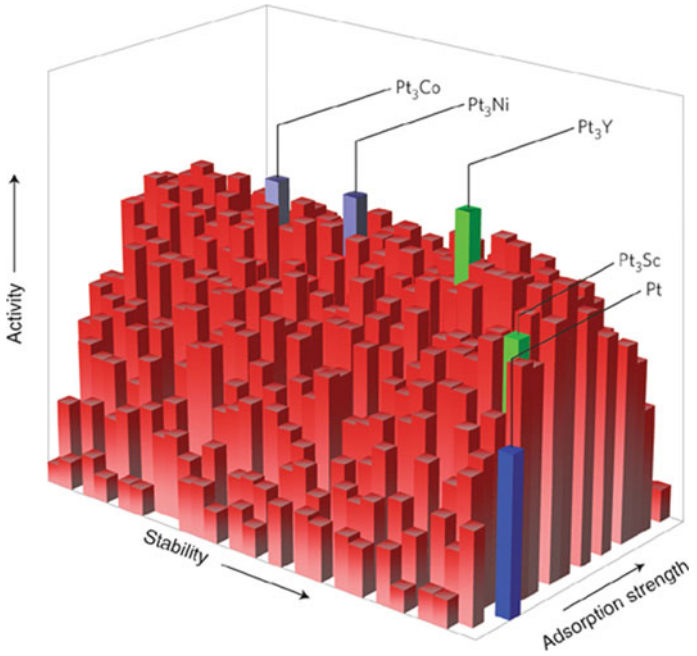

Fig. 4.14 Volcanic diagram of the activity, stability, and adsorption strength of a Pt-based bimetallic ORR catalyst [174]. Reprinted with permission. [174] Copyright (2009) Elsevier

at 0.9 V (vs. RHE) of Pt_xY bimetallic alloy ORR catalyst with a size of 9 nm reached 3050 mA mg^{-1}_{Pt}, and its performance remained very good after 9,000 cycles.

Research on Pt-based alloy ORR catalysts at home and abroad has been very extensive and in-depth, and some companies currently doing fuel cell catalysts also have corresponding products. However, for researchers, there are still many challenges in this field, including (1) ORR activity needs to be further improved to further reduce the amount of Pt and reduce costs; (2) although some researches have obtained some results about the mechanism of Pt-based alloy catalysts for enhancing ORR activity in some aspects, the systematic mechanism explanation needs to be achieved through the combination of further theoretical calculations and experiments, so as to provide theoretical guidance for the preparation of the entire Pt-based alloy ORR catalyst; (3) In an acidic medium, the second transition metal of the Pt-based alloy catalyst with high ORR activity is easily dissolved during battery operation. As a result, its ORR activity is reduced and the metal ions have a great destructive effect on the proton exchange membrane, thereby reducing the performance of the entire fuel cell. Therefore, it is necessary to solve this problem through innovative preparation technology.

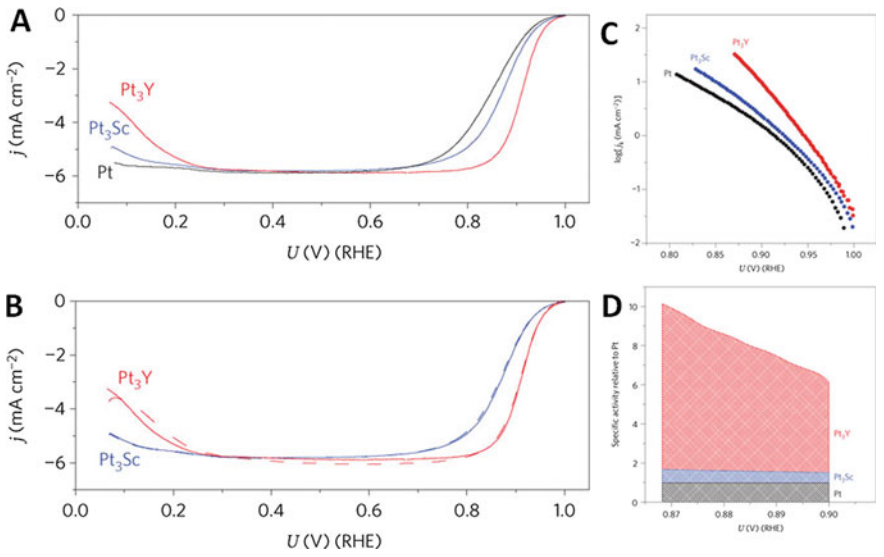

Fig. 4.15 **a** Comparison of ORR performance of Pt_3Sc, Pt_3Y, and Pt/C catalysts in 0.1 M $HClO_4$. **b** Comparison of ORR performance of Pt_3Sc and Pt_3Y catalysts before and after the 90-min ORR cycle test. (C) Tafel curve of Pt_3Sc, Pt_3Y and Pt/C catalyst. (D) Comparison of ORR specific activity of Pt_3Sc, Pt_3Y and Pt/C catalysts [132]. Reprinted with permission. [132] Copyright (2009) Springer

4.2.3 Pt-Based Nanostructured ORR Catalyst

The development of nanotechnology and the preparation of controllable morphology of nanomaterials have attracted more and more researchers' interest. This is because the morphology of nanomaterials has a great influence on its performance, even a decisive influence, especially the adjustment of its catalytic, optical, electronic, and magnetic properties can greatly expand the application of nanomaterials in devices, sensors, thermals, and catalysis [167–170]. For Pt-based ORR catalysts, their morphology also has a very large effect on their ORR performance [171].

For metals with a fcc structure such as Pt, their nanocrystalline morphology and their surface structure are very similar. Polyhedral single crystals, such as octahedron and rhombic dodecahedron, consist of three base crystal planes {111}, {100}, and {110} at the nodes. With three different surfaces with a high crystal plane index, such as {hk0}, {hkk}, and {hhl} crystal planes ($h \neq k \neq l \neq 0$), the polyhedrons that are the boundary are on the three sides of the triangle. A polyhedron consisting of {hkl} ($h \neq k \neq l$) crystal planes is inside the triangle. Successfully synthesized single crystal polyhedrons with fcc structures include tetrahexahedron (THH) [169, 172, 173], concave cubes [174], and truncated complex square prisms [175, 176] which consist of {hk0} planes, trisoctahedron [177] composed of {hhl} faces, octapod [178] composed of {hkk} crystal faces, and Concave hexoctahedron [179] composed of {hkl} crystals. The appearance of twin boundaries greatly enriched the morphology

of nanocrystals composed of special crystal planes. For example, although single crystal polyhedrons consisting of {111} crystal planes can only be octahedron, tetrahedron, and truncated tetrahedron, a large number of other polyhedrons consisting of {111} crystal planes and twin boundary are synthesized.

Wang et al. [180] reduced platinum acetylacetone in oleylamine and oleic acid solution at 200 °C in the presence of a small amount of $Fe(CO)_5$, and Pt nanocubes with a size of 8 nm are obtained, as shown in Fig. 4.16. The presence of a small amount of $Fe(CO)_5$ is crucial for the preparation of Pt nanocubes. In the absence of $Fe(CO)_5$, only spherical Pt nanoparticles can be obtained. In the range of 0.9 to

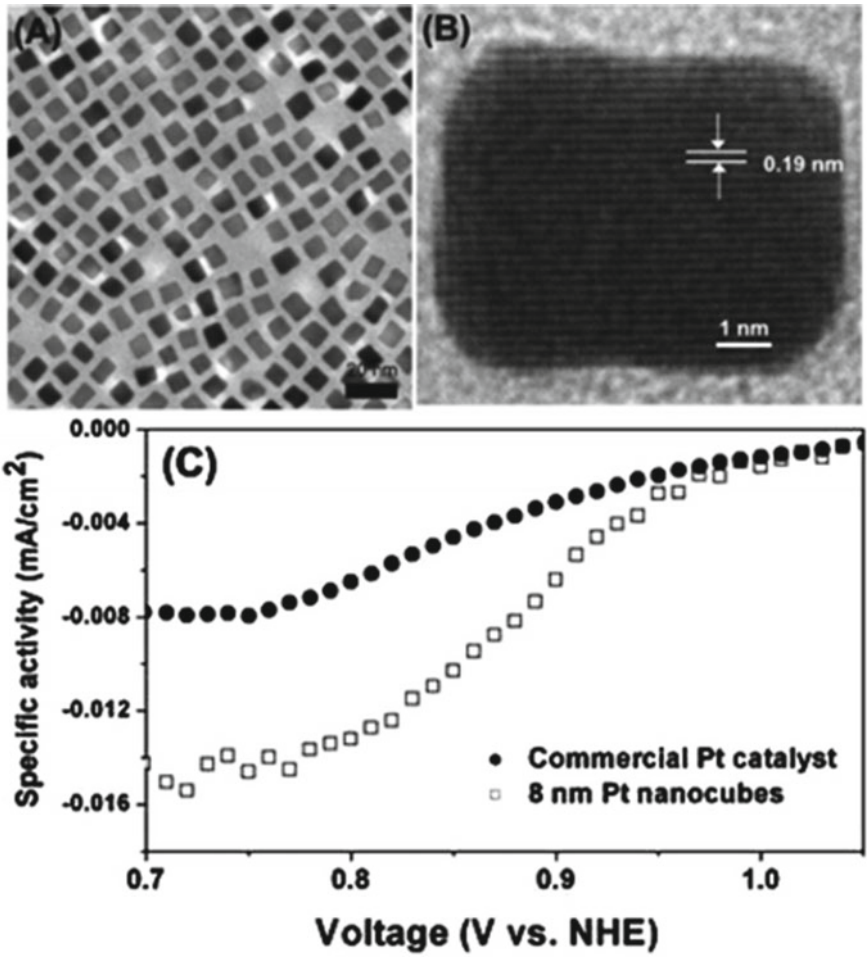

Fig. 4.16 **a** TEM images of Pt nanocube, **b** TEM images of Pt nanocube, **c** Comparison of ORR specific activity of Pt nanocube and Pt/C catalyst in 0.5 M H_2SO_4. [180] Reprinted with permission. [180] Copyright (2007) American Chemical Society

0.8 V (vs. RHE), the specific activity of the 8 nm Pt nanocubes was more than twice the commercial Pt/C spherical nanoparticles. In addition, the morphology of the Pt nanocube did not change after the ORR performance test.

Liang et al. [181] first synthesized ultra-fine Te nanowires with large length–diameter ratio [182], and then used ultra-fine Te nanowires as templates, and coated the outer layer with carbon to form Te@C nanocables by hydrothermal method. Then, a Pt nanowire (Pt NW@C) is formed by a substitution reaction between Te and $PtCl_6^{2-}$. Finally, the outer carbon is removed at 400° C for one hour to obtain the final Pt NW. In 0.5 M H_2SO_4, the specific activity of Pt NW at 0.85 V (vs. RHE) was 2.1 and 1.8 times that of Pt/C and Pt black, respectively. In addition, the Tafel curve corrected by the diffusion current shows that Pt NW has the highest kinetic current density in all voltage ranges. They believe that the ORR performance improvement of Pt nanowires to Pt comes from (1) one-dimensional nanostructures that are more inclined to expose specific crystal planes; (2) this nanowire structure has fewer defects; (3) the network structure of one-dimensional nanowires facilitates the transport of electrons and the diffusion of gases on the electrodes [183, 184]. Koenigsmann et al. [185] placed 2.5 mL of chloroplatinic acid ($H_2PtCl_6 \cdot xH_2O$, > 99.9%, 10.0 mM) in 20 mL of dimethylformamide, 12.5 mL of toluene, and 2.5 mL of triethylamine. During the stirring process, 20 mg of sodium borohydride was added, and the reaction was performed for 3 h, finally the Pt nanowires were obtained. The average diameter of Pt nanowires is 1.8 ± 0.3 nm and the length is 100 ± 25 nm. After pickling, the diameter can be further reduced to 1.3 ± 0.4 nm, as shown in Fig. 4.17. The Pt nanowires they prepared have a more positively ORR curve. At 0.9 V (vs. RHE), their specific activity reached 1.45 mA cm^{-2}, which is 7 times that of commercial Pt/C catalysts (0.21 mA cm^{-2}).

Although Pt catalysts with special nanostructures have greatly improved their ORR performance due to their nano-effects and structural effects, especially these special nano-structures greatly increase the stability of Pt. But they cannot fundamentally change the electronic structure of Pt, so that ORR activity can be greatly improved. An effective way is to introduce a second transition metal while forming a special nanostructure of Pt to form a PtM alloy with a special nanostructure. Xiaoqing Huang et al. [186] designed a new control method to prepare a high specific surface area Pt–Co nanowire with a zigzag structure, and its surface has a higher density of high index crystal plane, as shown in Fig. 4.18. The evaluation results of its oxygen reduction reaction catalysis data show that the mass activity of the zigzag Pt–Co nanowires for oxygen reduction catalysis reaches nearly 4 A/mg @ 0.9 V, which is 33 times that of commercial Pt/C. Theoretical calculations show that the high ORR activity on PtCo nanowires is mainly derived from [158] and the Empty site of high index crystal plane [310] on the nanowire surface [186].

Wu et al. [165] used $Pt(acac)_2$ as the precursor of Pt, and used $Ni(acac)_2$, $HAuCl_4$, and $Pd(acac)_2$ as the precursors of the second added metal, respectively. In the mixed solution of oleylamine, oleic acid, and diphenyl ether, Pt–M (M = Au, Ni and Pd) icosahedral nanocrystals were synthesized by filling a certain flow of CO gas during the heating reduction process. The size of the synthesized Pt_3Ni icosahedrons is 13 ± 0.3 nm, as shown in Fig. 4.19. The HRTEM image shows a five-fold symmetrical

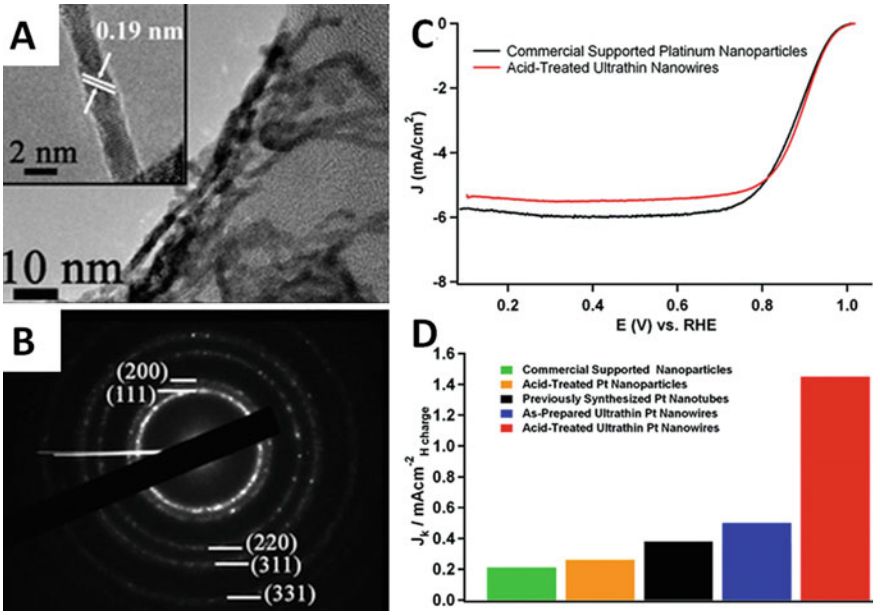

Fig. 4.17 **a** TEM images of Pt nanowires, the inset is the HRTEM image of Pt nanowires, **b** selected area electron diffraction images, **c** ORR Curve of Pt nanowires and Pt/C catalyst in 0.1 M $HClO_4$ **d** Comparison of ORR specific activity of Pt nanowires and Pt/C catalysts [185]. Reprinted with permission. [185] Copyright (2010) American Chemical Society

structure and double twin boundaries. Pt_3Ni icosahedrons are basically composed of {111} facets. Among the Pt–M icosahedral nanocrystals, the ORR activity of Pt_3Ni was the highest, and the specific activity and mass activity at 0.9 V (vs. RHE) reached 1.83 mA $cm^{-2}{}_{Pt}$ and 620 mA $mg^{-1}{}_{Pt}$. In addition, they also compared the ORR activity of this Pt_3Ni decahedrons and Pt_3Ni octahedrons, and found that the specific activity of the Pt_3Ni decahedrons was 50% higher than that of the Pt3Ni octahedrons. The density functional theory and molecular dynamic calculation results show that this difference in ORR performance may be due to the electronic effect caused by strain. Choi et al. [209] used $Pt(acac)_2$ and $Ni(acac)_2$ precursor, and added the above precursors to a mixed solution of oleic acid, oleylamine, and benzyl ether. Under the protection of Ar gas, $W(CO)_6$ was added at 130 °C, then the temperature was raised to 230 °C, and then the Ar gas was stopped, and the reaction was performed at 230 °C for 40 min to obtain Pt–Ni octahedrons. The size of the obtained Pt–Ni octahedron is 9 nm, and the addition of $W(CO)_6$ as a CO gas source can promote the formation of {111} crystal planes under the effcet of Ni. They further treated the obtained Pt–Ni octahedrons with acetic acid for 2 and 10 h, and finally loaded these Pt–Ni octahedrons onto the carbon powder. The mass activity of Pt–Ni octahedrons at 0.9 V (vs. RHE) before acetic acid treatment reached 3100 mA $mg^{-1}{}_{Pt}$, while the Pt–Ni octahedrons after 2 h acetic acid treatment at 0.9 V (vs. RHE) reached 3300 mA $mg^{-1}{}_{Pt}$, which is 17 times of the commercial Pt/C (200 mA $mg^{-1}{}_{Pt}$). Their

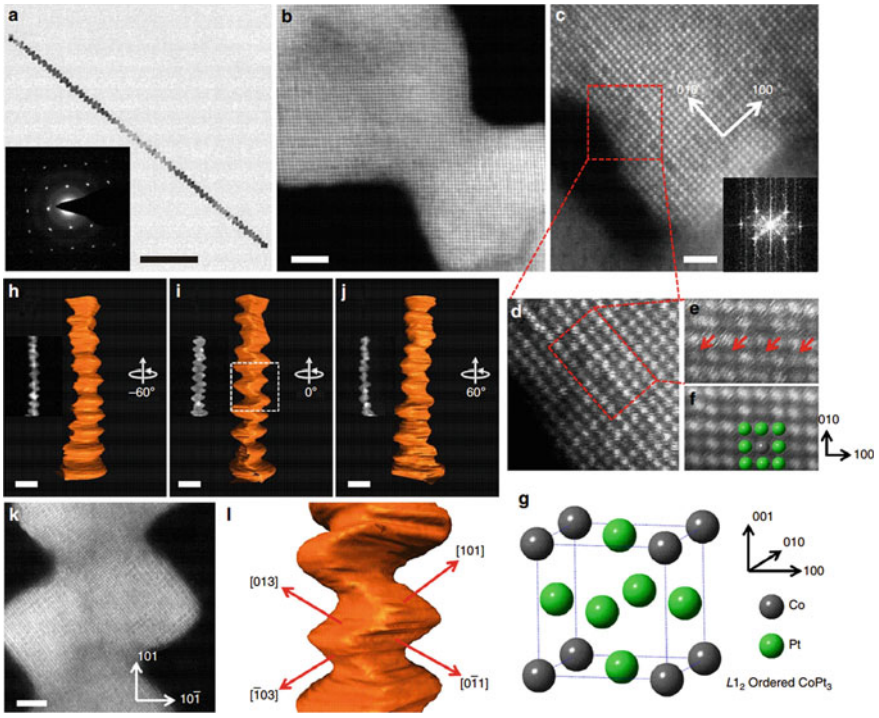

Fig. 4.18 Structure analysis of a zigzag Pt–Co nanowires. [186] Reprinted with permission. [186] Copyright (2016) Springer

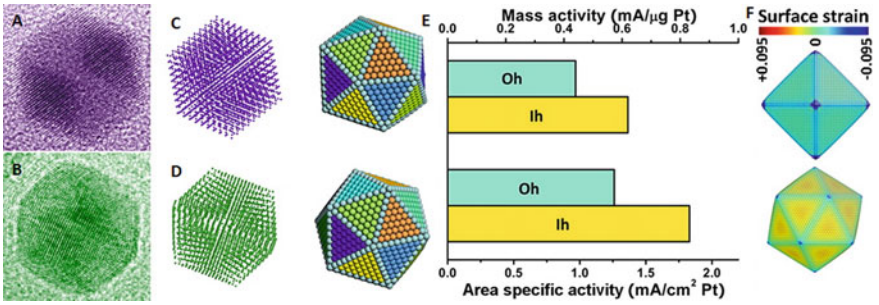

Fig. 4.19 **a-d** HRTEM images of Pt_3Ni icosahedral nanocrystals and their three-dimensional models in different directions, with a scale of 2 nm, **e** Comparison of specific activity and mass activity of Pt_3Ni icosahedral nanocrystals and Pt_3Ni decahedral nanocrystals at 0.9 V (vs. RHE), **f** Surface strain field distribution of Pt_3Ni icosahedral nanocrystals and Pt_3Ni decahedral nanocrystals [142]. Reprinted with permission. [142] Copyright (2012) American Chemical Society

analysis suggests that this significant increase in activity comes from its clean surface and the exposure of the rich {111} crystal planes of Pt–Ni octahedrons.

At present, the research on ORR catalysts for building Pt-based nanostructures is very rich, and some exciting results have been achieved. In particular, the synthesis of Pt-based nanostructure alloys has raised the activity and stability of Pt-based ORR to a new level, and is a powerful candidate for cathode catalysts used in cheap and efficient PEMFCs in the future. However, the preparation process of such Pt-based nanostructured ORR catalysts is usually more complicated, especially in the synthesis process, some special templates are used or some organic surfactants are required. The application of templates and the removal and addition of surfactants not only increases the complexity of the synthesis process, increases the cost of preparation, and poses a very large challenge to its batch preparation process.

4.2.4 M@Pt Core–Shell ORR Electrocatalyst

ORR is a surface-catalyzed electrochemical process. For Pt nanoparticles, only Pt atoms distributed on its surface can be used to catalyze oxygen reduction reaction, while Pt atoms inside the nanoparticles cannot directly participate in the ORR process [188]. Therefore, the traditional ORR activity utilization rate of pure Pt nanoparticles is very low, which results in its low ORR activity and the large amount of Pt nanoparticles in PEMFCs, which drives up the cost of application. Although alloying can increase the activity of Pt-based ORR catalysts, reduce the amount of Pt, and increase the Pt utilization rate, many Pt atoms inside the Pt-based alloy nanoparticles are still not used. Based on this, researchers have developed novel core–shell Pt-based ORR catalysts, as shown in Fig. 4.20. Since the traditional pure Pt nanoparticles only have the outer Pt atomic layer participating in the ORR process, and the inner Pt atoms cannot be utilized, so researchers have replaced the Pt atoms inside the Pt particles with other transition metals. Pt atoms are exposed on the surface, forming a M@Pt

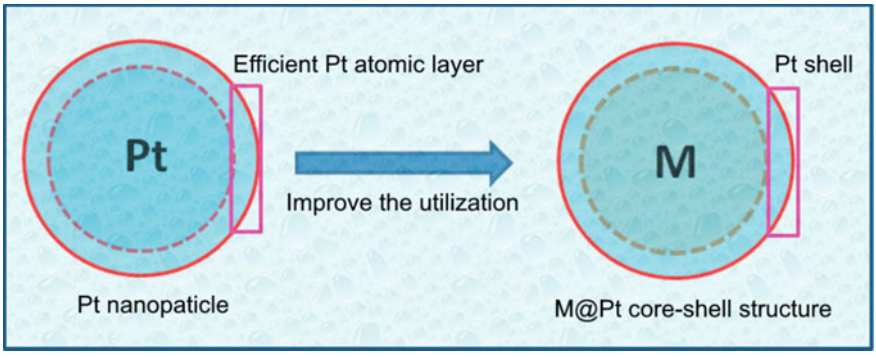

Fig. 4.20 Schematic diagram of M@Pt core–shell ORR catalyst

core–shell structure (M = Fe, Co, Ni, Cu, Pd, Ag, etc.) [189–192]. Most of Pt atoms of this M@Pt core–shell structure participate in the ORR process, which greatly improves the utilization of Pt.

According to the distribution of Pt atoms in the core–shell structure, M@Pt core–shell structure can be divided into two basic types: ideal mono/multil atomic layer mode and Pt-enriched surface layer mode.

(1) **ideal mono/multil atomic layer mode**

The ideal mono/multil atomic layer mode means that single or multiple layers of Pt atoms are ideally divided on the outer surface layer of the transition metal M nanoparticles to form an ideal M@Pt core–shell structure. This M@Pt core–shell structure of ideal mono/multil atomic layer mode is generally prepared by the "in-situ replacement" method: using the characteristics of large standard reduction potential of Pt, the nano-nanoparticles of metal M (Fe, Co, Ni, Cu, etc.) with a small standard reduction potential undergo a replacement reaction in a Pt precursor, forming a single or multiple layers of Pt atoms on the surface of M.

If the standard reduction potential between M (for example, Pd) and Pt is too small, this replacement method is difficult to obtain the core–shell structure, which can be prepared by combining with the "underpotential deposition" (UPD) method. Adzic and others took the lead in combining the "in-situ replacement" and "underpotential deposition" methods to successfully prepare Co@Pd@Pt sandwich core–shell structures [193], as shown in Fig. 4.21: First, the Co@Pd core was prepared by "in-situ replacement," and then Co@Pd@Cu structure was prepared by the method of "underpotential deposition." Finally, the Co@Pd@Pt sandwich core–shell structure was prepared by the method of "in-situ replacement."

Because the "underpotential deposition" method can deposit a single atomic layer of Cu on the surface of metal nanoparticles, it has a wide reference meaning in the design of core–shell structure catalysts. Combined with the "in-situ replacement" method, researchers have achieved many nanoelectrocatalysts of "core–shell structure." Pt (111) will form an oxide layer on the surface, thereby suppressing its ORR activity and causing the dissolution of Pt during the ORR process. However, Au atoms can affect this process and play a stabilizing role. Zhang et al. [154] deposited Au clusters of 2–3 nm on the surface of Pt (111) to form Au/Pt/C. Through the stability test, they found that after 30,000 cycles, the ORR curve of Au/Pt/C has hardly changed, and the corresponding electrochemically active area has not decreased.

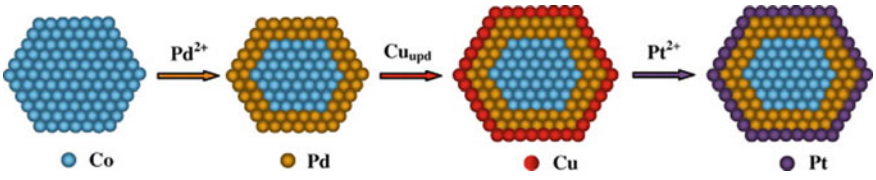

Fig. 4.21 The preparing process of in-situ replacement, underpotential deposition, and in-situ replacement of Co@Pd@Pt [193]. Reprinted with permission. [193] Copyright (2007) Elsevier

The commercial Pt/C catalysts tested under the same conditions have decreased a lot. Although Au has been shown to greatly improve the stability of Pt, its initial ORR activity has not improved much. The use of Au's stabilization combined with a shell-core structure is considered to be a very promising design scheme of ORR catalysts. Sasaki et al. [154] first prepared Pd_9Au_1 nanoparticles on a carbon support by wet impregnation method, and then used a "underpotential deposition" method to deposit a monoatomic layer of Cu on the surface of Pd_9Au_1 nanoparticles. Finally, the core–shell structure Pt_{ML}/ Pd_9Au_1/C with a single-layer Pt atom was obtained by the replacement method. The size of final prepared particle was 3.8 ± 1.2 nm, as shown in Fig. 4.22.

In fuel cell tests, the mass activity of this Pt_{ML}/Pd_9Au_1/C core–shell structure ORR catalyst at 0.9 V (vs. RHE) reached 310 mA $mg^{-1}{}_{Pt}$, which is three times of that of commercial Pt/C (100 mA $mg^{-1}{}_{Pt}$). They performed a 100000 cycle test on

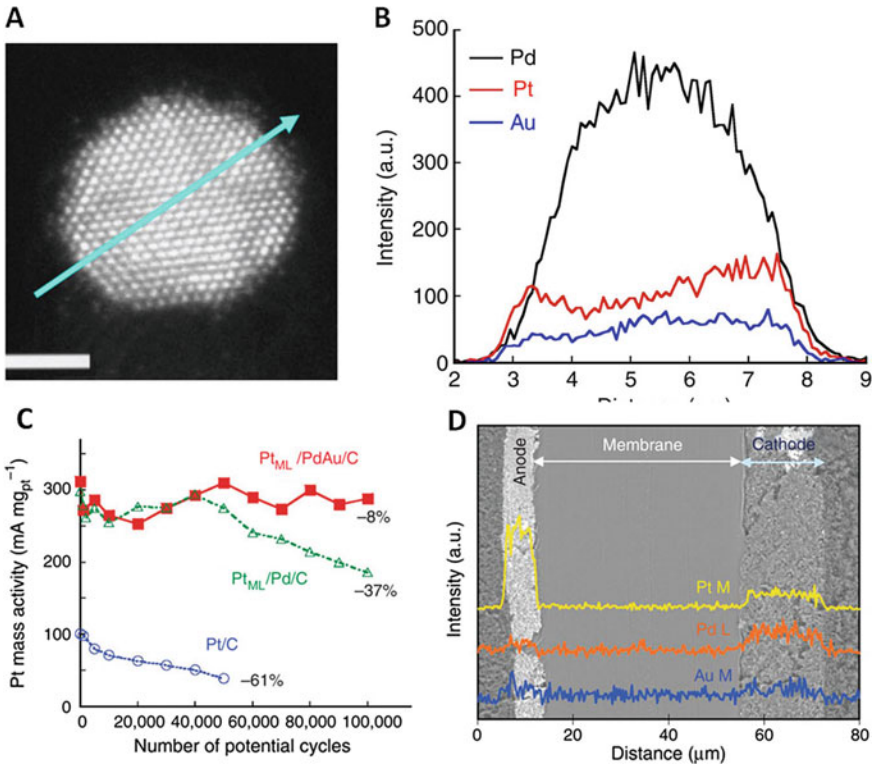

Fig. 4.22 **a** HAADF-STEM picture of Pt_{ML}/Pd_9Au_1 nanoparticles with a scale bar of 2 nm, **b** element line scan distribution of Pt_{ML}/Pd_9Au_1 nanoparticles in the direction of the arrow line of A in Figure A, **c** Mass activity and stability test diagram at 0.9 V (vs. RHE) of Pt_{ML}/Pd_9Au_1/C, Pt_{ML}/Pd/C and Pt/C catalyst, **d** after 100,000 cycle stability test, SEM image of MEA cross section of Pt_{ML}/Pd_9Au_1/C and its element line scan distribution [154]. Reprinted with permission. [154] Copyright (2012) Springer

the fuel cell at a voltage range of 0.6 to 1.0 V at 80 °C and found that the activity of $Pt_{ML}/Pd_9Au_1/C$ core–shell structure only decreased by 8%, which is far less than the 40% reduction target set by DOE for 30,000 cycles. As a comparison, the initial ORR activity of $Pt_{ML}/Pd/C$ core–shell structure is equivalent to that of $Pt_{ML}/Pd_9Au_1/C$, but under the same stability test conditions, the activity decreased by 37%, which is much greater than $Pt_{ML}/Pd_9Au_1/C$. Under the same stability test conditions, commercial Pt/C dropped by 61% after 50 000 cycles.

They further calculated the stability of the system using density functional theory and found that during the separation and stratification process, Au atoms would preferentially remain at the defect sites left by the surface Pt, and then inhibit the further dissolution of Pd and Pt [195]. As a result, its stability has been greatly improved.

(2) **Pt-enriched surface layer mode**

The Pt-enrich core–shell structure in the surface layer means that Pt atoms are mainly distributed on the surface layer of the nanoparticles, and there are only a small number of Pt atoms inside. This type of core–shell structure can be prepared by heat-treating a PtM (M = Fe, Co, Ni, Cu, etc.) alloy in a specific atmosphere (CO, NO, O_2, H_2, etc.) [196]. During the heat treatment of PtM in these atmospheres, these gases can induce the Pt atoms to the surface of the alloy nanoparticles. Different PtM alloys use different gases for the surface heat treatment of Pt atom.

For example, heat treatment of PtCo alloy in CO atmosphere can induce most Pt atoms to the surface of catalyst particles [197]. In addition, a M@Pt core–shell ORR catalyst with a Pt-rich surface can be prepared by adding a precursor capable of decomposing the above-mentioned gases during the preparation of the PtM alloy. For example, in a special high-temperature solvent and protected by nitrogen, thermal decomposition of $Pt(acac)_2$ and $Co_2(CO)_8$ can prepare M@Pt core–shell catalyst with a Pt-rich surface [198, 199].

Wang et al. [200] first took $H_2PtCl_6{\cdot}6H_2O$ and $CoCl_2{\cdot}6H_2O$ as precursors, and mixed them with carbon powder (Vulcan XC-72) in the liquid phase, and then reduced them in a H_2/N_2 atmosphere at 150°C in a H_2 atmosphere. Finally, heat treatment was performed at 400 °Cand 700 °C for 2 h to obtain Pt_3Co/C-400 and Pt_3Co/C-700 with a size of about 5 nm. These Pt_3Co/C-400 and Pt_3Co/C-700 have a core–shell structure after heat treatment at 400 °C and 700 °C in a H_2 atmosphere. The thickness of the outer layer is 0.5 nm, which is the 2–3 atomic layer of Pt-rich shell. Compared with commercial Pt/C, the ORR half-wave potential ($E_{1/2}$) of Pt_3Co/C-700 is positively shifted by approximately 7 mV, and its mass activity at 0.9 V (vs. RHE) reaches 520 mA $mg^{-1}{}_{Pt}$ which is nearly 9 times that of commercial Pt/C (60 mA mg −1Pt). In addition, Pt_3Co/C-700 also showed better stability than Pt/C. After 5 000 cycles of stability tests, its half-wave potential was negatively shifted by less than 10 mV.

Huang Xiaoqing et al. [201] synthesized a PtPb-Pt core–shell nanoplate with a Pt atomic shell layer of about 1 nm thick, and the two exposed surfaces are both Pt(110) crystal planes. Biaxial compressive stress was found on the Pt(110) crystal plane. ORR test results show that the specific activity and mass activity of the catalyst

reach 7.8 mA/cm^2 @ 0.9 V and 4.3 A/mg$_{Pt}$@0.9 V, respectively. Different from the traditional view, the density functional theory analysis thinks that the moderate expansion stress on the Pt(110) crystal plane is helpful to reduce the interaction between Pt-O and achieve a better value.

Compared with pure Pt nanoparticle catalysts, the M@Pt core–shell catalysts have improved Pt utilization obviously. However, the enhancement of ORR performance of the M@Pt core–shell electrocatalyst in structural design is not limited to the improvement of the utilization of Pt atoms. This core–shell structure also makes an important contribution to the improvement of ORR activity in the following aspects: (1) The formation of the core–shell double-layer structure can affect and change the electronic structure and properties of the outer Pt layer, and it can even adjust the electronic structure and properties of the Pt atoms on the surface by adjusting the change of the thickness of inner transition metal and Pt layer; (2) Surface modification through surface functionalization can increase the stability and dispersibility of catalyst particles; (3) Further assembly of core–shell nanoparticles will also generate new physical and chemical properties.

The M@Pt core–shell electrocatalyst can achieve higher ORR activity and stability with less Pt, which greatly reduces the cost of PEMFC. The optimized design of the M@Pt core–shell ORR electrocatalyst can furtherly accelerate the commercialization process of PEMFC [202].

4.2.5 Pt-Based Nanoframes and Nanocages ORR Electrocatalyst

ORR is a surface-catalyzed electrochemical process, so only Pt atoms on the surface can participate in the catalytic reaction, while Pt atoms inside the particles cannot directly participate in the ORR catalytic process [188]. Although the utilization of Pt nanoparticles can be increased through the core–shell structure, it is still the goal of researchers to further improve the utilization of internal Pt atoms. Therefore, researchers have proposed a method to etch the surface and core of nanomaterials to obtain a framework-only nanoframe structure or nanocage structure material. By increasing the specific surface area of the catalyst, the exposure and utilization of internal Pt atoms can be increased, and increase the catalytic performance of oxygen reduction of nanomaterials.

Peidong Yang et al. [204] reported for the first time the synthesis of Pt-Ni nanocrystals with a fully transparent framework structure. First, $PtNi_3$ nanocrystals with a rhombic dodecahedron structure were synthesized. Dispersed in a non-polar solvent for two weeks, such as n-hexane and chloroform, these nanocrystals are transformed into Pt_3Ni nanoframework, and its symmetry and size have not been changed. The open frame structure of Pt_3Ni nanoframes and Pt(111) surface skin make the active site fully exposed. Therefore, in the oxygen reduction reaction catalysis, the mass activity of the Pt_3Ni nanoframe is as high as 5.7 A/mg$_{Pt}$@0.9 V, which is 36 times

that of commercial Pt/C catalyst. This article can be said to be the continuation of Stamenkovic et al. proposal of single crystal $Pt_3Ni(111)$ with super high activity in 2007 [159].

Younan Xia et al. [204] reported for the first time the synthesis of Pt-based icosahedron nanocages, whose surface is surrounded by {111} planes and twin boundaries, and the wall thickness can be made as thin as six atomic layers. First, Pd icosahedron was synthesized, then $Pd@Pt_{nL}$ core–shell icosahedron was prepared, and finally $Pd@Pt_{4.5L}$ icosahedron was derived by selectively etching away Pd in the core. During the etching process, the nanocrystals can fully retain multiple twin crystal structures, while the Pt atoms in the walls are reconstructed to eliminate the corrugated structure built in the original Pt shell, as shown in Fig. 4.23. For the oxygen reduction reaction, Pt-based icosahedral nanocages showed a specific activity of 3.50 mA cm^{-2}, which is much larger than Pt-based octahedral nanocages (1.98 mA cm^{-2}) and commercial Pt/C catalyst (0.35 mA cm^{-2}). After 5,000 cycles of accelerated durability test, the mass activity of the Pt-based icosahedron nanocages decreased from 1.28 to 0.76 A mg^{-1}_{Pt}, which is still about 4 times that of the original commercial Pt/C catalyst (0.19 A mg^{-1}_{Pt}).

In Pt-based polyhedral nanocrystal materials, the non-Pt portion is etched to make the surface or core of polyhedrons disappear and present a nanoframe structure or a nanocage-like structure, which can significantly improve the exposure and utilization

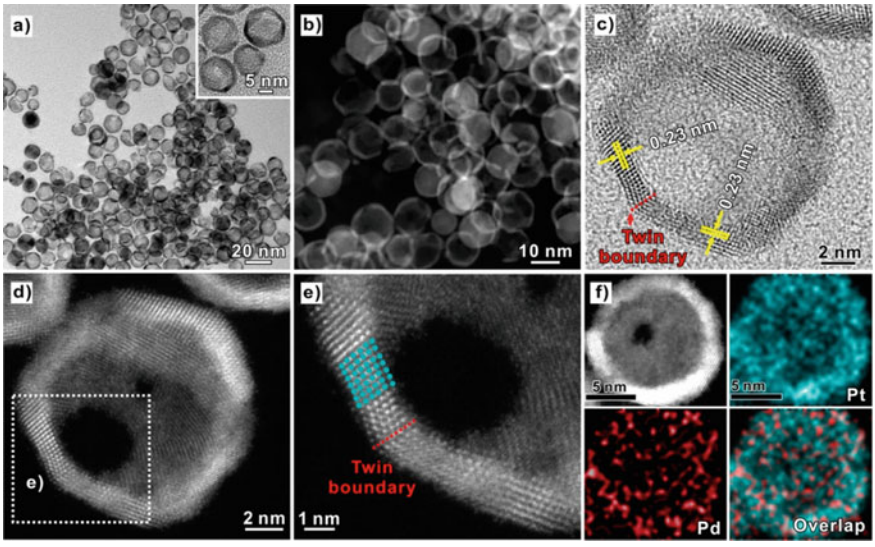

Fig. 4.23 **a** TEM and **b** low-magnification HAADF-STEM images of the Pt icosahedral nanocages. **c** Bright-field and **d** atomic-resolution HAADF-STEM images taken from a single nanocrystal along a twofold symmetry axis. **e** HAADF-STEM image taken from the edge marked by a box in (**d**), revealing a wall thickness of only six atomic layers and a twin boundary. **f** HAADF-STEM image of an icosahedral nanocage and the corresponding EDX mapping of Pd and Pt [204]. Reprinted with permission. [204] Copyright (2016) American Chemical Society

of Pt atoms. This structure is also conducive to mass transfer. In addition, during the etching process, Pt atoms will rearrange and present the surface of the Pt skin, which is not only conducive to improving the catalytic performance but also improving the durability and stability. Nanoframe or nanocage formation through etching can greatly improve the catalytic efficiency and reduce the cost of commercialization.

4.3 Pt-Cocatalyst System

Other substances added to the catalyst are not active or less active, but can change some properties of the catalyst, such as chemical composition, ionic valence, acidity and alkalinity, surface structure, and grain size, which can improve activity, selectivity, anti-toxicity, or stability. This effect is usually called "synergistic effect," and it is generally called "one plus one greater than two." For a Pt-based ORR catalyst, if the addition of a foreign substance can promote the activity or stability, we can call the foreign substance a synergistic component or co-catalyst to form a Pt-cocatalyst. At present, there are mainly three types of promoters that have a "synergistic effect" on Pt: (1) transition metal oxides, (2) transition metal carbides, and (3) graphene and doped graphene.

4.3.1 Transition Metal Oxide ORR Co-Catalyst

The research on the Pt-cocatalyst system can be traced back to 1974, when Tseung et al. [205] found that antimony-doped SnO_2 in 85% $H3PO_4$ aqueous solution could significantly enhance the oxygen reduction performance of Pt electrocatalyst. They believe that the antimony-doped SnO_2′s effect on ORR activity of Pt is a so-called "oxygen overflow," that is, the oxygen molecules adsorbed on the Pt active site can be transferred to the antimony-doped SnO_2 surface, forming continuous oxygen transport and proximity storage effect, while greatly improves the oxygen reduction kinetics. Later, we found that many oxides can improve the ORR activity of Pt, including CeO_2, WO_3, NiO_x, TiO_2, MnO_2, NbO_2, and $Sn_{0.96}Sb_{0.04}O_{2-\delta}$, etc. [140, 205–208]. These oxides can not only improve the ORR activity of Pt, but also some of them can improve the alcohol resistance and anti-toxicity of Pt. However, researchers have found that most oxides have poor electrochemical stability under acidic conditions, making the "synergistic effect" unsustainable.

Among many oxides, due to its high electrochemical stability in acidity, there have been many studies using TiO_2 as a co-catalyst for Pt, but because the outer electrons are involved in bonding, which result in its interaction with Pt is limited. In addition, the band gap of TiO_2 is very large, and its conductivity is very poor, which is very unfavorable as a co-catalyst for Pt-based ORR catalysts. Based on this, researchers have developed a hypoxic type of Magnéli phase Ti_nO_{2n-1}($3 \leq n \leq 10$) as a co-catalyst for Pt-based ORR catalysts [140, 209]. This material possess

high conductivity, and due to the presence of oxygen vacancies, Ti_nO_{2n-1} has the characteristics of under-d electrons and can interact with Pt with super-d electron characteristics. This electronic interaction between Ti_nO_{2n-1} and Pt can promote ORR activity of Pt [209, 210].

4.3.2 Transition Metal Carbides ORR Co-Catalyst

In 2005, based on the previously discovered tungsten oxide (WO_3) synergistically enhanced Pt-based electrocatalyst [211], P.K. Shen et al. first discovered the enhanced effect of tungsten carbide on Pt ORR activity [212, 213]: Under the "synergistic effect" of tungsten carbide, the ORR on-set potential of Pt has a significant positive shift, and when it gets the same performance as Pt/C, it can reduce the amount of Pt by 2/3. Moreover, the tungsten carbide is more stable than tungsten oxide. This work has attracted widespread attention at home and abroad, and researchers have invested in this field in anticipation of the development of more excellent Pt-based ORR catalysts [139, 204–216]. Hsu et al. [217] deposited different number of layers of Pt atomic layer on the surface of WC by atomic layer deposition method. They found that in 0.5 M H_2SO_4 medium, only 20 Atomic layer thickness of Pt deposit on the surface of WC, its ORR performance is equivalent to ordinary Pt catalyst.

Because the synthesis temperature of WC is relatively high, the particles of WC prepared earlier are relatively large and the specific surface area is relatively small. To maximize the synergistic effect of WC, it is necessary to synthesize WC with small particles and large specific surface area. Yan et al. [218] used an ion exchange resin to exchange the precursors of W and Fe, and found a new way to synthesize WC, which greatly reduced the synthesis temperature, and obtained WC nanoparticles smaller than 2 nm, which is the smallest WC nanoparticles currently synthesized. Its ORR mass activity at 0.9 V (vs. RHE) reached 257.7 mA $mg^{-1}{}_{Pt}$, which is more than twice the commercial Pt/C (124.6 mA $mg^{-1}{}_{Pt}$). Wang et al. [219] first prepared microspheres using ammonium metatungstate and glucose as precursors, and then heat-treated at 950 °C to obtain tungsten carbide microspheres (TCMSs). Its specific surface area reached 256 $m^2\ g^{-1}$. After compounding with Pt, the ORR activity of Pt/TCMSs was increased by 200% compared with commercial Pt/C.

They further performed stability tests on Pt-WC_{THP}/G. After 6,000 cyclic voltammetry tests, the ECSA of the commercial Pt/C catalyst after the end of the stability test was reduced to 42.4%, while the ECSA of Pt-WC_{THP}/G still remained 89.2%. After 6,000 cycles of cyclic voltammetry stability tests, the Pt-WC_{THP}/G catalyst's half-wave potential for oxygen reduction was only 7 mV lower than the initial, while the half-wave potential of commercial Pt/C negatively shift 36 mV. The mass activity of the Pt-WCTHP/G catalyst still reached 480 mA $mg^{-1}{}_{Pt}$ (0.9 V vs. REH) after the stability test, which is more than 8 times the mass specific activity of commercial Pt/C (56 mA $mg^{-1}{}_{Pt}$) after the stability test, as shown in Fig. 4.24.

In order to uncover the mechanism of WC's activity enhancement for Pt-based ORR catalysts, Professor P.K. Shen et al. [220] used the Gaussian 03 program to

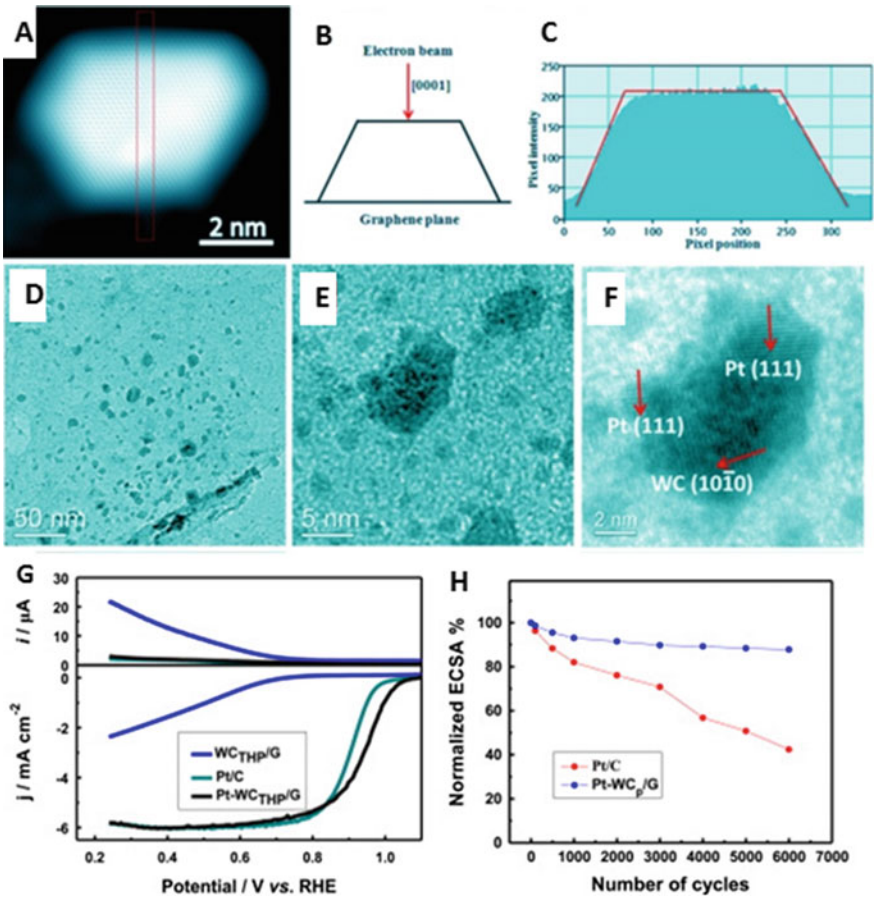

Fig. 4.24 **a** Atomic resolution HAADF-STEM image of a WC_{THP} particle, **b** A cross-sectional view of a transmitted electron beam projected onto a WC_{THP} particle, **c** HAADF-STEM signal intensity distribution of a WC_{THP} particle, **d**, **e** TEM image of Pt-WC_{THP}/G, **f** HRTEM image of Pt-WC_{THP}/G, **g** Oxygen reduction curves of WC_{THP}/G, Pt/C and Pt- WC_{THP}/G in 0.1 M $HClO_4$, **h** ECSA changes of Pt/C and Pt-WC_{THP}/G during the stability test with the number of test cycles [139]. Reprinted with permission. [139] Copyright (2014) Elsevier

calculate the surface electrostatic potential of Pt_9 clusters, WC and Pt_7/WC, as shown in Fig. 4.25. Figure 4.25 show the structure and surface electrostatic potential of the Pt_9 cluster and WC, respectively. It can be seen from the figure that the regions with high negative electron density are concentrated in the red central atomic region, indicating that they all have "strong electron-donating" characteristics. It is worth noting that W atom clusters have a higher negative electron density, which means that W atom clusters have a stronger electron-donating ability. In addition, when Pt is supported on a WC carrier, its negative electron center is transferred to the periphery of Pt, and W atoms no longer have a high negative electron density around them.

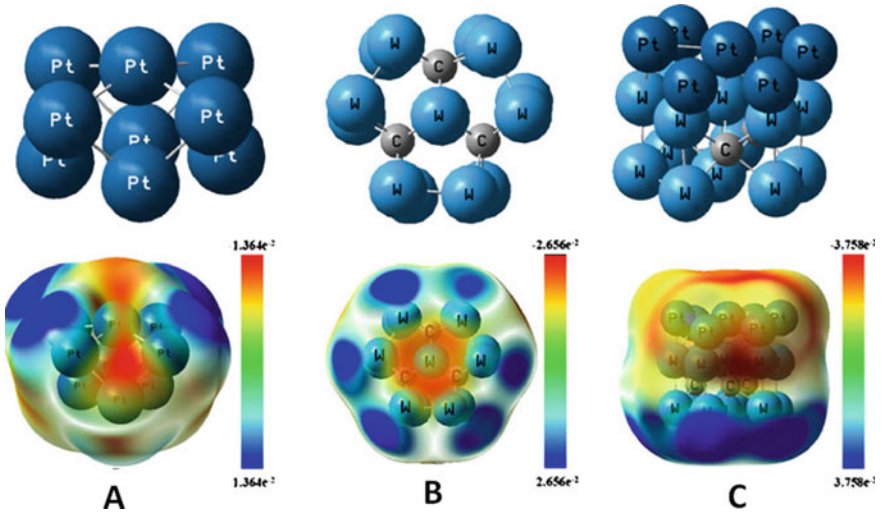

Fig. 4.25 Structure and surface electrostatic potential of various catalysts: **a** Pt_9 clusters, **b** WC, and **c** Pt_7/WC [220]. Reprinted with permission. [220] Copyright (2011) Elsevier

The negative electron density of Pt in the Pt / WC composite structure is as high as –3.758 e^{-2}, which is twice that of pure Pt (−1.364 e^{-2}). This result can be interpreted as the "strong electron-donating" characteristic of the WC carrier which imparts a higher electron density of the Pt cluster, thereby promoting the improvement of its ORR activity.

In addition to tungsten carbide, other transition metal carbides have also been found to have the same synergistic effects as WC, such as molybdenum carbide, vanadium carbide, etc. [221, 222]. In addition, the transition metal bimetallic tungsten carbide has also been found to promote the ORR activity of Pt. Ma et al. [223] adsorbed Mo and Co precursor using an ion exchange resin method, and then prepared a $Co_6Mo_6C_2$/GC composite by a simple heat treatment. Compared with commercial Pt/C catalyst, its ORR activity has been significantly improved, and its half-wave potential has been positively shifted by 80 mV. At 0.9 V, the mass activity of Pt-$Co_6Mo_6C_2$/GC is 271.7 mA $mg^{-1}{}_{Pt}$, which is more than 2.5 times that of commercial Pt/C(108.6 mA $mg^{-1}{}_{Pt}$). In addition, after 1,000 cyclic voltammetry stability tests, the half-wave potential of Pt-$Co_6Mo_6C_2$/GC was only negatively shifted by 6 mV, while the Pt/C was negatively shifted by 27 mV, indicating that the stability of Pt-$Co_6Mo_6C_2$/GC also has great improvement. They believe that this enhancement effect is similar to the enhancement effect between Pt and WC. $Co_6Mo_6C_2$ nanoparticles have the same "electron-donating effect," which leads to the enhancement of ORR activity of Pt nanoparticles.

4.3.3 Graphene and Doped Graphene ORR Co-Catalyst

Graphene is a single-layer graphite sheet that was first discovered in 2004 by Andre Geim and Konstantin Novoselov at University of Manchester, UK [224]. Graphene will form a large delocalized π bond in a two-dimensional plane, making graphene have many peculiar mechanical [145–147] and electronic properties [148–150], such as charge carriers(electrons or holes) have a static mass of zero, and their charge carriers have a high transmission rate in honeycomb crystals of graphene, which can reach three thousandths of the speed of light [151, 152]. These peculiar properties have attracted a large number of scientific and technological workers to study it. For example, people are looking forward to using graphene as a substrate to prepare high-speed nanoelectronic devices. In addition, by changing the stacking or modification of graphene, the band gap, carrier type, and carrier concentration of graphene can be adjusted [153]. These unique properties make graphene a very broad application prospect [154–156].

American scientist Dai et al. reported that graphene and its supported nanoparticles have close bonding and synergistic coupling effects, which further improved the oxygen reduction activity of graphene-based composites [158, 159]. The fast electron power provided by graphene can significantly promote the reaction rate and efficiency of ORR in fuel cells [160]. Shao et al. [161] prepared Pt/GNP and Pt/CNT by depositing Pt nanoparticles on PDDA-modified graphene nanoplatelets (GNP) and CNT. The stability of Pt/GNP is better than Pt/CNT and is 2–3 times better than commercial Pt/C catalyst. They believe that the stability of Pt/GNP results from the high degree of graphitization of GNP and the interaction between Pt and GNP. He et al. [162] loaded Pt nanoparticles on Graphene Quantum Dots (GQDs), and the results confirmed that such GQDs can promote the ORR activity of Pt. They believe that this promotion is due to the fact that defects on GQDs can not only reduce the activation energy of O_2 molecular dissociation through electron transfer between Pt and O_2, but also reduce the energy barrier of this rate-determining step by weakening the binding of HO*. The close relationship between the graphene support and Pt nanoparticles changes the d-band center of Pt, and changes the charge transport kinetics in the ORR process, and thus promotes the ORR activity of Pt [163].

In graphene, the doping of impurity atoms introduced into the framework will change its electronic characteristics and can adjust the band structure of graphene materials [164]. This change in electronic properties and energy bands will greatly change the original properties of grapheme [165]. Bai et al. [166] found that the catalyst formed by supporting Pt with nitrogen-doped graphene can improve its ORR performance in both acid and alkali medium. Vinayan et al. [167] reported that after nitrogen-doped graphene was loaded with Pt (Pt/N-HEG) and PtCo alloy (Pt_3Co/N-HEG) nanoparticles. The Pt/N-HEG catalyst can achieve a power density of 512 mW cm^{-2}, which is more than twice that of commercial Pt/C (241 mW cm^{-2}). The maximum power density of Pt_3Co/N-HEG reaches 805 mW cm^{-2}, which is more than 3 times that of commercial Pt/C.

When graphene and doped graphene support Pt-based ORR catalysts, due to their high specific surface area, high electrical conductivity, and high chemical/electrochemical stability, they are an ideal carrier for Pt-based nanoparticles, which was proved by experimental and theoretical calculations [168, 169]. The effect of the electronic coupling effect between Pt-based nanoparticles and graphene and doped graphene on the ORR activity of Pt-based nanoparticles further increases its application prospect in the design of low-Pt ORR catalysts in the future.

4.4 Non-Platinum Catalyst

Pt-based catalysts are currently the best ORR catalyst. However, due to the expensive price and scarcity of Pt, it is difficult to use them on a large scale as ORR catalysts in fuel cells. Pd is considered to be an ORR catalyst that can replace Pt. Compared with Pt, Pd is a cheaper metal and has richer reserves on the earth. Although the ORR activity of Pd is less than that of Pt, its anti-toxicity performance is better and has better cathodic selectivity, because it is not active in acidic medium for the oxidation of methanol and its intermediates, etc. [170, 171]. In alkaline media, Ag can be used as a cathodic oxygen reduction catalyst [172, 173]. Ag is a cheaper metal and its reserves on earth are much larger than those of Pt and Pd. In addition, other metal materials have also been used for research because of their ORR activity, such as gold [174], nano-gold [175], and ruthenium [176].

Since Jasinski [177] discovered that cobalt phthalocyanine (CoPC) has catalytic oxygen reduction performance in 1964, a large number of researchers have researched to find new and effective cheap transition metal-based oxygen reduction catalysts [178–181]. This type of catalyst is also called non-precious metal catalyst. In addition, some oxides are also active for oxygen reduction, such as Mn_2O_3 [182], Mn_3O_4 [182], MnOOH [183], Co_3O_4 [158], Fe_3O_4 [184], $MnCo_2O_4$ [159]. Moreover, sandwich-structured polypyrrole and $CoFe_2O_4$ nanoparticles [185] have been reported as oxygen reduction catalysts.

4.4.1 Pd-Based ORR Catalyst

The current price of palladium (Pd) metal is only half or less of Pt. Because the ORR performance of Pd in alkaline is comparable to that of Pt, currently, Pd-based non-platinum electrocatalysts have been widely used in cathode reactions of alkaline alcohol fuel cell. In acidic media, the ORR activity of Pd is much worse than that of Pt, which is not enough for direct application to proton exchange membrane fuel cells. The current research focuses on the structural modification, electronic property adjustment and carrier enhancement of Pd to increase its ORR activity. There have been many significant advances in related research and it is expected to be applied and promoted in proton exchange membrane fuel cells.

For nanomaterials, their performance is often determined by structure and morphology. Xiao et al. [186] proved the decisive relationship between Pd nanostructure and ORR activity. By adjusting the solubility of the precursors, they prepared Pd nanostructures with different morphologies by electrodeposition: under the same conditions, they are to electrodeposit in 10^{-5} M $PdCl_2$ solution to obtain Pd nanoparticles(Pd-NPs) and electrodeposit in 3×10^{-4} M $PdCl_2$ solution to obtain Pd nanorods(Pd-NRs). The morphology of Pd-NRs is shown in Fig. 4.26a, b, with a diameter of about 5 nm and a length-to-diameter ratio of about 8. The morphology of Pd nanostructures gradually changed from nanoparticles to nanorods during the increase of $PdCl_2$ solution from 10^{-5} M to 3×10^{-4} M. Compared with traditional Pd-NPs, the ORR activity of Pd-NRs has been greatly improved. As shown in Fig. 4.26c, Pd-NPs and Pt are compared quite ORR performance. The specific activity of Pd-NRs is 10 times higher than that of Pd-NPs, which is equivalent to Pt, as shown in Fig. 4.26d. Erikson et al. [187] prepared 26.9 ± 3.9 nm cubic Pd nanoparticles with ascorbic acid as the reducing agent and cetyltrimethylammonium bromide (CTAB) as the surfactant. Compared with spherical Pd-NPs with a size of 2.8 ± 0.4 nm in

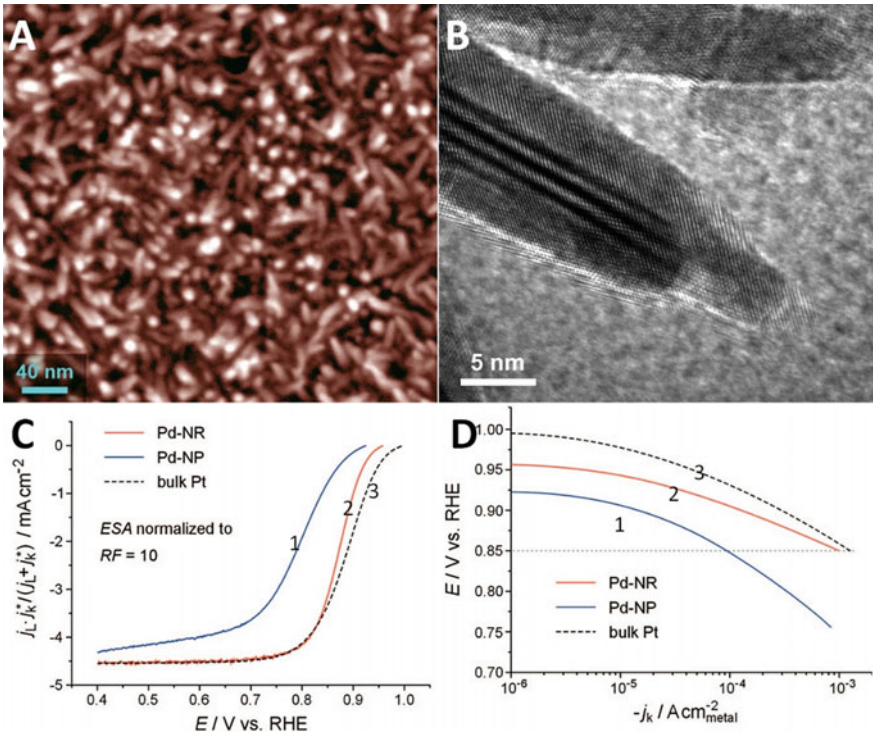

Fig. 4.26 **a** High magnification SEM image of Pd-NRs, **b** High-resolution TEM image of Pd-NRs, **c** ORR performance curve of Pd-NRs (1), Pd-NPs (2) and Pt (3) in O_2 saturated 0.1 M $HClO_4$ solution and **d** Comparison of ORR specific activity of Pd-NRs, Pd-NPs and Pt [186]. Reprinted with permission. [186] Copyright (2009) American Chemical Society

O_2 saturated 0.5 M H_2SO_4 solution, the kinetic current density of cubic Pd-NPs increased three times at 0.85 V (vs. RHE). In addition, in 0.1 M KOH, the dynamic current density of cubic Pd-NPs at 0.95 V (vs. RHE) is also three times higher than that of spherical Pd-NPs [187]. Shao et al. [188] synthesized octahedral and cubic Pd nanocrystals using Cl^- and Br^- as capping agents. The cubic Pd nanocrystals have the best ORR performance, which is equivalent to Pt.

For Pt, its catalytic activity has a large determinant relationship with its atomic structure arrangement [189]. The ORR activity of each crystal plane of Pt has been studied in detail. In a 0.1 M $HClO_4$ solution without strong ion adsorption, the ORR activity of each low-index crystal plane of Pt is as follows: Pt (100) < Pt (111) < Pt (110) [147]. Kondo et al. [148] studied the ORR activity of Pd's low-index crystal planes using a rotating ring-disc electrode (RRDE). The different crystal planes of Pd are obtained by using the reflected beam orientation of the He–Ne laser. After polishing and grinding, anneal it to remove the surface distortion to obtain Pd with different low-index crystal planes, including (111), (100), and (110). Figure 4.27a compares the ORR activities of Pd(111), (100), (110), and Pt (110) crystal planes. It can be seen that the activity of Pd (100) is the highest in 0.1 M $HClO_4$ solution, even exceeding Pt(110). The ORR activity of each low-index crystal plane of Pd is as follows: Pd(110) < Pd(111) < Pd (100). Figure 4.27b compares the ORR activities of the Pt (111), (100), and (110) crystal planes. Table 1 lists the specific activity

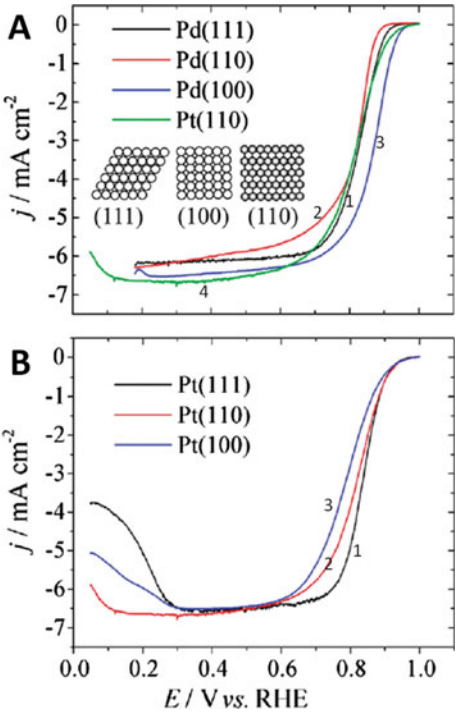

Fig. 4.27 **a** ORR polarization curves of Pd (111)-1, (110)-2 and (100)-3 and Pt (110) crystal plane in 0.1 M $HClO_4$ solution, **b** ORR polarization curves of Pt (111)- 1, (100)-2 and (110)-3 crystal planes [148]. Reprinted with permission. [148] Copyright (2009) American Chemical Society

comparisons of the low-index crystal planes of Pt and Pd at 0.9 V (vs. RHE). The preparation of Pd nanostructures with exposed dominant crystal planes is an effective way to improve the ORR activity of Pd.

Jiang et al. [190] used commercial Pd/C (20wt%, E-TEK) to anneal in a mixture H_2/N_2 (5 vol% H_2) at an annealing temperature of 300 °C, 400 °C, 500 °C, and 600 °C to obtain Pd/C-300, -400, -500, and -600, and Pd nanoparticle sizes increased from 3 to 16.7 nm. When the Pd nanoparticles increased from 3 to 5 nm, their mass activity in the 0.1 M NaOH electrolyte increased to 1.3 times of the original, and then their mass activity decreased as the size of the Pd nanoparticles increased. Since the hydrogen adsorption/desorption region of Pd cannot reflect the active site of the Pd surface, the active surface area (S_{act}) cannot be calculated based on the hydrogen desorption peak of Pd. The S_{act} of Pd can be calculated from the reduction peak of a single-layer oxide (PdO) formed on the surface of Pd particles in the cyclic voltammetry curve of Pd in the electrolyte. The charge constant for PdO reduction is 405 $\mu C\ cm^{-2}$. The specific activity calculated according to S_{act} increases with the increase of Pd particle size. When the size of Pd nanoparticles increases from 3 to 16.7 nm, the specific activity increases three times. Koenigsmann et al. [191] revealed the relationship between the diameter of one-dimensional Pd nanowires and their ORR performance. They used polycarbonate as a template to synthesize ordered self-supporting nanowire arrays of 270 and 45 nm sizes. In addition, they also used palladium nitrate as a precursor, in a solution of octadecylamine and dodecyltrimethylammonium bromide in toluene, and reduced with $NaBH_4$ as reducing agent under an inert atmosphere to obtain 2 nm Pd nanowires, which were then loaded on carbon powder (Vulcan XC-72). In 0.1 M $HClO_4$ solution, when the diameter of Pd nanowires was reduced from 270 to 2 nm, the specific activity at 0.8 V (vs. RHE) doubled from 1.84 to 3.62 mA cm^{-2}. The ORR activity of 45 and 2 nm Pd nanowires is higher than that of commercial Pd/C. The area specific activity of commercial Pd/C at 0.8 V (vs. RHE) is 1.8 mA cm^{-2}. Because the ORR activity of Pd (100) is higher than that of Pd (111), the prepared Pd nanowires are analyzed based on TEM results to show that the crystal surface exposed is (100), while the crystal surface exposed by commercial Pd/C is (111) [198], so the ORR of the prepared Pd nanowires is higher than that of commercial Pd/C.

ORR is a very complicated reaction process, which is related to the composition, structure, and chemical state of the electrode material. Because Pd has a similar crystal structure and electronic structure as Pt, Pd exhibits an ORR activity similar to Pt, but the kinetics of single-phase Pd catalyzed ORR is still relatively slow and it is difficult to achieve commercial application. The introduction of another transition metal for doping modification to form an alloy can significantly change the electronic structure of Pd and improve its kinetics of catalyzing ORR. Yang et al. [217] prepared Pd_3Fe (111) single crystal by sputtering under high vacuum, and then prepared five different Pd_3Fe (111) surfaces under ultra-high vacuum: (1) Pd_3Fe (111) with a rough atomic surface was prepared by sputtering with 1 keV Ar to spray clean Pd_3Fe (111) crystal surface, and the surface content of Fe reached 25%; (2) 0.8 single-layer Fe atoms were precisely dispensed on the Pd_3Fe (111) surface, and then annealed at 1000 K for 20 s to obtain Pd_3Fe (111) with flat atomic surface; (3) Annealed at

1250 K to obtain Pd_3Fe (111) with 11% Fe on the surface; (4) Annealed at 900 K, Pd_3Fe with a surface Fe content of 11% was obtained; (5) Pd_3Fe was annealed at 1000 K, then deposit 0.5 single-layer Pd atoms on it, and then annealed at 900 K to obtain Pd_{ML}/Pd_3Fe (111) with a surface Pd content of 98%. Among them, when annealed at 1250 K, Pd_3Fe (111) has the highest ORR performance. Its half-wave potential ($E_{1/2}$) is positively shifted by 27 mV from Pd_{ML}/Pd_3Fe (111), and is positively shifted by 62 mV than Pd (111). In the voltage range of 0.8–0.9 V (vs. RHE), the kinetic current density of Pd_3Fe (111) obtained by annealing at 1250 K is 2 to 3 times that of Pd_{ML}/ Pd_3Fe (111), and is 5 to 8 times higher than the annealed Pd (111). In PdFe alloys, the content and state of Fe on the catalyst surface play an important role in its ORR performance. The presence of Fe on the surface will affect the adsorption and dissociation of O_2, and these two steps are critical steps in the process of ORR, even rate-determining steps. Although the mechanism of heterogeneous metal incorporation and Pd-forming alloys to enhance ORR performance is still controversial, it can be determined that heterogeneous metal incorporation will change the electronic structural properties of Pd, resulting in different ORR properties. Compared with Pd (111), the d electron center of Pd_{ML}/Pd_3Fe (111) is reduced by 0.25 eV, which significantly reduces the binding energy between O and OH and the catalyst surface, thereby promoting the removal of O and OH through protonation 145]. The synergistic effect of the ORR enhancement of Pd_3Fe (111) with a Fe content of 11% obtained by annealing at 1250 K can be explained by the surface oxygen overflow effect: O_2 adsorption and dissociation at the Fe site, and then overflow to the Pd to be reduced. The calculated structure according to the density functional theory shows that the first O of O_2 dissociated at the Fe position can easily diffuse to the Pd position with an energy barrier of only 0.25 eV, while the second O has a higher diffusion energy barrier to reach with 1.25 eV. This high energy barrier will cause irreversible adsorption on Fe and cause blocking of Fe active sites, but it will not affect the dissociation of O_2 at the corresponding Fe position, because its energy barrier is only 0.4 eV. Furthermore, the next O diffusion at the Fe position is greatly promoted, and the energy barrier is reduced from 1.25 to 0.75 eV. This characteristic keeps the dissociation of O_2 and the diffusion of O in equilibrium, so that the reaction kinetics of ORR are maintained at a very high rate.

Liu et al. [170] prepared carbon-supported PdCo and PdNi nanoparticles by NaBH4 reduction method, and further heat-treated under H_2 atmosphere to obtain carbon-supported PdCo and PdNi nanoparticles with different grain sizes. In 0.1 M $HClO_4$ solution, the ORR activity of carbon-supported PdCo and PdNi nanoparticles obtained after heat treatment can exceed that of Pt/C catalyst. The ORR activity is related to the lattice constant. As shown in Fig. 4.28, the lattice constant of the alloyed Pd can be changed between 0.3802–0.3948 nm. The corresponding specific activity decreases as the lattice constant increases, while the mass activity increases as the lattice constant increases. This change in the lattice constant is thought to affect the d-band center of Pd, and thus the ORR activity. In addition to Fe, Co, Ni, other transition metals Au, Cu, Ir, Mo, etc. can also form alloys with Pd, thereby improving the ORR activity of the catalyst [194–196]. Figure 4.29a shows the relationship between the d-band center (ϵ_d, related to the Fermi level) of Pd, Pd-based alloy and Pt and

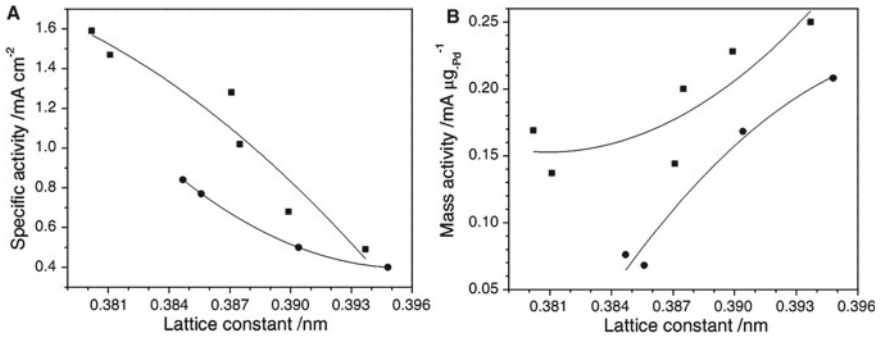

Fig. 4.28 Relationship between **a** area activity and **b** mass activity and lattice constant of PdCo alloy (■) and PdNi alloy (●). [170] Reprinted with permission. [170] Copyright (2014) Springer

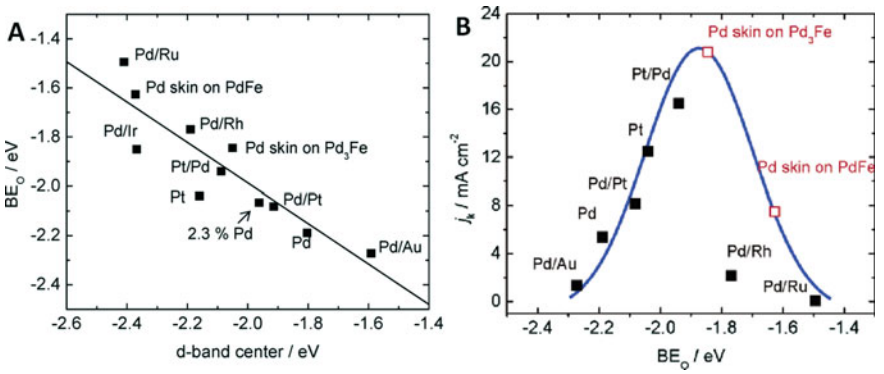

Fig. 4.29 **a** The relationship between the d-band center (ϵ_d, related to the Fermi level) of Pd, Pd-based alloy and Pt and the binding energy of atomic oxygen, **b** Diagram of the binding energy of Pd and oxygen on different single crystal planes and kinetic current density [193]. Reprinted with permission. [193] Copyright (2007) American Chemical Society

the binding energy of atomic oxygen. The binding energy of atomic oxygen is an important factor affecting ORR activity. For the adsorption of oxygen, an increase in ϵ_d will increase the interaction between the 2p state of oxygen and the d state of the metal, forming a stronger metal–oxygen bond. Conversely, a decrease in ϵ_d will form a weaker metal–oxygen bond. The Pd layer on the Ru(0001) and PdFe(111) planes is in the upper left corner of the figure. The value of ϵ_d is very low, indicating that the interaction between oxygen and the Pd layer is weak [197]. While Pd/Au (111) is located in the lower right corner, the value of ϵ_d is high, which indicates that the interaction between the oxygen and Pd layers is strong. The stronger the interaction between Pd–O, the easier the electrons are transferred, and the easier the O–O bond is to split. At this time, the ORR rate control step is the adsorption intermediate state (O and OH) formed after the O–O bond is broken. On the other hand, this weak Pd–O bond facilitates desorption. Therefore, a good ORR catalyst should follow the

Sabatier rule that the metal–oxygen interaction cannot be too strong or too weak, and an appropriate value is needed. The ORR activity of the Pd layer on Ru (0001) and PdFe (111) faces is not good because its kinetics of rate-determining step is slow, while Pd and Pd/Au (111) are too strong for their oxygen binding, which ORR performance is also limited. Figure 4.29b shows the relationship between Pd–O binding energy and kinetic current density on different single crystal faces. On the left side of the figure, the ORR activity of the catalyst increases with the weakening of the metal–oxygen bond, and the ORR kinetics depend on the desorption of the intermediate products. On the Pd layer on the surface of Pd3Fe alloy, the ORR activity reached the maximum, and the binding energy BE_0 at this time was –1.86 eV, which was 0.2 eV weaker than –2.04 eV of Pt, which was consistent with the prediction of Stamenkovic et al. [152]. In addition to binary alloys based on Pd, ternary alloys of Pd have also been studied as modified ORR catalysts. Park et al. [198] prepared and studied 66 ternary alloys Pd-Ir-Ce with impregnation method, and studied their ORR activity in acidic medium to find the optimal component is Pd: Ir: Ce is 79: 12: 9. At 0.85 V (vs. RHE), the ORR activity of $Pd_{79}Ir_{12}Ce_9$/C is 1.5 times that of Pd/C.

Another method to improve the activity of Pd-based ORR catalysts is to add a co-catalyst to produce a synergistic effect with Pd. Li et al. [199] used ion exchange resin to exchange anions in ammonium metatungstate ($(NH_4)_6H_2W_{12}O_{40}$) and sodium cobalt nitrite ($Na_3Co(NO_2)_6$), and prepared graphitized carbon-supported bimetal carbide Co_3W_3C (Co_3W_3C /GC). Finally, a Pd/ Co_3W_3C/GC catalyst was prepared by chemical adsorption/reduction method. In acidic media, the ORR performance test results of this Pd/Co_3W_3C/GC catalyst show that its half-wave potential $E_{1/2}$ is positively shifted by 90 mV from Pd/C and is more positive than commercial Pt/C, as shown in Fig. 4.30a. The mass activity of the Pd /Co_3W_3C/GC catalyst at 0.9 V (vs. RHE) has reached 110 mA mg^{-1}, which exceeds the commercial Pt/C (107 mA mg^{-1}) and is more than seven times of Pd/C (16 mA mg^{-1}), as shown in Fig. 4.30b. They attributed the improved ORR performance of Pd/Co_3W_3C/GC

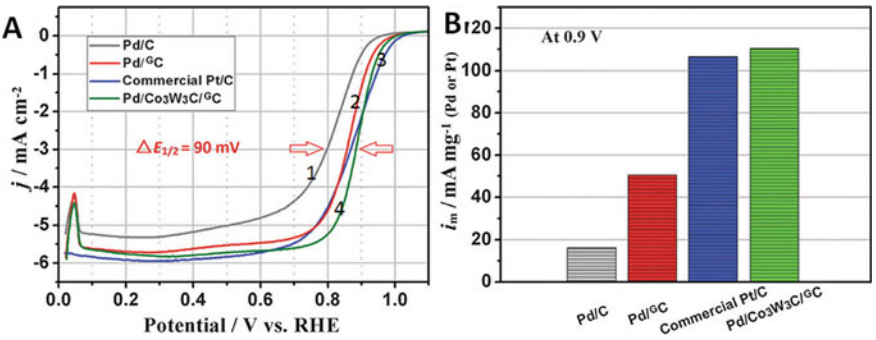

Fig. 4.30 **a** Polarization curves of ORR in 0.1 M $HClO_4$ solution for different catalysts: (1) Pd/C, (2) Pd/GC, (3) Commercial Pt/C, (4) PPd/Co_3W_3C/GC, **b** Comparison of mass activity at 0.9 V of different catalysts [199]. Reprinted with permission. [199] Copyright (2014) The Royal Society of Chemistry

catalysts to the synergistic effect between Pd and Co_3W_3C with electron-donating properties [200]. Yin et al. [171] prepared a WC/C supported PdFe-WC/C catalyst by a interstitial microwave method. In an acidic medium, as a non-Pt catalyst, the ORR performance of this PdFe-WC/C alloy catalyst is comparable to that of a Pt/C catalyst. In addition, in an acidic medium containing 1.0 M ethanol, the ORR performance of the PdFe-WC/C alloy catalyst is almost unaffected, indicating that the PdFe-WC/C alloy catalyst has alcohol resistance and cathodic selectivity, making it have considerable application prospects in direct alcohol fuel cells. They also attributed the improved ORR performance of PdFe-WC/C alloy catalysts to the synergistic effect between Pd, Fe, and WC.

4.4.2 Other Non-Pt Metal-Based (Au, Ru, Ag) ORR Catalysts

The electrochemical reduction of oxygen and hydrogen peroxide on single crystal Au electrodes is a typical reaction with pH effect and structure sensitivity. Blizanac et al. [174] studied the oxygen reduction on the Au (100) surface in 0.1 M $HClO_4$ and 0.1 M KOH media using a rotating ring disk electrode. In an acidic medium, at 0.46 V (vs. RHE), the kinetic current of the Au (100) plane $i_k = 2.74$ mA cm^{-2}; in an alkaline medium, at 0.8 V (vs. RHE), the kinetic current of the Au (100) plane $i_k = 10.93$ mA cm^{-2}. Understanding the energy properties of the Au surface and the correlation between the surface adsorption molecules O_2 and the reduction intermediates is the key to studying the kinetics of the ORR reaction at the Au-solution interface. Combining the study of its K-L curve and Tafel curve, the reaction kinetics of oxygen on the Au (100) surface can be expressed as shown in Fig. 4.31 in the entire pH range:

It can be seen from the above schematic diagram that on Au (100), hydrogen peroxide will be generated before the O–O bond is broken. In addition, hydrogen peroxide may be further reduced to H_2O or may not be reduced, so the rate-determining step is the first electron transfer process: $O_2 + e^- = O_{2,ad}{}^-$ ($E^o = -0.3$ V + $\Delta G_{ad}/F$ *vs* SHE).

Prakash et al. [176] studied the electrochemical reduction of O_2 on Ru electrodes by voltammetry and rotating ring-disk electrode. The current on the ring electrode is the reduction of H_2O_2 under diffusion control. Compared with the reduction of O_2 on the disk electrode, its current is very small and almost negligible, which indicates that the amount of H_2O_2 produced by the reduction of O_2 on the Ru electrode is

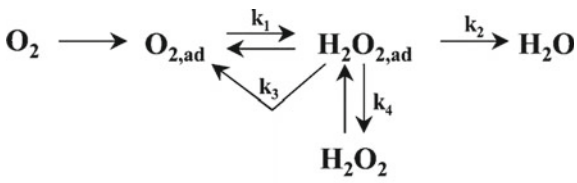

Fig. 4.31 Reaction kinetics of oxygen on Au (100) surface

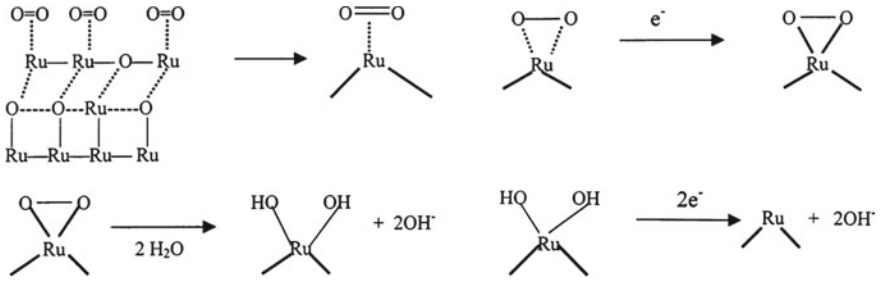

Fig. 4.32 Reduction process of O_2 on Ru electrode [176]. Reprinted with permission. [176] Copyright (2000) Elsevier

extremely small, indicating that the reduction of O_2 on the Ru electrode is a direct four-electron process. During the electrochemical reaction, the surface of Ru appears in the form of an oxidation state. Anastasijevic et al. [220] believed that the oxidation state of Ru surface exists in a sandwich-like form Ru/O/Ru, and they explained that the reduction of O_2 on Ru is through the O–O bridge structure on Ru atoms. The formation and subsequent breaking of the bond is achieved. The side adsorption of oxygen on the electrode surface and the formation of O–O bridged structures require a suitable space for Ru atoms on the surface. In this case, one O_2 molecule is adsorbed on each Ru atom. Because RuO_x on the surface of the Ru electrode is negatively charged, which is not conducive to the adsorption of O_2, which is also negatively charged, thereby the process is followed by a slow first electron transfer process. The interaction of adsorbed oxygen on the surface of Ru metal is shown as the interaction of Ru metal d_z^2 orbitals and π orbitals of peroxy ion, where peroxy ion has the reverse key of π^* from partially filled d_{xy} or d_{yz} orbitals of Ru to oxygen. There is a strong metal–oxygen interaction, this interaction leads to an increase in the O–O bond length, so the break of the O–O bond forms a direct four-electron process of O_2 reduction. The reduction process of O_2 on Ru is as follows (Fig. 32):

Meng et al. [172] prepared a tungsten carbide-reinforced Ag-based catalyst (WC/Ag/C) by a interstitial microwave method. They used WC/Ag/C as an ORR catalyst for the first time. Their research found that in 0.1 M KOH medium, although WC/C and Ag/C both have ORR activity, compared with Pt/C, their activities are very poor, and their overpotentials are very high. However, after recombination, the prepared WC/Ag/C has ORR activity comparable to that of Pt/C, as shown in Fig. 4.33c. Compared with WC/C and Ag/C, the ORR overpotential of WC/Ag/C has dropped significantly. They attribute this enhancement of ORR performance to the synergistic effect between Ag and WC. In addition, WC/Ag/C has good alcohol resistance and cathode selectivity. Because the price of Ag is nearly two orders of magnitude cheaper than Pt, and its earth reserves are very large, the development of Ag-based non-Pt ORR catalysts has great commercial application prospects.

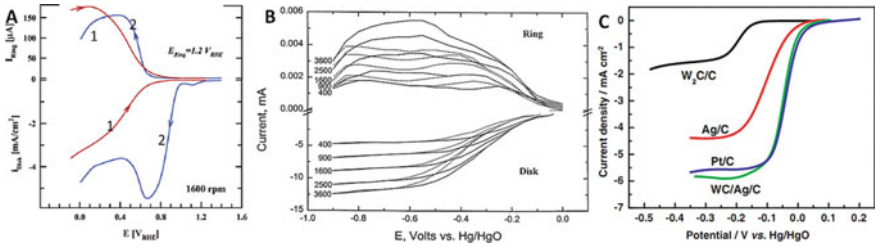

Fig. 4.33 **a** ORR performance of Au(100) electrode in different media: (1) 0.1 M $HClO_4$ solution, (2) 0.1 M KOH [174], Reprinted with permission. [174] Copyright (2004) American Chemical Society. **b** ORR performance of Ru electrode in 0.1 M KOH medium [176], Reprinted with permission. [176] Copyright (2000) Elsevier. **c** Comparison of ORR performance of Ag/C, WC/C, WC/Ag/C and Pt/C catalysts in 0.1 M KOH medium [172]. Reprinted with permission. [172] Copyright (2006) Elsevier

4.4.3 Other Non-Precious Metal ORR Catalysts

Non-noble metal ORR catalysts are low-cost electrocatalysts based on inexpensive metals (such as Fe, Co, Ni, etc.). The research of ORR catalysts based on inexpensive metals has attracted great attention from scientists around the world decades ago. Currently, Me/N/C (Me = Fe, Co, Ni, etc.) is widely studied. Due to the low price and large reserves on the earth, the research on non-precious metal ORR catalysts has special significance for fuel cell applications and is the most promising technical method to achieve its large-scale commercial application and thereby solve human energy and environmental problems.

4.4.3.1 Me-N–C (M = Fe, Co, Ni)-Based Catalyst

It has been found that macrocyclic compounds containing nitrogen-containing transition metals, such as phthalocyanine [201–204], porphyrin [1205], and CoTAA [206], all have electrochemical reduction properties for oxygen. These macrocyclic compounds all have N_4-Me structure. Because this structure can promote the rapid decomposition of the intermediate product H_2O_2 during the O_2 reduction process to achieve the four-electron reduction of O_2, the transition metal macrocyclic compounds containing 4 nitrogen atoms are considered that is hoped to replace Pt as a cathode catalyst for hydrogen–oxygen fuel cells. For this reason, a great deal of research has been conducted on its oxygen reduction effect. The active site of this nitrogen-containing transition metal macrocyclic compound is its planar configuration N_4-Me. Recently, many studies have shown that in addition to the MeN_4 structure, the MeN_2 and MeN_{2+2} structures may also be active sites for oxygen reduction [207]. Therefore, the structure general formula of the active sites of Me/N/C non-noble metal electrocatalysts can be expressed as $Me/N_x/C$(Me = Fe, Co, Ni, Mn,

etc., N is the chelating agent nitrogen x = 2 or 4 or 2 + 2, C is generally sp^2 carbon) (see Fig. 4.34).

Li et al. [213] designed and synthesized an efficient and stable non-precious metal ORR catalyst (Fe-SPc) based on iron phtalocyanine. This Fe-SPc is prepared by a non-pyrolytic method so that its surface properties derived from the structure and material can be appropriately adjusted. Fe-SPc has an initial ORR activity equivalent to that of commercial Fe-Pc, but after 10 cycles of scanning, the current density of Fe-SPc is 4.6 times that of Fe-Pc, and after 100 cycles of scanning, the current

Fig. 4.34 Active site structure of oxygen reduction of **a** MeN4, **b** MeN2 and **c** MeN_{2+2}. [208] (Without copyright)

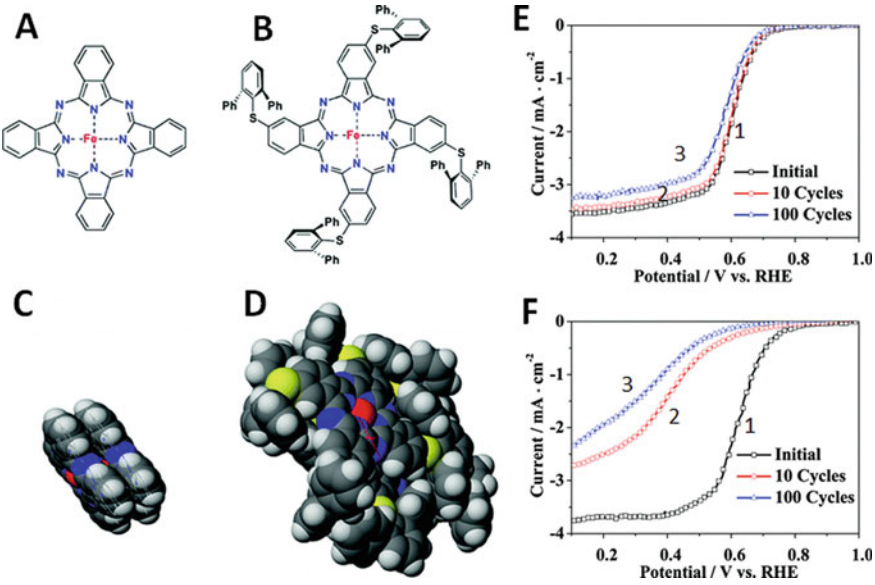

Fig. 4.35 **a** Fe-Pc and **b** Fe-SPc's atomic structure and space stacking mode. Side view of **c** Fe-Pc (d_{Fe-Fe}: 4.119 Å) and **d** Fe-SPc (d_{Fe-Fe}: 6.945 Å), ORR polarization curves of **e** Fe-SPc/KJ300 and **f** Fe-Pc/KJ300 in 0.1 M $HClO_4$ solution, including the initial ORR polarization curve (1) and after 10 cycles (2) and after 100 cycles (3) [203]. Reprinted with permission. [203] Copyright (2010) American Chemical Society

density of Fe-SPc is 7.4 times that of Fe-Pc, as shown in Fig. 4.35e-f. Fe-SPc's high ORR activity and stability stem from the insertion of its electron donor functional groups and the isolation of active sites due to high steric hindrance. Robert et al. [206] prepared CoHPX (cobalt hangman porphyrins) by a simple, fast, and high-yield method, and then fixed CoHPX on multi-walled carbon nanotubes (MWCNTs) to prepare CoHPX-MWCNTs. CoHPX-MWCNTs catalyze the reduction of O_2 to H_2O by a four-electron catalyst through a single co-plane center. Faubert et al. [208] studied the catalytic process of Fe macrocyclic compounds to oxygen and found that the simultaneous existence of Fe and N is necessary for the formation of active center, but it is not certain whether they constitute active center. PEMFC test results show that the open-circuit voltage of this battery is 0.926 V. At a voltage of 0.5 V and a temperature of 50 °C, the output current density of the battery is equivalent to 1/3 of Pt, and this performance can be maintained for 300 h.

Although transition metal macrocyclic compounds have fairly good ORR activity, their poor stability limits their application prospects of cathode catalysts in fuel cell. In 1978, Bagotzky first proposed that non-precious metal electrocatalysts with stable properties were prepared by treating macrocyclic compounds at high temperature [209]. In this study, a macrocyclic compound (cobalt phthalocyanine, tetraphenylporphine, etc.) and a binder Teflon were uniformly mixed and coated on a carbon electrode, and then an oxygen reduction reaction electrode was prepared by high-temperature treatment above 800°C in an inert atmosphere. Studies have shown that the non-noble metal electrode exhibits high oxygen reduction activity and stability in sulfuric acid electrolyte. After that, many research results also proved that the proper heat-treatment process is not only conducive to the improvement of its ORR activity, but also the stability of the catalyst has been greatly enhanced [210–213]. Gojkovics et al. [214] compared the ORR activity and stability of FeTPP/C catalysts obtained by pyrolyzing FeTMPP–Cl (iron (III) tetramethoxyphenyl porphyrin chloride) to FeTPP/C catalysts at a temperature of 200 °C to 1000 °C. The performance of the catalyst prepared under the conditions of 700–900 °C is the best, and the ORR performance under alkaline conditions can be comparable to Pt/C. The improvement of its stability makes it have a high practical application prospect. Further research indicates that the ORR activity of Me/N/C catalysts obtained by pyrolysis depends on different carbon sources (carbon support), nitrogen sources, metal sources, and high-temperature treatment conditions [179, 215].

In 2009, ORR research on Me/N/C made a major breakthrough. Professor Dodelet reported on Science that the ORR performance of Fe/N/C non-precious metal catalyst is very close to commercial Pt/C [216]. They mixed a high specific surface area microporous carbon (BP2000), an iron source(ferrous acetate), and a pore filler (3,4,9,10-fluorenetetracarboxylic dianhydride or 1,10-o-phenanthroline), Then treat at high temperature in NH_3 atmosphere. Because the pore size of microporous carbon is less than 2 nm, fillers and iron sources can form a large number of FeN_{2+2} active sites in the micropores. When performing the full-cell characterization on their ORR performance, they found that when the cell voltage was $\geq$0.9 V, the best Fe/N/C catalyst with a loading of 0.4 mg m^{-2} were prepared by their method, which is equivalent to commercial Pt/C. The best non-noble metal ORR catalyst prepared by

them achieved a kinetic current density of 99 A cm^{-3} at 0.8 V by volume, and the best data previously reported was 2.7 A cm^{-3}, which is very close to the 2010 target (130 A cm^{-3}) set by DOE.

Another breakthrough work was obtained by Wu et al. [217] in 2011. They mixed carbon powder with large specific surface area, PANI-FeCo-C, transition metal precursor (cobalt nitrate or ferric chloride), and short-chain aniline oligomer, and then added $(NH_4)_2S_2O_8$ as an oxidant to completely polymerize the aniline. After polymerization, heat treatment was performed in a nitrogen atmosphere, and the obtained sample was treated in a 0.5 M H_2SO_4 solution at about 80 °C to remove unstable metals. Full-cell performance tests show that the ORR performance of PANI-FeCo-C as a non-noble metal catalyst is comparable to Pt/C. The H_2/O_2 battery using PANI-FeCo-C as the cathode catalyst runs at 0.4 V for 700 h, and there is almost no degradation in performance. At different voltages, when PANI-FeCo-C is characterized by a rotating disk electrode method, its ORR performance does not substantially decrease after 9,000 cycles, and in full-cell characterization, its current density after 30,000 cycles also rarely decrease.

In general, these compounds with catalytic activity must meet the following four conditions: (1) contains a transition metal, mainly Fe, Co, Ni; (2) the source of N can be a metal precursor compounds, N groups on the surface of the modified carbon support, or nitrogen-containing gas in the reactor; (3) the source of carbon is the macrocyclic compound and the support carbon; (4) generally at a high temperature of 800 °C or higher. Although the treatment temperature is low and the catalyst has high catalytic activity, it cannot maintain stability.

4.4.3.2 Me-P–C (M = Fe, Co, Ni) Based Catalyst

P and N are elements of the V_A group, which have the same outer electrons and similar chemical properties. Compared with N, P has a larger atomic radius and lower electronegativity. Density functional theory (DFT) calculations show that when P is doped into single-walled carbon nanotubes (SWCNTs), P can change the electron transport properties of SWCNTs and show stronger adsorption capacity for acceptor molecules(O_2, etc.) [217, 218]. However, compared with the extensive research of Me-N–C system, the research of Me-P–C-based catalysts is still in its infancy.

Wu et al. [219] first prepared carbon powder by hydrothermally hydrothermal method using sucrose as a raw material, then used $Co(NO_3)_2$ as a catalyst precursor, $H3PO_4$ as a P source, and heat-treated at 800° C for 1 h. After 12 h of treatment using a 1 M HCl solution, Co was removed from the sample, and its P doping amount was 1.84%. They compared the ORR performance of the samples before and after the removal of Co, and found that although the pure non-metallic P-doped carbon powder had a much improved ORR performance with the undoped carbon powder, the ORR performance of the P-doped carbon powder with Co has been greatly improved compared with non-metallic P-doped carbon powder, indicating that Co plays an important role in it, as shown in Fig. 4.36. In the process of preparing P-doped carbon powder with Co as a catalyst, P will combine with Co to form a Co-P

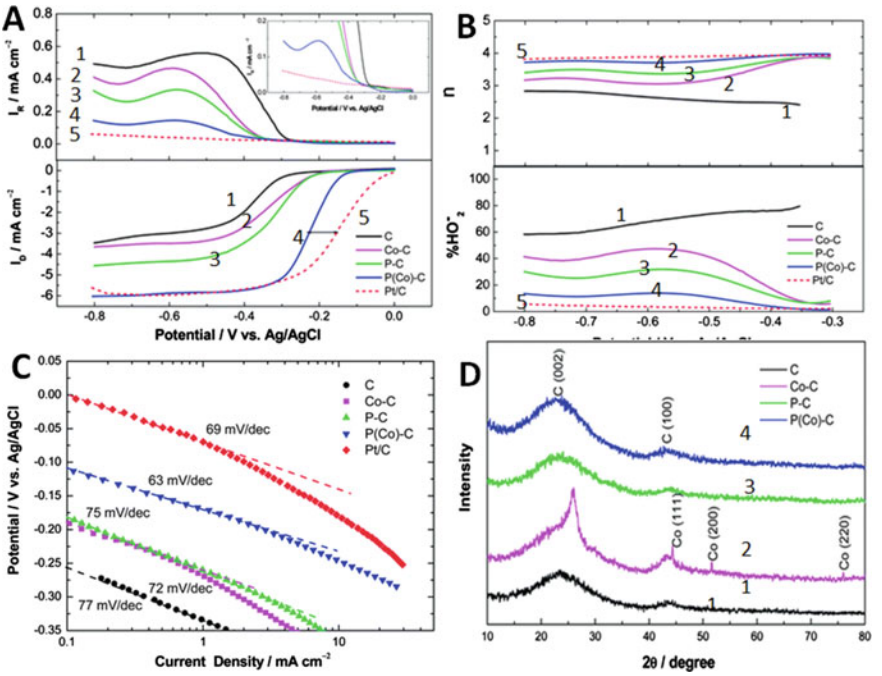

Fig. 4.36 Oxygen reduction polarization curve of **a** C (1), Co–C (2), P–C (3), P-Co–C (4) and commercial Pt/C (5) in O_2 saturated 0.1 M KOH solution with a rotation speed of 1600 rpm and a scan rate of mV s^{-1}, **b** the number of electron transfers and the yield of H_2O_2 calculated from Figure A, **c** Tafel curves of C, Co–C, P–C, P-Co–C and commercial Pt/C, **d** XRD patterns of C, Co–C, P–C and P-Co–C [217]. Reprinted with permission. [217] Copyright (2000) The Royal Society of Chemistry

bond. The formation of this Co-P bond can promote the transfer of electrons to C atoms, thereby reducing the local work function of the C atom surface, which in turn promotes the occurrence of ORR. Thereafter, Wu et al. [200] used the soft template method again, using phenol and formaldehyde as the C source, tetraphenylphosphine bromide ($(C_6H_5)_4P(Br)$) as the P source, cobalt nitrate as the Co source, and F127 (triblock copolymer Pluronic F127) was used as template to prepare mesoporous carbon (MC) doped with P and Co. They believe that this increase in activity comes from the synergistic effect produced when P and Co are co-doped.

Choi et al. [221] heat-treated at 900 °C with dicyandiamide (DCDA), phosphoric acid, cobalt chloride and ferric chloride in an argon atmosphere, to obtain Co-PNC materials with large specific surface areas and various morphologies. In the case of constant N content, an increase in the added amount of P will reduce the degree of carbon crystallization and increase its defectivity. In 1 M $HClO_4$ solution, the ORR on-set potential of this Co-P-N–C material reached 0.6 V (vs. Ag/AgCl). Compared to Co–N-C materials with only N-doping, its mass activity at 0.5 V (vs. Ag/AgCl) has increased from 0.69 mA mg^{-1} to 2.88 mA mg^{-1}, which has increased by four

times. In addition, the incorporation of P can also change the pathway of ORR. Their research results show that the yield of H_2O_2 in the ORR process of Co-PNC is less than 4%, while the H_2O_2 production of P-doped Co–N-C material can reach 10%. Zhu et al. [222] prepared a quaternary Co–N–P–C oxygen reduction catalyst by a one-step method using a cheap aminophosphonic acid chelate resin. They used aminophosphonic acid chelate resin. A simple heat treatment with a mixture of cobalt chloride gave a quaternary Co–N–P–C oxygen reduction catalyst. Compared with Co–N–C and non-metallic N–P–C in 0.1 M $HClO_4$ solution, Co–N–P–C showed better ORR activity and showed good stability.

According to the current research on Me-P–C (M = Fe, Co, Ni)-based catalysts, there is currently research on the characterization of ORR performance of half-cells, and there is still no research on its characterization in full-cells in fuel cells. Moreover, related research is mainly concentrated in alkaline media. Although it has been also reported in acidic media [221], compared with the more in-depth studies of Me-N–C(M = Fe, Co, Ni)-based catalysts, there is still a gap between them. Because the ORR performance of this non-noble metal catalyst has a great relationship with its preparation technology, material structure, chemical composition and other factors, Me-P–C (M = Fe, Co, Ni)-based catalysts still need to be systematically researched to develop higher performance Me-P–C (M = Fe, Co, Ni)-based catalysts. In short, the research on Me-P–C (M = Fe, Co, Ni)-based catalysts has great developing space and potential.

4.4.3.3 Transition Metal Oxide ORR Catalyst

People have been studying the catalytic effect of metal oxides on oxygen reduction. In alkaline media, it has been found that on the surface of Nafion-modified Au electrodes (without MnO_x), the reduction of O_2 is a two-electron process, and the product produced is HO_2^-. In the presence of MnO_x (including Mn_2O_3, Mn_3O_4, Mn_5O_8, and MnOOH), the current density of first reduction peak of O_2 reduction on the surface of the Nafion-modified Au electrode significantly increased, while the reduction peak current of HO_2^- further reduced to of OH^-. And the process of O_2 reduction changes from a two-electron process to a four-electron process, which indicates that MnO_x has the catalytic activity to further reduce HO_2^- to OH^- [183]. Gorlin et al. [182] prepared MnO_x (MnO, Mn_3O_4, Mn_2O_3, and MnO_2) nanoparticles by sputtering and selectively deposited them on a glassy carbon substrate (GC) (see Fig. 4.37). In a variety of MnO_x/GC and MnO_x/pGC (pGC is porous GC) catalysts, 14 nm-sized MnO particles are supported on the pGC carrier compared to the GC. In addition to the increased diffusion limit current, its on-set potential was not improved. When MnO nanoparticles are transformed into Mn_3O_4 nanoparticles, the oxygen reduction catalytic activity of Mn_3O_4/pGC is greatly improved, and its on-set potential is increased to 0.8 V(vs. RHE), and the ORR process becomes completely four-electron process. The specific and mass activities at 0.75 V (vs. RHE) reached 3700 $\mu A \cdot cm^{-2}{}_{cat}$ and 3100 $A \cdot g^{-1}{}_{cat}$.

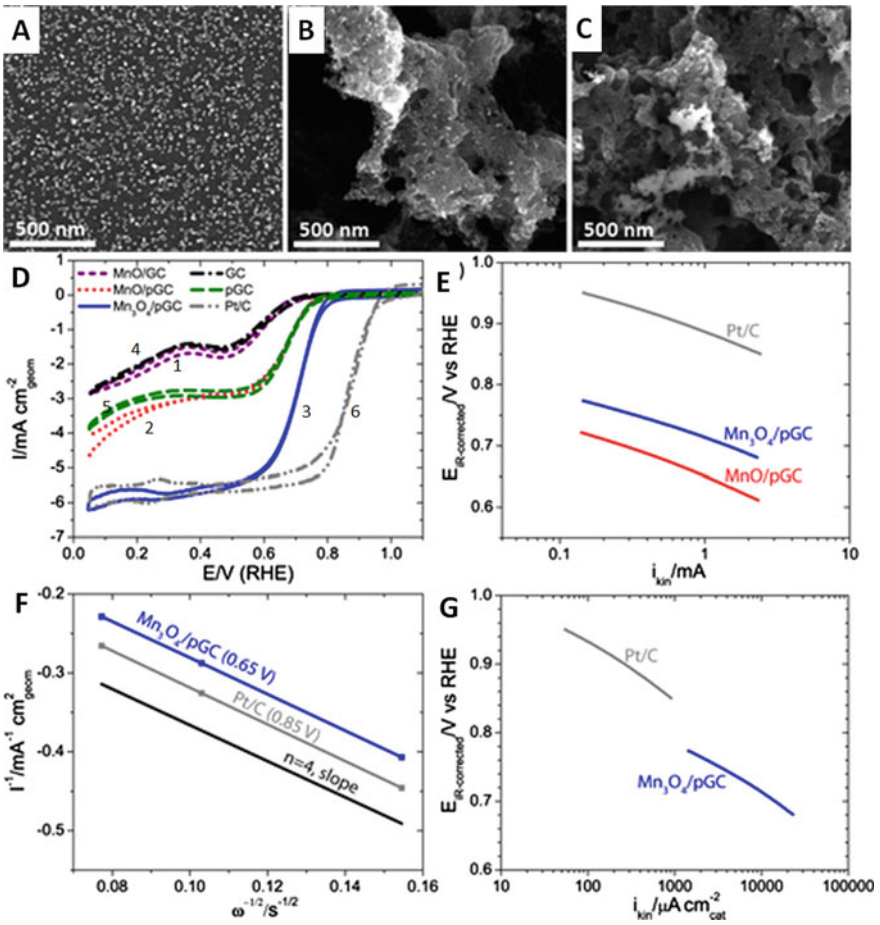

Fig. 4.37 **a** SEM image of 14 nm MnO_x nanoparticles deposited on GC substrate, **b** SEM image of 14 nm MnO_x nanoparticles deposited on pGC substrate, **c** SEM image of MnOx nanoparticles after 500 °C heat treatment, **d** Polarization curve of oxygen reduction of MnO/GC (1), MnO/pGC (2), Mn_3O_4/pGC (3), GC (4), pGC (5) and Pt/C (6) in O_2 saturated 0.1 M KOH solution, with a rotation speed of 1600 rpm and a scan rate of 20 mV s^{-1}, **e** Tafel curve of kinetic current of MnO/pGC 、 Mn_3O_4/pGC and Pt/C, **f** Koutecky–Levich curve of Mn_3O_4/pGC and Pt/C, **g** Comparison of specific activity of Mn_3O_4/pGC and Pt/C [182]. Reprinted with permission. [182] Copyright (2012) American Chemical Society

In addition to MnO_x having ORR activity, some other transition metal oxides, such as Co_3O_4, Fe_3O_4, and $MnCo_2O_4$ also have ORR activity. Liang et al. [158] prepared Co_3O_4 nanoparticles on graphene and nitrogen-doped graphene by a two-step method: firstly synthesize Co_3O_4 on a graphene oxide sheet in a liquid phase, then crystallize Co_3O_4 at 150 °C and reduce graphite oxide. Nitrogen-doped graphene can be obtained by adding NH_4OH during the preparation process. In 0.1 M KOH solution, Co_3O_4/rmGO showed good ORR activity, and its on-set potential reached

0.88 V (vs. RHE), which was greatly improved compared to Co_3O_4. When graphene becomes nitrogen-doped graphene, its ORR activity can be further improved, and its on-set potential can reach more than 0.9 V (vs. RHE). The materials were loaded on teflon-treated carbon fiber paper for full-cell characterization. At 0.7 V, the ORR current densities of Co_3O_4/rmGO and Co_3O_4/N-rmGO reached 12.3 mA cm^{-2} and 52.6 mA cm^{-2}, respectively, which are very close to 68.0 mA cm^{-2} of Pt/C. To reveal this mechanism of activity enhancement, the researchers did X-ray absorption near edge structure (XANES) tests. Compared with N-rmGO, Co_3O_4/N-rmGO has a significantly enhanced carbon K-edge strength at 288 eV, corresponding to carbon atoms in graphene attached to oxygen or other substances [223, 224]. This indicates that Co–O–C and Co–N–C bonds may be formed at the Co_3O_4/N-rmGO interface. As shown in Fig. 4.38, in the K-edge XANES of oxygen, the unoccupied O 2p–Co 3d hybrid state (532 eV [225]) of Co_3O_4/N-rmGO has a significant decrease. Combined with the L-edge of Co XANES peak, compared with pure Co_3O_4 nanocrystals, Co_3O_4/N-rmGO has a higher electron density at the oxygen position and a lower electron density at the Co position, which leads to a higher Co–O ionic bond [226]. The bond formed between Co_3O_4 and N-rmGO and the changes in the

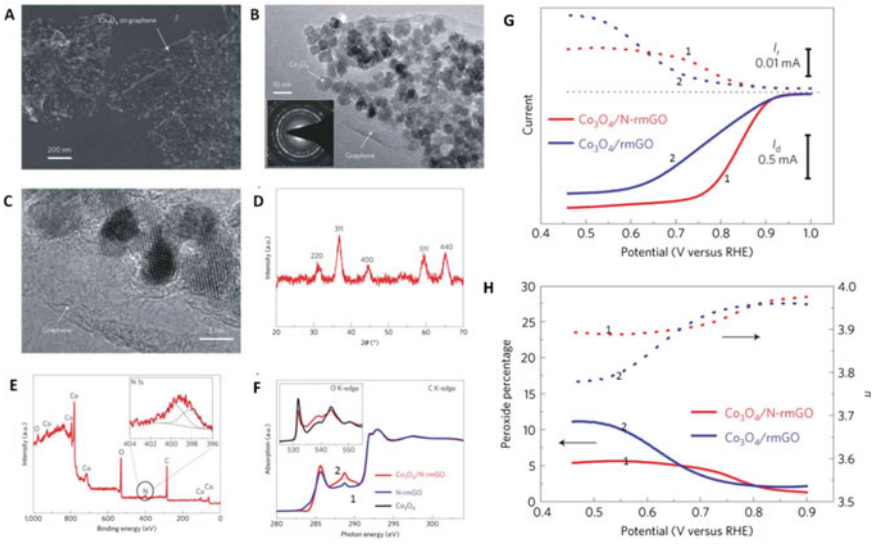

Fig. 4.38 **a** SEM image of Co_3O_4/N-rmGO. **b** Low-magnification TEM image of Co_3O_4/N-rmGO. The illustration shows the selected electron diffraction pattern. **c** High-resolution TEM image of Co_3O_4/N-rmGO. **d** XRD pattern of Co_3O_4/N-rmGO. **e** XPS spectrum of Co_3O_4/N-rmGO, in which the illustration is a high-resolution XPS spectrum of N1s. **f** Carbon K-edge XANES of N-rmGO (1) and Co_3O_4/N-rmGO (2), the illustration of which is its oxygen K-edge XANES, **g** Oxygen reduction polarization curve of Co_3O_4/N-rmGO (1) and Co_3O_4/rmGO (2) in O_2 saturated 0.1 M KOH solution, with the rotation speed is 1600 rpm, **h** The number of electron transfers and the yield of H_2O_2 calculated from G [158]. Reprinted with permission. [158] Copyright (2011) Springer

chemical environment around C, O, and Co are the reasons for the synergy between Co_3O_4 and N-rmGO.

Similar to Co_3O_4/N-rmGO, Liang et al. [144] also prepared spinel $MnCo_2O_4$ and nitrogen-doped graphene composites($MnCo_2O_4$/N-rmGO) by a similar method. Compared with Co_3O_4/N-rmGO, the ORR performance of $MnCo_2O_4$/N-rmGO in 0.1 M KOH solution has been further improved, and it is closer to Pt/C catalyst. They used the same X-ray absorption near edge structure analysis to reveal the synergy between $MnCo_2O_4$ and N-rmGO, and reached similar conclusions. Because of the synergistic effect with nitrogen-doped graphene, the ORR performance of its composites Fe_3O_4 nanoparticles supported on three-dimensional nitrogen-doped graphene aerogel (Fe_3O_4/N-GAs) [184], Mn_3O_4 nanoparticles supported on nitrogen-doped grapheme [227] and so on, has been improved. As an ORR catalyst, this type of transition metal oxide has an ORR activity that is very close to that of a Pt/C catalyst. However, this type of catalyst has a big limitation that its application as an ORR catalyst can only be used in alkaline media, and such materials are unstable in acidic media. However, with the development of alkaline fuel cells, more in-depth research on such materials and exploring such new catalysts with ORR performance closer to or even exceeding Pt/C catalysis have great research and application significance and requirements.

4.4.3.4 Transition Metal Sulfur/Selenide ORR Catalyst

Transition metal sulfides and selenides have very high ORR catalytic activity in acidic media [228, 229], but such catalysts are very unstable under acidic conditions. When the catalyst is run for a period of time, its catalytic activity gradually decreases. The main reason is that S/Se atoms are gradually replaced partially or completely by O. For example, Co_3S_4/C nanoparticles have an ORR open-circuit potential of about 0.67 V in an acidic medium, and have good thermodynamic stability in an air atmosphere at 300 oC. However, due to the poor chemical stability of Co_3S_4/C, Co_3S_4/C will be converted into $CoSO_4$ during operation, which will lead to performance degradation [230].

The process of the ORR reaction that occurs on the transition metal sulfur/selenide surface is as follows:

1. $O_2 + H^+ + e^- + {}^* \rightarrow HOO^*$
2. $HOO^* + H^+ + e^- \rightarrow H_2O + O^*$
3. $O^* + H^+ + e^- \rightarrow OH^*$
4. $OH^* + H^+ + e^- \rightarrow H_2O^{+*}$

Where $*$ is the active position of the reaction, e^- is the electron in the electrode, and H^+ is the proton in the electrolyte. The reaction rate-determining step of the ORR process of the material on the left of the volcano is the reaction of electron/proton conversion to OH^*, that is, reaction step 4. The reaction rate-determining step of the ORR process of the material on the right of the volcano is the step of converting protons and electrons to adsorbed O_2, that is, reaction step 1. Metal Pt is at the top

of the volcano map, and its surface has the highest ORR activity. Among them, the activity of chalcogenide of Rh is the same as that of Ru. The ORR activity of Rh selenide is higher than its sulfide, which is consistent with experimental results [231].

Feng et al. [229] used XC-72 carbon powder as a carrier to prepare Co_3S_4 and $CoSe_2$ nanoparticles without using a surfactant. The obtained composite catalyst particles are small and uniformly supported. In 0.5 M H_2SO_4 solution, the on-set potential of both catalysts can reach 0.7 V (vs. RHE). Nekooi et al. [232] used microwave-assisted/polyol method to prepare CoSe nanoparticles with a particle size of 8 nm on nanopore carbon. Its on-set potential reached 0.823 V (vs. SHE). The calculated results according to the Koutecky–Levich equation indicate that the reaction ORR process is a four-electron process. In addition, such materials are resistant to methanol and formic acid.

4.5 Metal-Free Catalysts

The discovery and research of metal-free catalysts have opened up new approaches and directions to replace precious metal oxygen reduction catalysts. The current research results show that compared with metal-based catalysts, non-metallic oxygen reduction catalysts have unparalleled advantages in terms of stability and anti-toxicity performance, which is a solution to the current stability and anti-toxicity of metal-based oxygen reduction catalysts A new approach to performance issues. At present, the discovery of non-metal catalysts is mainly focused on carbon materials doped with impurity atoms.

4.6 Doped-CNT

Carbon nanotubes (CNTs), also known as Ba based tube, is a one-dimensional quantum material with special structure (radial size is nanometer, axial size is micron, and both ends of the tube are basically sealed) (see Fig. 4.39). CNTs were first discovered by Dr. Sumio Iijima [314], a scientist at NEC laboratory, in 1991 when he observed the cathode deposits of arc evaporated graphite with high-resolution transmission electron microscope. He called the one-dimensional tubular nanostructured carbon nanotubes. It is mainly composed of carbon atoms arranged in hexagon to form coaxial tubes with several to dozens of layers. The fixed distance between layers is about 0.34 nm, the diameter is generally from several nanometers to dozens of nanometers, and the length can reach the order of micrometer or even millimeter. Tang Zikang et al. [315] prepared single-walled carbon nanotubes with a diameter of only 0.4 nm in 2000, and prepared smaller single-walled carbon nanotubes with a diameter of only 0.3 nm in 2008, which is the smallest one found at present [316]. The structure of carbon nanotubes is curled into a cylindrical graphite sheet. Because the carbon atoms in carbon nanotubes are SP^2 hybrid, compared with SP^3 hybrid, the S orbital

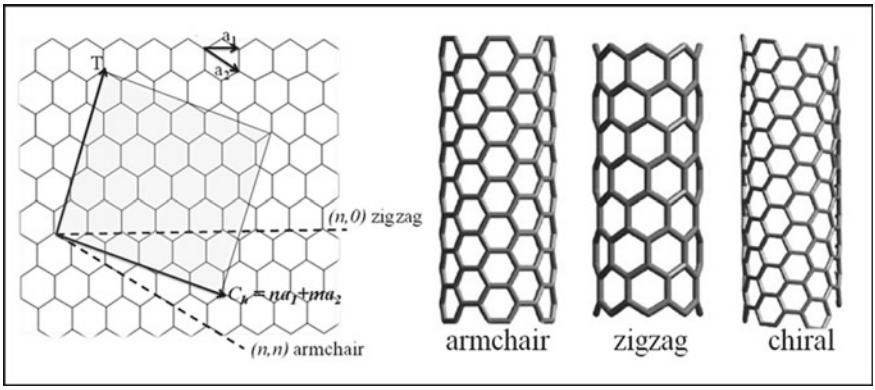

Fig. 4.39 Graphene sheets curl to form three types of CNTs: armchair, zigzag and chiral [326]

component in SP^2 hybrid is larger, which makes carbon nanotubes have high modulus and high strength. CNTs have many excellent properties due to its perfect graphite structure. The research of carbon nanotubes is considered to be a very promising direction for the future development of science and technology. CNTs have excellent electronic conductivity, high thermal conductivity, strong mechanical strength, and large specific surface area, which make CNTs in hydrogen storage [317, 318] and Pt. It has great application prospects in precious metal carrier materials [319], transistors, field emission devices [320], nonlinear optics [321], sensors [322], lithium-ion batteries, super capacitors, and other electrochemical energy storage devices [323–25], especially in the field of new energy materials and environmental science. It is expected to break through the traditional bottleneck in related research, resulting in huge economic and social benefits.

4.6.1 Nitrogen-Doped CNTs

The perfect sp2 structure of CNTs makes its surface chemically inert. In addition, CNTs are hydrophobic and cannot form a homogeneous dispersion system in aqueous solutions [327]. These disadvantages limit their application in many chemical catalysis. However, chemical modification can change the surface state of CNTs and increase their hydrophilicity. In this respect, the surface of CNTs was treated with super strong acid oxidation or oxygen ion sputtering, which made the CNTs surface with clear water functional groups such as carboxyl and hydroxyl groups [328, 329]. The structure of CNTs can be modified by heteroatom doping. NCNTs (nitrogen-doped CNTs) are a kind of doped carbon materials which replace the carbon atoms in the carbon lattice on the wall of carbon nanotubes with nitrogen atoms. After the nitrogen atom enters the SP^2 hybrid structure of CNTs, it can produce local structural defects, which can adjust the structural transformation of CNTs from tubular

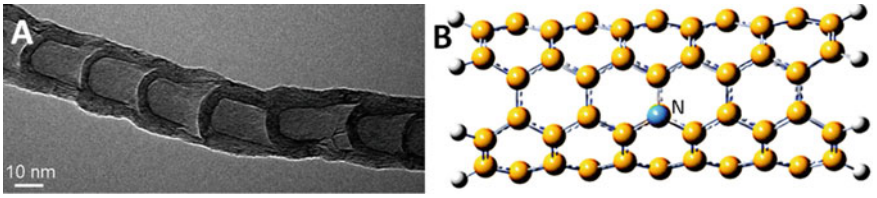

Fig. 4.40 **a** typical TEM of NCNTs, showing bamboo structure [333], **b** NCNTs structure diagram

structure to bamboo-like structure (Fig. 4.40a). In addition, because the nitrogen atom has more outer valence electrons than the carbon atom, the C atom adjacent to the N atom in NCNTs has the property of positive charge distribution, which can effectively change its electronic structure, resulting in better and more unique electronic structure, special physical and chemical properties, which enhance the ability of electron transfer and change its reaction activity [330–333]. There are three main states of nitrogen atoms doped into the CNTs skeleton: pyridine nitrogen, pyrrole nitrogen, and graphite nitrogen. The corresponding binding energies are 398.55, 400.04, and 401.10 eV, respectively [332]. A pyridine-type nitrogen atom refers to a nitrogen atom formed at the edge or defect of a graphite plane and is connected to two carbon atoms to form a six-membered ring. The nitrogen atom provides a P electron to the conjugated π-bond system, and the remaining pair of lone electrons. During the oxygen reduction process, it can adsorb O^2 molecules and their intermediates; a nitrogen atom of the pyrrole-type graphite forms a five-membered ring connected to two carbon atoms at the edge or defect of the graphite, with two p electrons and conjugated to the π bond system. The nitrogen atom of graphite type refers to completely replacing the carbon atoms in the sp2 hybrid six-membered ring in graphite, which is connected to three carbon atoms to form a six-membered ring. Since the outer layer of the nitrogen atom has one more valence electron than the carbon atom, the existence of graphite-type nitrogen atoms in CNTs will make NCNTs have a positive charge effect, which can significantly enhance their catalytic oxygen reduction activity. It is worth noting that the pyrrole-type nitrogen atoms are sp3 hybridized bonds, while the pyridine- and graphite-type nitrogen atoms are sp2 hybridized bonds.

4.6.1.1 Oxygen Reduction Performance of NCNTs

Dai et al. [334] of Dayton University, Ohio, found in 2009 that nitrogen-doped carbon nanotube arrays (VA NCNTs) can be used as efficient and stable oxygen reduction catalysts. By placing a compound containing carbon, nitrogen, and iron on a quartz substrate and then heating it in ammonia, they generate VA-NCNTs that grow perpendicular to the surface of the substrate. The structure of X-ray photoelectron spectroscopy (XPS) shows that the doping amount of nitrogen atom is 4–6%. In order to test the intrinsic catalytic activity of VA-NCNTs for oxygen reduction, the residual

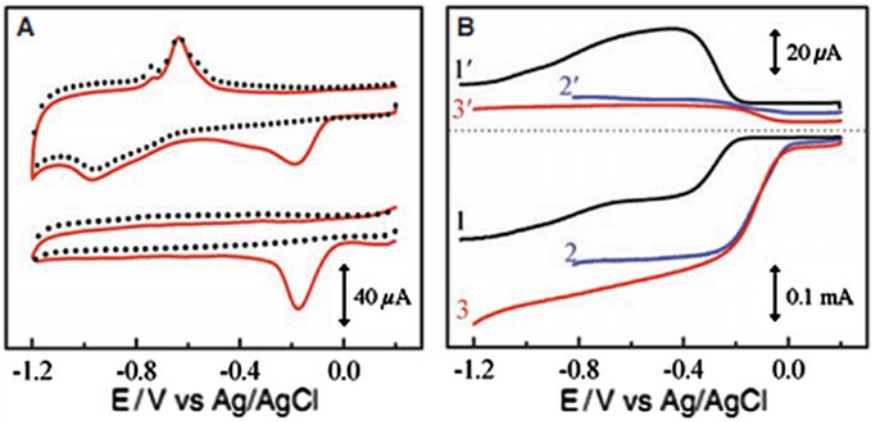

Fig. 4.41 **a** cyclic voltammograms of 0.1 M KOH in saturated argon (dotted line) and saturated air (solid line) at the unpurified (curve above) and electrochemically purified (curve below) VA-NCNTs / GC electrodes, **b** Oxygen reduction polarization curves of undoped carbon nanotubes VA-NCNTs/GC) (curves 1 and 1'), Pt-C / GC (curves 2 and 2′), and NA-NCNT/GC (curves 3 and 3'), at 0.1 M KOH [335]

iron in the nanotube array was completely removed by electrochemical method and then used as oxygen reduction catalyst. As shown in the curve at the lower part of Fig. 4.41a, the characteristic peak of VA-NCNTs iron at about –0.6 V (vs. Ag / AgCl) disappears after removing iron by electrochemical method. When the solution is saturated with N^2, the VA-NCNTs cyclic voltammetry curve is a non-characteristic square curve, which shows the characteristics of charge and discharge of a double-layer capacitor. When the solution is saturated with air, there is a reduction peak near - 0.2 (vs. Ag / AgCl), which indicates that VA-NCNTs has oxygen reduction activity. In 0.1mkoh electrolyte, they found that the steady-state current density was 4.1 mA cm^{-2} at - 0.22 V (vs. Ag / AgCl) on VA-NCNTs electrode, and 1.1 mA cm^{-2} at - 0.20 V (vs. Ag / AgCl) on Pt / C catalyst. They attributed the high activity of the n-doped nanotube catalyst to the ability of the nitrogen atom to capture electrons, which makes the carbon atom adjacent to it have a net positive charge, so it is easy to attract electrons from the anode to promote the oxygen reduction reaction.

ORR is a multi-step reaction involving many intermediates and depends on electrode materials, catalysts, and electrolytes. In alkaline medium, there are two reaction processes: direct four-electron and indirect dielectronic reaction.

Direct four-electron reaction: $O_2 + 2H_2O + 4e^- \rightarrow 4OH^-$.

Indirect dielectronic reaction:

$$O_2 + H_2O + 2e^- \rightarrow HO_2^- + OH^- \tag{4.1}$$

$$HO_2^- + H_2O + 2e^- \rightarrow 3OH^-$$

The direct four-electron reaction has low overpotential and high conversion efficiency, However, the over potential of indirect dielectronic process is high and the conversion efficiency is low, and the hydrogen peroxide ion (HO^{2-}) will cause serious corrosion to the proton exchange membrane in the membrane electrode assembly (MEA), which makes the performance of MEA decline rapidly. The number of electronic reactions (n) of each oxygen molecule reduced by oxygen can be calculated by the following formula [336]:

$$n = 4I_d/(I_d + (I_R/N)) \tag{4.2}$$

$$i^{-1} = i_k^{-1} + i_L^{-1} \tag{4.3}$$

where N represents the collection efficiency of the rotating ring disk electrode, I_d is the Faraday current on the surface of the disk electrode, I_R is the Faraday current on the surface of the ring electrode, i is the current obtained from the experimental test, i_L is the diffusion limit current, and i_k is the dynamic current on the surface of the electrode. In addition, n can also be calculated by K-L equation [337]:

$$i_k = nFAK_{cat}C_0. \tag{4.4}$$

$$i_L = 0.620nFAD_0^{2/3}\omega^{1/2}\upsilon^{-1/6}C_0 = B\omega^{1/2} \tag{4.5}$$

where, F represents Faraday constant ($F = 96{,}485\ Cmol^{-1}$), A is the area of electrode, K is the constant of electron transfer rate ($k = 0.1\ cm^2\ s^{-1}$), Γ_{cat} is the catalyst load on the electrode surface, C_O is the solubility of O_2 ($C_O = 1.2 \times 10^{-3}$ M in 0.1 M KOH), υ is the kinematic viscosity of 0.1 M KOH solution (($\upsilon = 0.1\ cm^2\ s^{-1}$), ω is the rotational angular velocity of disk electrode, D_0 is the O_2 at 0.1 M KOH solution diffusion coefficient ($D_0 = 1.9 \times 10^{-5}\ cm\ s^{-1}$). The electron transfer numbers of VA-CNNTs and VA-NCNTs catalysts calculated by Eq. (4.2) are 1.8 and 3.9, respectively. It shows that the catalytic oxygen reduction of VA-NCNTs is a four-electron process [337], while VA-NCNTs is a two-electron process.

As we all know, in the practical application of fuel cells, the anode fuel (such as methanol) and intermediate products (such as CO) will reach the cathode through the proton exchange membrane, resulting in the mixed reaction of the cathode and catalyst poisoning, making the performance of fuel cells rapidly decline [338]. However, at present, Pt-based catalysts are not selective, which is easy to produce mixed potential and catalyst poisoning caused by intermediate products [339]. Figure 4.42a compares the effects of CO on VA-NCNTs/GC and Pt-C / GC catalysts. It is clear that when CO is injected into the electrolyte, the surface current of Pt-C / GC catalyst drops rapidly, which is because the active site of Pt surface is occupied by CO, so that its ORR activity drops sharply. However, CO had no effect on the ORR activity of VA-NCNTs / GC. In addition, the ORR stability of NCNTs is better than that of Pt-C catalyst. Due to Ostwald ripening, Pt nanoparticles will grow up and agglomerate

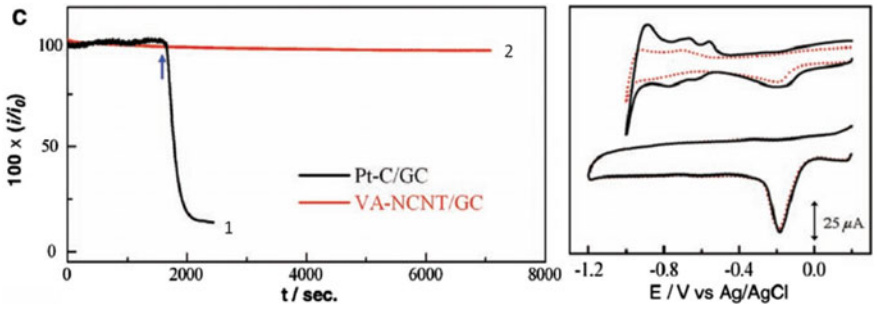

Fig. 4.42 **a** chronoampelarization curves of Pt-C/GC (1) and VA-NCNTs/GC (2) catalysts against Co, **b** VA-NCNTs / GC (below) and Pt-C/GC (above) catalyst cycle scan ~100,000 times stability comparison [335]

in the process of ORR reaction, resulting in the decrease of electrochemical active area, thus the performance of ORR will decline [339]. Because of the stability of NCNTs and C-N structure, NCNT can maintain good stability in the process of ORR reaction.

The enhancement of ORR activity of NCNTs is due to the change of electronic structure caused by the doping of N atom in CNTs, so the activity of NCNTs should be related to the content and form of N atom. Sun et al. [341] studied the effect of nitrogen content on the oxygen reduction performance of nitrogen-doped carbon nanotubes. They controlled the nitrogen content in carbon nanotubes by adjusting the amount of melamine added during the growth of carbon nanotubes. Their research has shown that their oxygen reduction performance increases with the increase of

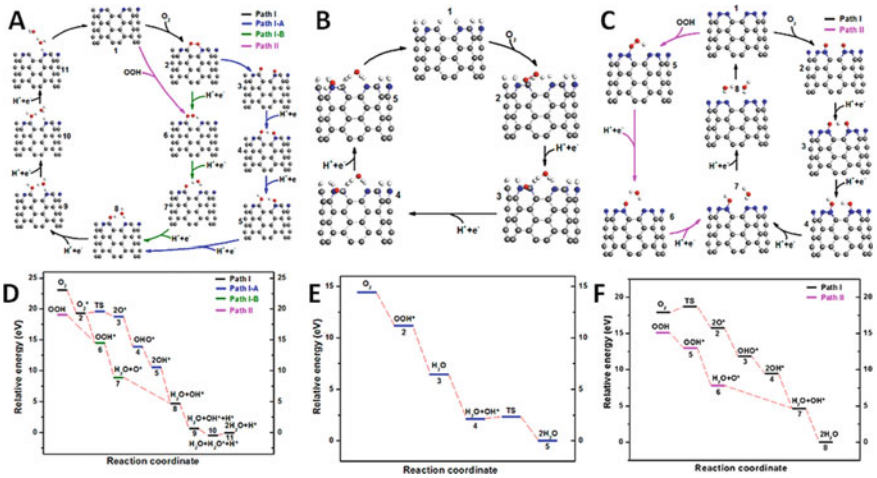

Fig. 4.43 **a-c** possible catalytic ORR reaction steps of C − N, HN − CNT, and FN − CNTs bond active sites, **d-f** corresponding reaction energy barrier [361]

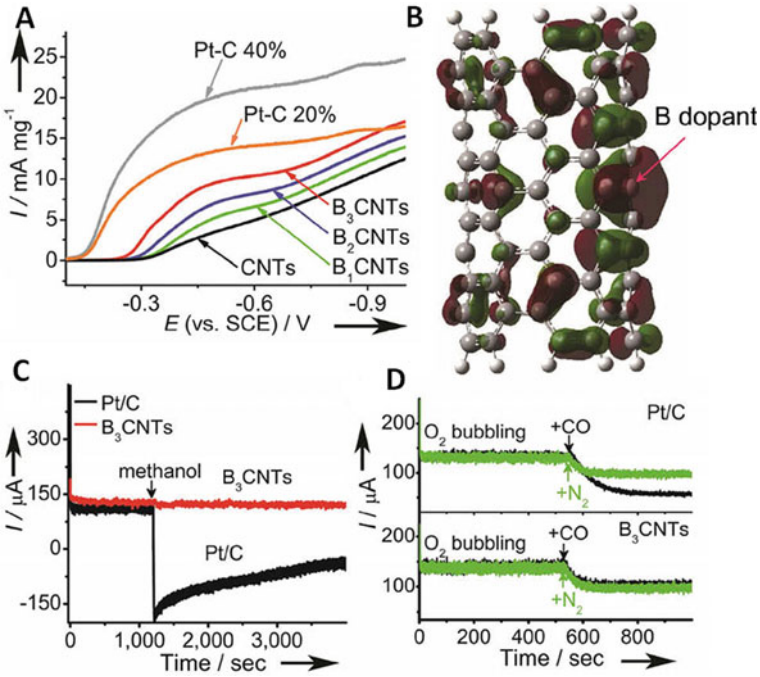

Fig. 4.44 **a** Oxygen reduction polarization curve of BCNTs and Pt/C at 0.1 M NaOH, **b** HOMO-1 of BCNTs (5,5), **c** Chronoampelarization curves of BCNTs and Pt/C catalysts against methanol in 0.1 mol L^{-1} NaOH solution saturated with O^2, **d** Chronoampelarization curves of BCNTs and Pt / C catalysts against CO in 0.1 mol L^{-1} NaOH solution saturated with O^2 [371]

nitrogen content in the catalyst under the same conditions. Zhu et al. [332] used melamine (C3H6N6) as the precursor to prepare NCNTs with high N content, and the nitrogen content was close to 20%. When using these NCNTs with high N content for ORR catalyst, its ORR performance did not improve compared with that of NCNTs with low content [334, 342]. In the case of very low N content, NCNTs still has considerable ORR performance. Borghei et al. [343] coated CNTs treated with polyaniline (PANI) at high temperature to obtain NCNTs with N content as low as 0.56%, still showing considerable ORR activity. The ORR properties of NCNTs with different N content are listed in Table 4.1.

Table 4.1 Comparison of kinetic current density of different crystal planes of Pt and Pd at 0.9 V (vs. RHE) in 0.1 M $HClO_4$ solution [148]. Reprinted with permission. [148] Copyright (2009) American Chemical Society

Pt (hkl)	$j_{ORR,0.9\ V}$/mA cm^{-2}	Pd (hkl)	$j_{ORR,0.9\ V}$/mA cm^{-2}
(100)	1.67	(100)	0.43
(111)	0.12	(111)	0.59
(110)	0.4	(110)	0.60

Table 4.2 Comparison of ORR kinetic current density of different catalysts in 0.1 M $HClO_4$ solution

Catalysts	j_k[a]/mA cm^{-2}			
	$E_{1/2}$ mV	900 mV	850 mV	800 mV
Annealed $Pd_3Fe(111)$, 1250 K	877	1.62	8.99	26.5
Annealed $Pd_3Fe(111)$, 900 K	858	1.18	6.85	20.6
Pd monolayer on $Pd_3Fe(111)$	845	0.741	3.73	11.84
Pt(111)	850	0.921	3.94	16.2
Pd(111)	815	0.221	1.55	5.92
Sputtered $Pd_3Fe(111)$	822	0.372	2.03	7.02

j_k[a]: kinetic current density

4.6.1.2 ORR Performance of NCNTs in Acid

The research on the oxygen reduction performance of nitrogen-doped carbon nanomaterials mentioned above is carried out in the alkaline electrolyte. Although gratifying progress has been made, the performance of the alkaline fuel cell will decline sharply due to the CO_2 in the air and the carbonate produced by the alkaline medium in the alkaline fuel cell. In addition, the development of the alkaline fuel cell is limited due to the immature technology of the alkaline proton exchange membrane. It is more urgent for the commercialization of fuel cell to find an oxygen reduction catalyst which can replace Pt in acid.

Dai et al. [352] prepared metal-free catalyst nitrogen-doped SWNTs by plasma etching technology. They studied the nitrogen-doped SWNTs at 0.5 M H_2SO_4. Compared with the undoped CNTs, the performance of nitrogen-doped SWNTs has been greatly improved, but there is still a big gap compared with Pt / C catalyst. Jiang et al. [353] coated silicon wafer with 100 nm thick silicon, then deposited iron (II) phthalocyanine as catalyst and carbon source at 850 °C for 2 h in Ar, H_2, and NH_3 atmosphere, and finally removed Fe. Although the obtained nitrogen-doped carbon nanotube arrays (VA-NCNTs) have obvious oxygen reduction characteristics, the overpotential is still more than 200 mV different from that of Pt / C catalyst. Lyth et al. [354] used diethanolamine as a precursor to prepare graphene foam by hydrothermal method. After high-temperature heat treatment, nitrogen-doped graphene foam was obtained. In 0.1 M $HClO_4$ solution, the peak potential of this nitrogen-doped graphene foam can reach 0.82 V, but the current density is small, and the gap is very large compared with the Pt/C catalyst.

4.6.1.3 Preparation of NCNTs

Since J. bernholc et al. [355] studied the doping of CNTs in 193, researchers have invented many methods to prepare NCNTs, such as chemical vapor deposition (CVD), solid phase growth, arc discharge, laser evaporation, high-temperature

cracking, ball milling, and hydrothermal method. These methods can be summarized in two ways: one is to dope n simultaneously in the process of synthesis of CNTs, which is called in situ method; the other is to carry out post-processing on the synthesized CNTs to achieve N-doping, which is called post-processing [343]. In the process of in-situ doping, N atoms from the precursors are incorporated into the framework of CNTs in the process of CNTs growth. N atoms can come from different precursors, such as transition metal macrocycles [344], ammonia [356], acetonitrile [357], pyridine [358], melamine [236] and polymers. This in-situ doping method usually requires the use of transition metals such as Fe, Co, Ni, Mn as catalysts for NCNTs growth. After heat treatment, simple acid treatment can not completely remove these transition metals, which have a great impact on the ORR performance of the samples [344, 359]. In order to avoid the influence of these transition metals on ORR performance, acid treatment and electrochemical treatment should be carried out before electrochemical test, which may damage the structure of NCNTs and the N in NCNTs. The preparation of NCNTs by heat treatment of purified CNTs and N-source precursors without transition metals can effectively avoid the influence of transition metals in the synthesis process. The precursors of this post-treatment method include ammonia [342], urea [351], dicyandiamide, polyaniline (PANI) [343, 350], polypyrrole [360], etc.

Different methods of preparation will affect the morphology, structure, specific surface area, nitrogen content, nitrogen doping form of NCNTs, etc. These characteristics will affect the ORR performance of NCNTs. Table 4.3 lists the NCNTs prepared by different methods. These NCNTs prepared by different methods show different ORR properties. Finding a method for preparing NCNTs with the best ORR performance has become a research hotspot in this field.

4.6.1.4 ORR Mechanism of NCNTs

Until now, there is no perfect explanation for the enhancement mechanism of nitrogen-doped carbon materials on oxygen reduction performance, but it is certain that the nitrogen atoms and their bonding states play a decisive role in oxygen reduction performance. Dai et al. [334] thought that nitrogen of pyridine type and pyrrole type played an important role in the process of oxygen reduction, and through DFT (density functional theory) calculation shows that the substitution of nitrogen atom for carbon atom will lead to the change of asymmetric spin density and atomic charge density, and make the carbon atom near it have net positive charge, thus the adsorption mode of oxygen molecule changes from Pauling mode on carbon nanotube to bridge mode on nitrogen-doped carbon nanotube, weakening the O = O bond, which is conducive to the dissociation adsorption of oxygen. This kind of charge transfer can promote oxygen reduction reaction. Gao et al. [361] used the spin polarization density function theory of the first principle to study the process of ORR catalyzed by NCNTs open boundary. O_2 and OOH can be chemically adsorbed on the C-N bond at the NCNTs boundary without energy barrier, and can be partially reduced; the adsorbed O_2, OOH, and H^+ in the surrounding environment can be combined

Table 4.3 ORR activity comparison of NCNTs catalyst reported in literature

Method	Precursor of N	Nitrogen content (at.%)	Electrolyte	Peak potential (vs. Ag / AgCl)	n_e	References
In situ synthesis	pyrolyzing iron(II) phthalocyanine (FePc)	4–6	0.1 M KOH	0.02,	3.9	[334]
	Melamine	20	0.1 M KOH	−0.1,	2.6	[315]
	melamine	8.4	0.1 M KOH	−0.1	3.7	[316]
	Poly(2-methyl-1-vinylimdazole)	~8	0.5 M H_2SO_4	−0.05	3.8	[346]
	Acetonitrile	1.37	0.1 M KOH	−0.085	–	[317]
	sodium 4-[4′-(dimethylamino)phenyldiazo]phenylsulfonate	5.2	0.1 M KOH	−0.021	3.92	[318]
	Pyridine	3–6	0.1 M H_2SO_4	−0.1	2.7−3	[319]
Post-treatment	Ammonia	2.9–6	0.1 M NaOH	0.05	–	[342]
	Polyaniline	7.6–3.3	0.4 M HCl	–	–	[320]
	Urea	5	0.1 M KOH	−0.05	3−3.5	[321]
	Polyaniline	0.56	0.1 M KOH	−0.03	3.74	[332]

and reduced to form two H_2O molecules without energy barrier. The energy barrier of 0.49 eV is required to complete the catalytic process in the second H_2O molecule desorption process, so the desorption of H_2O is a rate-determining step. On the boundary HN-CNT site, the formation of ORR and H_2O can be completed efficiently. For the FN-CNTs sites where both C atoms at the boundary are replaced by N atoms, the reduction and dissociation of O_2 need to overcome the energy barrier of 0.81 eV, and the formation of H_2O is spontaneous at the same time; ooh can adsorb and reduce on the N–N bond in FN-CNTs, and then generate H_2O spontaneously.

4.6.2 Boron-Doped Carbon Nanotubes

When the N atom with one more valence electron than the C atom is doped into the π bond formed by SP^2 hybrid structure of CNTs, the extra electrons provided by the N atom will enhance the electronic density of the system and increase the maximum energy level of Homo of SP^2 hybrid C atom, thus promoting the ORR reaction. When the B atom with few electrons is doped into CNTs to form boron-doped CNTs (BCNTs), the delocalized π electrons in the conjugated system act on the 2pz space orbit of B, resulting in electron accumulation, which can also promote ORR [362]. Ma et al. [363] prepared BCNTs with B content of 0–2.13% by chemical vapor deposition (CVD) with benzene, triphenylborane, and ferrocene as precursors. With the increase of B content, the morphology of BCNTs changed from hollow structure of CNTs to bamboo-like structure, then to twisted nanotubes. The analysis of XPS results shows that the performance of BCNTs is much better than that of CNTs, and the performance of BCNTs increases with the increase of B content. In addition, like ncnts, BCNTs are inert to methanol, CO, and other fuels or intermediates, and it is also an ORR catalyst with cathode selectivity and anti-toxic performance. Different from NCNTs, in NCNTs, the adsorption of O^2 occurs on the C atom with positive charge distribution adjacent to the N atom, while in BCNTs, the adsorption of O^2 occurs on the B atom with doping. B in BCNTs has one less valence electron than C. In BCNTs, the delocalized π electron in the conjugated structure of C will transfer to the doped B atom. This charge transfer can make O^2 chemically adsorb on the B atom as a bridge; in addition, it can weaken the O–O bond, thus promoting the occurrence of ORR.

4.6.3 Doped Graphene

Graphene was first discovered in 2004 by Andre Geim and Konstantin Novoselov, University of Manchester in the United Kingdom [363]. Graphene is a single-layer SP^2 hybrid carbon structure and the basic unit of graphitic carbon. Graphene can form many kinds of graphite allotrope. For example, it can be rolled up to form zero-dimensional materials such as C_{60} fullerenes, or it can be rolled up to form

one-dimensional carbon nanotubes (CNTs), and multilayer graphene is stacked to form graphite, as shown in Fig. 4.45. Since its discovery, graphene has attracted more and more researchers to participate in the research of graphene, and because of its unique structure, graphene has many unique mechanical [364–366] and electronic properties [367–370], For example, the static mass of charge carriers (electrons or holes) in graphene is zero, and its charge carriers have a high transmission rate in graphene honeycomb crystals, which can reach three thousandths of the speed of light [36, 371].

In graphene, the doping of impurity atoms will change its electronic properties and adjust the band structure of graphene [372, 373]. The change of electronic properties and energy band will greatly expand the application of graphene-based materials. Through the incorporation of nitrogen, boron, sulfur, and other atoms into the skeleton of graphene, these doped graphene materials show excellent catalytic oxygen reduction performance [374–376].

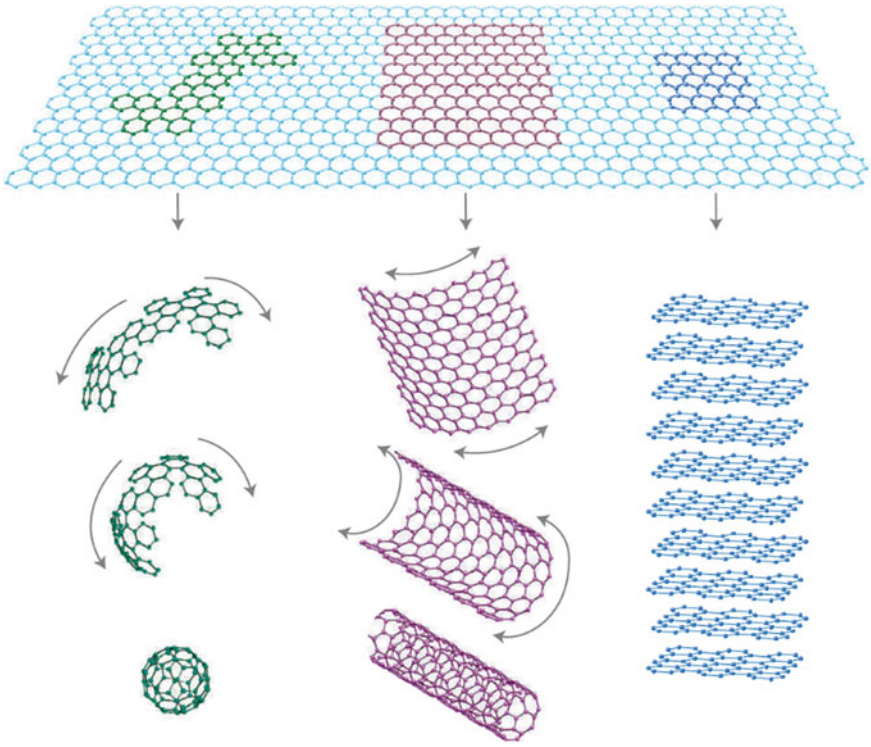

Fig. 4.45 carbon allotropes of fullerene, carbon nanotubes, graphite, etc. with graphene as the basic unit [36]

4.6.4 Nitrogen-Doped Graphene

4.6.4.1 Oxygen Reduction Properties of Nitrogen-Doped Graphene

In 2010, Qu et al. [377] found that nitrogen-doped graphene (N-graphene) has the ORR performance similar to nitrogen-doped carbon nanotubes, which opened the prelude of graphene as a non-noble metal ORR catalyst. He et al. [378] successfully prepared less than three layers of N-graphene (Fig. 4.46a) by using the resin containing cyano (-CN) (propylene cyanogen, stilbene, allyl trinitrate copolymer) and $CoCl_2.6H_2O$ as the precursor, after the removal of Co by simple heat treatment and acid treatment. The N-graphene prepared by them showed ORR activity comparable to that of Pt/C: compared with Pt/C catalyst, N-graphene at –0.20 V (vs. Ag/AgCl), the calculated kinetic currents of N-graphene and Pt/C catalysts are 14.24 mA cm^{-2} and 14.69 mA cm^{-2}, respectively.

The electron transfer number of N-graphene catalyst calculated by the formula is 3.9, so the catalytic oxygen reduction of N-graphene is a four-electron process. Similar to NCNTs, methanol and CO have no effect on the ORR of N-graphene, that is to say, N-graphene is also a selective and anti-toxic non-metallic ORR catalyst. Shi et al. [379] used F127 as a soft template to reduce graphene oxide and PMF (phenol–melanine–formaldehyde) to obtain nanoporous nitrogen-doped graphene.

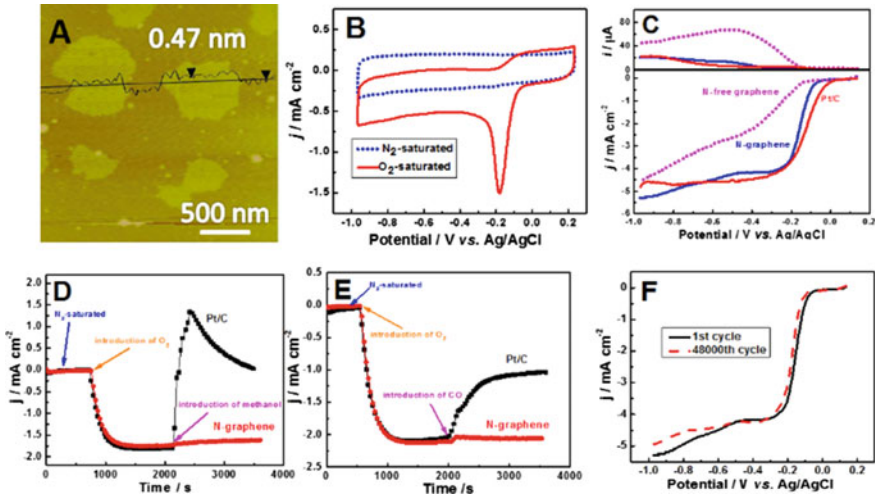

Fig. 4.46 **a** AFM picture of N-graphene sample on newly peeled mica sheet, **b** Cyclic voltammetry of N-graphene in 0.1 mol L^{-1} KOH solution saturated with N_2 and O_2, **c** Oxygen reduction curves of n-graphene, Pt/C and N-free graphene in 0.1 mol L^{-1} KOH solution of O_2, **d** Chronoampelarization curves of n-graphene and Pt/C catalysts against methanol in 0.1 mol L^{-1} KOH solution of saturated O_2, **e** The chronoampelarization curves of N-graphene and Pt/C catalysts against CO in 0.1 mol L^{-1} KOH solution of saturated O_2, **f** Comparison of the reduction performance of circulating oxygen before and after 48,000 times of n-graphene catalyst stability scanning [378]

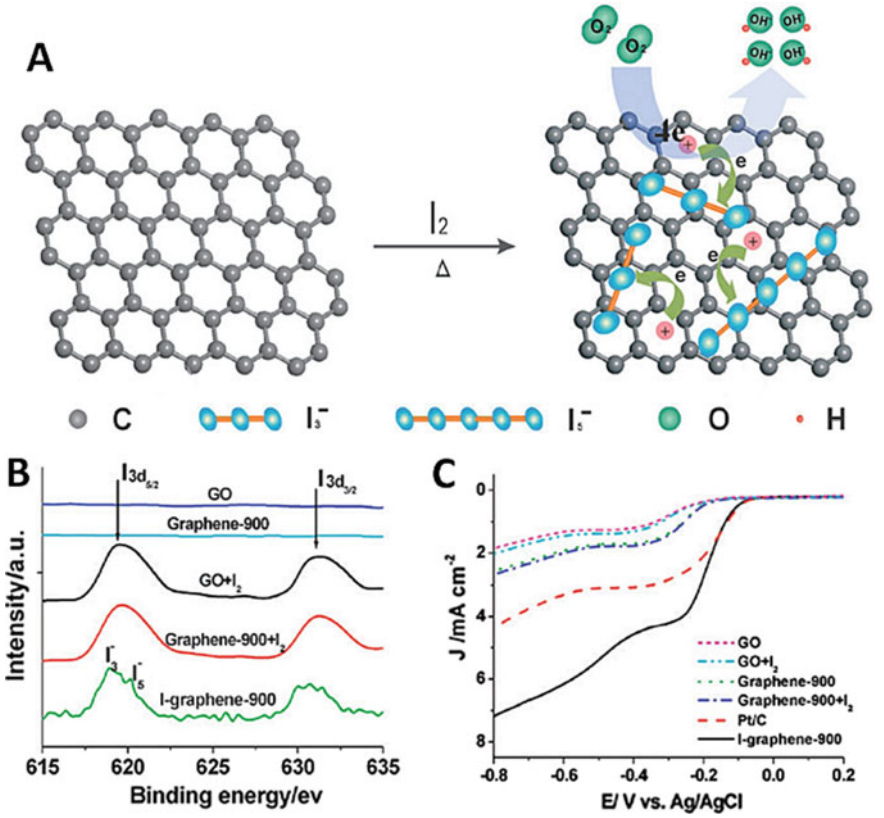

Fig. 4.47 **a**I-graphene sample preparation diagram, **b** XPS spectrum of i-graphene, **c** Oxygen reduction curves of I-graphene, Pt/C, Nitrogen-free GO and graphene-900 and their mixture with I_2 in a 0.1 mol L^{-1} KOH solution of O_2 [400]

The mesoporous / graphene / mesoporous sandwich materials exhibit high oxygen reduction activity, stability, and selectivity. Sun et al. [380] heat-treated graphene in the mixture of ammonia and argon to obtain N-graphene. Their research found that when the heat treatment temperature was 900 °C, the N-graphene obtained had the best performance. Compared with the electrode with a load of 4.85 μgpt cm^{-2}, it showed similar or better oxygen recovery performance. Li et al. [381] synthesized nitrogen-doped graphene quantum dots by a simple and effective method. In addition to their unique luminescent properties, these nitrogen-doped graphene quantum dots have oxygen reduction properties similar to Pt/C catalyst. Li et al. [382] further studied the influence of the size of nitrogen-doped graphene quantum dots on the oxygen reduction performance. Their research shows that nitrogen-doped graphene quantum dots with 176 carbon atoms have the best oxygen reduction performance, close to Pt/C catalyst.

4.6.4.2 Reparation of N-Graphene

At present, the main methods of N-doping for graphene are plasma treatment [383, 384], arc discharge [385], chemical vapor deposition in NH3 atmosphere [377, 386], carbon nitrogen segregation [387]. Guo et al. [388] annealed graphene treated by N^+ ion irradiation in NH_3 atmosphere, and prepared N-graphene with nitrogen content of 1.1%. P-graphene and N-graphene can be selectively prepared by controlling doping experimental parameters. Wang et al. [383] first prepared graphene by chemical method, and then treated graphene by nitrogen plasma to obtain N-graphene with nitrogen content of 1.26%. Qu et al. [377] successfully prepared N-graphene with nitrogen content of 4% on Ni-modified SiO_2/Si substrate by CVD in a mixed gas (NH_3: CH_4: H_2: Ar = 10:50:65:200), and the N-graphene showed good ORR performance.

Geng et al. [380] first prepared graphene by heat treatment of graphene oxide, and then heat treatment in NH_3 atmosphere, successfully prepared N-graphene with nitrogen content of 2.8%. Li et al. [389] used NH_3 as reducing agent and nitrogen source to prepare n-graphene by one-step heat treatment of graphene oxide. When the heat treatment temperature was 500 °C, the nitrogen content could reach 5%.Li et al. [390] prepared N-graphene with thickness of 2–6 by DC arc method using NH_3 as discharge medium and pure graphite as electrode. Similar to the preparation methods of NCNTs, the preparation methods of N-graphene can be divided into two categories: one is to prepare n-graphene by one-step method [377, 389]; the other is to prepare graphene first, and then, by plasma containing N or chemical treatment to obtain N-graphene [383, 388].

4.6.4.3 ORR Mechanism of N-Graphene

In explaining the enhancement of ORR activity of CNTs by nitrogen doping, it is generally believed that the charge transfer caused by N-doping can promote the adsorption and dissociation of O_2, thus promoting ORR, while different N-doping forms play different roles in promoting ORR. For N-graphene, the theoretical research results of density functional theory show that the pyridine nitrogen and pyrrole nitrogen formed by N atom replacing C atom in graphene will lead to asymmetric distribution of spin density and atomic charge density, and the ORR performance of N-graphene may come from this [391]. Sheng et al. [392] prepared N-graphene mainly doped with pyridine type nitrogen by heat treatment of the mixture of GO and melamine, and confirmed the promoting effect of pyridine type nitrogen on ORR by experiments. An important reason for the slow kinetics of ORR reaction is that ORR is a complex multi-step reaction process. Boukhvalov et al. [393] compared the energy barriers of graphene, N-graphene, and Pt surfaces in different ORR reaction steps. The results show that N-graphene has the lowest energy barrier in each ORR reaction step. Their research also shows that the ORR performance of N-graphene with about 4% N-doping content is the best. In many ORR reaction steps, the energy barrier of the first electron transfer step is often the highest, which makes

it often the rate-determining step of ORR. Compared with three different types of doped N atoms, graphite nitrogen can maximally reduce the energy barrier of the first electron transfer in the ORR reaction process, and has the highest selectivity for the four-electron process of ORR, so the graphite nitrogen in N-graphene may have the highest ORR activity [394]. He et al. [378] synthesized N-graphene, which is mainly graphite type nitrogen doped. It is one of the best non-metallic ORR catalysts.

4.6.5 Other Impurity Atoms Doped Graphene

When B atom is doped into the skeleton of graphene, B atom has one less valence electron than C atom, and it will show strong electron absorption characteristics. When graphene doped with B atom (B-graphene) is used as non-metallic ORR catalyst, the borate covalent bond formed by combining with oxygen and the BO_3–G formed by combining with graphene can effectively break the O = O covalent bond, which is the key step for the reduction of O_2 to H_2O [395].

Sheng et al. [396] prepared B-graphene with boron doping of 3.2% by heat treatment of graphene with boron oxide. In alkaline medium, this B-graphene showed very good ORR activity, and its peak potential was - 0.05v (vs. Ag / AgCl), which was a direct four-electron reaction process. Similar to N-graphene, B-graphene also shows cathode selectivity, good anti-toxic ability, and good stability.

Tam et al. [396] adding glucose, boric acid, and graphene mixture to prepare boron-doped graphene hydrogels by hydrothermal method. They can be used as HER, OER, ORR three functional electrocatalysts and applied to zinc air batteries. The flexible solid zinc air battery can achieve 1.40 V open-circuit voltage, and the peak power density is 112 mW cm^{-2}, which is 10 mA cm^{-2} as water electrolysis. Requires only 1.61 V. Zhang et al. [397] prepared 1.32% P-graphene with triphenylphosphine (TPP) and GO by heat treatment. P-graphene doped into graphene exists in P–C bond and P-O bond. This P-graphene shows very good ORR activity, and its peak potential is -0.07 V (vs. Ag/AgCl). Different from N-graphene, P-graphene is a mixing process of two electrons and four electrons. Similar to N-graphene, P-graphene also shows cathode selectivity, good anti-toxic ability, and good stability. Unlike B, N, and C, which form the SP^2 hybrid orbital plane, P is located in the third period, and its covalent radius is larger than C, so the SP^3 orbital configuration is formed. The part of P covalently bound with C is oxidized to form tetrahedral C_3PO, C_2PO_2, and CPO_3. The partially oxidized P doping causes the charge redistribution of graphene. The O atom with the highest electronegativity will first polarize the P atom, and then bridge the P atom to attract electrons from the C atom, making the C atom adjacent to the P atom generate positive charge, becoming the active site of O_2 adsorption and weakening the O–O bond, and then promote the reduction of O_2 to OH^- [398] by attracting electrons from the positive electrode.

Yang et al. [399] prepared S-graphene with sulfur content of 1.30% by using GO and BDS (benzyldisulfide) as precursors. This S-graphene has the same ORR

activity as Pt/C catalyst, and has better cathode selectivity, anti-toxic ability, and stability than Pt/C.

Yao et al. [400] heat-treated the mixture of GO and I_2 at 500–1100 °C, XPS results showed that I was I^{3-} and I^{5-}, and compared with Pt/C catalyst, I-graphene, as ORR catalyst, had the same peak potential as Pt/C, but had a higher surface current density, similar to N-graphene, I-graphene also showed cathode selectivity, good anti-toxic ability, and good stability. In addition, the catalytic ORR process of I-graphene is also a direct four-electron process.

The doping of impurity atoms will change or adjust the electronic structure of graphene, which will change the structure and electronic properties of graphene. The doped atoms can be divided into two categories: one is more valence electrons than C atoms (such as N, P, S, I). This kind of doping will make the neighboring C atoms produce positron effect, which can significantly promote the adsorption and dissociation of oxygen on their surface; The other is the atom with less valence electrons than the C atom (such as B). The atom doped into graphene will interact with the large delocalization π bond of graphene to form the electron absorption effect, while the position of B atom will promote the adsorption and dissociation of oxygen on its surface.

4.6.6 Co-Doped Graphene

Co-doped graphene refers to the doped graphene formed by doping two or more impurity atoms in the skeleton of graphene at the same time.

B- and N-doped graphene have many different physical and chemical properties. B, N-graphene has different application prospects in many fields. Because the radii of C, B, and N atoms are close to each other, the doping ratio and form of B and N will have a great space to adjust. The electronic structures of B/N-graphene with different composition and bonding form are different, which widens the application fields of B/N-graphene. According to the different bonding, B, N-graphene can be divided into two types: one is B and N are single-phase doped graphene (h-BCN); the other is independent structure of h-BN (hexagonal born nitride) doped into the skeleton of graphene (s-BCN).

For h-BCN, B atom and N atom are co-doped into the skeleton of graphene. The extra electrons provided by N atom and the empty orbits provided by B atom are combined into the conjugation system of C in graphene to change the electronic structure of graphene and generate new electronic states, for example, to change the density distribution of electronic states and increase the spin density of electrons [375, 402]. For s-BCN, the neutral N-atom lone pair electrons and N-atom empty orbits have no effect on the delocalization π bond of graphene. Because h-BN is not conductive, s-BCN is equivalent to graphene with nanopores [403]. Therefore, the ORR activity of s-BCN is only equivalent to that of graphene, in which h-BN is inert to ORR, so when preparing B and N Co-doped graphene as ORR catalyst, s-BCN should be avoided.

Zheng et al. [402] prepared B, N-graphene by two-step method. Firstly, GO was annealed at a lower temperature (500 °C) in an NH_3 atmosphere to form N-graphene, and then the mixture of N-graphene and $H3BO_3$ was heat-treated at a high temperature (900 °C) to form B, N-graphene. B atom is further doped into N-graphene to form B, N-graphene. The N content of B, N-graphene is 4.22% and the B content is 2.17%, in which the bond form of B is only B-C bond. Compared with the preparation of single impurity atom doped N-graphene and B-graphene, the ORR performance of B, N-graphene in 0.1 M kOH is significantly improved.

Density functional theory calculation shows that the synergistic effect caused by the chemical coupling between B and N is the reason for the enhanced ORR performance of B, N-graphene. In the benzene ring structure of B-C-N, 2p orbit, and N of C atom located between N and B atoms produce polarization, providing additional electrons to B atom nearby; 2p orbit of B atom is occupied by electrons, the synergistic coupling effect of charge transfer can effectively improve the adsorption and binding of HO_2, thus promoting the occurrence of ORR. In this synergistic effect, the functions of N and B with different doping forms are different. Unlike in N-graphene, graphite nitrogen promotes the adsorption of HO_2 on the neighboring C atom, in B, N-graphene, only pyridine nitrogen can promote the adsorption of HO_2 on the active B site [402].

Wang et al. [375] prepared a series of B/N Co-doped graphene (BCN) with adjustable content by heat treating the mixture of go and boric acid in the atmosphere of NH_3. The ORR activity of BCN was higher than that of Pt/C catalyst. Wang et al. [404] prepared N and S Co-doped graphene (NSG) by one-step method: using go and thiourea as precursors, NSG was obtained by heat treatment in argon atmosphere, in which thiourea was used as both N source and S source, and the N content decreased with the increase of heat treatment temperature, while the S content increased with the increase of heat treatment temperature. In addition, thiourea also partially reduced go during heat treatment. NSG showed good ORR activity in 0.1 M kOH medium: high peak potential, high current density, and high stability. See Table 4.4 for ORR activity comparison of doped graphene non-metallic catalyst.

4.6.7 Other Doped Carbon Materials

The special structure of carbon material makes it rich in diversity. Carbon nanotubes and graphene are two kinds of very special nanocarbon materials. Since Dai et al. [334] found that VA -NCNTs as a non-metallic catalyst showed excellent ORR activity, other forms of doped carbon nanomaterials have attracted a lot of attention and research. Klaus et al. [406] have studied ordered nitrogen-doped mesoporous graphite arrays with moderate nitrogen content (Nitrogen-Doped Ordered Mesoporous Graphitic Arrays, NOMGAs), The oxygen reduction activity, stability, and anti-toxic ability of nomgas in 0.1 M kOH are higher than that of Pt/C catalyst. In their research, they found that graphite-like nitrogen atoms play an important role in the process of oxygen reduction, and pointed out that the catalyst with high graphite

Table 4.4 ORR activity comparison of doped graphene non-metal catalysts reported in literature

Doping mode	Precursor	Doped atomic weight (at.%)	Up peak potential (*vs.* Ag/AgCl)	n_e	References
N-doped	NH_3:CH_4:H_2:Ar = 10:50:65:200	4%	−0.14	3.6–4	65
	N-resin	1.8%	−0.04	3.9	66
B-doped	GO/B_2O_3	3.2%	−0.05	3.5	85
P-doped	GO/triphenylphosphine (TPP)	1.81%	−0.07	3.0–3.8	86
	GO/1-butyl-3-methlyimidazolium hexafluorophosphate	1.16%	−0.049	3.9	87
S-doped	GO/benzyldisulfide	1.3%	−0.05	3.82	88
I-doped	GO/I_2	0.83%	−0.06	3.86	89
B/N-co-doped	GO/ $H3BO_3$/NH_3	N:11%/B:12%	0	~4	63
	GO/ $H3BO_3$/NH_3	N:4.22%/B:2.17%	−0.25	3.97	91
N/S-co-doped	GO/NH_4SCN	N:wt12.3% S:wt18.4%	~ −0.15	3.9	94
	GO/ thiourea	N:5.1%/S:0.65%	~ − 0.11	3.91	93

nitrogen content has higher oxygen reduction activity. Yang et al. [407] prepared porous nitrogen-doped carbon with high surface area using silicon nanoparticles as template. The specific surface area of the material reached 1500 m^2 g^{-1}, and it had narrow mesoporous distribution (12 nm), and its oxygen reduction performance was discussed. They found that the oxygen reduction activity of these materials was close to that of commercial Pt/C catalyst, and that the porous nitrogen-doped carbon with high specific surface area obtained by carbonizing base materials had better performance.

Han et al. [408] prepared hollow carbon hemispheres (HCHs) with nitrogen content of 10.9 wt% by template method: (1) using silicon spheres with diameter of about 300 nm as template, 3-MBP-dca (3-metal-1-butylpyridine Dicya nide), or CMIM-Cl (3 - (3-cyanopropyl) - 1-methyl-1 h-imida-zol-3-iumchloride) is coated on the silicon ball; (2) the coated silicon ball is carbonized; (3) the template is removed with NH_4HF_2; (4) the high-temperature (900 °C) annealing treatment is carried out to form the structure of porous hemisphere, as shown in Fig. 4.48a-d. The ORR performance of the obtained nitrogen-doped HCHs is close to that of Pt/C catalyst, as shown in Fig. 4.48e.

BO et al. [409] prepared ordered mesoporous boron-doped carbons (BOMCs) using SBA-15 as template, 4- hydroxyphenylboronic acid as carbon source and boron source. The specific surface area of BOMCs can reach 900 m^2g^{-1}, the average pore diameter is 6.4 nm, and the nitrogen content is 1.3%. The ORR performance test results in 0.1 M KOH solution show that its peak potential reaches 0.16 (VS. Ag/AgCl), and the electron transfer number obtained by K-L equation is 3.86, indicating that the ORR process of BOMCs is mainly a direct four-electron process. There are many forms of B doping into C structure, including BC_3, BC_4, BC_2O, BCO_2, etc. Among them, BC_3 and BC_4 are considered to play a key role in ORR process, and their content also directly affects the performance of ORR. The higher the content, the greater the ORR activity [410].

The P atom has the same valence electrons and similar chemical properties as N, but because the larger atomic radius and stronger electronegativity of the P atom are weaker than that of C, the combination of P and C will make C have positive charge, thus promoting ORR like N-doping. Yang et al. [411] prepared P-doped ordered mesoporous carbon (POMC) using SBA-15 as a template and a method of co-splitting P source and C source under the condition of not using any metal: firstly, using P-containing carbon source triphenylphosphine, (TPP) and initial carbon source (phenol) are immersed in template SBA-15 at room temperature, then cracked at 900 °C under argon atmosphere, and finally the template is removed by HF treatment, as shown in Fig. 4.49a. Under the same conditions, the ORR performance of POMC is very close to Pt/C, as shown in Fig. 4.49e. Their research shows that the ORR activity of POMC with different lengths prepared from templates of different sizes will be different. The shorter the length, the better the ORR activity, because the shorter the length, the smaller the charge transfer resistance.

Wu et al. [412] first use resorcinol and formaldehyde as c sources and $Co(NO_3)_2$ as catalyst precursors, first prepare Co–C precursors by sol–gel method, then add H_3PO_4(P source), heat treat at 800 oC for 1 h, and then treat with 1 M HCl solution

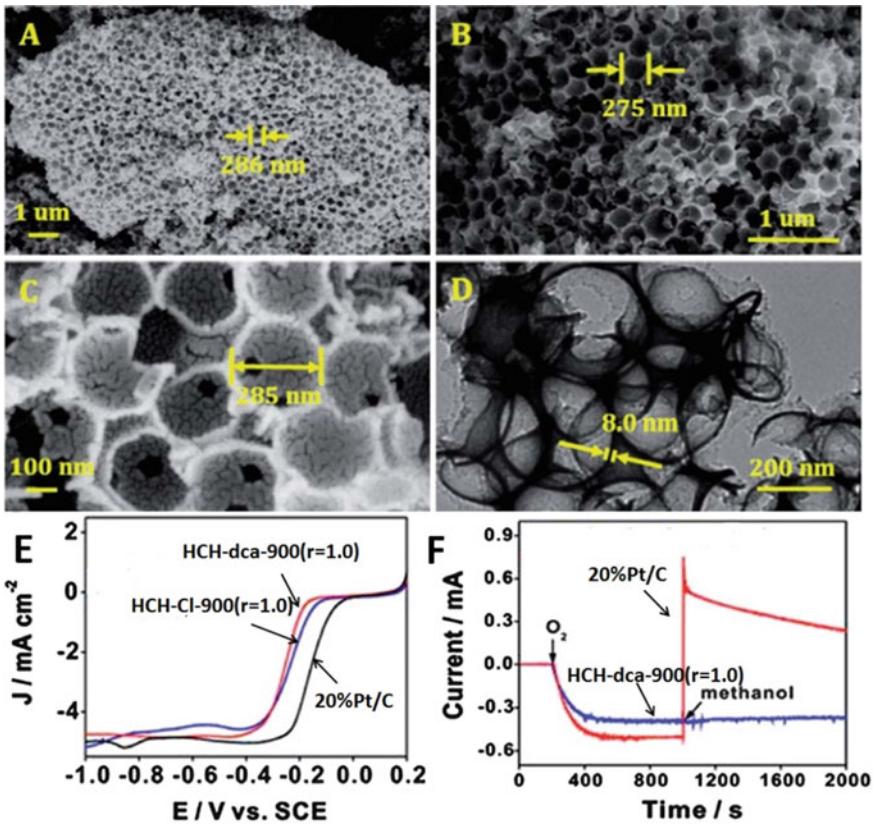

Fig. 4.48 **a**-**c** SEM images of nitrogen-doped HCHs at different magnifications show a porous hemispherical structure, **d** SEM images of nitrogen-doped HCHs, **e** oxygen reduction curves of nitrogen-doped HCHs and Pt/C obtained from different precursors in 0.1 mol L^{-1} KOH solution of O_2, and **f** chronopotentiometric response curves of nitrogen-doped HCHs and Pt/C after methanol addition

for 12 h to remove Co in the sample, thus obtaining p-doped carbon gel with p doping amount of 0.76 ~ 3.56% of the samples obtained according to different ratios of Co–C and $H3PO_4$ of the precursors. Compared with the ORR performance of samples doped with different P, the ORR performance of samples doped with 1.64% P is the best. When the doping amount is less than this value, its ORR performance increases with the increase of doping amount, while when it is greater than this doping amount, its ORR performance decreases with the increase of doping amount.

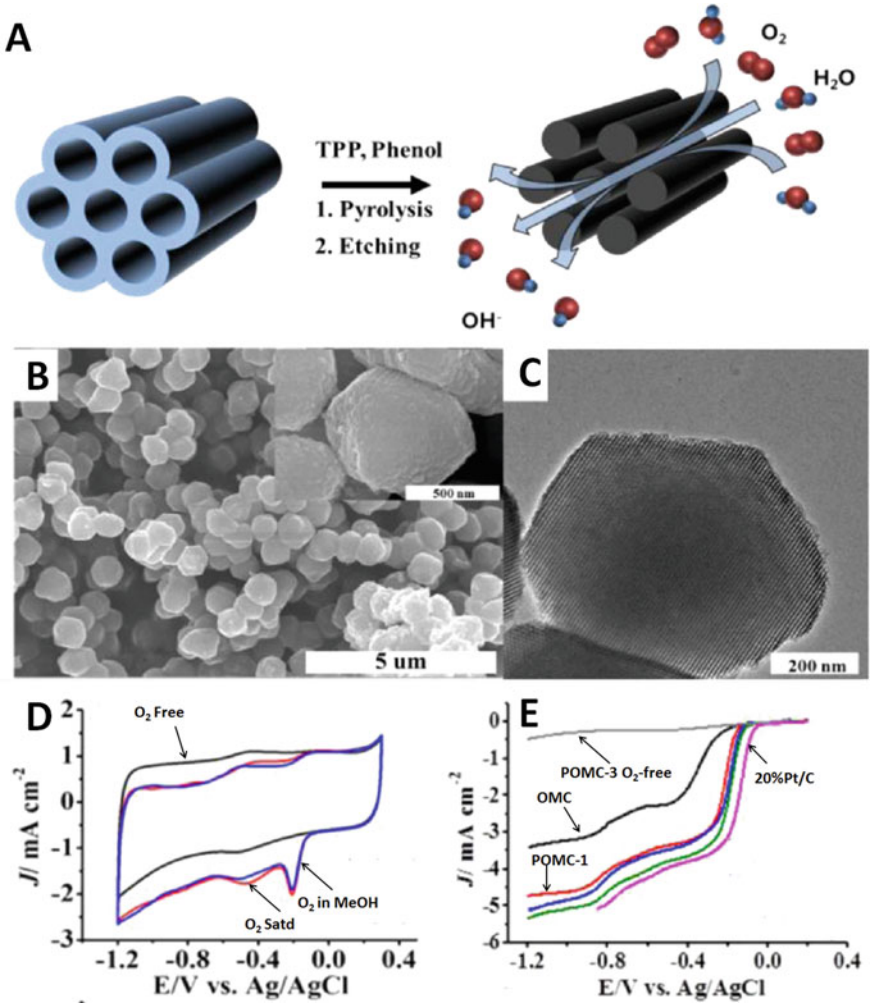

Fig. 4.49 **a** Schematic illustration of POMC preparation, **b** FE-SEM image with an inset showing magnified image of POMC-3, **c** TEM image, **d** CVs for the ORR at 100 mV s^{-1} for POMC-3, **e** LSV curves for OMC, POMC-1, and Pt/C catalyst at 1600 rpm along with O_2-free current of POMC-3 [411]

References

1. Zhang S, Shao Y, Yin G, Lin Y (2013) Recent progress in nanostructured electrocatalysts for PEM fuel cells. J Mater Chem A 1:4631–4641
2. Shao Y, Liu J, Wang Y, Lin Y (2009) Novel catalyst support materials for PEM fuel cells: current status and future prospects. J Mater Chem 19:46–59
3. Sharma S, Pollet BG (2012) Support materials for PEMFC and DMFC electrocatalysts-a review. J Power Sourc 208:96–119

4. Xie X, Liu J, Li T, Song Y, Wang F (2018) Post-formation copper-nitrogen species on carbon black: their chemical structures and active sites for oxygen reduction reaction. Che-Eur J 24:9968–9975
5. Planeix J, Coustel N, Coq B, Brotons V, Kumbhar P, Dutartre R, Geneste P, Bernier P, Ajayan P (1994) Application of carbon nanotubes as supports in heterogeneous catalysis. J Am Chem Soc 116:7935–7936
6. Peng XW, Zhang L, Chen ZX, Zhong LX, Zhao DK, Chi X, Zhao XX, Li LG, Lu XH, Leng K, Liu CB, Liu W, Tang W, Loh KP (2019) Hierachically porous carbon plates derived from wood as bifunctional ORR/OER electrodes. Adv Mater, 1900341
7. Guo YY, Yuan PF, Zhang JN Xia HC, Cheng FY, Zhou MF, Li J, Qiao YY, Mu SC, Xu Q (2018) Co_2P-CoN double active centers confined in N-doped carbon nanotube: heterostructural engineering for trifunctional catalysis toward HER, ORR, OER, and Zn-Air batteries driven water splitting. Adv Funct Mater 1805641
8. Qin Q, Chen LL, Wei T, Wang YM, Liu X (2019) Ni/NiM_2O_4 (M=Mn or Fe) supported on N-doped carbon nanotubes as trifunctional electrocatalysts for ORR. OER and HER Catal Sci Technol 9:1595–1601
9. Li X, Wang H, Yu H, Liu Z, Peng F (2014) An opposite change rule in carbon nanotubes supported platinum catalyst for methanol oxidation and oxygen reduction reactions. J Power Sourc 260:1–5
10. Arici E, Kaplan BY, Mert AM, Gursel SA, Kinayyigit S (2019) An effective electrocatalyst based on platinum nanoparticles supported with graphene nanoplatelets and carbon black hybrid for PEM fuel cells. Int J Hydrogen Energ 44:14175–14183
11. Martins M, Metin Ö, Šljukić B, Sevim B, Sequeira C, Santos D (2019) PdNi alloy nanoparticles assembled on cobalt ferrite-carbon black composite as a fuel cell catalyst. Int J Hydrogen Energ 44:14193–14200
12. Muneeb O, Chino I, Saenz A, Haan JL (2019) An ascorbate fuel cell with carbon black nanoparticles as anode and cathode. J Power Sourc 413:216–221
13. Berber MR, Fujigaya T, Nakashima N (2018) A potential polymer formulation of a durable carbon-black catalyst with a significant fuel cell performance over a wide operating temperature range. Mater Today Energy 10:161–168
14. Yılmaz MS, Kaplan BY, Gürsel SA, Metin Ö (2019) Binary CuPt alloy nanoparticles assembled on reduced graphene oxide-carbon black hybrid as efficient and cost-effective electrocatalyst for PEMFC. Int J Hydrogen Energ 44:14184–14192
15. Uchida M, Fukuoka Y, Sugawara Y, Eda N, Ohta A (1996) Effects of microstructure of carbon support in the catalyst layer on the performance of polymer-electrolyte fuel cells. J Electrochem Soc 143:2245–2252
16. Geping Y, Yuyan S, Jiajun W, Yunzhi G, Pengfei S (2006) Multi-walled carbon nanotubes based Pt electrodes prepared with in situ ion exchange method for oxygen reduction. J Power Sourc 161:47–53
17. Cheng W, Mahesh W, Xin W, Tang JM, Haddon RC, Yushan Y (2004) Proton exchange membrane fuel cells with carbon nanotube based electrodes. Nano Lett 4:345–348
18. Sheng Z, Yuyan S, Geping Y, Yuehe L (2010) Carbon nanotubes decorated with Pt nanoparticles via electrostatic self-assembly: a highly active oxygen reduction electrocatalyst. J Mater Chem 20:2826–2830
19. Lee J, Kim J, Hyeon T (2006) Recent progress in the synthesis of porous carbon materials. Adv Mater 18:2073–2094
20. Joo SH, Pak C, You DJ, Lee S-A, Lee HI, Kim JM, Chang H, Seung D (2006) Ordered mesoporous carbons (OMC) as supports of electrocatalysts for direct methanol fuel cells (DMFC): Effect of carbon precursors of OMC on DMFC performances. Electrochim Acta 52:1618–1626
21. Joo JB, Kim P, Kim W, Kim J, Yi J (2006) Preparation of mesoporous carbon templated by silica particles for use as a catalyst support in polymer electrolyte membrane fuel cells. Catal Today 111:171–175

22. Vaarmets K, Sepp S, Nerut J, Härk E, Tallo I, Lust E (2013) Electrochemical and physical characterization of Pt-Ru alloy catalyst deposited onto microporous-mesoporous carbon support derived from Mo_2C at 600 °C. J Solid State Electrochem 17:1729–1741
23. Chan K-Y, Ding J, Ren J, Cheng S, Tsang KY (2004) Supported mixed metal nanoparticles as electrocatalysts in low temperature fuel cells. J Mater Chem 14:505–516
24. Chang H, Joo SH, Pak C (2007) Synthesis and characterization of mesoporous carbon for fuel cell applications. J Mater Chem 17:3078–3088
25. Wang W, Liu YC, Li J, Chen SL (2018) NiFe LDH nanodots anchored on 3D macro/mesoporous carbon as high-performance ORR/OER bifunctional electrocatalyst. J Mater Chem A 6:14299–14306
26. Chu D, Jiang RZ (2002) Novel electrocatalysts for direct methanol fuel cells. Solid State Ionics 148:591–599
27. Rodriguez NM, Kim M-S, Baker RTK (1994) Carbon nanofibers: a unique catalyst support medium. J Phys Chem 98:13108–13111
28. Endo M, Kroto HW (1992) Formation of carbon nanofibers. J Phys Chem 96:6941
29. Kaixue W, Yonggang W, Yarong W, Hosono E, Haoshen Z (2009) Mesoporous carbon nanofibers for supercapacitor application. J Phys Chem C 113:1093–1097
30. Yin J, Qiu Y, Yu J (2013) Nitrogen-doped carbon nanofibers as highly active metal-free electrocatalysts for oxygen reduction reactions in acidic media. Chem Lett 42:413–415
31. Sebastian D, Garcia RA, Suelves I, Moliner R, Jesus LM, Baglio V, Stassi A, Arico AS (2012) Enhanced oxygen reduction activity and durability of Pt catalysts supported on carbon nanofibers. Appl Catal B 115:269–275
32. Zhong R (2013) Cathode oxygen reduction performance of carbon nanofiber groups and their supported pin catalysts. Master Thesis of East China University of Technology
33. Sui Z (2005) Study on catalytic oxidative dehydrogenation of propane with carbon nanofibers. East China University of Science and Technology
34. Stankovich S, Dikin DA, Piner RD, Kohlhaas KA, Kleinhammes A, Jia Y, Wu Y, Nguyen ST, Ruoff RS (2007) Synthesis of graphene-based nanosheets via chemical reduction of exfoliated graphite oxide. Carbon 45:1558–1565
35. Enoki T, Kobayashi Y, Fukui KI (2007) Electronic structures of graphene edges and nanographene. Int Rev Phys Chem 26:609–645
36. Geim AK, Novoselov KS (2007) The rise of graphene. Nat Mater 6:183–191
37. Mortazavibc B, Madjetd ME, Shahrokhi M, Ahzi S, Zhuang XY, Rabczuk T (2019) Nanoporous graphene: A 2D semiconductor with anisotropic mechanical, optical and thermal conduction properties. Carbon 147:377–384
38. Lee J-H, Choi HK, Yang L, Chueng S-TD, Choi J-W, Lee K-B (2018) Nondestructive real-time monitoring of enhanced stem cell differentiation using a graphene-Au hybrid nanoelectrode array. Adv Mater, 1802762
39. Novoselov KS, Fal V, Colombo L, Gellert P, Schwab M, Kim K (2012) A roadmap for graphene. Nature 490:192–200
40. Dikin DA, Stankovich S, Zimney EJ, Piner RD, Dommett GH, Evmenenko G, Nguyen ST, Ruoff RS (2007) Preparation and characterization of graphene oxide paper. Nature 448:457–460
41. Avouris P, Dimitrakopoulos C (2012) Graphene: synthesis and applications. Mater Today 15:86–97
42. Souza AL, Sivaraman G, Hertkorn J, Rodrigo GA, Maria F, Wanderlã LS (2019) Hybrid 2D nanodevices (graphene/h-BN): selecting NOx gas through the device interface. J Mater Chem A 7:8905–8911
43. Shao X, Srinivasan A, Ang WK, Anjam K (2018) A high-brightness large-diameter graphene coated point cathode field emission electron source. Nat Commun 9:1288
44. Wu J, Chen LF, Li SY, Du C, Zhang QZ, Zheng CL, Xu JM, Song KX (2018) Improved field emission performances for graphene/ZnO nanowires/graphene sandwich composites. Mater Lett 213:391–393

45. Li Y, Li Z, Shen PK (2013) Simultaneous formation of ultrahigh surface area and three-dimensional hierarchical porous graphene-like networks for fast and highly stable supercapacitors. Adv Mater 25:2474–2480
46. Li Y, Li Z, Zhang Q, Shen PK (2014) Sulfur-infiltrated three-dimensional graphene-like material with hierarchical pores for highly stable lithium-sulfur batteries. J Mater Chem A 2:4528–4533
47. Geng P, Zheng S, Tang H, Zhu RM, Zhang L, Cao S, Xue HG, Pang H (2018) Transition metal sulfides based on graphene for electrochemical energy storage. Adv Energy Mater 8:1703259
48. Kim T, Jung G, Yoo S, Suh KS, Ruoff RS (2013) Activated graphene-based carbons as supercapacitor electrodes with macro-and mesopores. ACS Nano 7:6899–6905
49. Cadore AR, Mania E, Alencar AB, Rezende NP, Olivera SD, Watanabe K, Taniguchi K, Chacham H, Campos LC, Lacerda RG (2018) Enhancing the response of NH_3 graphene-sensors by using devices with different graphene-substrate distances. Sensors Actuat B-Chem 266:438–446
50. Mackin C, Schroeder V, Zurutuza A, Su C, Kong J, Swager TM, Palacios T (2018) Chemiresistive graphene sensors for ammonia detection. ACS Appl Mater Inter 10:16169–16176
51. Potts JR, Dreyer DR, Bielawski CW, Ruoff RS (2011) Graphene-based polymer nanocomposites. Polymer 52:5–25
52. Su DW, Ahn HJ, Wang GX (2013) SnO_2@ graphene nanocomposites as anode materials for Na-ion batteries with superior electrochemical performance. Chem Commun 49:3131–3133
53. Chang H, Wu H (2013) Graphene-based nanocomposites: preparation, functionalization, and energy and environmental applications. Energy Environ Sci 6:3483–3507
54. Zhao XL, Tao GQ, Gong XJ, Yang XY, Ge HH, Wang J (2019) Dual engineering interface-driven complementary graphene oxide-protein dimer supramolecular architecture enables nucleus imaging and therapy. ACS Appl Bio Mater 2:2896–2906
55. Edwards RS, Coleman KS (2013) Graphene Synthesis: Relationship to Applications. Nanoscale 5:38–51
56. Soldano C, Mahmood A, Dujardin E (2010) Production, properties and potential of graphene. Carbon 48:2127–2150
57. Zhu Y, Murali S, Cai W, Li X, Suk JW, Potts JR, Ruoff RS (2010) Graphene and graphene oxide: synthesis, properties, and applications. Adv Mater 22:3906–3924
58. Allen MJ, Tung VC, Kaner RB (2009) Honeycomb carbon: a review of graphene. Chem Rev 110:132–145
59. Rethinasabapathy M, Kang SM, Haldorai Y, Jonna N, Jankiraman M, Lee GW, Jang SC, Natesan B, Roh C, Huh YS (2019) Quaternary PtRuFeCo nanoparticles supported N-doped graphene as an efficient bifunctional electrocatalyst for low-temperature fuel cells. J Ind Eng Chem 69:285–294
60. Kou R, Shao Y, Wang D, Engelhard MH, Kwak JH, Wang J, Viswanathan VV, Wang C, Lin Y, Wang Y, Aksay IA, Liu J (2009) Enhanced activity and stability of Pt catalysts on functionalized graphene sheets for electrocatalytic oxygen reduction. Electrochem Commun 11:954–957
61. Yang HJ, Geng L, Zhang YT, Chang G, Zhang ZL, Liu X, Lei M, He YB (2019) Graphene-templated synthesis of palladium nanoplates as novel electrocatalyst for direct methanol fuel cell. Appl Surf Sci 466:385–392
62. Guo S, Sun S (2012) FePt Nanoparticles assembled on graphene as enhanced catalyst for oxygen reduction reaction. J Am Chem Soc 134:2492–2495
63. Xin Y, Liu J-G, Zhou Y, Liu W, Gao J, Xie Y, Yin Y, Zou Z (2011) Preparation and characterization of Pt supported on graphene with enhanced electrocatalytic activity in fuel cell. J Power Sourc 196:1012–1018
64. Guo S, Dong S, Wang E (2010) Three-Dimensional Pt-on-Pd bimetallic nanodendrites supported on graphene nanosheet: facile synthesis and used as an advanced nanoelectrocatalyst for methanol oxidation. ACS Nano 4:547–555
65. Li Y, Tang L, Li J (2009) Preparation and electrochemical performance for methanol oxidation of Pt/graphene nanocomposites. Electrochem Commun 11:846–849

66. Dai L (2013) Functionalization of graphene for efficient energy conversion and storage. Acc Chem Res 46:31–42
67. Zheng X, Wu J, Cao X, Abbott J, Jin C, Wang HB, Strasser P, Yang RZ, Chen X, Wu G (2019) N-, P-, and S-doped graphene-like carbon catalysts derived from onium salts with enhanced oxygen chemisorption for Zn-air battery cathodes. Appl Catal B-Environ 241:442–451
68. Liu H, Liu Y, Zhu D (2011) Chemical doping of graphene. J Mater Chem 21:3335–3345
69. Wang H, Maiyalagan T, Wang X (2012) Review on recent progress in nitrogen-doped graphene: synthesis, characterization, and its potential applications. ACS Catal 2:781–794
70. Zhang L, Xia Z (2011) Mechanismsof oxygen reduction reaction on nitrogen-doped graphene for fuel cells. J Phys Chem C 115:11170–11176
71. Qu L, Liu Y, Baek J-B, Dai L (2010) Nitrogen-doped graphene as efficient metal-free electrocatalyst for oxygen reduction in fuel cells. ACS Nano 4:1321–1326
72. Ojeda-Aristizabal C, Bao W, Fuhrer M (2013) Thin-film barristor: A gate-tunable vertical graphene-pentacene device. Phys Rev B 88:035435
73. Martini L, Chen Z, Mishra N, Barin GB, Fantuzzi P, Ruffieux P, Fasel R, Feng XL, Narita A, Coletti C, Müllen K, Candini A (2019) Structure-dependent electrical properties of graphene nanoribbon devices with graphene electrodes. Carbon 146:36–43
74. Manthiram A, Fu Y, Su YS (2013) Challenges and prospects of lithium-sulfur batteries. Acc Chem Res 46:1125–1134
75. Evers S, Nazar LF (2012) New approaches for high energy density lithium-sulfur battery cathodes. Acc Chem Res 46:1135–1143
76. Wang D, Zeng Q, Zhou G, Yin L, Li F, Cheng HM, Gentle I, Lu GQ (2013) Carbon/sulfur composites for Li-S batteries: status and prospects. J Mater Chem A 1:9382–9394
77. Zhou GM, Yin LC, Wang DW, Li L, Pei SF, Gentle IR, Li F, Cheng HM (2013) Fibrous hybrid of graphene and sulfur nanocrystals for high-performance lithium-sulfur batteries. ACS Nano 7:5367–5375
78. Song HJ, Zhang LC, He CL, Qu Y, Tian YF, Lv Y (2011) Graphene sheets decorated with SnO_2 nanoparticles: in situ synthesis and highly efficient materials for cataluminescence gas sensors. J Mater Chem 21:5972–5977
79. Zhao Y, Hu C, Hu Y, Cheng H, Shi G, Qu L (2012) A versatile, ultralight, nitrogen-doped graphene framework. Angew Chem Int Edit 124:11533–11537
80. Li C, Shi G (2012) Three-dimensional graphene architectures. . Nanoscale 4:5549–5563
81. Yin S, Niu Z, Chen X (2012) Assembly of graphene sheets into 3D macroscopic structures. Small 8:2458–2463
82. Xiao XY, Beechem TE, Brumbach MT, Lambert TN, Davis DJ, Michael JR, Washburn CM, Wang J, Brozik SM, Wheeler DR (2012) Lithographically defined three-dimensional graphene structures. ACS Nano 6:3573–3579
83. Wu Z-S, Yang S, Sun Y, Parvez K, Feng X, Müllen K (2012) 3D nitrogen-doped graphene aerogel-supported Fe_3O_4 nanoparticles as efficient electrocatalysts for the oxygen reduction reaction. J Am Chem Soc 134:9082–9085
84. Maiyalagan T, Dong X, Chen P, Wang X (2012) Electrodeposited Pt on three-dimensional interconnected graphene as a free-standing electrode for fuel cell application. J Mater Chem 22:5286–5290
85. Ma Y, Sun L, Huang W, Zhang L, Zhao J, Fan Q, Huang W (2011) Three-dimensional nitrogen-doped carbon nanotubes/graphene structure used as a metal-free electrocatalyst for the oxygen reduction reaction. J Phys Chem C 115:24592–24597
86. Su Y, Zhang Y, Zhuang X, Li S, Wu D, Zhang F, Feng X (2013) Low-temperature synthesis of nitrogen/sulfur Co-doped three-dimensional graphene frameworks as efficient metal-free electrocatalyst for oxygen reduction reaction. Carbon 62:296–301
87. Xue Y, Yu D, Dai L, Wang R, Li D, Roy A, Lu F, Chen H, Liu Y, Qu J (2013) Three-dimensional B, N-doped graphene foam as a metal-free catalyst for oxygen reduction reaction. Phys Chem Chem Phys 15:12220–12226
88. Yang Z, Yao Z, Li G, Fang G, Nie H, Liu Z, Zhou X, Chen XA, Huang S (2011) Sulfur-doped graphene as an efficient metal-free cathode catalyst for oxygen reduction. ACS Nano 6:205–211

89. Liang J, Jiao Y, Jaroniec M, Qiao SZ (2012) Sulfurand nitrogen dual-doped mesoporous graphene electrocatalyst for oxygen reduction with synergistically enhanced performance. Angew Chem Int Ed 51:11496–11500
90. He C, Zhang JJ, Shen PK (2014) Nitrogen-self-doped graphene-based non-precious metal catalyst with superior performance to Pt/C catalyst toward oxygen reduction reaction. J. Mater. Chem. A 2:3231–3236
91. He C, Li Z, Cai M, Cai M, Wang J-Q, Tian Z, Zhang X, Shen PK (2013) A strategy for mass production of self-assembled nitrogen-doped graphene as catalytic materials. J Mater Chem A 1:1401–1406
92. Wang YJ, Wilkinson DP, Zhang J (2011) Noncarbon support materials for polymer electrolyte membrane fuel cell electrocatalysts. Chem Rev 111:7625–7651
93. Sabawa JP, Aliaksandr S (2019) Bandarenka, Degradation mechanisms in polymer electrolyte membrane fuel cells caused by freeze-cycles: Investigation using electrochemical impedance spectroscopy. Electrochim Acta 311:21–29
94. Liu Y, Shrestha S, Mustain WE (2012) Synthesis of nanosize tungsten oxide and its evaluation as an electrocatalyst support for oxygen reduction in acid media. ACS Catal 2:456–463
95. Awaludin Z, Suzuki M, Masud J, Okajima T, Ohsaka T (2011) Enhanced electrocatalysis of oxygen reduction on Pt/TaOx/GC. J Phys Chem C 115:25557–25567
96. Korovina A, Garsany Y, Epshteyn A, Purdy AP, More K, Swider-Lyons KE, Ramaker DE (2012) Understanding oxygen reduction on tantalum oxyphosphate and tantalum oxide supported platinum by X-ray absorption spectroscopy. J Phys Chem C 116:18175–18183
97. Xu L, Jiang QQ, Xiao ZH, Li AXY, Huo J, Wang SY (2016) Plasma-engraved Co_3O_4 nanosheets with oxygen vacancies and high surface area for the oxygen evolution reaction. Angew Chem Int Edit 128:5363–5367
98. Tong Y, Chen P, Zhou T, Xu K, Chu W, Wu C, Xie Y (2017) A bifunctional hybrid electrocatalyst for oxygen reduction and evolution: Cobalt oxide nanoparticles strongly coupled to B. N-decorated Graphene Angew Chem Int Edit 129:7227–7231
99. Liardet L, Hu X (2018) Amorphous cobalt vanadium oxide as a highly active electrocatalyst for oxygen evolution. ACS Catal 8:644–650
100. Zhang L, Wang L, Holt CM, Zahiri B, Li Z, Malek K, Navessin T, Eikerling MH, Mitlin D (2012) Highly corrosion resistant platinum-niobium oxide-carbon nanotube electrodes for the oxygen reduction in PEM fuel cells. Energy Environ Sci 5:6156–6172
101. Huang S-Y, Ganesan P, Park S, Popov BN (2009) Development of a titanium dioxide-supported platinum catalyst with ultrahigh stability for polymer electrolyte membrane fuel cell applications. J Am Chem Soc 131:13898–13899
102. Sasaki K, Zhang L, Adzic RR (2008) Niobium oxide-supported platinum ultra-low amount electrocatalysts for oxygen reduction. Phys Chem Chem Phys 10:159–167
103. Saha MS, Li R, Cai M, Sun X (2007) High electrocatalytic activity of platinum nanoparticles on SnO_2 nanowire-based electrodes. Electrochem Solid-State Lett 10:B130–B133
104. Kulesza PJ, Miecznikowski K, Baranowska B, Skunik M, Fiechter S, Bogdanoff P, Dorbandt I (2006) Tungsten oxide as active matrix for dispersed carbon-supported $RuSe_x$ nanoparticles: Enhancement of the electrocatalytic oxygen reduction. Electrochem Commun 8:904–908
105. Levy RB, Boudart M (1973) Platinum-like behavior of tungsten carbide in surface catalysis. Science 181:547–549
106. Lu C, Tranca D, Zhang J, Rodríguez Hernández FN, Su Y, Zhuang X, Zhang F, Seifert G, Feng X (2017) Molybdenum carbide-embedded nitrogen-doped porous carbon nanosheets as electrocatalysts for water splitting in alkaline media. ACS Nano 11:3933-3942
107. Lin H, Liu N, Shi Z, Guo Y, Tang Y, Gao Q (2016) Cobalt-doping in molybdenum-carbide nanowires toward efficient electrocatalytic hydrogen evolution. Adv Funct Mater 26:5590–5598
108. Nie M, Shen PK, Wei Z (2007) Nanocrystaline tungsten carbide supported Au-Pd electrocatalyst for oxygen reduction. J Power Sourc 167:69–73
109. Meng H, Shen PK (2005) Tungsten carbide nanocrystal promoted Pt/C electrocatalysts for oxygen reduction. J Phys Chem B 109:22705–22709

110. Keller N, Pietruszka B, Keller V (2006) A new one-dimensional tungsten carbide nanostructured material. Mater Lett 60:1774–1777
111. Shao Y, Yin G, Gao Y (2007) Understanding and approaches for the durability issues of Pt-based catalysts for PEM fuel cell. J Power Sourc 171:558–566
112. Shao Y, Yin G, Wang Z, Gao Y (2007) Proton exchange membrane fuel cell from low temperature to high temperature: material challenges. J Power Sourc 167:235–242
113. Shanmugam S, Jacob DS, Gedanken A (2005) Solid state synthesis of tungsten carbide nanorods and nanoplatelets by a single-step pyrolysis. J Phys Chem B 109:19056–19059
114. Zellnera MB, Chen JG (2005) Surface science and electrochemical studies of WC and W_2C PVD films as potential electrocatalysts. Catal Today 99:299–307
115. Chhina H, Campbell S, Kesler O (2007) Thermal and electrochemical stability of tungsten carbide catalyst supports. J Power Sourc 164:431–440
116. Chen JG (1996) Carbide and nitride overlayers on early transition metal surfaces: preparation, characterization, and reactivities. Chem Rev 96:1477–1498
117. McGee RC, Bej SK, Thompson LT (2005) Basic properties of molybdenum and tungsten nitride catalysts. Appl Catal A 284:139–146
118. Youn DH, Bae G, Han S, Kim JY, Jang J-W, Park H, Choi SH, Lee JS (2013) A highly efficient transition metal nitride-based electrocatalyst for oxygen reduction reaction: TiN on a CNT-graphene hybrid support. J Mater Chem A 1:8007–8015
119. Chen J, Takanabe K, Ohnishi R, Lu D, Okada S, Hatasawa H, Morioka H, Antonietti M, Kubota J, Domen K (2010) Nano-sized TiN on carbon black as an efficient electrocatalyst for the oxygen reduction reaction prepared using an mpg-C_3N_4 template. Chem Commun 46:7492–7494
120. Luo JM, Tang HB, Tian XL, Liao SJ, Ren JW, Zhao WY, Qiao XC (2019) Glucose-derived carbon supported well-dispersed CrN as competitive oxygen reduction catalysts in acidic medium. Electrochim Acta 314:202–211
121. Chen J, Wei X, Zhang J, Luo Y, Chen YH, Wang G, Wang RL (2019) Titanium Nitride Hollow Spheres Consisting of TiN Nanosheets and Their Controllable Carbon-Nitrogen Active Sites as Efficient Electrocatalyst for Oxygen Reduction Reaction. Ind Eng Chem Res 588:2741–2748
122. Cui Z, Burns RG, DiSalvo FJ (2013) Mesoporous $Ti_{0.5}Nb_{0.5}N$ ternary nitride as a novel noncarbon support for oxygen reduction reaction in acid and alkaline electrolytes. Chem Mater 25:3782–3784
123. Yang M, Van Wassen AR, Guarecuco R, Abruna HD, DiSalvo FJ (2013) Nano-structured ternary niobium titanium nitrides as durable non-carbon supports for oxygen reduction reaction. Chem Commun 49:10853–10855
124. Yang M, Cui Z, DiSalvo FJ (2012) Mesoporous vanadium nitride as a high performance catalyst support for formic acid electrooxidation. Chem Commun 48:10502–10504
125. Kumar R, Pasupathi S, Pollet BG, Scott K (2013) Nafion-stabilised platinum nanoparticles supported on titanium nitride: An efficient and durable electrocatalyst for phosphoric acid based polymer electrolyte fuel cells. Electrochim Acta 109:365–369
126. Pan Z, Xiao Y, Fu Z, Zhan G, Wu S, Xiao C, Hu G, Wei Z (2014) Hollow and porous titanium nitride nanotubes as high performance catalyst support for oxygen reduction reaction. J Mater Chem A 2:13966–13975
127. Chen Z, Higgins D, Yu A, Zhang L, Zhang J (2011) A review on non-precious metal electrocatalysts for PEM fuel cells. Energy Environ Sci 4:3167–3192
128. Ham DJ, Lee JS (2009) Transition metal carbides and nitrides as electrode materials for low temperature fuel cells. Energies 2:873–899
129. Greeley J, Rossmeisl J, Hellmann A, Norskov J (2007) Theoretical trends in particle size effects for the oxygen reduction reaction. Zeitschrift Für Physikalische Chemie 221(9–10):1209–1220
130. Han B, Miranda C, Ceder G (2008) Effect of particle size and surface structure on adsorption of O and OH on platinum nanoparticles: A first-principles study. Phy Rev B 77(7):075410

131. Tritsaris G, Greeley J, Rossmeisl J, Nørskov JK (2011) Atomic-scale modeling of particle size effects for the oxygen reduction reaction on Pt. Catal Lett 141(7):909–913
132. Greeley J, Stephens I, Bondarenko A, Johansson TP, Hansen HA, Jaramillo T, Rossmeisl J, Chorkendorff I, Nørskov JK (2009) Alloys of platinum and early transition metals as oxygen reduction electrocatalysts. Nat Chem 1(7):552–556
133. Mani P, Srivastava R, Strasser P (2011) Dealloyed binary PtM3 (M= Cu Co, Ni) and ternary PtNi3M (M= Cu Co, Fe, Cr) electrocatalysts for the oxygen reduction reaction: performance in polymer electrolyte membrane fuel cells. J Power Sources 196(2):666–673
134. Koenigsmann C, Santulli AC, Gong K, Vukmirovic MB, Zhou W-P, Sutter E, Wong SS, Adzic RR (2011) Enhanced electrocatalytic performance of processed, ultrathin, supported Pd–Pt core–shell nanowire catalysts for the oxygen reduction reaction. J Am Chem Soc 133(25):9783–9795
135. Yoo SJ, Kim S-K, Jeon T-Y, Hwang SJ, Lee J-G, Lee S-C, Lee K-S, Cho Y-H, Sung Y-E, Lim T-H (2011) Enhanced stability and activity of Pt–Y alloy catalysts for electrocatalytic oxygen reduction. Chem Commun 47(41):11414–11416
136. Carpenter MK, Moylan TE, Kukreja RS, Atwan MH, Tessema MM (2012) Solvothermal synthesis of platinum alloy nanoparticles for oxygen reduction electrocatalysis. J Am Chem Soc 134(20):8535–8542
137. Yu W, Porosoff MD, Chen JG (2012) Review of Pt-based bimetallic catalysis: from model surfaces to supported catalysts. Chem Rev 112(11):5780–5817
138. He C, Meng H, Yao X, Shen PK (2012) Rapid formation of nanoscale tungsten carbide on graphitized carbon for electrocatalysis. Int J Hyd Energy 37(10):8154–8160
139. He C, Shen PK (2014) Pt loaded on truncated hexagonal pyramid WC/graphene for oxygen reduction reaction. Nano Energy 8:52–61
140. Senevirathne K, Hui R, Campbell S, Ye S, Zhang J (2012) Electrocatalytic activity and durability of Pt/NbO2 and Pt/Ti4O7 nanofibers for PEM fuel cell oxygen reduction reaction. Electrochim Acta 59:538–547
141. Tan Y, Fan J, Chen G, Zheng N, Xie Q (2011) Au/Pt and Au/Pt 3 Ni nanowires as self-supported electrocatalysts with high activity and durability for oxygen reduction. Chem Commun 47(42):11624–11626
142. Wu J, Qi L, You H, Gross A, Li J, Yang H (2012) Icosahedral platinum alloy nanocrystals with enhanced electrocatalytic activities. J Am Chem Soc 134(29):11880–11883
143. Xu X, Zhang X, Sun H, Yang Y, Dai X, Gao J, Li X, Zhang P, Wang HH, Yu NF (2014) Synthesis of Pt–Ni alloy nanocrystals with high-index facets and enhanced electrocatalytic properties. Angew Chem 126(46):12730–12735
144. Joo SH, Kwon K, You DJ, Pak C, Chang H, Kim JM (2009) Preparation of high loading Pt nanoparticles on ordered mesoporous carbon with a controlled Pt size and its effects on oxygen reduction and methanol oxidation reactions. Electrochim Acta 54(24):5746–5753
145. Maillard F, Martin M, Gloaguen F, Leger J-M (2002) Oxygen electroreduction on carbon-supported platinum catalysts. Particle-size effect on the tolerance to methanol competition. Electrochimica Acta 47(21):3431–3440
146. Kinoshita K (1990) Particle size effects for oxygen reduction on highly dispersed platinum in acid electrolytes. J Electrochem Soc 137(3):845–848
147. Marković N, Adžić R, Cahan B, Yeager E (1994) Structural effects in electrocatalysis: oxygen reduction on platinum low index single-crystal surfaces in perchloric acid solutions. J Electr Chem 377(1–2):249–259
148. Kondo S, Nakamura M, Maki N, Hoshi N (2009) Active sites for the oxygen reduction reaction on the low and high index planes of palladium. J Phy Chem C 113(29):12625–12628
149. Imaoka T, Kitazawa H, Chun W-J, Omura S, Albrecht K, Yamamoto K (2013) Magic number Pt13 and misshapen Pt12 clusters: which one is the better catalyst? J Am Chem Soc 135(35):13089–13095
150. Nesselberger M, Roefzaad M, Hamou RF, Biedermann PU, Schweinberger FF, Kunz S, Schloegl K, Wiberg GK, Ashton S, Heiz U (2013) The effect of particle proximity on the oxygen reduction rate of size-selected platinum clusters. Nat Mater 12(10):919–924

151. Nørskov JK, Rossmeisl J, Logadottir A, Lindqvist L, Kitchin JR, Bligaard T, Jonsson H (2004) Origin of the overpotential for oxygen reduction at a fuel-cell cathode. J Phys Chem B 108(46):17886–17892
152. Stamenkovic V, Mun BS, Mayrhofer KJ, Ross PN, Markovic NM, Rossmeisl J, Greeley J, Nørskov JK (2006) Changing the activity of electrocatalysts for oxygen reduction by tuning the surface electronic structure. Angew Chem Int Ed 45(18):2897–2901
153. Zhang H, Jin M, Wang J, Li W, Camargo PH, Kim MJ, Yang D, Xie Z, Xia Y (2011) Synthesis of Pd− Pt bimetallic nanocrystals with a concave structure through a bromide-induced galvanic replacement reaction. J Am Chem Soc 133(15):6078–6089
154. Zhang J, Sasaki K, Sutter E, Adzic R (2007) Stabilization of platinum oxygen-reduction electrocatalysts using gold clusters. Science 315(5809):220–222
155. Zhang Y, Duan Z, Xiao C, Wang G (2011) Density functional theory calculation of platinum surface segregation energy in Pt3Ni (111) surface doped with a third transition metal. Surf Sci 605(15–16):1577–1582
156. Ramírez-Caballero GE, Balbuena PB (2011) Confinement-induced changes in magnetic behavior of a Ti monolayer on Pt. Chem Phys Lett 507(1–3):117–121
157. Nørskov JK, Bligaard T, Rossmeisl J, Christensen CH (2009) Towards the computational design of solid catalysts. Nat Chem 1(1):37
158. Lim B, Jiang M, Camargo PH, Cho EC, Tao J, Lu X, Zhu Y, Xia Y (2009) Pd-Pt bimetallic nanodendrites with high activity for oxygen reduction. Science 324(5932):1302–1305
159. Stamenkovic VR, Fowler B, Mun BS, Wang G, Ross PN, Lucas CA, Marković NM (2007) Improved oxygen reduction activity on Pt3Ni (111) via increased surface site availability. Science 315(5811):493–497
160. Kitchin JR, Nørskov JK, Barteau MA, Chen J (2004) Role of strain and ligand effects in the modification of the electronic and chemical properties of bimetallic surfaces. Phys Rev Lett 93(15):156801
161. Strasser P, Koh S, Anniyev T, Greeley J, More K, Yu C, Liu Z, Kaya S, Nordlund D, Ogasawara H (2010) Lattice-strain control of the activity in dealloyed core–shell fuel cell catalysts. Nat Chem 2(6):454
162. Cui C, Gan L, Heggen M, Rudi S, Strasser P (2013) Compositional segregation in shaped Pt alloy nanoparticles and their structural behaviour during electrocatalysis. Nat Mater 12(8):765–771
163. Zhang H, Shen PK (2012) Recent development of polymer electrolyte membranes for fuel cells. Chem Rev 112(5):2780–2832
164. Mayrhofer KJ, Arenz M (2009) Fuel cells: log on for new catalysts. Nat Chem 1(7):518
165. Yoo SJ, Hwang SJ, Lee J-G, Lee S-C, Lim T-H, Sung Y-E, Wieckowski A, Kim S-K (2012) Promoting effects of La for improved oxygen reduction activity and high stability of Pt on Pt–La alloy electrodes. Energy Environ Sci 5(6):7521–7525
166. Hernandez-Fernandez P, Masini F, McCarthy DN, Strebel CE, Friebel D, Deiana D, Malacrida P, Nierhoff A, Bodin A, Wise AM (2014) Mass-selected nanoparticles of Pt x Y as model catalysts for oxygen electroreduction. Nat Chem 6(8):732
167. Sau TK, Rogach AL, Jäckel F, Klar TA, Feldmann J (2010) Properties and applications of colloidal nonspherical noble metal nanoparticles. Adv Mater 22(16):1805–1825
168. De Marco L, Manca M, Giannuzzi R, Belviso MR, Cozzoli PD, Gigli G (2013) Shape-tailored TiO 2 nanocrystals with synergic peculiarities as building blocks for highly efficient multi-stack dye solar cells. Energy Environ Sci 6(6):1791–1795
169. Tian N, Zhou Z-Y, Sun S-G, Ding Y, Wang ZL (2007) Synthesis of tetrahexahedral platinum nanocrystals with high-index facets and high electro-oxidation activity. Science 316(5825):732–735
170. Mazumdar S, Bhattacharyya AJ (2013) Dependence of electron recombination time and light to electricity conversion efficiency on shape of the nanocrystal light sensitizer. Energy Environ Sci 6(5):1494–1498
171. Porter NS, Wu H, Quan Z, Fang J (2013) Shape-control and electrocatalytic activity-enhancement of Pt-based bimetallic nanocrystals. Acc Chem Res 46(8):1867–1877

172. Ming T, Feng W, Tang Q, Wang F, Sun L, Wang J, Yan C (2009) Growth of tetrahexahedral gold nanocrystals with high-index facets. J Am Chem Soc 131(45):16350–16351
173. Tian N, Zhou Z-Y, Yu N-F, Wang L-Y, Sun S-G (2010) Direct electrodeposition of tetrahexahedral Pd nanocrystals with high-index facets and high catalytic activity for ethanol electrooxidation. J Am Chem Soc 132(22):7580–7581
174. Zhang J, Langille MR, Personick ML, Zhang K, Li S, Mirkin CA (2010) Concave cubic gold nanocrystals with high-index facets. J Am Chem Soc 132(40):14012–14014
175. Personick ML, Langille MR, Zhang J, Mirkin CA (2011) Shape control of gold nanoparticles by silver underpotential deposition. Nano Lett 11(8):3394–3398
176. Tran TT, Lu X (2011) Synergistic effect of Ag and Pd ions on shape-selective growth of polyhedral Au nanocrystals with high-index facets. J Phy Chem C 115(9):3638–3645
177. Ma Y, Kuang Q, Jiang Z, Xie Z, Huang R, Zheng L (2008) Synthesis of trisoctahedral gold nanocrystals with exposed high-index facets by a facile chemical method. Angew Chem Int Ed 47(46):8901–8904
178. Huang X, Zhao Z, Fan J, Tan Y, Zheng N (2011) Amine-assisted synthesis of concave polyhedral platinum nanocrystals having 411 high-index facets. J Am Chem Soc 133(13):4718–4721
179. Zhou Z-Y, Tian N, Huang Z-Z, Chen D-J, Sun S-G (2009) Nanoparticle catalysts with high energy surfaces and enhanced activity synthesized by electrochemical method. Faraday Discuss 140:81–92
180. Wang C, Daimon H, Lee Y, Kim J, Sun S (2007) Synthesis of monodisperse Pt nanocubes and their enhanced catalysis for oxygen reduction. J Am Chem Soc 129(22):6974–6975
181. Liang HW, Cao X, Zhou F, Cui CH, Zhang WJ, Yu SH (2011) A free-standing Pt-nanowire membrane as a highly stable electrocatalyst for the oxygen reduction reaction. Adv Mater 23(12):1467–1471
182. Liang HW, Liu S, Gong JY, Wang SB, Wang L, Yu SH (2009) Ultrathin Te nanowires: an excellent platform for controlled synthesis of ultrathin platinum and palladium nanowires/nanotubes with very high aspect ratio. Adv Mater 21(18):1850–1854
183. Sun S, Jaouen F, Dodelet JP (2008) Controlled growth of Pt nanowires on carbon nanospheres and their enhanced performance as electrocatalysts in PEM fuel cells. Adv Mater 20(20):3900–3904
184. Sun S, Zhang G, Geng D, Chen Y, Banis MN, Li R, Cai M, Sun X (2010) Direct growth of single-crystal Pt nanowires on Sn@ CNT nanocable: 3D electrodes for highly active electrocatalysts. Chem–A Eur J 16(3):829–835
185. Koenigsmann C, Zhou W-P, Adzic RR, Sutter E, Wong SS (2010) Size-dependent enhancement of electrocatalytic performance in relatively defect-free, processed ultrathin platinum nanowires. Nano Lett 10(8):2806–2811
186. Bu L, Guo S, Zhang X, Shen X, Su D, Lu G, Zhu X, Yao J, Guo J, Huang X (2016) Surface engineering of hierarchical platinum-cobalt nanowires for efficient electrocatalysis. Nat Commun 7(1):1–10
187. Choi S-I, Xie S, Shao M, Odell JH, Lu N, Peng H-C, Protsailo L, Guerrero S, Park J, Xia X (2013) Synthesis and characterization of 9 nm Pt–Ni octahedra with a record high activity of 3.3 A/mgPt for the oxygen reduction reaction. Nano Lett. 13(7):3420–3425
188. Mukerjee S (1990) Particle size and structural effects in platinum electrocatalysis. J Appl Electrochem 20(4):537–548
189. Zhang J, Vukmirovic MB, Sasaki K, Nilekar AU, Mavrikakis M, Adzic RR (2005) Mixed-metal Pt monolayer electrocatalysts for enhanced oxygen reduction kinetics. J Am Chem Soc 127(36):12480–12481
190. Mazumder V, Chi M, More KL, Sun S (2010) Core/shell Pd/FePt nanoparticles as an active and durable catalyst for the oxygen reduction reaction. J Am Chem Soc 132(23):7848–7849
191. Zhang H, Yin Y, Hu Y, Li C, Wu P, Wei S, Cai C (2010) Pd@ Pt core− shell nanostructures with controllable composition synthesized by a microwave method and their enhanced electrocatalytic activity toward oxygen reduction and methanol oxidation. J Phy Chem C 114(27):11861–11867

192. Chen Y, Yang F, Dai Y, Wang W, Chen S (2008) Ni@ Pt core− shell nanoparticles: synthesis, structural and electrochemical properties. J Phy Chem C 112(5):1645–1649
193. Shao M, Sasaki K, Marinkovic NS, Zhang L, Adzic RR (2007) Synthesis and characterization of platinum monolayer oxygen-reduction electrocatalysts with Co–Pd core–shell nanoparticle supports. Electrochem Commun 9(12):2848–2853
194. Sasaki K, Naohara H, Choi Y, Cai Y, Chen W-F, Liu P, Adzic RR (2012) Highly stable Pt monolayer on PdAu nanoparticle electrocatalysts for the oxygen reduction reaction. Nat Commun 3(1):1–9
195. Zhang H, Watanabe T, Okumura M, Haruta M, Toshima N (2012) Catalytically highly active top gold atom on palladium nanocluster. Nat Mater 11(1):49–52
196. Mayrhofer KJ, Juhart V, Hartl K, Hanzlik M, Arenz M (2009) Adsorbate-induced surface segregation for core–shell nanocatalysts. Angew Chem Int Ed 48(19):3529–3531
197. Tao F, Grass ME, Zhang Y, Butcher DR, Renzas JR, Liu Z, Chung JY, Mun BS, Salmeron M, Somorjai GA (2008) Reaction-driven restructuring of Rh-Pd and Pt-Pd core-shell nanoparticles. Science 322(5903):932–934
198. Lee M-H, Wang P-S, Do J-S (2008) Effect of acid treatment of Co rich core–Pt rich shell/C electrocatalyst on oxygen reduction reaction. J Solid State Electrochem 12(7–8):879–884
199. Lee MH, Do JS (2009) Kinetics of oxygen reduction reaction on Corich core-Ptrich shell/C electrocatalysts. J Power Sources 188(2):353–358
200. Wang D, Xin HL, Hovden R, Wang H, Yu Y, Muller DA, DiSalvo FJ, Abruña HD (2013) Structurally ordered intermetallic platinum–cobalt core–shell nanoparticles with enhanced activity and stability as oxygen reduction electrocatalysts. Nat Mater 12(1):81
201. Bu L, Zhang N, Guo S, Zhang X, Li J, Yao J, Wu T, Lu G, Ma J-Y, Su D, Huang X (2016) Biaxially strained PtPb/Pt core/shell nanoplate boosts oxygen reduction catalysis. Science 354(6318):1410–1414
202. Wu J, Yang H (2013) Platinum-based oxygen reduction electrocatalysts. Acc Chem Res 46(8):1848–1857
203. Chen C, Kang Y, Huo Z, Zhu Z, Huang W, Xin HL, Snyder JD, Li D, Herron JA, Mavrikakis M (2014) Highly crystalline multimetallic nanoframes with three-dimensional electrocatalytic surfaces. Science 343(6177):1339–1343
204. Wang X, Figueroa-Cosme L, Yang X, Luo M, Liu J, Xie Z, Xia Y (2016) Pt-based icosahedral nanocages: using a combination of 111 facets, twin defects, and ultrathin walls to greatly enhance their activity toward oxygen reduction. Nano Lett 16(2):1467–1471
205. Tseung A, Dhara S (1974) The reduction of oxygen on platinised Sb doped SnO2 in 85% phosphoric acid. Electrochim Acta 19(12):845–848
206. Altamirano-Gutiérrez A, Fernández A, Varela FR (2013) Preparation and characterization of Pt-CeO2 and Pt-Pd electrocatalysts for the oxygen reduction reaction in the absence and presence of methanol in alkaline medium. Int J Hydrogen Energy 38(28):12657–12666
207. Huang S-Y, Ganesan P, Park S, Popov BN (2009) Development of a titanium dioxide-supported platinum catalyst with ultrahigh stability for polymer electrolyte membrane fuel cell applications. J Am Chem Soc 131(39):13898–13899
208. Yan Z, Wei W, Xie J, Meng S, Lü X, Zhu J (2013) An ion exchange route to produce WO3 nanobars as Pt electrocatalyst promoter for oxygen reduction reaction. J Power Sources 222:218–224
209. Vračar LM, Krstajić N, Radmilović V, Jakšić M (2006) Electrocatalysis by nanoparticles–oxygen reduction on Ebonex/Pt electrode. J Electroanal Chem 587(1):99–107
210. Babić B, Gulicovski J, Gajić-Krstajić L, Elezović N, Radmilović VR, Krstajić N, Vračar LM (2009) Kinetic study of the hydrogen oxidation reaction on sub-stoichiometric titanium oxide-supported platinum electrocatalyst in acid solution. J Power Sources 193(1):99–106
211. Shen PK, Xu C (2006) Alcohol oxidation on nanocrystalline oxide Pd/C promoted electrocatalysts. Electrochem Commun 8(1):184–188
212. KangáShen P (2005) The beneficial effect of the addition of tungsten carbides to Pt catalysts on the oxygen electroreduction. Chem Commun 35:4408–4410

213. Meng H, Shen PK (2005) Tungsten carbide nanocrystal promoted Pt/C electrocatalysts for oxygen reduction. J Phys Chem B 109(48):22705–22709
214. Ham DJ, Lee JS (2009) Transition metal carbides and nitrides as electrode materials for low temperature fuel cells. Energies 2(4):873–899
215. Esposito DV, Chen JG (2011) Monolayer platinum supported on tungsten carbides as low-cost electrocatalysts: opportunities and limitations. Energy Environ Sci 4(10):3900–3912
216. Elezović N, Babić BM, Gajić-Krstajić L, Ercius P, Radmilović VR, Krstajić N, Vračar LM (2012) Pt supported on nano-tungsten carbide as a beneficial catalyst for the oxygen reduction reaction in alkaline solution. Electrochim Acta 69:239–246
217. Hsu IJ, Hansgen DA, McCandless BE, Willis BG, Chen JG (2011) Atomic layer deposition of Pt on tungsten monocarbide (WC) for the oxygen reduction reaction. J Phys Chem C 115(9):3709–3715
218. Yan Z, Cai M, Shen PK (2013) Nanosized tungsten carbide synthesized by a novel route at low temperature for high performance electrocatalysis. Sci Rep 3:1646
219. Wang Y, Song S, Maragou V, Shen PK, Tsiakaras P (2009) High surface area tungsten carbide microspheres as effective Pt catalyst support for oxygen reduction reaction. Appl Catal B 89(1–2):223–228
220. Cui G, Shen PK, Meng H, Zhao J, Wu G (2011) Tungsten carbide as supports for Pt electrocatalysts with improved CO tolerance in methanol oxidation. J Power Sources 196(15):6125–6130
221. He G, Yan Z, Cai M, Shen PK, Gao MR, Yao HB, Yu SH (2012) Ion-exchange-assisted synthesis of Pt-VC nanoparticles loaded on graphitized carbon: a high-performance nanocomposite electrocatalyst for oxygen-reduction reactions. Chem–A Eur J 18(27):8490–8497
222. Yan Z, He G, Shen PK, Luo Z, Xie J, Chen M (2014) MoC–graphite composite as a Pt electrocatalyst support for highly active methanol oxidation and oxygen reduction reaction. J Mater Chems 2(11):4014–4022
223. Ma X, Meng H, Cai M, Shen PK (2012) Bimetallic carbide nanocomposite enhanced Pt catalyst with high activity and stability for the oxygen reduction reaction. J Am Chem Soc 134(4):1954–1957
224. Novoselov KS, Geim AK, Morozov SV, Jiang D, Zhang Y, Dubonos SV, Grigorieva IV, Firsov AA (2004) Electric field effect in atomically thin carbon films. Science 306(5696):666–669
225. Gómez-Navarro C, Burghard M, Kern K (2008) Elastic properties of chemically derived single graphene sheets. Nano Lett 8(7):2045–2049
226. Bunch JS, Van Der Zande AM, Verbridge SS, Frank IW, Tanenbaum DM, Parpia JM, Craighead HG, McEuen PL (2007) Electromechanical resonators from graphene sheets. Science 315(5811):490–493
227. Lee C, Wei X, Kysar JW, Hone J (2008) Measurement of the elastic properties and intrinsic strength of monolayer graphene. Science 321(5887):385–388
228. McCann E, Fal'ko VI (2006) Landau-level degeneracy and quantum Hall effect in a graphite bilayer. Phys Rev Lett 96(8):086805
229. Peres N, Guinea F, Neto AC (2006) Electronic properties of disordered two-dimensional carbon. Phys Rev B 73(12):125411
230. Berger C, Song Z, Li X, Wu X, Brown N, Naud C, Mayou D, Li T, Hass J, Marchenkov AN (2006) Electronic confinement and coherence in patterned epitaxial graphene. Science 312(5777):1191–1196
231. Novoselov KS, Geim AK, Morozov S, Jiang D, Katsnelson MI, Grigorieva I, Dubonos S, Firsov, AA (2005) Two-dimensional gas of massless Dirac fermions in graphene. Nature 438(7065):197–200
232. Geim AK, Novoselov KS (2010) The rise of graphene. In Nanoscience and technology: a collection of reviews from nature journals. World Scientific, pp 11–19
233. Castro EV, Novoselov K, Morozov S, Peres N, Dos Santos JL, Nilsson J, Guinea F, Geim A, Neto AC (2007) Biased bilayer graphene: semiconductor with a gap tunable by the electric field effect. Phys Rev Lett 99(21):216802

234. Ratinac KR, Yang W, Ringer SP, Braet F (2010) Toward Ubiquitous Environmental Gas Sensors Capitalizing on the Promise of Graphene. Environ Sci Technol 44(4):1167–1176
235. Pumera M (2011) Graphene-based nanomaterials for energy storage. Energy Environ Sci 4(3):668–674
236. Xiang Q, Yu J, Jaroniec M (2012) Graphene-based semiconductor photocatalysts. Chem Soc Rev 41(2):782–796
237. Zhang Y, Zhang L, Zhou C (2013) Review of chemical vapor deposition of graphene and related applications. Acc Chem Res 46(10):2329–2339
238. Liang Y, Li Y, Wang H, Zhou J, Wang J, Regier T, Dai H (2011) Co 3 O 4 nanocrystals on graphene as a synergistic catalyst for oxygen reduction reaction. Nat Mater 10(10):780–786
239. Liang Y, Wang H, Zhou J, Li Y, Wang J, Regier T, Dai H (2012) Covalent hybrid of spinel manganese–cobalt oxide and graphene as advanced oxygen reduction electrocatalysts. J Am Chem Soc 134(7):3517–3523
240. Tang L, Wang Y, Li Y, Feng H, Lu J, Li J (2009) Preparation, structure, and electrochemical properties of reduced graphene sheet films. Adv Func Mater 19(17):2782–2789
241. Shao Y, Zhang S, Wang C, Nie Z, Liu J, Wang Y, Lin Y (2010) Highly durable graphene nanoplatelets supported Pt nanocatalysts for oxygen reduction. J Power Sources 195(15):4600–4605
242. He G, Song Y, Liu K, Walter A, Chen S, Chen S (2013) Oxygen reduction catalyzed by platinum nanoparticles supported on graphene quantum dots. Acs Catalysis 3(5):831–838
243. Lim D-H, Wilcox J (2012) Mechanisms of the oxygen reduction reaction on defective graphene-supported Pt nanoparticles from first-principles. J Phy Chem C 116(5):3653–3660
244. Deifallah M, McMillan PF, Cora F (2008) Electronic and structural properties of two-dimensional carbon nitride graphenes. J Phy Chem C 112(14):5447–5453
245. Shao Y, Zhang S, Engelhard MH, Li G, Shao G, Wang Y, Liu J, Aksay IA, Lin Y (2010) Nitrogen-doped graphene and its electrochemical applications. J Mater Chem 20(35):7491–7496
246. Bai J, Zhu Q, Lv Z, Dong H, Yu J, Dong L (2013) Nitrogen-doped graphene as catalysts and catalyst supports for oxygen reduction in both acidic and alkaline solutions. Int J Hydrogen Energy 38(3):1413–1418
247. Vinayan BP, Nagar R, Rajalakshmi N, Ramaprabhu S (2012) Novel platinum-cobalt alloy nanoparticles dispersed on nitrogen-doped graphene as a cathode electrocatalyst for PEMFC applications. Adv Func Mater 22(16):3519–3526
248. Li Y, Li Y, Zhu E, McLouth T, Chiu C-Y, Huang X, Huang Y (2012) Stabilization of high-performance oxygen reduction reaction Pt electrocatalyst supported on reduced graphene oxide/carbon black composite. J Am Chem Soc 134(30):12326–12329
249. Tiwari JN, Nath K, Kumar S, Tiwari RN, Kemp KC, Le NH, Youn DH, Lee JS, Kim KS (2013) Stable platinum nanoclusters on genomic DNA–graphene oxide with a high oxygen reduction reaction activity. Nat Commun 4(1):1–7
250. Liu L, Samjeske G, Nagamatsu S-I, Sekizawa O, Nagasawa K, Takao S, Imaizumi Y, Yamamoto T, Uruga T, Iwasawa Y (2014) Dependences of the oxygen reduction reaction activity of Pd–Co/C and Pd–Ni/C alloy electrocatalysts on the nanoparticle size and lattice constant. Top Catal 57(6–9):595–606
251. Yin S, Cai M, Wang C, Shen PK (2011) Tungsten carbide promoted Pd–Fe as alcohol-tolerant electrocatalysts for oxygen reduction reactions. Energy Environ Sci 4(2):558–563
252. Meng H, Shen PK (2006) Novel Pt-free catalyst for oxygen electroreduction. Electrochem Commun 8(4):588–594
253. He G, Song Y, Phebus B, Liu K, Deming CP, Hu P, Chen S (2013) Electrocatalytic activity of organically functionalized silver nanoparticles in oxygen reduction. Sci Adv Mater 5(11):1727–1736
254. Blizanac BB, Lucas CA, Gallagher ME, Arenz M, Ross PN, Marković N (2004) Anion adsorption, CO oxidation, and oxygen reduction reaction on a Au (100) surface: The pH effect. J Phys Chem B 108(2):625–634

255. Zhang Y, Suryanarayanan V, Nakazawa I, Yoshihara S, Shirakashi T (2004) Electrochemical behavior of Au nanoparticle deposited on as-grown and O-terminated diamond electrodes for oxygen reduction in alkaline solution. Electrochim Acta 49(28):5235–5240
256. Prakash J, Joachin H (2000) Electrocatalytic activity of ruthenium for oxygen reduction in alkaline solution. Electrochim Acta 45(14):2289–2296
257. Jasinski R (1964) A new fuel cell cathode catalyst. Nature 201(4925):1212–1213
258. Jaouen F, Dodelet J-P (2007) Average turn-over frequency of O2 electro-reduction for Fe/N/C and Co/N/C catalysts in PEFCs. Electrochim Acta 52(19):5975–5984
259. Chen Z, Higgins D, Yu A, Zhang L, Zhang J (2011) A review on non-precious metal electrocatalysts for PEM fuel cells. Energy Environ Sci 4(9):3167–3192
260. Ma S, Goenaga GA, Call AV, Liu DJ (2011) Cobalt imidazolate framework as precursor for oxygen reduction reaction electrocatalysts. Chem–A Eur J 17(7):2063–2067
261. Wu G, Johnston CM, Mack NH, Artyushkova K, Ferrandon M, Nelson M, Lezama-Pacheco JS, Conradson SD, More KL, Myers DJ (2011) Synthesis–structure–performance correlation for polyaniline–Me–C non-precious metal cathode catalysts for oxygen reduction in fuel cells. J Mater Chem 21(30):11392–11405
262. Gorlin Y, Chung C-J, Nordlund D, Clemens BM, Jaramillo TF (2012) Mn3O4 supported on glassy carbon: an active non-precious metal catalyst for the oxygen reduction reaction. Acs Catalysis 2(12):2687–2694
263. Mao L, Zhang D, Sotomura T, Nakatsu K, Koshiba N, Ohsaka T (2003) Mechanistic study of the reduction of oxygen in air electrode with manganese oxides as electrocatalysts. Electrochim Acta 48(8):1015–1021
264. Wu Z-S, Yang S, Sun Y, Parvez K, Feng X, Müllen K (2012) 3D nitrogen-doped graphene aerogel-supported Fe3O4 nanoparticles as efficient electrocatalysts for the oxygen reduction reaction. J Am Chem Soc 134(22):9082–9085
265. Malviya M, Singh J, Singh R (2005) Electrochemical characterization of polypyrrole/cobalt ferrite composite films for oxygen reduction
266. Xiao L, Zhuang L, Liu Y, Lu J (2009) Activating Pd by morphology tailoring for oxygen reduction. J Am Chem Soc 131(2):602–608
267. Erikson H, Sarapuu A, Tammeveski K, Solla-Gullón J, Feliu JM (2011) Enhanced electrocatalytic activity of cubic Pd nanoparticles towards the oxygen reduction reaction in acid media. Electrochem Commun 13(7):734–737
268. Shao M, Yu T, Odell JH, Jin M, Xia Y (2011) Structural dependence of oxygen reduction reaction on palladium nanocrystals. Chem Commun 47(23):6566–6568
269. Marković N, Ross P Jr (2002) Surface science studies of model fuel cell electrocatalysts. Surf Sci Rep 45(4–6):117–229
270. Jiang L, Hsu A, Chu D, Chen R (2009) Size-dependent activity of palladium nanoparticles for oxygen electroreduction in alkaline solutions. J Electrochem Soc 156(5):B643–B649
271. Koenigsmann C, Santulli AC, Sutter E, Wong SS (2011) Ambient surfactantless synthesis, growth mechanism, and size-dependent electrocatalytic behavior of high-quality, single crystalline palladium nanowires. ACS Nano 5(9):7471–7487
272. Yang X, Hu J, Fu J, Wu R, Koel BE (2011) Role of surface iron in enhanced activity for the oxygen reduction reaction on a Pd3Fe (111) Single-Crystal Alloy. Angew Chem Int Ed 50(43):10182–10185
273. Shao M, Liu P, Zhang J, Adzic R (2007) Origin of enhanced activity in palladium alloy electrocatalysts for oxygen reduction reaction. J Phys Chem B 111(24):6772–6775
274. Koenigsmann C, Sutter E, Chiesa TA, Adzic RR, Wong SS (2012) Highly enhanced electrocatalytic oxygen reduction performance observed in bimetallic palladium-based nanowires prepared under ambient, surfactantless conditions. Nano Lett 12(4):2013–2020
275. Sarkar A, Murugan AV, Manthiram A (2008) Synthesis and characterization of nanostructured Pd− Mo electrocatalysts for oxygen reduction reaction in fuel cells. J Phys Chem C 112(31):12037–12043
276. Lv J-J, Li S-S, Wang A-J, Mei L-P, Feng J-J, Chen J-R, Chen Z (2014) One-pot synthesis of monodisperse palladium–copper nanocrystals supported on reduced graphene oxide

nanosheets with improved catalytic activity and methanol tolerance for oxygen reduction reaction. J Power Sources 269:104–110
277. Greeley J, Nørskov JK, Mavrikakis M (2002) Electronic structure and catalysis on metal surfaces. Annu Rev Phys Chem 53(1):319–348
278. Park SH, Choi CH, Koh JK, Pak C, Jin S-A, Woo SI (2013) Combinatorial high-throughput screening for highly active Pd–Ir–Ce based ternary catalysts in electrochemical oxygen reduction reaction. ACS Combin Sci 15(11):572–579
279. Liao H, Zhu J, Hou Y (2014) Synthesis and electrocatalytic properties of PtBi nanoplatelets and PdBi nanowires. Nanoscale 6(2):1049–1055
280. Böhm H (1970) New non-noble metal anode catalysts for acid fuel cells. Nature 227(5257):483–484
281. Anastasijević N, Dimitrijević Z, Adžić R (1992) Oxygen reduction on a modified ruthenium electrode. Electrochim Acta 37(3):457–464
282. Bashyam R, Zelenay P (2006) A class of non-precious metal composite catalysts for fuel cells. Nature 443(7107):63–66
283. Li W, Yu A, Higgins DC, Llanos BG, Chen Z (2010) Biologically inspired highly durable iron phthalocyanine catalysts for oxygen reduction reaction in polymer electrolyte membrane fuel cells. J Am Chem Soc 132(48):17056–17058
284. Zhang C, Hao R, Yin H, Liu F, Hou Y (2012) Iron phthalocyanine and nitrogen-doped graphene composite as a novel non-precious catalyst for the oxygen reduction reaction. Nanoscale 4(23):7326–7329
285. Ahmed J, Yuan Y, Zhou L, Kim S (2012) Carbon supported cobalt oxide nanoparticles–iron phthalocyanine as alternative cathode catalyst for oxygen reduction in microbial fuel cells. J Power Sources 208:170–175
286. McGuire R Jr, Dogutan DK, Teets TS, Suntivich J, Shao-Horn Y, Nocera DG (2010) Oxygen reduction reactivity of cobalt (II) hangman porphyrins. Chem Sci 1(3):411–414
287. Charreteur F, Jaouen F, Ruggeri S, Dodelet J-P (2008) Fe/N/C non-precious catalysts for PEM fuel cells: Influence of the structural parameters of pristine commercial carbon blacks on their activity for oxygen reduction. Electrochim Acta 53(6):2925–2938
288. Faubert G, Côté R, Guay D, Dodelet J, Dénès G, Poleunis C, Bertrand P (1998) Activation and characterization of Fe-based catalysts for the reduction of oxygen in polymer electrolyte fuel cells. Electrochim Acta 43(14–15):1969–1984
289. Jaouen F, Herranz J, Lefevre M, Dodelet J-P, Kramm UI, Herrmann I, Bogdanoff P, Maruyama J, Nagaoka T, Garsuch A (2009) Cross-laboratory experimental study of non-noble-metal electrocatalysts for the oxygen reduction reaction. ACS Appl Mater Interfaces 1(8):1623–1639
290. Van Veen J, Colijn H, Van Baar J (1988) On the effect of a heat treatment on the structure of carbon-supported metalloporphyrins and phthalocyanines. Electrochim Acta 33(6):801–804
291. Franke R, Ohms D, Wiesener K (1989) Investigation of the influence of thermal treatment on the properties of carbon materials modified by N4-chelates for the reduction of oxygen in acidic media. J Electr Chem Inter Electr 260(1):63–73
292. Wiesener K (1986) N4-chelates as electrocatalyst for cathodic oxygen reduction. Electrochim Acta 31(8):1073–1078
293. Van Der Putten A, Elzing A, Visscher W, Barendrecht E (1986) Oxygen reduction on pyrolysed carbon-supported transition metal chelates. J Electr Chem Int Electr 205(1–2):233–244
294. Gojković SL, Gupta S, Savinell R (1999) Heat-treated iron (III) tetramethoxyphenyl porphyrin chloride supported on high-area carbon as an electrocatalyst for oxygen reduction: Part II. Kinetics of oxygen reduction. J Electroanalyt Chem 462(1):63–72
295. Jaouen F, Proietti E, Lefèvre M, Chenitz R, Dodelet J-P, Wu G, Chung HT, Johnston CM, Zelenay P (2011) Recent advances in non-precious metal catalysis for oxygen-reduction reaction in polymer electrolyte fuel cells. Energy Environ Sci 4(1):114–130
296. Lefèvre M, Proietti E, Jaouen F, Dodelet J-P (2009) Iron-based catalysts with improved oxygen reduction activity in polymer electrolyte fuel cells. Science 324(5923):71–74
297. Wu G, More KL, Johnston CM, Zelenay P (2011) High-performance electrocatalysts for oxygen reduction derived from polyaniline, iron, and cobalt. Science 332(6028):443–447

298. Cruz-Silva E, Lopez-Urias F, Munoz-Sandoval E, Sumpter BG, Terrones H, Charlier J-C, Meunier V, Terrones M (2011) Phosphorus and phosphorus–nitrogen doped carbon nanotubes for ultrasensitive and selective molecular detection. Nanoscale 3(3):1008–1013
299. Cruz-Silva E, Lopez-Urias F, Munoz-Sandoval E, Sumpter BG, Terrones H, Charlier J-C, Meunier V, Terrones M (2009) Electronic transport and mechanical properties of phosphorus- and phosphorus− nitrogen-doped carbon nanotubes. ACS Nano 3(7):1913–1921
300. Wu J, Yang Z, Li X, Sun Q, Jin C, Strasser P, Yang R (2013) Phosphorus-doped porous carbons as efficient electrocatalysts for oxygen reduction. J Mater Chem 1(34):9889–9896
301. Wu J, Yang Z, Wang Z, Sun Q, Yang R (2014) Synthesis and electrocatalytic activity of phosphorus and Co co-doped mesoporous carbon for oxygen reduction. Electrochem Commun 42:46–49
302. Choi CH, Park SH, Woo SI (2012) Phosphorus–nitrogen dual doped carbon as an effective catalyst for oxygen reduction reaction in acidic media: effects of the amount of P-doping on the physical and electrochemical properties of carbon. J Mater Chem 22(24):12107–12115
303. Zhu J, Shen PK (2013) Chelate resin self-assembled quaternary Co–N–P–C catalyst for oxygen reduction reaction. RSC Advances 3(34):14686–14690
304. Zhang L-S, Liang X-Q, Song W-G, Wu Z-Y (2010) Identification of the nitrogen species on N-doped graphene layers and Pt/NG composite catalyst for direct methanol fuel cell. Phy Chem Chem Phy 12(38):12055–12059
305. Zhou J, Fang H, Hu Y, Sham T, Wu C, Liu M, Li F (2009) Immobilization of RuO2 on carbon nanotube: An x-ray absorption near-edge structure study. J Phy Chem C 113(24):10747–10750
306. Rojas TC, Sánchez-López JC, Sayagués MJ, Reddy EP, Caballero A, Fernández A (1999) Preparation, characterization and thermal evolution of oxygen passivated nanocrystalline cobalt. J Mater Chem 9(4):1011–1017
307. Zhou J, Fang H, Maley J, Murphy M, Ko JP, Cutler J, Sammynaiken R, Sham T, Liu M, Li F (2009) Electronic structure of TiO 2 nanotube arrays from X-ray absorption near edge structure studies. J Mater Chem 19(37):6804–6809
308. Bag S, Roy K, Gopinath CS, Raj CR (2014) Facile single-step synthesis of nitrogen-doped reduced graphene oxide-Mn3O4 hybrid functional material for the electrocatalytic reduction of oxygen. ACS Appl Mater Interfaces 6(4):2692–2699
309. Behret H, Binder H, Sandstede G (1975) Electrocatalytic oxygen reduction with thiospinels and other sulphides of transition metals. Electrochim Acta 20(2):111–117
310. Feng Y, He T, Alonso-Vante N (2008) In situ free-surfactant synthesis and ORR-electrochemistry of carbon-supported Co3S4 and CoSe2 nanoparticles. Chem Mater 20(1):26–28
311. Vante NA, Jaegermann W, Tributsch H, Hoenle W, Yvon K (1987) Electrocatalysis of oxygen reduction by chalcogenides containing mixed transition metal clusters. J Am Chem Soc 109(11):3251–3257
312. Cao D, Wieckowski A, Inukai J, Alonso-Vante N (2006) Oxygen reduction reaction on ruthenium and rhodium nanoparticles modified with selenium and sulfur. J Electrochem Soc 153(5):A869–A874
313. Nekooi P, Akbari M, Amini MK (2010) CoSe nanoparticles prepared by the microwave-assisted polyol method as an alcohol and formic acid tolerant oxygen reduction catalyst. Int J Hyd Energy 35(12):6392–6398
314. Iijima S (1991) Helical microtubules of graphitic carbon. Nature 354:56–58
315. Wang N, Tang ZK, Li GD, Chen JS (2000) Materials science: single-walled 4 a carbon nanotube arrays. Nature 408:50–51
316. Tang ZK, Zhai JP, Tong YY et al (2008) Resonant raman scattering of the smallest single-walled carbon nanotubes. Phys Rev Lett 101:047402
317. Dillon AC, Jones KM, Bekkedahl TA et al (1997) Storage of hydrogen in single-walled carbon nanotubes. Nature 386:377–379
318. Liu M, Xiao X, Zhao S et al (2018) ZIF-67 derived Co@CNTs nanoparticles: remarkably improved hydrogen storage properties of MgH_2 and synergetic catalysis mechanism. Int J Hydrogen Energ 44:1059–1069

319. Noyce SG, Doherty JL, Cheng ZH et al (2019) Electronic stability of carbon nanotube transistors under long-term bias stress. Nano Lett 19:1460–1466
320. Tripathi P, Gupta BK, Bhatnagar A et al. (2018) Highly efficient field emission properties of radially aligned carbon nanotubes. J Mater Chem C, 6:6584–6590
321. Avouris P, Freitag M, Perebeinos V (2008) Carbon-Nanotube Photonics and Optoelectronics Nat Photon 2:341–350
322. Hadi B, Fahimeh M, Somayeh T et al (2018) A review on the effects of introducing CNTs in the modification process of electrochemical sensors. Electroanal 30:1–10
323. Ruopian F, Ke C, Lichang Y, et al. (2018) The regulating role of carbon nanotubes and graphene in lithium-ion and lithium-sulfur batteries. Adv Mater, 1800863
324. Yuan M, Yanjiao M, Dominic B et al (2018) Cobalt disulfide nanoparticles embedded in porous carbonaceous micro-polyhedrons interlinked by carbon nanotubes for superior lithium and sodium storage. ACS Nano 12:7220–7231
325. Yan M, Chen H, Yu Y, et al. (2018) 3D Ferroconcrete-like aminated carbon nanotubes network anchoring sulfur for advanced lithium-sulfur battery. Adv Energy Mater, 1801066
326. Chen J (1998) Solution Properties of single-walled carbon nanotubes. Science 282:95–98
327. Kuznetsova A, Popova I, Yates JT et al (2001) Oxygen-containing functional groups on single-wall carbon nanotubes: NEXAFS and vibrational spectroscopic studies. J Am Chem Soc 123:10699–10704
328. Xu T, Yang J, Liu J et al (2007) Surface modification of multi-walled carbon nanotubes by O2 plasma. Appl Surf Sci 253:8945–8951
329. Mabena LF, Sinha Ray S, Mhlanga SD, et al. (2011) Nitrogen-doped carbon nanotubes as a metal catalyst support. Appl Nanosci. 1: 67–77
330. Maciel IO, Campos-Delgado J, Cruz-Silva E et al (2009) Synthesis, Electronic Structure, and Raman Scattering of Phosphorus-Doped Single-Wall Carbon Nanotubes. Nano Lett 9:2267–2272
331. Lim S, Elim H, Gao X et al (2006) Electronic and optical properties of nitrogen-doped multiwalled carbon nanotubes. Phys Rev B 73:045402
332. Wang Z, Jia R, Zheng J et al (2011) Nitrogen-promoted self-assembly of N-doped carbon nanotubes and their intrinsic catalysis for oxygen reduction in fuel cells. ACS Nano 5:1677–1684
333. Feng L, Yan Y, Chen Y et al (2011) Nitrogen-doped carbon nanotubes as efficient and durable metal-free cathodic catalysts for oxygen reduction in microbial fuel cells. Energy Environ Sci 4:1892–1899
334. Gong K, Du F, Xia Z et al (2009) Nitrogen-doped carbon nanotube arrays with high electrocatalytic activity for oxygen reduction. Science 323:760–764
335. Banhart F, Kotakoski J, Krasheninnikov AV (2010) Structural defects in graphene. ACS Nano 5:26–41
336. Meng H, Shen PK (2006) Novel Pt-free catalyst for oxygen electroreduction. Electrochem Commun 8:588–594
337. Zheng Y, Jiao Y, Chen J et al (2011) Nanoporous graphitic-C_3N_4@Carbon metal-free electrocatalysts for highly efficient oxygen reduction. J Am Chem Soc 133:20116–20119
338. Zhang H, Shen PK (2012) Recent development of polymer electrolyte membranes for fuel cells. Chem Rev 112:2780–2832
339. Yin S, Cai M, Wang C et al (2011) Tungsten carbide promoted Pd–Fe as alcohol-tolerant electrocatalysts for oxygen reduction reactions. Energy Environ Sci 4:558–563
340. Tiwari JN, Nath K, Kumar S et al (2013) Stable platinum nanoclusters on genomic DNA-graphene oxide with a high oxygen reduction reaction activity. Nat Commun 4:1–7
341. Geng D, Liu H, Chen Y et al (2011) Non-noble metal oxygen reduction electrocatalysts based on carbon nanotubes with controlled nitrogen contents. J Power Sourc 196:1795–1801
342. Nagaiah TC, Kundu S, Bron M et al (2010) Nitrogen-doped carbon nanotubes as a cathode catalyst for the oxygen reduction reaction in alkaline medium. Electrochem Commun 12:338–341
343. Borghei M, Kanninen P, Lundahl M, et al. (2014) High oxygen reduction activity of few-walled carbon nanotubes with low nitrogen content. Appl Catal B: Environ 158–159: 233–241

344. Chen Z, Higgins D, Chen Z (2010) Nitrogen doped carbon nanotubes and their impact on the oxygen reduction reaction in fuel cells. Carbon 48:3057–3065
345. Li H, Liu H, Jong Z et al (2011) Nitrogen-doped carbon nanotubes with high activity for oxygen reduction in alkaline media. Int J Hydr Energy 36:2258–2265
346. Rao CV, Cabrera CR, Ishikawa Y (2010) In search of the active site in nitrogen-doped carbon nanotube electrodes for the oxygen reduction reaction. J Phys Chem Lett 1:2622–2627
347. Liu S, Zhang Y, Lin Y et al (2014) Tailoring the structure and nitrogen content of nitrogen-doped carbon nanotubes by water-assisted growth. Carbon 69:247–254
348. You C, Liao S, Li H et al (2014) Uniform nitrogen and sulfur co-doped carbon nanospheres as catalysts for the oxygen reduction reaction. Carbon 69:294–301
349. Li L, Qin Z-Y, Liang X et al (2009) Facile Ffabrication of uniform core-shell structured carbon nanotube-polyaniline nanocomposites. J Phys Chem C 113:5502–5507
350. Jin C, Nagaiah TC, Xia W et al (2013) Metal-free and electrocatalysis of oxygen reduction on nitrogen-containing multi-walled carbon nanotube modofied glassy carbon electrodes. Electrochim Acta 87:709–716
351. Vikkisk M, Kruusenberg I, Joost U et al (2013) Electrocatalysis of oxygen reduction on nitrogen-containing multi-walled carbon nanotube modified glassy carbon electrodes. Electrochim Acta 87:709–716
352. Yu D, Zhang Q, Dai L (2010) Highly efficient metal-free growth of nitrogen-doped single-walled carbon nanotubes on plasma-etched substrates for oxygen reduction. J Am Chem Soc 132:15127–15129
353. Xiong W, Du F, Liu Y et al (2010) 3-D carbon nanotube structures used as high performance catalyst for oxygen reduction reaction. J Am Chem Soc 132:15839–15841
354. Liu J, Sasaki K, Lyth SM (2013) Electrochemical oxygen reduction on metal-free nitrogen-doped graphene foam in acidic media. ECS Trans 58:1529–1540
355. Yi J-Y, Bernholc J (1993) Atomic structure and doping of microtubules. Phys Rev B 47:1708–1711
356. Susi T, Kaskela A, Zhu Z et al (2011) Nitrogen-doped single-walled carbon nanotube thin films exhibiting anomalous sheet resistances. Chem Mater 23:2201–2208
357. Liu Y, Zhan F, Wang BQ et al (2019) Three-dimensional composite catalysts for Al-O_2 batteries composed of $CoMn_2O_4$ nanoneedles supported on nitrogen-doped carbon nanotubes/graphene. ACS Appl Mater Interfaces 11:21526–21535
358. Su H, Wang X-T, Hu J-X, et al. (2019) Co-Mn spinel supported self-catalysis induced N-doped carbon nanotubes with high efficiency electron transport channels for zinc-air batteries. J Mater Chem A
359. Wiggins-Camacho JD, Stevenson KJ (2011) Mechanistic discussion of the oxygen reduction reaction at nitrogen-doped carbon nanotubes. J Phys Chem C 115:20002–20010
360. Zhao H, Xing T, Li L et al (2019) Synthesis of cobalt and nitrogen co-doped carbon nanotubes and its ORR activity as the catalyst used in hydrogen fuel cells. Int. J, Hydrogen Energy
361. Gao F, Zhao G-L, Yang S (2014) Catalytic reactions on the open-edge sites of nitrogen-doped carbon nanotubes as cathode catalyst for hydrogen fuel cells. ACS Catal 4:1267–1273
362. Yang L, Jiang S, Zhao Y et al (2011) Boron-doped carbon nanotubes as metal-free electrocatalysts for the oxygen reduction reaction. Angew Chem Int Ed 50:7132–7135
363. Novoselov KS, Geim AK, Morozov SV et al (2004) Electric field effect in atomically thin carbon films. Science 306:666–669
364. Li H, Sun C, Liu H et al (2019) Aerogels fabricated with origami graphene part I: preparation and mechanical behavior. J Alloy Comp 783:486–493
365. Bunch JS, Van Der Zande AM, Verbridge SS et al (2007) Electromechanical resonators from graphene sheets. Science 315:490–493
366. Lee C, Wei X, Kysar JW et al (2008) Measurement of the elastic properties and intrinsic strength of monolayer graphene. Science 321:385–388
367. Mortazavi B, Shahrokhi M, Raeisi M et al (2019) Outstanding strength, optical characteristics and thermal conductivity of graphene-like BC_3 and BC_6N semiconductors. Carbon 149:733–742

368. Li H, Li XM, Park J-H et al (2019) Restoring the photovoltaic effect in graphene-based van der Waals heterojunctions towards self-powered high-detectivity photodetectors. Nano Energy 57:214–221
369. Berger C (2006) Electronic confinement and coherence in patterned epitaxial graphene. Science 312:1191–1196
370. Gao X, Shen YQ, Ma YY (2019) Graphene/g-GeC bilayer heterostructure: Modulated electronic properties and interface contact via external vertical strains and electric field. Carbon 146:337–347
371. Novoselov K, Geim AK, Morozov S et al (2005) Two-dimensional gas of massless Dirac fermions in graphene. Nature 438:197–200
372. Deifallah M, McMillan PF, Corà F (2008) Electronic and structural properties of two-dimensional carbon nitride graphenes. J Phys Chem C 112:5447–5453
373. Wehling T, Novoselov K, Morozov S et al (2008) Molecular doping of graphene. Nano Lett 8:173–177
374. Gautam J, Thanh TD, Maiti K et al (2018) Highly efficient electrocatalyst of N-doped graphene-encapsulated cobalt-iron carbides towards oxygen reduction reaction. Carbon 137:358–367
375. Hu E, Yu X-Y, Chen F et al (2018) Graphene Layers-wrapped Fe/Fe5C2 nanoparticles supported on N-doped graphene nanosheets for highly efficient oxygen reduction. Adv Energy Mater 8:1702476
376. Zhao L, Sui XL, Li JZ et al (2018) Supramolecular assembly promoted synthesis of three-dimensional nitrogen doped graphene frameworks as efficient electrocatalyst for oxygen reduction reaction and methanol electrooxidation. Appl Catal B-Environ 231:224–233
377. Qu L, Liu Y, Baek J-B et al (2010) Nitrogen-doped graphene as efficient metal-free electrocatalyst for oxygen reduction in fuel cells. ACS Nano 4:1321–1326
378. He C, Li Z, Cai M et al (2013) A strategy for mass production of self-assembled nitrogen-doped graphene as catalytic materials. J Mater Chem A 1:1401
379. Sun Y, Li C, Shi G (2012) Nanoporous nitrogen doped carbon modified graphene as electrocatalyst for oxygen reduction reaction. J Mater Chem 22:12810–12816
380. Geng D, Chen Y, Chen Y et al (2011) High oxygen-reduction activity and durability of nitrogen-doped graphene. Energy Environ Sci 4:760–764
381. Li Y, Zhao Y, Cheng H et al (2011) Nitrogen-doped graphene quantum dots with oxygen-rich functional groups. J Am Chem Soc 134:15–18
382. Li Q, Zhang S, Dai L et al (2012) Nitrogen-doped colloidal graphene quantum dots and their size-dependentelectrocatalytic activity for the oxygen reduction reaction. J Am Chem Soc 134:18932–18935
383. Duan L, Zhao L, Cong H, et al (2019) Plasma treatment for nitrogen-doped 3D graphene framework by a conductive matrix with sulfur for high performance Li-S batteries. Small, 1804347
384. Bigras GR, Glad X, Vandsburger L et al (2019) Low-damage nitrogen incorporation in graphene films by nitrogen plasma treatment: Effect of airborne contaminants. Carbon 144:532–539
385. Zhou YL, Wang N, Muhammand J et al (2019) Graphene nanoflakes with optimized nitrogen doping fabricated by arc discharge as highly efficient absorbers toward microwave absorption. Carbon 148:204–213
386. Wei D, Liu Y, Wang Y et al (2009) Synthesis of N-doped graphene by chemical vapor deposition and its electrical properties. Nano Lett 9:1752–1758
387. Zhang C, Fu L, Liu N et al (2011) Synthesis of nitrogen-doped graphene using embedded carbon and nitrogen sources. Adv Mater 23:1020–1024
388. Guo B, Liu Q, Chen E et al (2010) Controllable N-doping of graphene. Nano Lett 10:4975–4980
389. Li X, Wang H, Robinson JT et al (2009) Simultaneous nitrogen doping and reduction of graphene oxide. J Am Chem Soc 131:15939–15944
390. Li N, Wang Z, Zhao K et al (2010) Large scale synthesis of N-doped multi-layered graphene sheets by simple arc-discharge method. Carbon 48:255–259
391. Zhang L, Xia Z (2011) Mechanisms of oxygen reduction reaction on nitrogen-doped graphene for fuel cells. J Phys Chem C 115:11170–11176

392. Sheng Z-H, Shao L, Chen J-J et al (2011) Catalyst-free synthesis of nitrogen-doped graphene via thermal annealing graphite oxide with melamine and its excellent electrocatalysis. ACS Nano 5:4350–4358
393. Boukhvalov DW, Son Y-W (2012) Oxygen reduction reactions on pure and nitrogen-doped graphene: a first-principles modeling. Nanoscale 4:417–420
394. Kim H, Lee K, Woo SI et al (2011) On the mechanism of enhanced oxygen reduction reaction in nitrogen-doped graphene nanoribbons. Phys Chem Chem Phys 13:17505
395. Ferrighi L, Datteo M, Di Valentin C (2013) Boosting graphene reactivity with oxygen by boron doping: density functional theory modeling of the reaction path. J Phys Chem C 118:223–230
396. Tam TV, Kang SG, Kim MH et al (2019) Novel graphene hydrogel/B-doped graphene quantum dots composites as trifunctional electrocatalysts for Zn-Air batteries and overall Water Splitting. Adv Energy Mater 9:1900945
397. Zhang C, Mahmood N, Yin H et al (2013) Synthesis of phosphorus-doped graphene and its multifunctional applications for oxygen reduction reaction and lithium ion batteries. Adv Mater 25:4932–4937
398. Li R, Wei Z, Gou X et al (2013) Phosphorus-doped graphene nanosheets as efficient metal-free oxygen reduction electrocatalysts. RSC Adv 3:9978–9984
399. Yang Z, Yao Z, Li G et al (2011) Sulfur-doped graphene as an efficient metal-free cathode catalyst for oxygen reduction. ACS Nano 6:205–211
400. Yao Z, Nie H, Yang Z et al (2012) Catalyst-free synthesis of iodine-doped graphene via a facile thermal annealing process and its use for electrocatalytic oxygen reduction in an alkaline medium. Chem Commun 48:1027
401. Song L, Liu Z, Reddy ALM et al (2012) Binary and ternary atomic layers built from carbon, boron, and nitrogen. Adv Mater 24:4878–4895
402. Zheng Y, Jiao Y, Ge L et al (2013) Two-step boron and nitrogen doping in graphene for enhanced synergistic catalysis. Angew Chem Int Ed 52:3110–3116
403. Ci L, Song L, Jin C et al (2010) Atomic layers of hybridized boron nitride and graphene domains. Nat Mater 9:430–435
404. Wang X, Wang J, Wang D et al (2014) One-pot synthesis of nitrogen and sulfur co-doped graphene as efficient metal-free electrocatalysts for the oxygen reduction reaction. Chem Commun 50:4839–4842
405. Su Y, Zhang Y, Zhuang X et al (2013) Low-temperature synthesis of nitrogen/sulfur co-doped three-dimensional graphene frameworks as efficient metal-free electrocatalyst for oxygen reduction reaction. Carbon 62:296–301
406. Liu R, Wu D, Feng X et al (2010) Nitrogen-doped ordered mesoporous graphitic arrays with high electrocatalytic activity for oxygen reduction. Angew Chem Int Ed 49:2565–2569
407. Yang W, Fellinger T-P, Antonietti M (2010) Efficient metal-free oxygen reduction in alkaline medium on high-surface-area mesoporous nitrogen-doped carbons made from ionic liquids and nucleobases. J Am Chem Soc 133:206–209
408. Han C, Wang J, Gong Y et al (2014) Nitrogen-doped hollow carbon hemispheres as efficient metal-free electrocatalysts for oxygen reduction reaction in alkaline medium. J Mater Chem A 2:605–609
409. Bo X, Guo L (2013) Ordered mesoporous boron-doped carbons as metal-free electrocatalysts for the oxygen reduction reaction in alkaline solution. Phys Chem Chem Phys 15:2459–2465
410. Jo G, Shanmugam S (2012) Single-step synthetic approach for boron-doped carbons as a non-precious catalyst for oxygen reduction in alkaline medium. Electrochem Commun 25:101–104
411. Yang D-S, Bhattacharjya D, Inamdar S et al (2012) Phosphorus-doped ordered mesoporous carbons with different lengths as efficient metal-free electrocatalysts for oxygen reduction reaction in alkaline media. J Am Chem Soc 134:16127–16130
412. Wu J, Yang Z, Sun Q et al (2014) Synthesis and electrocatalytic activity of phosphorus-doped carbon xerogel for oxygen reduction. Electrochim. Acta 127:53–60
413. Jin J, Pan F, Jiang L et al (2014) Catalyst-free synthesis of crumpled boron and nitrogen Co-doped graphite layers with tunable bond structure for oxygen reduction reaction. ACS Nano 8:3313–3321
414. Jiang H, Zhu Y, Feng Q et al (2014) Nitrogen and phosphorus dual-doped hierarchical porous carbon foams as efficient metal-free electrocatalysts for oxygen reduction reactions. Chem-Eur J 20:3106–3112

Chapter 5
Preparation of the Catalysts

Shuiping Luo, Min Tang, Yujia Liao, and Pei Kang Shen

Abstract Electrocatalysts are crucial to modern society and economy. To facilitate the application of electrocatalysts and boost their catalytic properties (activity, selectivity and stability), convenient and controllable preparation methods are highly desirable. Herein, we introduce the typical preparation methods used in laboratories, followed by the controllable synthesis of multimetallic catalysts. Then, we present valuable physical techniques that are frequently employed in promoting the preparation of catalysts. In addition, we emphasize the posttreatment and activation of the catalysts, which are indispensable to enhance electrocatalytic performance. Finally, specific examples are given to show the large-scale preparation of electrocatalysts.

Keywords Preparation of the catalysts · Multimetallic catalysts · Post-treatment · Large-scale synthesis · Hydrothermal/solvothermal

The preparation process determines the size, shape, composition and surface of the catalyst, and that directly tunes their catalytic activity, selectivity and stability. Over the past two decades, a great deal of research has focused on the development of novel, facile and controllable preparation methods to construct highly efficient catalysts with well-defined structure toward specific electrochemical reactions. Meanwhile, the post-treatment and activation of catalysts have attracted much attention on electrocatalysis in fuel cells [1–3].

In laboratory, a few milligrams of catalysts are prepared in one batch, which can be used to systematically evaluate the effects of structural properties on their catalytic performance. However, the grams of high quality catalysts should be prepared in one batch to meet the tonnage demand for industry and market usage [4, 5]. Therefore,

S. Luo · M. Tang · Y. Liao
Department of Chemistry, Southern University of Science and Technology (SUSTech), Shenzhen 518055, China

P. K. Shen (✉)
Collaborative Innovation Center of Sustainable Energy Materials, Guangxi Key Laboratory of Electrochemical Energy Materials, College of Chemistry and Chemical Engineering, Guangxi University, Nanning 530004, People's Republic of China
e-mail: pkshen@gxu.edu.cn

P. K. Shen, *Electrochemical Oxygen Reduction*,
https://doi.org/10.1007/978-981-33-6077-8_5

highly controllable and reliable protocols are required to avoid great waste in work force and material resources. More importantly, environment, energy and economic benefits should be seriously considered during the design and synthesis of catalysts in large-scale and green synthesis methods should be developed in priority [6, 7].

5.1 Preparation Methods in Laboratories

To prepare catalysts, solid-phase method, gas-phase method and liquid-phase method are mainly adopted in the laboratory [8–15]. Solid-phase method produces materials by solid-phase reaction, which is simple to produce catalysts in large quantities. However, this method possesses disadvantages of high energy consumption (high temperature is required for solid phase reaction), low purity of products, and it cannot achieve the precise control over the structure of product. The gas-phase method can fabricate nanoparticles with high purity and controllability by gaseous chemical reaction. However, it is limited by the use of complex equipment and low yield of product [11, 16–18]. On the other hand, liquid-phase method is the ideal way to synthesize nanocrystals by chemical reaction in mixed solution, which is not only convenient in operation but also flexible in controlling size, morphology and composition [19–23]. The liquid-phase method typically includes impregnation method, hydrothermal/solvothermal method and sol–gel method. Specially, in the preparation of multimetallic catalysts, coreduction method, seed-mediated growth method and replacement method are most used. In addition, physical techniques such as sputtering, ultrasonic, microwave and illumination contribute to the preparation of catalysts. Examples are given as below.

5.1.1 Impregnation Method

Impregnation method is the main way to prepare supported metal catalysts by means of that the active components are impregnated and then loaded onto the support materials. Usually, the support material is first impregnated with metal salts in aqueous solution, then the metal salts permeate into the carrier through capillary pressure, and finally the active components could gradually diffuse into the holes and adsorb on the surface of carrier. When the impregnation reaches balance, the solution is removed and the solid product is obtained by drying, grinding, calcining and activating (reduction), forming supported catalysts [24–27]. The impregnation method is economical and easy in optimizing the shape, surface area and porosity of catalysts. To prepare uniformly supported catalysts, the reaction parameters such as impregnation time, temperature, pH value and reactant concentration should be finely controlled. Occasionally, competitive adsorbents are introduced to ensure evenly adsorbed active components over the whole carrier. In addition, selecting the reasonable solvent and reducing agent is also very important [26].

Qin Xin et al. used XC-72R carbon powder as carrier, $H_2PtCl_6 \cdot 6H_2O$ as precursor, and formaldehyde as reducing agent, respectively. In the typical synthesis, pH value of the mixed solution is adjusted to 14 by adding NaOH, and the solution is impregnated for 15 min and heated to 90 °C. After reaction for 3 h, sedimentation promoters are added, and the solid 40 wt% Pt/C catalyst is fabricated by washing and drying. The as-obtained Pt nanoparticles are uniformly dispersed with an average particle size of 2.6 nm (Fig. 5.1). However, if the impregnation time is changed to 36 h, the catalyst will be agglomerated with uneven particle sizes (1.5–400 nm), indicating the great influence of impregnation time on the dispersion and size of Pt particles [26].

The impregnation method can also be used to prepare supported bimetallic catalysts [28]. Deli Wang et al. prepared a highly active Pt–Co/C catalyst with structurally ordered nanostructure by ultrasonic impregnating $H_2PtCl_6 \cdot 6H_2O$, $CoCl_2 \cdot 6H_2O$ with XC-72 carbon support in aqueous solution, following evaporating/drying/grinding steps, and reducing at high temperature in H_2. Using the impregnation method with H_2 reduction, other homogeneous bimetallic catalysts such as Pt–Cu and Pt–Ru are synthesized as well. In the preparation of PtRu/C by impregnation method, it is revealed that the alloying degree of Pt–Ru is lowering with the increase of drying temperature, which is probably owing to the partial conversion of $RuCl_3$ into unreducible RuO_x under high drying temperature [27].

More importantly, the impregnation process can be further simplified. Xiaoqing Huang et al. used a facile one-pot method to directly prepare octahedral PtNi/C and PtNiCo/C catalysts, which eliminated the evaporation, drying, calcination and other steps. This one-pot method could reduce metal ions to metal atoms by using dimethyl formamide (DMF) as both solvent and reducing agent, which in-situ depositing and growing into octahedral alloy on various carbon supports (carbon black, carbon nanotubes, reduced graphene oxide, etc.). The octahedral PtNi and PtNiCo alloy are uniformly distributed and exhibit enhanced activity than commercial Pt/C catalyst (Fig. 5.2) [29].

5.1.2 Hydrothermal/Solvothermal Method

Hydrothermal/solvothermal method refers to the chemical synthesis of materials in aqueous or nonaqueous under high temperature and pressure. The reaction usually takes place in sealed pressure vessels, such as polytetrafluoroethylene (PTFE), contains sealed with stainless steel. For security purposes, the volume of contain is typically less than 1000 mL, the reaction temperature is less than 220 °C, the pressure is less than 10 MPa, and the feeding coefficient should be less than 0.8. Under high temperature and pressure, insoluble reagents in atmospheric conditions can be well dissolved or reacted. Originating from the temperature difference of reaction solution in the autoclave, supersaturated state of metal ions would be reached by convection, forming nucleates and then growing into various nanostructures in the presence of surfactant. This method is very simple to handle, which can effectively prevent the volatilization of toxic substances and prepare air-sensitive precursors in a closed

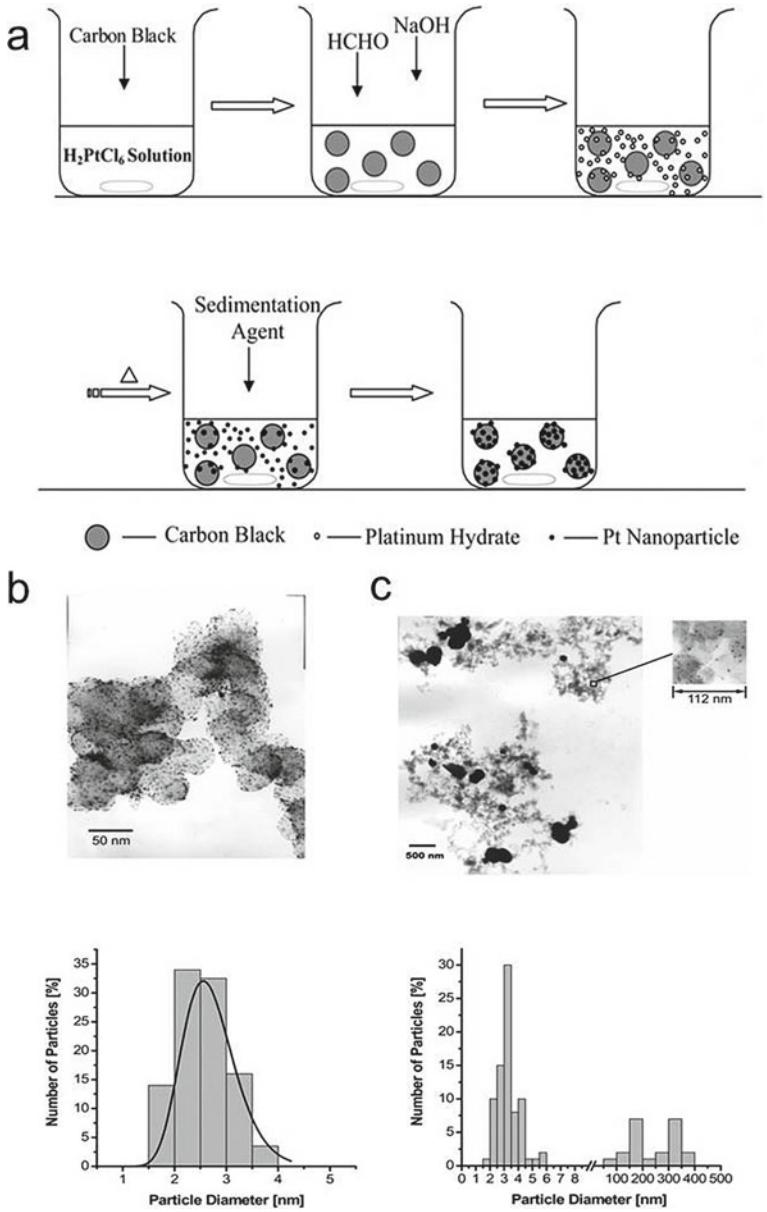

Fig. 5.1 The preparation process of catalyst by impregnation method. Reprinted from Ref. [26]. Copyright 2004, with permission from the Royal Society of Chemistry

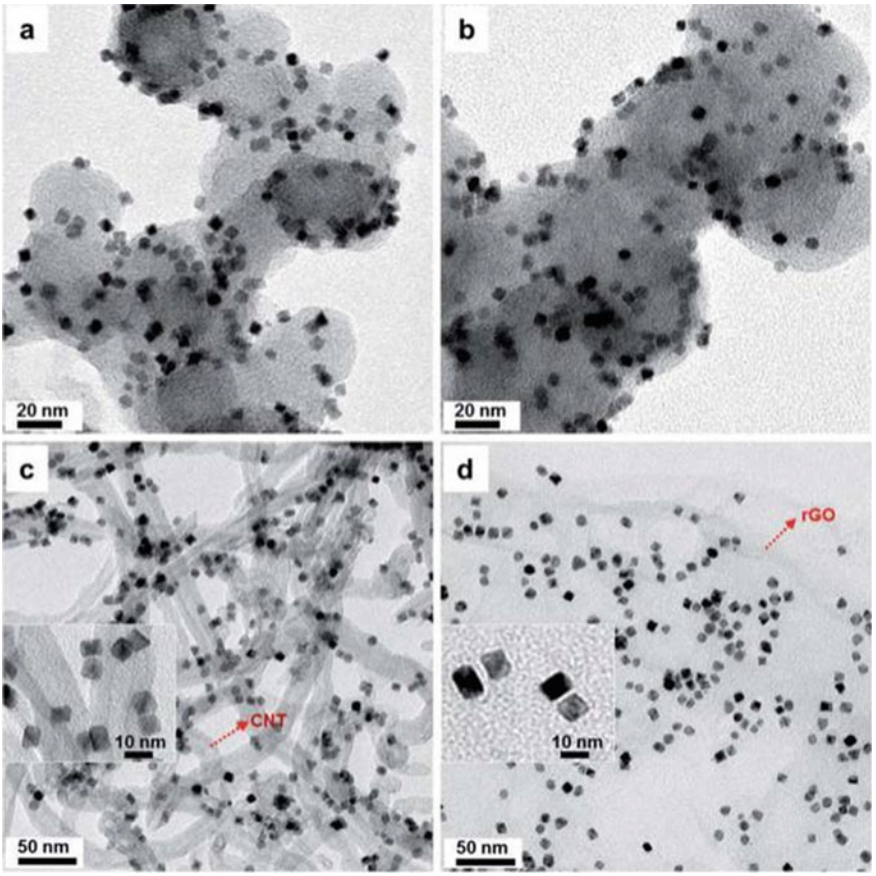

Fig. 5.2 The PtNi/C catalysts prepared by one-pot impregnation method. Reprinted from Ref. [29]. Copyright 2014, with permission from the Royal Society of Chemistry

system. Benefiting from their maneuverability and adjustability, the hydrothermal and solvothermal method boosts the development of synthetic chemistry and attracts much attention in the preparation of nanostructured catalysts, achieving a variety of highly efficient catalysts [11, 19, 21, 30–36].

In the preparation of supported catalysts by hydrothermal/solvothermal method, the detailed experimental process usually includes: dissolution of precursors, mixing of solution, transferring the mixed solution to containers, sealing the containers by stainless steel, putting the devices into heater (such as oven, tube furnace, heating mantle, oil bath, microwave oven, etc.), and adjusting the heating–cooling reaction parameters. Finally, the as-synthesized products are precipitated, washed, dispersed on carbon supports and appropriately treated before obtaining the supported catalysts [37, 38].

Hydrothermal/solvothermal method possesses the advantages of simple operation, reproducible, low cost in production, wide range of raw materials, low reaction temperature, one-step in synthesis and multiple simultaneous reactions, etc. It is effective in preparing multimetallic catalysts with high crystalline, high purity, good dispersion and diverse morphology. In addition, the size, morphology, and composition of products can be well regulated by choosing different surfactants or capping agents. Surfactant and capping agent are usually adsorbed on the specific surface of reduced metal atoms, which can effectively prevent the agglomeration of nanoparticles and ensure the anisotropic growth to form nanostructured catalysts. Surfactant and capping agent can also coordinate with metal ions and manipulate the reduction rate to control the size, morphology, composition and surface of nanocrystals [39, 40].

Nanfeng Zheng's group has developed the small adsorbate-assisted shape control of Pt and Pd-based catalysts with intriguing morphology and catalytic performance. For example, carbon monoxide, halogen anion, formaldehyde and other small molecules are added in the reaction system to prepare catalysts with various morphologies such as sheets, rods, cubes and tetrahedrons. Among them, carbon monoxide can be specifically adsorbed on the (111) surface of Pd and the (100) surface of Pt. Halogen anions can be adsorbed on the (100) surface of Pd and can also coordinate with noble metal ions, forming $PdBr_4^{2-}$ and PdI_4^{2-}, and thus affecting the morphology and surface structure of catalysts [31]. At present, it is still difficult to understand the adsorption behavior and mechanism of small molecules on specific crystal surfaces of metals at molecular scale. In the process of synthesis, small molecules cannot prevent nanoparticles from agglomeration, so polymer and surfactant need to be added together. Therefore, before testing the catalytic performance, the absorbents on the surface of nanoparticles should be removed as much as possible.

In recent years, some new technologies, such as microwave, have been introduced into hydrothermal/solvothermal method to prepare a series of unique catalyst nanomaterials, making it widely used and one of the most important preparation methods. However, there are some main problems existing, such as: difficult in theoretical simulation, in-situ observation, and mechanism analyses; high equipment requirements (resistance to acid, alkali, high temperature and high pressure); sensitive to reactant concentration, temperature, reaction time, selected reagents and other factors; difficult to adjust parameters and conditions; difficult to produce catalysts in large scale. Besides, the introduction of some organic reagents such asoleylamine and polyvinyl pyrrolidone also makes it hard to clean the as-obtained nanoparticles and limits their catalytic applications [2].

5.1.3 Sol–Gel Method

Sol–gel method has developed rapidly in the past 10 years, which has shown great advantages and broad application prospects in the inorganic nonmetallic materials field [41, 42]. In the typical sol–gel synthesis, the first step is dispersing the hydrolysable precursors, such as metal alkoxides and other components into solvents. The active monomer is formed and turns into a stable transparent sol after hydrolysis and condensation reaction. Then, a gel with a certain spatial network structure is formed by aging. Finally, the desirable nanoparticles are prepared through drying and heat treatment. Sol–gel method could fabricate various functional materials at low temperature with uniform size, high purity and well-defined composition, and it enables the design and engineering of nanomaterials at the molecular level. Benefiting from those advantages, sol–gel method has become an important way to prepare self-supported nanocatalysts [43, 44].

In recent years, sol–gel method has developed as an effective and environmentally friendly method for preparing noble metallic aerogel catalysts with high specific surface area and large porosity [45–47]. As shown in Fig. 5.3, the preparation of noble metallic aerogel catalysts is mainly achieved through two strategies. Strategy I is that metal ions are reduced to form dispersed nanoparticles, which are gelled after appropriate treatment to form hydrogels, and then porous aerogels with high specific surface area are obtained through supercritical drying. In the second strategy (Strategy II), the hydrogels are spontaneously formed by the in situ reduction of noble metal precursors, and then porous aerogels are obtained through supercritical drying. At present, a wide range of noble monometallic aerogel catalysts, including Au, Ag, Pt and Pd, and multimetallic aerogel catalysts, including Au–Ag, Au–Pd, Pt–Ag, Pd–Ag, Pt–Pd, Au–Ag–Pt, Au–Pt–Pd, Ag–Pt–Pd and Au–Ag–Pt–Pd have been successfully prepared (Fig. 5.4) [48]. The drying process of hydrogels is very important. If dried directly, the network structure of hydrogels will shrink or collapse. As a widely used strategy in the preparation of noble metal aerogel catalysts by sol–gel method, supercritical CO_2 drying method effectively ensures the preserved internal structure of hydrogels during drying hydrogels into aerogels.

The main disadvantage of sol–gel method is that the process of sol preparation is complex and the raw materials are expensive. Thus, it is only suitable for laboratory research at present. Generally, the whole sol–gel process takes a long time, usually several days or weeks. High contents of residual pores, residual hydroxyl and residual carbon in the gel are retained. During drying process, gases and organics will escape, lead to the shrink of hydrogels, and the organic solvents are harmful to human body. Nevertheless, sol–gel method is still reliable and needs further development.

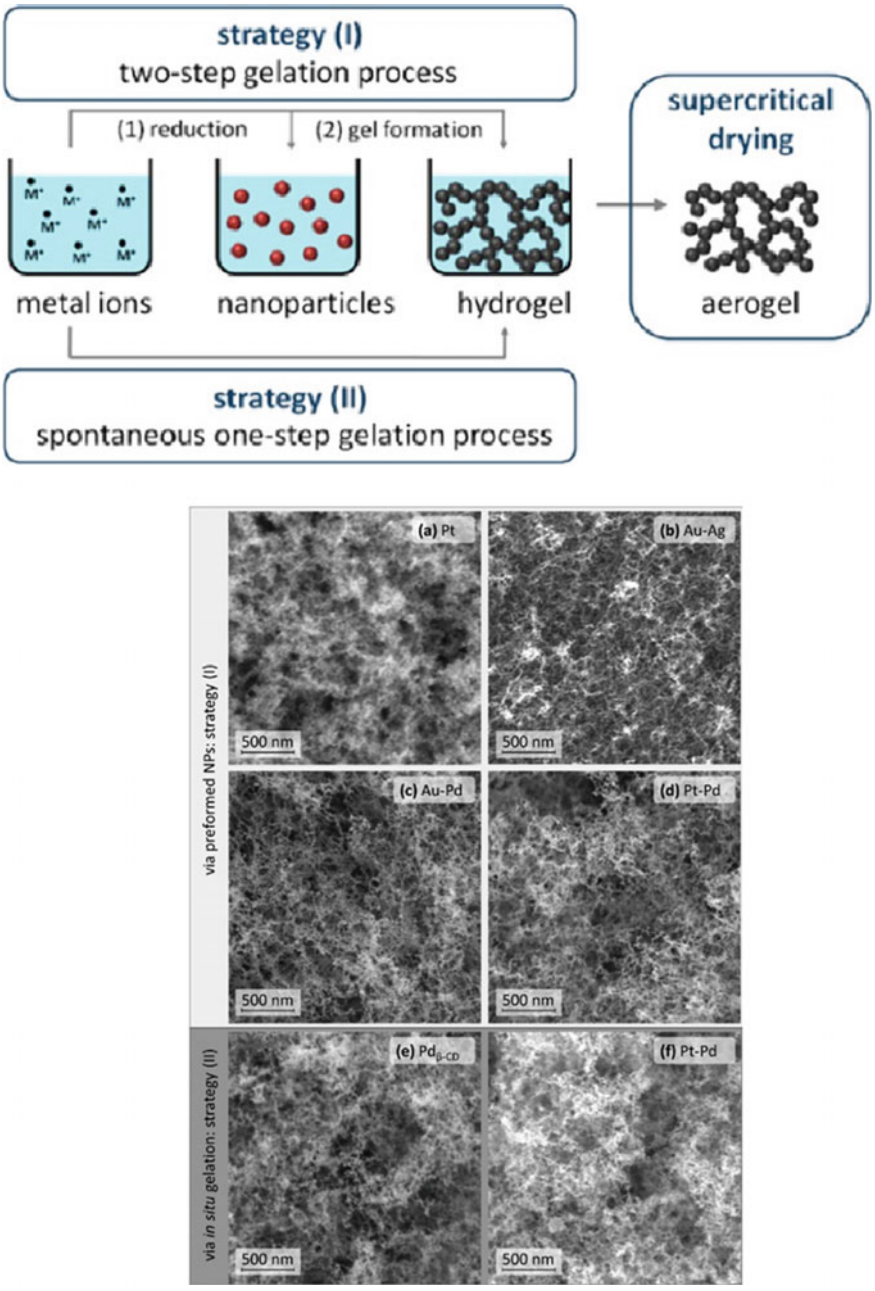

Fig. 5.3 Two strategies for preparing aerogel catalysts by sol–gel method. Reprinted from Ref. [45]. Copyright 2014, with permission from American Chemical Society

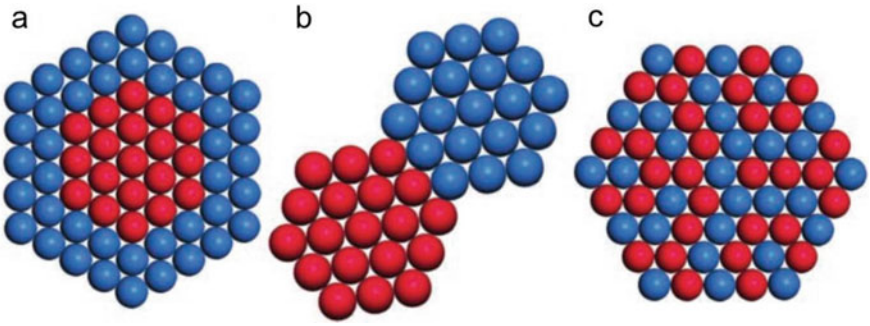

Fig. 5.4 Typical bimetallic nanocrystals with different structure: **a** core/shell; **b** heterostructure; **c** alloyed or intermetallic structures. Reprinted from Ref. [15]. Copyright 2011, with permission from Wiley–VCH Verlag GmbH & Co. KGaA, Weinheim

5.2 Preparation of Multimetallic Catalysts

Bimetallic and multimetallic catalysts have attracted much attention because they could control the electronic structure, morphology and spatial distribution of Pt, thus improving the utilization, activity, selectivity and stability of catalysts [49, 50]. In particular, the preparation methods of PtNi, PtCo, PtFe and PtNiCo catalysts, have been widely studied due to their superior activity [51]. Compared with monometallic catalysts, the preparation of multimetallic catalysts is more complex and difficult to control, and it is hard to understand their synthesis mechanism and reaction processes. The most common preparation methods of multimetallic catalysts are coreduction method and seed-mediated growth method [15].

5.2.1 Coreduction Method

Coreduction method refers to the reduction of two metal salts in appropriate solvent to prepare bimetallic catalysts. It is also the main method to synthesize multimetallic catalysts by hydrothermal/solvothermal and sol–gel methods.

The coreduction method requires appropriate reductants and reaction systems, because uniform nanoparticles are typically produced by effective separation of nucleation and growth processes [52]. If the reducing ability of reductant is too strong, the rapid reduction of metal ions makes the separate nucleation of two metals, which often leads to the aggregation of two metal nanoparticles. Without proper surfactant added in the system, the nucleation and growth processes cannot be effectively separated to avoid the agglomeration of nanoparticles. The different redox potentials of various metals make it tough to control the reduction and nucleation of different metals simultaneously. Generally, metal ions with higher redox potential are reduced first, and the final structure of nanoparticles is determined by the chemical behavior

of the latter reduced metal. As shown in Fig. 5.4, if the second metal atoms are deposited symmetrically on the nucleus of the first metal, a core–shell structure will be formed [53, 54]. If deposition occurs only on a specific surface of the nucleus of the first metal, a heterostructured nanocrystal will be synthesized [55]. If the second metal atoms diffuse into the lattice of the first metal to form a metal–metal bond, an alloy or intermetallic compound will be obtained [56–58]. The chemical behavior of metals is closely related to their intrinsic properties and that tends to be dynamically stable. Specially, reaction conditions such as solvents, ligands and surfactants can change the dynamic equilibrium state of materials, thus affecting the structure of as-synthesized products. For example, for the coreduction of metals A and B, if the redox potential of A is higher than that of B, nanoparticles with A-core/B-shell structure are usually formed. However, a B-core/A-shell structure can be produced by adding surfactants that can strongly bind to A. In practical synthesis, the coreduction method could easily fabricate alloys or intermetallic compounds [59].

By adopting appropriate reductant and reaction system, many researchers prepared bimetallic catalysts with controllable components, uniform size and well-defined shape, which greatly promoted the development of coreduction method. Sodium borohydride is a strong reductant, but the nucleation and growth of the two metals can be well controlled by choosing appropriate reaction processes and conditions, and adding surfactants or ligands that can effectively adsorb on the surface of nucleus [60]. High-quality nanoparticles with tunable size can be synthesized by the introduction of surfactants and foreign ions, or adjusting other reaction parameters. In addition, the composition of bimetallic nanoparticles can be controlled by changing the feeding molar ratio of two metal precursors, and their morphology can be controlled with the coreaction path.

5.2.2 Seed-Mediated Growth Method

To prepare multimetallic catalysts with complex and tunable nanostructure, especially the core–shell structured or heterostructured catalysts, seed-mediated growth method is an available and effective strategy, which can fabricate catalysts with sophisticated structure that are usually difficult to achieve by other methods. Utilizing the as-prepared nanoparticles as crystal seed, seed-mediated growth method ensures the reduction of other metal ions and nucleation on the seed in solution, then the deposition of atoms continuously, forming different structures [61–63].

If the metal atoms deposit uniformly and symmetrically on the surface of the seed, a core–shell structure with separated components will be formed. If the metal atoms deposit on a specific surface of the seed, a heterostructure will be formed. If the metal atoms diffuse into the lattice of seed, a homogeneous alloy structure will be formed. The size, composition, shape, facets and dispersity of seed will affect the final structure of products. Generally, seeds should be uniform in size and evenly dispersed. The surface of seed should be cleaned or properly treated, ensuring their uninform dispersion in the reaction solution. The interaction between

the metals used for deposition and the as-prepared seeds plays an important role in the synthesis of multimetallic catalysts, as physical parameters such as lattice matching degree, surface interaction, interface energy and electronegativity of the two metals determine the nucleation and growth processes [64]. The deposition and growth of metals are thermodynamically and dynamically controlled, and the precise control of those processes could enable the preparation of as-designed catalyst. This can be achieved by adjusting the reaction parameters, such as increasing temperature or decreasing the speed of adding precursors for uniform deposition, adding appropriate surfactants for the control of growth direction and speed, and using reductants with different reducing abilities for the regulation of nucleation and growth rate [65].

Younan Xia et al. have performed a lot of work in preparing nanostructured catalysts by seed-mediated growth method. They prepared PtPd dendritic catalysts at low temperature by using truncated octahedral Pd nanoparticles with a particle size of 9 nm as seeds and ascorbic acid as reductant. By adopting higher temperature and reducing the feed speed of Pt precursor, they avoided the formation of Pt island structure and achieved the evenly deposition of Pt atoms on the surface of cubic Pd nanoparticles to form PtPd core–shell structure (Fig. 5.5). By adjusting the feeding amount of Pt precursor, the Pt shell was successfully controlled in 1–6 atomic layers. Specially, the Pd@Pt 2–5 L catalyst exhibits the highest specific activity toward oxygen reduction reaction, while Pd@Pt 1 L catalyst shows the highest mass activity, which is three times higher than commercial Pt/C [63].

By using seed-mediated growth method, the deposition of alloy on seeds can also be achieved, and catalysts with diverse structure and composition can be prepared. For example, octahedral Pd@PtNi core–shell catalyst was formed by deposition of PtNi alloy on octahedral Pd seeds (Fig. 5.6), and Au@PtCu core–shell catalyst was formed by deposition of PtCu alloy on uniform Au nanoparticles [66].

The second metal can also diffuse into the lattice of seeds to form an alloy. Yadong Li et al. reported the fabrication of uniform PtNi alloy by using multidendritic Pt nanocrystals as seeds and the diffusion of Ni atoms into Pt seeds at high temperature (Fig. 5.7). The as-obtained PtNi multidendritic nanostructures exhibited 3.6 times higher catalytic activity than Pt nanoparticles for methanol oxidation reaction [67].

Seed-mediated growth method has great advantages in preparing complex structures and regulating the spatial distribution of components, thus attracting much attention in the preparation of catalysts in the laboratory. However, the experimental requirements for seed-mediated growth are very high, and the reaction conditions and parameters require precise control, which is not easy to satisfy for industrial large-scale synthesis at present.

5.3 Physical Techniques for Synthesis and Assistance

Compared with chemical synthesis like liquid-phase method, physical method could synthesize pure phase and less defective catalysts, such as nanoparticles, films, wires and other nanostructures in high vacuum environment, without chemical reactions

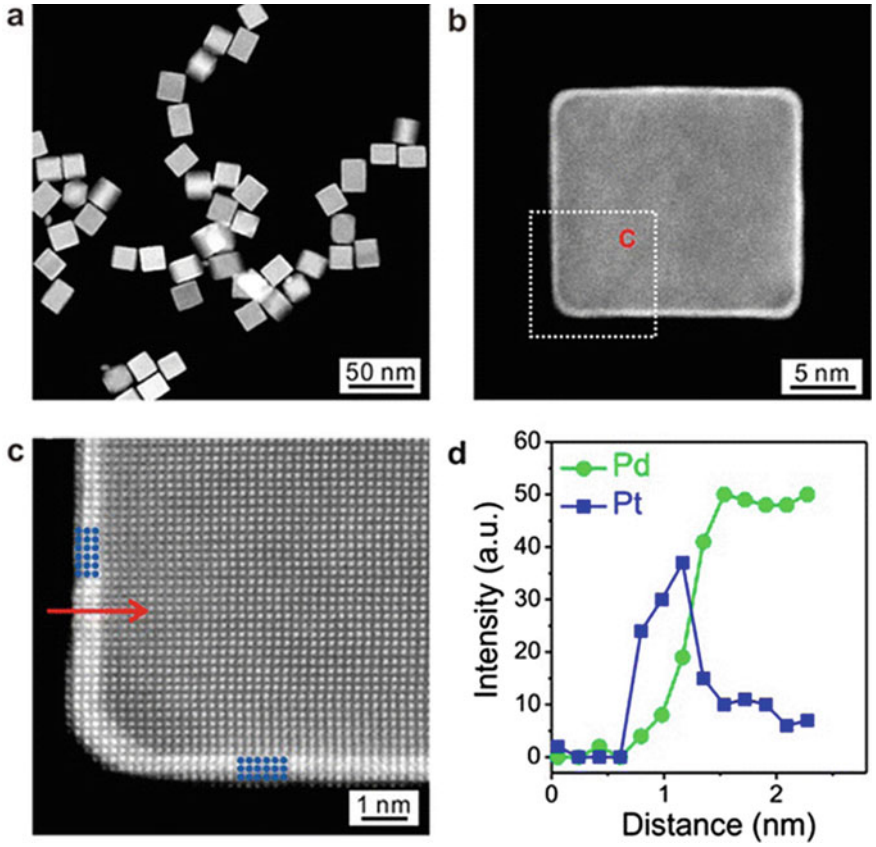

Fig. 5.5 The PtPd core–shell catalyst prepared by seed-mediated growth method. Reprinted from Ref. [63]. Copyright 2014, with permission from American Chemical Society

involved. The main disadvantages of the physical method are that the particles are not uniform, the shape is difficult to control and large-scale preparation of catalysts is difficult. On the other hand, some physical techniques, such as ultrasound, microwave, ultraviolet and high-energy ball milling, are frequently used as assistive means to help chemical synthesis in preparing efficient catalysts.

5.3.1 Sputtering

Sputtering is a commonly used physical technique for the preparation of thin films. The main principle is to bombard the target with charged particles. When the accelerated ions bombard the target, they will collide with the surface atoms of the target, and that results in the transfer of energy and momentum. The surface atoms of the

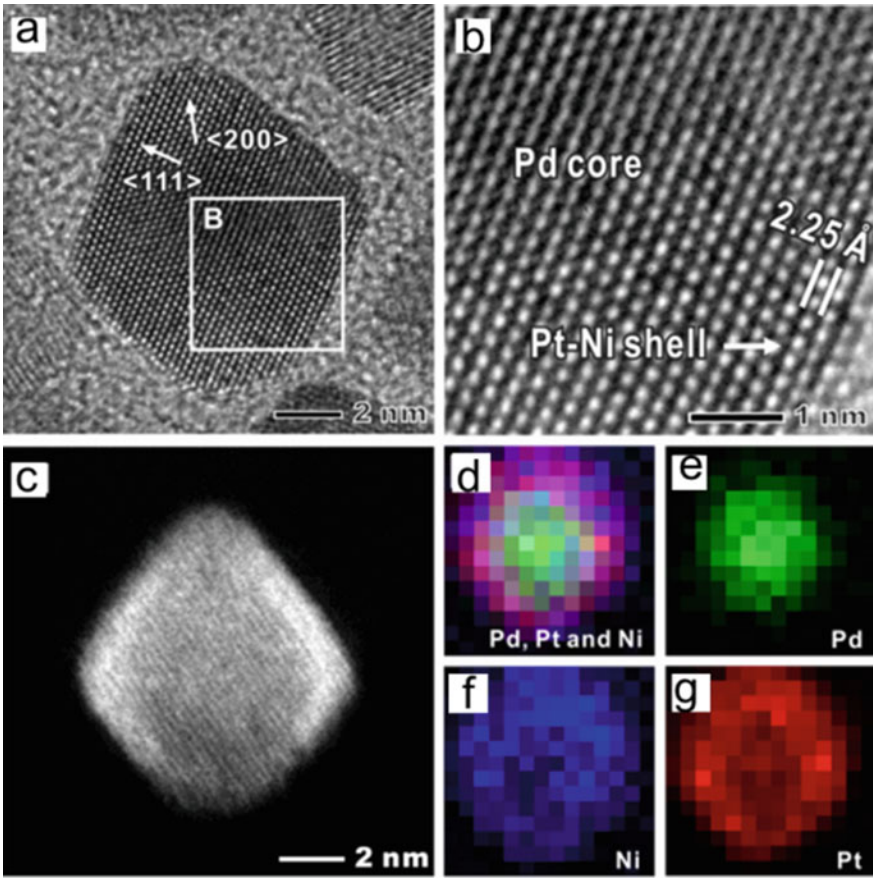

Fig. 5.6 The Pd@PtNi catalyst prepared by seed-mediated growth method. Reprinted from Ref. [66]. Copyright 2014, with permission from American Chemical Society

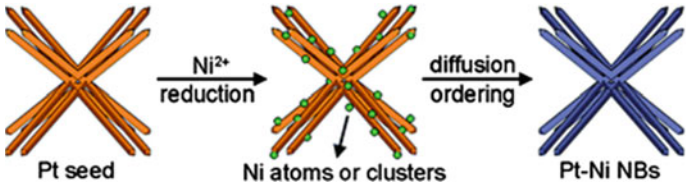

Fig. 5.7 PtNi multidendritic nanostructures prepared by seed-mediated diffusion method. Reprinted from Ref. [67]. Copyright 2012, with permission from the Royal Society of Chemistry

target will be sputtered out with certain kinetic energy, shooting toward the substrate in a certain direction, and then achieving the formation of films. According to its characteristics, it can be divided into five categories: DC sputtering, AC sputtering, reactive sputtering, magnetron sputtering and ion beam sputtering. Sputtering method is facile and effective in preparing films with high melting point, preparing uniform films on large continuous substrates, controlling the composition of films easily, preparing alloy films with different components, and preparing multilayered films.

Metal efficient catalysts with various structures such as nanoparticles, films and wires have been successfully prepared by sputtering. Stamenkovic et al. prepared the multimetallic mesostructured thin-film catalysts on a glassy carbon substrate with a diameter of 6 nm by magnetron sputtering. The carbon-free catalysts possess tunable composition and surface morphology, and exhibit 20-fold more active than commercial Pt/C catalyst for oxygen reduction reaction [68]. Debe et al. presented nanostructured thin film catalysts (NSTF) with widely varying compositions of Pt_xM_y and $Pt_xM_yN_z$ by sputtering, where M and N are Ni, Co, Zr, Hf, Fe, Mn, $0 \leq x, y, z < 1$. When measured in 50 cm^2 fuel cells, the whisker-like Pt_3Ni_7 nano-film catalyst showed a mass activity exceeds 350 mA $mg_{Pt}{}^{-1}$ at 0.9 V [69]. Sputtering can fabricate catalysts that cannot be prepared by traditional chemical methods, which is of great significance in experimental research. Compared with other preparation methods, sputtering has higher requirements in instrument and produces catalysts in low yield. Nevertheless, sputtering shows a certain industrial application prospect due to its advantages on easy realization of continuity and automation.

5.3.2 Sonochemical Synthesis Method

Sonochemical synthesis method, known as sonochemistry, uses ultrasound to accelerate chemical reactions and improve chemical yields. It mainly studies the changes of chemical reactions or chemical reaction processes aroused by ultrasound. Ultrasound is a kind of high frequency mechanical wave, which has the characteristics of concentrated energy, strong penetration, etc. When sound energy is high enough, the attraction between liquid molecules is broken and the cavitation nuclei are formed. Cavitation nucleus possesses a lifetime of about 0.1 μs, and it can produce local high temperature of about 4000–6000 K and high pressure of 100 MPa at the moment of explosion, and generate powerful micro jets with velocity of about 110 m s^{-1}, and those processes are called ultrasonic cavitation. These conditions are sufficient to induce chemical bond fracture, aqueous phase combustion, pyrolysis and free radical reaction of organics within the cavitation bubbles.

Ultrasound can boost the crystal growth, promote the formation of new phase, manipulate the particle morphology, improve dispersion and reaction selectivity, increase nucleation and chemical reaction rate, and shorten the reaction time. Besides, it can stimulate the chemical reactions that cannot occur in the absence of ultrasound. The device used for sonochemical synthesis method is shown in Fig. 5.8a, which has

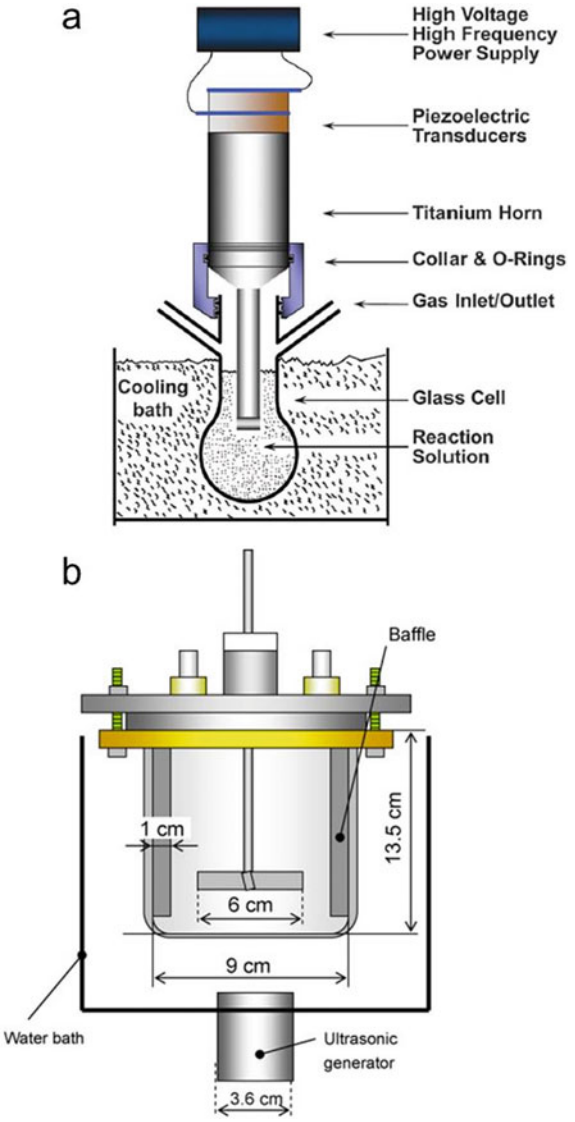

Fig. 5.8 Device for sonochemical preparation of catalysts. **a** Reprinted from Ref. [70]. Copyright 2010, with permission from John Wiley & Sons. **b** Reprinted from Ref. [71]. Copyright 2007, with permission from Elsevier

been widely reported as an effective and simple method for preparing nanomaterials [70].

In the preparation of catalysts, ultrasonic oscillation is often used as an assistive technique to promote dissolution and dispersion. Nagao et al. prepared PtRu alloy catalyst by sonochemistry method, and their reaction system is shown in Fig. 5.8b. Ultrasound was introduced to promote the dispersion of carbon powders and the dissolution of precursors in aqueous solution, and then sodium borohydride was added rapidly to reduce precursors with the assistance of ultrasound at 600 W. The

catalyst prepared by this method shows better dispersion and higher electrocatalytic activity than that prepared without ultrasound for methanol oxidation reaction [71].

5.3.3 Microwave Method

Microwave refers to the electromagnetic wave with a frequency of 300 MHz–300 GHz, namely the electromagnetic wave with a wavelength ranging from 1 to 1 mm. With strong penetration ability, microwave does not need heat transfer process and can realize internal and external heating simultaneously at the same time. The principle of microwave heating is that the dielectric materials consist of polar molecules and nonpolar molecules, and these polar molecules turn from random distribution to polar alignment according to electric field under the action of electromagnetic field. Under the action of high-frequency electromagnetic fields, these orientations change continuously according to the frequency of alternating electromagnetic fields, which causes the movement and friction of molecules and thus generates heat. Meanwhile, the field energy of the alternating electric field transformed into the heat energy makes the temperature of the medium-rise continuously.

Microwave method has the advantages of simple operation, fast reaction speed, mild reaction conditions, uniform heating, high reaction efficiency, and thus benefits the production of nanocrystals in high purity and even distribution. Owing to the significant advantages on the preparation of nanoparticles, microwave method has been widely used in the synthesis of organic and inorganic nanomaterials. Yanhui Yang et al. reported the preparation of PtM alloy catalysts (M = Fe, Co, Ni, Sn, Cu) supported on multiwalled carbon nanotubes by microwave method. The microwave method not only effectively reduces the reaction time but also strengthens the interaction between transition metals and the Pt active sites. The prepared alloy catalysts show better selective hydrogenation performance than those prepared by traditional impregnation method, among which the PtFe and PtCo alloy catalysts exhibit the best performance [72].

The main problem of the traditional continuous microwave method is that it is difficult to control the temperature of the reaction system, which results in partial agglomeration of metal nanoparticles. Therefore, a new intermittent microwave heating method has been developed. Peikang Shen et al. reported a highly dispersed Pt/C catalyst prepared by an improved intermittent microwave heating method, and the as-prepared Pt/C catalyst shows better catalytic performance than commercial Pt/C. In addition, using an intermittent microwave heating procedure with 5 s-on and 5 s-off and repeated that for six times, nanometer Pt–WC/C catalysts were prepared, which exhibits enhanced catalytic performance than the relative Pt–WC/C catalysts prepared by continuous microwave method for oxygen reduction reaction [73].

Another main disadvantage of microwave method is that it is tough to control the crystal growth process and prepare catalysts with well-defined shapes and structures. As an alternative strategy, the combination of microwave method and hydrothermal/solvothermal method can solve the shortcoming of slow heating of

solution in hydrothermal/solvothermal method, and accelerate the crystallization rate, which is widely used to prepare nanostructured catalysts at present.

5.4 Post-Treatment and Activation of Catalysts

After decades of efforts, many catalysts with well-defined nanostructure and enhanced performance have been synthesized by appropriate preparation techniques. However, prepared by the most frequently used liquid-phase synthesis method, catalysts usually possess many surfactants coating on their surface, smooth surface structure and poor composition distribution. Proper post-treatments of the as-prepared catalyst can optimize its structure, composition and surface, which will improve their catalytic activity and structural stability, and that attract widespread attention and application [1, 3, 74–77].

The commonly used post-treatments include cleaning, selective etching, surface composition segregation, electrochemical activation and so on. As a notable example, in 1924, American engineer Molly Raney treated a mixture of Ni and Si (Ni:Si = 1:1) with NaOH. As a result, Si reacted with NaOH, forming a porous catalyst, whose catalytic activity for hydrogenation of cottonseed oil was five times higher than that of Ni. Then, He treated Ni–Al alloy (Ni:Al = 1:1) with NaOH in high concentration. In this process, Al reacted with NaOH and dissolved, leaving the activated porous Raney Ni, which shows further enhanced catalytic activity. Due to its strong adsorption of hydrogen, high catalytic activity and thermal stability, Raney Ni is still widely used in many industrial processes and organic synthesis reactions up to now.

5.4.1 Etching

The phenomenon that metals and products made of them are destroyed by chemical or electrochemical action in natural environment or under working conditions is called etching. Typically, etching can be divided into wet etching and dry etching, which refer to the etching of metals in the presence of water or dry gases without liquid water, respectively. Due to the general presence of water in the atmosphere and the treatment of various aqueous solutions in chemical production, wet etching is most commonly observed. However, the harm caused by dry etching in high temperature operation can also not be ignored.

Etching of metals in aqueous solution is an electrochemical reaction, as an anode–cathode isolated etching cell is formed on the surface of metal. The metal loses electrons in the solution and turns into positive metallic ions, and this process is an oxidation reaction, namely the anodic process. Meanwhile, the generated electrons could be neutralized by some substance in the solution. The process of neutralizing electrons

is a cathodic reduction reaction, which include oxygen reduction, hydrogen production, reduction of oxidant, deposition of noble metals, etc. As etching proceeds, in most cases, the cathodic or anodic process will be blocked by the corrosion products due to the solution ions, resulting in the diffusion being blocked and the corrosion rate being slowed down. This phenomenon is called polarization, and the corrosion of the metal will be decreased with the effect of polarization.

By rational utilization and control of etching, catalysts with unique nanostructure can be synthesized. Younan Xia et al. controlled the etching of Pd nanoparticles by Cl^-/O_2, realized the selective elimination of twin formed at the early stage, and thus synthesized uniform and single-crystal Pd nanoparticles. This research not only proved the role of oxidative etching by Cl^-/O_2 on Pd nanoparticles but also demonstrated that the selective etching could optimize the shape of nanoparticles [78–80].

Etching is also commonly used for post-treatment. Peidong Yang et al. synthesized polyhedral Pt–Ni alloy using oleylamine as reductant, capping agent and solvent. The oleylamine-capped $PtNi_3$ polyhedrons were transformed into Pt_3Ni nanoframes, after dispersed in n-hexane solution and exposed to air (O_2) for 2 weeks (Fig. 5.9). This morphological evolution process could be finished in 12 h by increasing the solution temperature to 120 °C. However, if this process was performed in argon, nanoframes will not be formed due to the absence of etching [81–83].

Chemical etching is often adopted to remove templates, and etching of alloy could synthesis porous, hollow, rough and complex structures [84]. However, chemical etching suffers from some intrinsic drawbacks, including that the surface atoms of alloy are usually etched in random sites and the etching process is usually too drastic to control. It is a great challenge in making the chemical etching moderate and controllable. Yadong Li et al. proposed a mild and controllable chemical etching method at room temperature. After the synthesis of Pt–Ni alloy octahedrons, excessive dimethylglyoxime was used as etchant to react with nickel, forming nickel dimethylglyoxime. Then, dilute acetic acid was added to dissolve the generated nickel dimethylglyoxime. Finally, the concave Pt–Ni alloy catalysts were obtained (Fig. 5.10a). Owing to larger surface area and higher density of exposed atomic steps, the concave nanostructures exhibited superior activity compared with the

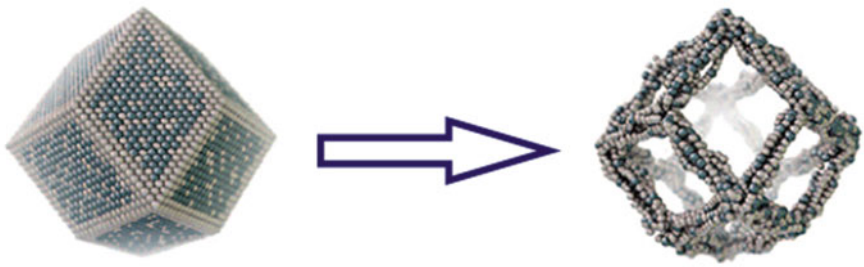

Fig. 5.9 Schematic illustrations of the samples during the evolution process from polyhedra to nanoframes [81]

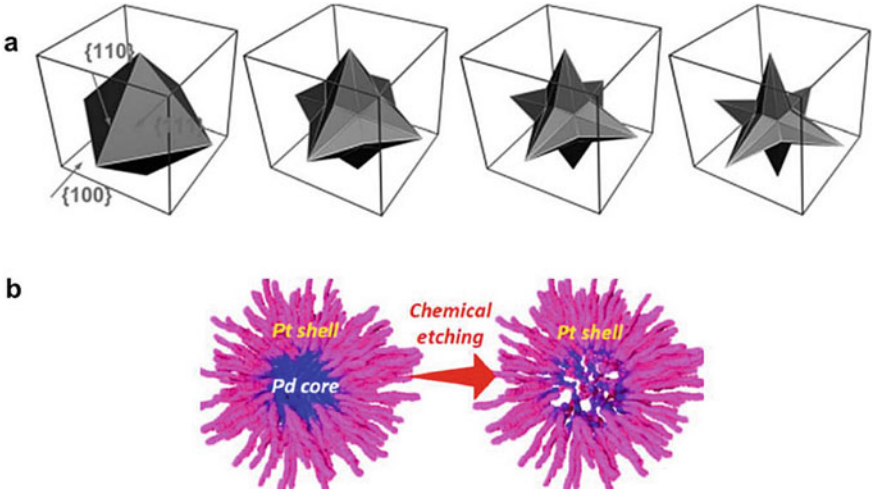

Fig. 5.10 The evolution of Pt-Ni nanoparticle (**a**) and PtPd dendritic catalyst (**b**). (a) Reprinted from Ref. [85]. Copyright 2012, with permission from John Wiley & Sons. (b) Reprinted from Ref. [86]. Copyright 2013, with permission from American Chemical Society

octahedral Pt-Ni alloy particles for methanol oxidation reaction [85]. As shown in Fig. 5.10b, Liang Wang et al. synthesized PtPd dendritic nanostructure with Pd core, then they selectively etched away Pd core by nitric acid and obtained hollow PtPd dendritic catalyst, which showed higher activity and stability toward methanol oxidation reaction than PtPd dendritic catalyst without etching [86].

Particularly, dealloying refers to the selective removal of one or more components in the alloys through chemical or electrochemical etching, which has attracted considerable attention due to its ability to prepare porous metal nanomaterials effectively. The performance of catalysts is sensitive to the distribution of their surface atoms and structure. Peter Strasser et al. have systematically investigated the effect of dealloying on the catalytic performance of various multimetallic catalysts [87–91]. For example, the dealloying of Pt-transition metals (Cu, Co) binary and multimetallic catalysts can remove unstable metal atoms on the surface, forming core-shellor porous nanostructure, and that effectively improving the activity and stability of the catalysts.

5.4.2 Composition Segregation

Alloying has been widely proved as an effective strategy to enhance the utilization of Pt, the intrinsic activity and antipoising ability of catalysts. The distribution of components in the alloy has great influence on their catalytic properties. Specially, catalysts with ordered composition, Pt-skin surface and Pt atoms concentered on

the edges and corners exhibit superior catalytic activity and stability. Many methods have been developed to prepare alloy nanocatalysts, which usually possess uniformly distributed components [25, 92–98]. To further improve their activity and stability, appropriate post-treatment is needed to ensure composition segregation, forming a nanostructure with optimized composition distribution. It is well known that, surface composition in the alloy is different from the corresponding bulk material, and the surface composition depends on the separation energy and surface mixing energy. In addition, the difference in the adsorption energy of gas on two metals can induce the separation of components. Héctor D. Abruña et al. described a new class of Pt–Co nanocatalysts composed of ordered Pt_3Co intermetallic cores with a two to three atomic-layer-thick platinum shell that segregated in hydrogen. This ordered catalysts prepared at 700 °C are more active and durable than the disordered Pt_3Co/C alloy prepared at 400 °C [24]. Zhichuan J. Xu et al. reviewed the surface segregation of bimetallic catalysts, discussed the causes of surface segregation and introduced some characterization methods. The rational control and application of surface segregation benefit the development of efficient multimetallic catalysts [99, 100].

5.4.3 Surface Cleaning

In the typical synthetic process, organic compounds or polymers are often used as surfactants, ligands, capping agents or organic solvents in the controllable synthesis of catalysts with well-defined structure and uniform dispersion (Fig. 5.11). Specially, surfactants can selectively adsorb on specific crystal surfaces, promoting the anisotropic growth of nanoparticles and forming unique structures. Ligands can coordinate with precursors and affect the reaction kinetics, thus determining the formation of nanostructures. Capping agents adsorb on the surface of nanoparticles, forming steric hindrance to prevent the agglomeration of nanoparticles, thus forming highly dispersed or monodisperse colloidal catalysts. On the other hand, oleylamine, dimethylformamide and ethylene glycol are widely used as effective multifunctional solvents to prepare a series of efficient catalysts [17, 18, 39].

Generally, washing the as-obtained nanocrystals by solvents (e.g., anhydrous ethanol for oleylamine/oleic acid, acetone for PVP) and high-speed centrifugation is used for the surface cleaning. Repeated washing by centrifugation can effectively remove excess capping agents on the surface of nanoparticles, but there will still be a certain amount of residual [2]. Annealing can effectively remove organic compounds from the surface, but high temperature could cause agglomeration and transforming of nanoparticles.

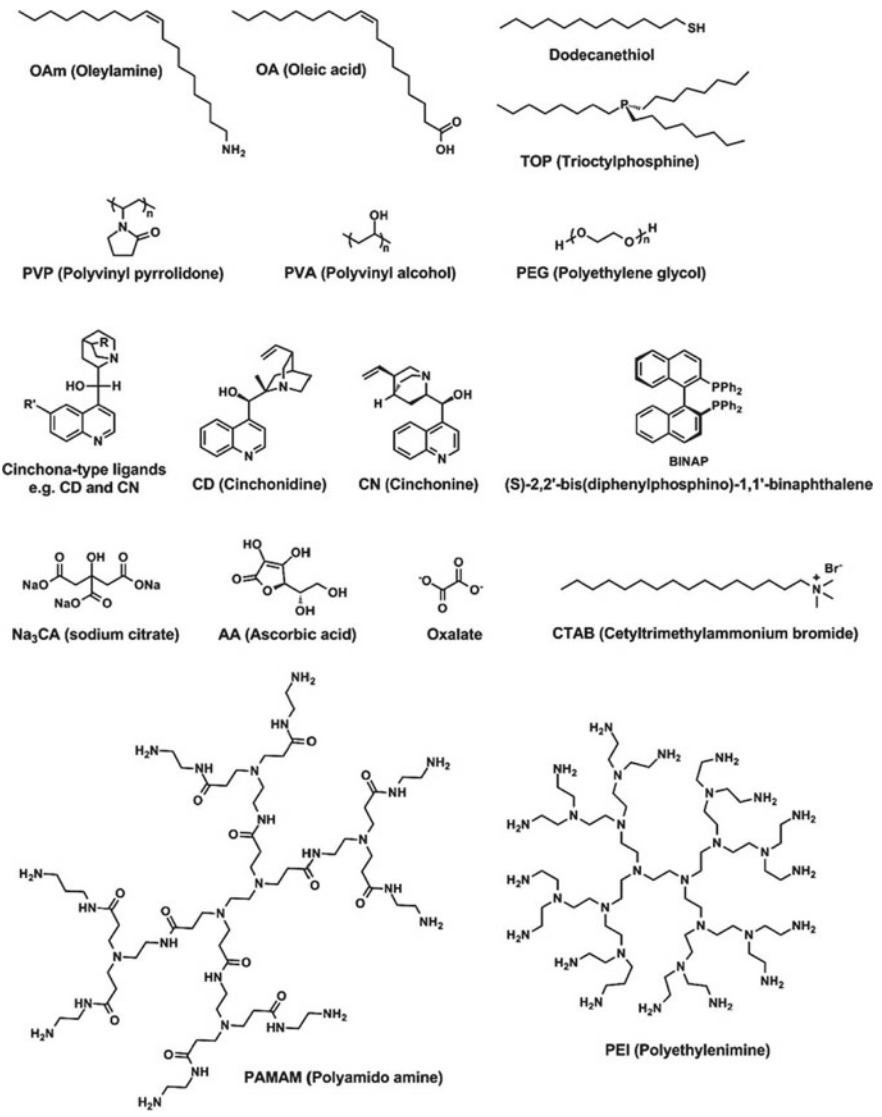

Fig. 5.11 Typical capping agents used in the preparation of nanocrystals, including long-chain hydrocarbons, polymers, chiral ligands, polycarboxylic acids, polyhydroxy compounds, cationic surfactant, etc. Reprinted from Ref. [2]. Copyright 2014, with permission from American Chemical Society

5.4.4 *Electrochemical Activation*

The electrochemical activation process can effectively remove adsorbents and unstable transition metals from the surface of catalyst, obtaining stable nanostructure and achieving optimized catalytic performance (Fig. 5.12) [101].

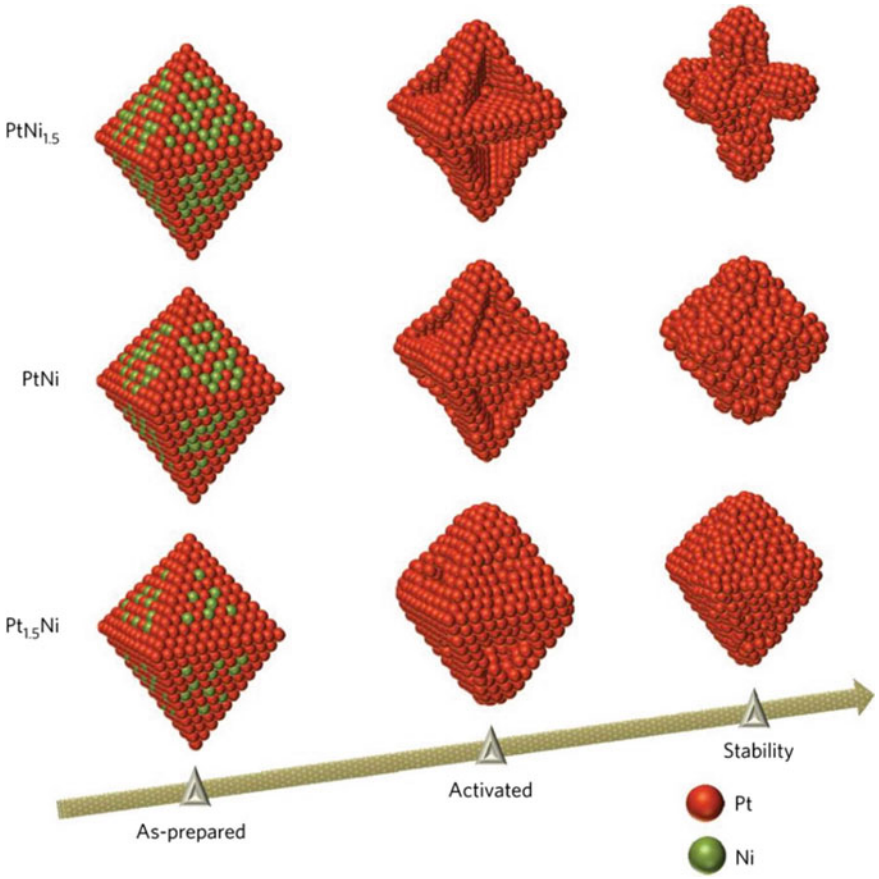

Fig. 5.12 Morphology and surface structural changes of Pt_xNi_{1-x} octahedrons. Reprinted from Ref. [101]. Copyright 2013, with permission from Springer Nature

5.5 Large-Scale Preparation of Catalysts: Examples and Discussion

Over the past decades, with the continuous development of preparation technologies, many efficient catalysts have been successfully synthesized, including: Pt-based bimetallic or multimetallic catalysts with tunable components (Pt–Ni, Pt–Co, Pt–Fe, Pt–Pd, Pt–Fe–Ni, Pt–Co–Ni, etc.); catalysts with diverse shapes (sphere, rod, wire, plate, cube, tetrahedron, octahedron, decahedron, icosahedron, etc.); catalysts with unique structures (core–shell, hollow, framework, dendrite, branch, etc.); and catalysts with high-index facets enclosed surface [39, 64, 102–109].

These catalysts with controllable composition, size, shape and surface enable the study of catalytic mechanism and structure–function relationship, and provide directions for improving the activity and stability of catalysts. Although these active catalysts reported show great application prospects as promising candidates for the next-generation catalysts, there is still a big gap between academic research and industrial application of nanocatalysts, because the large-scale preparation of catalysts is challenge. In most literatures, the preparation of catalysts is carried out in one batch, using flasks, vials and PTFE autoclave as reaction containers, and the yield of catalysts is typically limited at milligram level. For example, in a 50-mL flask, only 100 mg carbon-supported catalyst (metal load of 50%) can be synthesized in the 25 mL reaction solution. Using 10 mL reaction solution in PTFE autoclave with a volume of 25 mL, 20 mg carbon-supported catalyst (metal load of 50%) are normally produced. As for the conventional electrochemical deposition, only microgram catalysts could be produced in one batch. Therefore, the corresponding large-scale preparation technologies should be seek to achieve the synthesis of efficient catalysts at gram scale by one batch or kilogram-scale daily, satisfying the great needs of industry and market [6, 110].

At present, the main strategies for large-scale preparation are: (1) increasing the volume of reaction, and appropriately adjusting the quantity and parameters in the reaction system; (2) designing reactor for continuous synthesis; and (3) solid-phase reduction. In addition, in the large-scale preparation of catalysts, green synthesis technology should be preferred.

5.5.1 Increasing the Volume of Reaction

To realize large-scale preparation, increasing the volume of reaction is a common strategy. For example, in the hydrothermal/solvothermal synthesis of catalysts, the volume of reaction can be increased by more than 10 times (using a PTFE autoclave with volume greater than 500 mL). Using a flask with volume larger than 250 mL, the volume of reaction solution should be increased correspondingly, and a larger magnetic stirrer should be used to stir the solution (Fig. 5.13). By increasing the

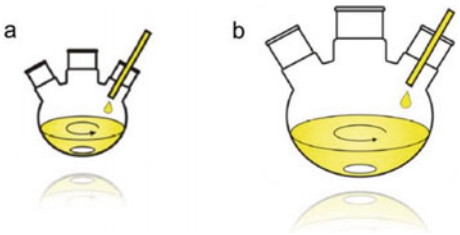

Fig. 5.13 Increasing reaction volume for large-scale synthesis. **a** small containers; **b** large container

volume of reaction, gram-scale preparation of catalysts can be successfully achieved in one batch, with the qualities of product well preserved.

Peidong Yang et al. synthesized 10 mg $PtNi_3$ polyhedrons by coreduction methodin 10 mL oleylamine, which serves as reductant, capping agent and solvent. By controlling the structural evolution, novel Pt_3Ni nanoframes were successfully synthesized. Further, 1 g carbon-support Pt_3Ni nanoframes (the load of Pt was 20%) were obtained in a single batch by increasing the reaction solution for tenfold, and using the same experimental parameters. However, if the reaction volume continues to be amplified, Pt_3Ni nanoframe catalyst with larger particle size (50 nm) will be formed [81].

The nucleation and growth of nanocrystals are highly sensitive to reaction details such as the way a reagent is introduced and mixed, stirringrate, heat management and variation of temperature. Thus, repeatability between batches is also a problem. If the large-scale synthesis by increasing the volume of reaction fails, lots of time, resource and efforts will be wasted and the environment will be polluted. In most cases, the yield of catalysts in a successful large-scale synthesis by increasing volume of reaction is usually no more than 2 g [111–113].

5.5.2 Solid-State Reduction

Many industrial heterogeneous catalysts are prepared by impregnating or precipitating metal precursors on supports, then drying, grinding and reducing [24]. This method is easy to operate and can prepare catalysts in large scale. Generally, the synthesized catalysts possess clean surfaces with size smaller than 10 nm. However, the catalysts are uneven in size distribution, shape, and dispersion of nanoparticles and they exhibit low catalytic activity, especially in a high metal loading. The above problems could be solved by reasonably improving experimental parameters and using mixed reducing gas. Although octahedral Pt–Ni alloy nanoparticles show excelling catalytic property toward oxygen reduction reaction, mass production of these nanomaterials at low cost remains a huge challenge. Zhenmeng Peng et al. prepared octahedral Pt–Ni/C by simply impregnating $Pt(acac)_2$ and $Ni(acac)_2$ on carbon support, and reducing the dried solids at 200 °C for 1 h in the CO/H_2 mixed reducing gas with flow rate of 120/5 cm^3 min^{-1}. As a result, one-batch preparation of

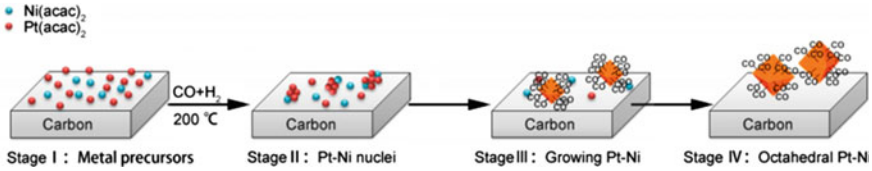

Fig. 5.14 Schematic illustration of the preparation of octahedral Pt–Ni nanoparticles on carbon support by solid-state reduction. Reprinted from Ref. [14]. Copyright 2014, with permission from American Chemical Society

2 g octahedral $Pt_{1.5}Ni/C$ (20 wt% Pt) is achieved (Fig. 5.14), indicating the potential application of solid-state reduction in the scalable production of efficient catalysts [14].

5.5.3 Continuous Synthesis in Droplet Reactors

Different from the traditional strategy that achieving large-scale preparation by increasing the volume of reaction, an alternative strategy is decreasing the volume of reaction solution by continuous synthesis in droplet reactors, which is similar to the production line in a factory. This method offers many attractive advantages, including: simultaneous synthesis in parallel; rapid reaction in the droplets; fast examination and feedback; timely stop in operation; less waste and consumption in the optimization process; in-situ monitoring of the reaction system; safe in toxic reactions (closed); and high yield daily [113, 114].

Droplets are small liquid with a diameter less than 200 μm, which can settle under static conditions and maintain suspended under turbulent conditions. In engineering, nozzles or small holes are usually used to disperse liquid into gas or another immiscible liquid, forming droplets, which greatly increases the contact area between two phases and speeds up the reaction. If 1 m^3 of liquid is divided into 2×10^{12} uniform droplets with a diameter of 100 μm through the nozzles, the total surface area reaches 60,000 m^2, which can greatly accelerate the vaporization of water in droplets.

Since 2002, continuous synthesis in droplet reactors has been applied to the synthesis of nanomaterials, then attracting wide attention and hundreds of related articles have been published. Due to the difference in size and shape, droplets move and behave different. The key issues remained and development direction in this technology is that: controlling the size and shape of droplets; mixing of reactants uniformly in droplets; forming stable and continuous separation droplets; controlling the interaction between droplets and fluids; realizing pollution-free and sediment-free pipelines; achieving reliable system with long life; maximizing the yield; and optimizing the products. After decades of development, this preparation technology is more mature, the synthetic materials are more extensive and superior, and the yield is gradually increased [6, 113–118]. Younan Xia et al. developed a fluidic

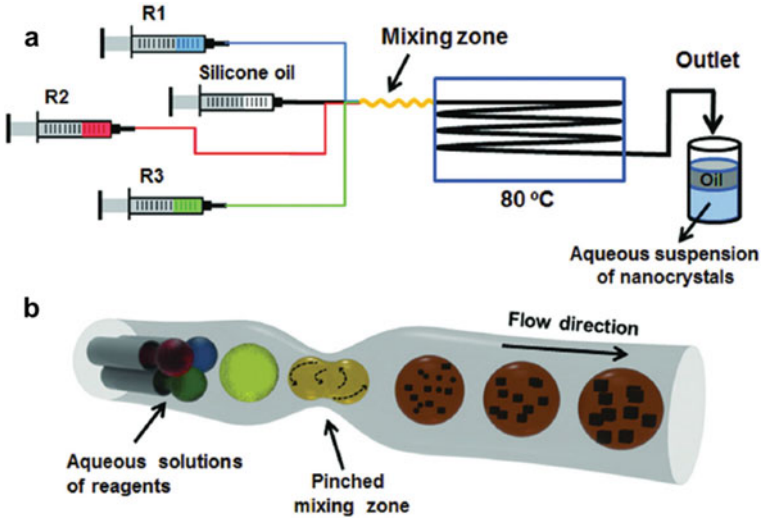

Fig. 5.15 **a** Schematic illustration of the experimental setup for droplet reactors; **b** generation of well-separated droplets of aqueous solutions in an oil carrier phase, followed by the nucleation and growth of nanocrystals inside the droplets. Reprinted from Ref. [6]. Copyright 2013, with permission from Wiley–VCH

device using silica capillaries, PTFE tube with an inner diameter of 1.58 mm, and silicone oil as fluid, producing four separated droplets per second (volume is 2.5 μL). These droplets can flow steadily and continuously in silicone oil, and the droplets are uniformly mixed when passing through a pinched mixing zone. After reaction at 80 °C, 36 mL of colloidal solution or 72 mg of solid product can be obtained within 1 h (Fig. 5.15). If the droplet-based system is operated continuously (24/7) and in parallel (with 100 or even more identical fluidic devices operated side by side), it will be feasible to produce 172.8 g catalysts in a day [118]. This output is sufficient to meet the needs of industrial-class catalysts.

5.5.4 Green Chemistry Synthesis

When preparing catalysts in large scale, the benefits related to environmental, energy and economic should be taken into consideration. In general, an ideal and reliable preparation method is usually to use a simple reaction process, which could quickly convert cheap, readily and available raw materials into the desired material at a high yield. Traditional synthetic chemistry usually uses a large number of solvents, reductants, capping agents and additives, causing serious pollution and damage, and even the discharge of toxic substances. Some traditional reaction processes require physical conditions of high temperature and high pressure, which require high experimental equipment and high energy consumption. Green chemistry synthesis is a

discipline to solve pollution problems from the source, which is in line with the concept of sustainable development. The ideal state is not to add reagents and raw materials that are harmful to the environment and human body, not to expel wastes and pollution, and not to deal with wastes and waste liquids. In recent years, more and more attention has been paid to green chemistry synthesis [7, 119, 120].

In view of the specific synthesis process, we should improve the solvent, reducing agent, synthesis strategy, capping agent and other aspects, so as to make it environmentally friendly and economical. Organic solvents such as oleylamine, dimethyl formamide, ethylene glycol are the most common solvents in the preparation of catalysts by liquid-phase method. Therefore, environmentally friendly organic solvents or water should be preferred in green synthesis, or ionic liquids and supercritical fluids should be used as reaction media. Electrochemical synthesis is the main method of green synthesis, the electrolysis process does not need to use toxic reaction reagents, and the synthesis process often occurs in the environmental conditions, so it is expected to be widely used in the green synthesis of catalysts. Sodium borohydride, formaldehyde, glycerin, hydrazine hydrate, carbon monoxide and other reductants, small molecules, polysaccharides or biological molecules as protective agents, are easy to clean and non-toxic. In addition, to reduce energy consumption and increase economic benefits, the preparation process should be conducted at ambient temperature and pressure as far as possible [7, 121, 122].

References

1. Li M, Zhao Z, Cheng T et al (2016) Ultrafine jagged platinum nanowires enable ultrahigh mass activity for the oxygen reduction reaction. Science 354(6318):1414–1419
2. Niu Z, Li Y (2013) Removal and utilization of capping agents in nano catalysis. Chem Mater 26(1):72–83
3. Li D, Wang C, Tripkovic D et al (2012) Surfactant removal for colloidal nanoparticles from solution synthesis: the effect on catalytic performance. ACS Catal 2(7):1358–1362
4. Roy C, Knudsen BP, Pedersen CM et al (2018) Scalable synthesis of carbon-supported platinum-lanthanide and rare-earth alloys for oxygen reduction. ACS Catal 8(3):2071–2080
5. Choi J, Jang J, Roh C et al (2018) Gram-scale synthesis of highly active and durable octahedral PtNi nanoparticle catalysts for proton exchange membrane fuel cell. Appl Catal B 225:530–537
6. Zhang L, Xia Y (2014) Scaling up the production of colloidal nanocrystals: should we increase or decrease the reaction volume. Adv Mater 26(16):2600–2606
7. Duan H, Wang D, Li Y (2015) Green chemistry for nanoparticle synthesis. 44(16):5778–5792
8. Zhang J, Du J, Han B et al (2006) Sonochemical formation of single-crystalline gold nanobelts. Angew Chem Int Ed 45(7):1116–1119
9. Langille MR, Zhang J, Mirkin CA (2011) Plasmon-mediated synthesis of heterometallic nanorods and icosahedra. Angew Chem Int Ed 50(15):3543–3547
10. Kim F, Song JH, Yang P (2002) Photochemical synthesis of gold nanorods. J Am Chem Soc 124(48):14316–14317
11. Wang X, Zhuang J, Peng Q et al (2005) A general strategy for nanocrystal synthesis. Nature 437(7055):121–124
12. Martínez-Rodríguez RA, Vidal-Iglesias FJ, Solla-Gullón J et al (2014) Synthesis of Pt nanoparticles in water-in-oil microemulsion: effect of HCl on their surface structure. J Am Chem Soc 136(4):1280–1283

13. Pileni M (2003) The role of soft colloidal templates in controlling the size and shape of inorganic nanocrystals. Nat Mater 2(3):145–150
14. Zhang C, Hwang SY, Trout A et al (2014) Solid-state chemistry-enabled scalable production of octahedral Pt-Ni alloy electrocatalyst for oxygen reduction reaction. J Am Chem Soc 136(22):7805–7808
15. Wang D, Li Y (2011) Bimetallic nanocrystals: liquid-phase synthesis and catalytic applications. Adv Mater 23(9):1044–1060
16. Wu Y, Wang D, Li Y (2014) Nanocrystals from solutions: catalysts. 43(7):2112–2124
17. Mourdikoudis S, Liz-Marzán LM (2013) Oleylamine in nanoparticle synthesis. Chem Mater 25(9):1465–1476
18. Muzart J (2009) N, N-Dimethylformamide: much more than a solvent. Tetrahedron 65(40):8313–8323
19. Luo S, Tang M, Shen PK et al (2017) Atomic-scale preparation of octopod nanoframes with high-index facets as highly active and stable catalysts. Adv Mater 29(8):160687
20. Luo S, Shen PK (2016) Concave platinum-copper octopod nanoframes bounded with multiple high-index facets for efficient electrooxidation catalysis. ACS Nano 11(12):11946–11953
21. Zhang Z, Liu G, Cui X et al (2018) Crystal phase and architecture engineering of lotus-thalamus-shaped Pt-Ni anisotropic superstructures for highly efficient electrochemical hydrogen evolution. Adv Mater 30(30):1801741
22. Du H, Luo S, Wang K et al (2017) High-quality and deeply excavated Pt_3Co nanocubes as efficient catalysts for liquid fuel electrooxidation. Chem Mater 29(22):9613–9617
23. Yang P, Yuan X, Hu H et al (2018) Solvothermal synthesis of alloyed PtNi colloidal nanocrystal clusters (CNCs) with enhanced catalytic activity for methanol oxidation. Adv Func Mater 28(1):1704774
24. Wang D, Xin HL, Hovden R et al (2013) Structurally ordered intermetallic platinum-cobalt core-shell nanoparticles with enhanced activity and stability as oxygen reduction electrocatalysts. Nat Mater 12(1):81–87
25. Wang D, Yu Y, Xin HL et al (2012) Tuning oxygen reduction reaction activity via controllable dealloying: amodel study of ordered Cu_3Pt/C intermetallic nanocatalysts. Nano Lett 12(10):5230–5238
26. Zhou Z, Wang S, Zhou W et al (2003) Preparation of highly active Pt/C cathode electrocatalysts for DMFCs by an improved aqueous impregnation method. Phys Chem Chem Phys 5(24):5485
27. Wang D, Zhuang L, Lu J (2007) An alloying-degree-controlling step in the impregnation synthesis of PtRu/C catalysts. J Phys Chem C 111(44):16416–16422
28. Ding K, Cullen DA, Zhang L et al (2018) A general synthesis approach for supported bimetallic nanoparticles via surface inorganometallic chemistry. Science 362(6414):560–564
29. Huang X, Zhao Z, Chen Y et al (2014) A rational design of carbon-supported dispersive Pt-based octahedra as efficient oxygen reduction reaction catalysts. Energy Environ Sci 7(9):2957–2962
30. Yu T, Kim DY, Zhang H et al (2011) Platinum concave nanocubes with high-index facets and their enhanced activity for oxygen reduction reaction. Angew Chem Int Ed 50(12):2773–2777
31. Chen M, Wu B, Yang J et al (2012) Small adsorbate-assisted shape control of Pd and Pt nanocrystals. Adv Mater 24(7):862–879
32. Lai J, Niu W, Luque R et al (2015) Solvothermal synthesis of metal nanocrystals and their applications. Nano Today 10(2):240–267
33. Carpenter MK, Moylan TE, Kukreja RS et al (2012) Solvothermal synthesis of platinum alloy nanoparticles for oxygen reduction electrocatalysis. J Am Chem Soc 134(20):8535–8542
34. Xia BY, Wu HB, Wang X et al (2012) One-pot synthesis of cubic $PtCu_3$ nanocages with enhanced electrocatalytic activity for the methanol oxidation reaction. J Am Chem Soc 134(34):13934–13937
35. Xia BY, Wu HB, Yan Y et al (2013) Ultrathin and ultralong single-crystal platinum nanowire assemblies with highly stable electrocatalytic activity. J Am Chem Soc 135(25):9480–9485
36. Xia BY, Wu HB, Li N et al (2015) One-pot synthesis of Pt-Co alloy nanowire assemblies with tunable composition and enhanced electrocatalytic properties. Angew Chem Int Ed 54(12):3797–3801

37. Yoshimura M, Byrappa K (2008) Hydrothermal processing of materials: past, present and future. J Mater Sci 43(7):2085–2103
38. Tang Y, Zhang Y, Deng J et al (2014) Mechanical force-driven growth of elongated bending TiO_2-based nanotubular materials for ultrafast rechargeable lithium ion batteries. Adv Mater 26(35):6111–6118
39. Gilroy KD, Ruditskiy A, Peng H et al (2016) Bimetallic nanocrystals: syntheses, properties, and applications. Chem Rev 116(18):10414–10472
40. Lee H, Yang KD, Yoon SM et al (2015) Concave rhombic dodecahedral Au nanocatalyst with multiple high-index facets for CO_2 Reduction. ACS Nano 9(8):8384–8393
41. Cai B, Hübner R, Sasaki K et al (2018) Core-shell structuring of pure metallic aerogels towards highly efficient platinum utilization for the oxygen reduction reaction. Angew Chem Int Ed 57(11):2963–2966
42. Cai B, Sayevich V, Gaponik N et al (2018) Emerging hierarchical aerogels: self-assembly of metal and semiconductor nanocrystals. Adv Mater 30(33):1707518
43. Hench LL, West JK (1990) The sol-gel process. Chem Rev 90:33–72
44. Sui R, Charpentier P (2012) Synthesis of metal oxide nanostructures by direct sol-gel chemistry in supercritical fluids. Chem Rev 112(6):3057–3082
45. Herrmann A, Formanek P, Borchardt L et al (2013) Multimetallic aerogels by template-free self-assembly of Au, Ag, Pt, and Pd nanoparticles. Chem Mater 26(2):1074–1083
46. Liu W, Rodriguez P, Borchardt L et al (2013) Bimetallic aerogels: high-performance electrocatalysts for the oxygen reduction reaction. Angew Chem Int Ed 52(37):9849–9852
47. Henning S, Kühn L, Herranz J et al (2017) Effect of acid washing on the oxygen reduction reaction activity of Pt-Cu aerogel catalysts. Electrochim Acta 233:210–217
48. Liu W, Herrmann A, Bigall NC et al (2015) Noble metal aerogels-synthesis, characterization, and application as electrocatalysts. Acc Chem Res 48(2):154–162
49. Rodriguez JA, Goodman DW (1992) The nature of the metal-metal bond in bimetallic surfaces. Science 257:897–903
50. Fang H, Yang J, Wen M et al (2018) Nanoalloy materials for chemical catalysis. Adv Mater 30(17):1705698
51. Zhang N, Shao Q, Xiao X et al (2019) Advanced catalysts derived from composition-segregated platinum-nickel nanostructures: new opportunities and challenges. Adv Func Mater 29(13):1808161
52. Lamer VK, Dinegar RH (1950) Theory, production and mechanism of formation of monodispersed hydrosols. 11(72):4847–4854
53. Duchesne PN, Li ZY, Deming CP et al (2018) Golden single-atomic-site platinum electrocatalysts. Nat Mater 17(11):1033–1039
54. Zhou M, Wang H, Elnabawy AO et al (2019) Facile one-pot synthesis of $Pd@Pt_{1L}$ octahedra with enhanced activity and durability toward oxygen reduction. Chem Mater 31(4):1370–1380
55. Lim B, Jiang M, Camargo PH et al (2009) Pd-Pt bimetallic nanodendrites with high activity for oxygen reduction. Science 324(5932):1302–1305
56. Luo S, Chen W, Cheng Y et al (2019) Trimetallic synergy in intermetallic PtSnBi nanoplates boosts formic acid oxidation. Adv Mater 1903683
57. Ma T, Wang S, Chen M et al (2019) Toward phase and catalysis control: tracking the formation of intermetallic nanoparticles at atomic scale. Chem 5(5):1235–1247
58. Wu L, Fournier AP, Willis JJ et al (2018) In situ X-ray scattering guides the synthesis of uniform PtSn nanocrystals. Nano Lett 18(6):4053–4057
59. Wang D, Peng Q, Li Y (2010) Nanocrystalline intermetallics and alloys. Nano Res 3(8):574–580
60. Vasquez Y, Sra AK, Schaak RE (2005) One-pot synthesis of hollow superparamagnetic CoPt nanospheres. J Am Chem Soc 127(36):12504–12505
61. Zhang Z, Liu Y, Chen B et al (2016) Submonolayered Ru deposited on ultrathin Pd nanosheets used for enhanced catalytic applications. Adv Mater 28(46):10282–10286
62. Yao Y, He DS, Lin Y et al (2016) Modulating FCC and HCP ruthenium on the surface of palladium-copper alloy through tunable lattice mismatch. Angew Chem Int Ed 55(18):5501–5505

63. Xie S, Choi S, Lu N et al (2014) Atomic layer-by-layer deposition of Pt on Pd nanocubes for catalysts with enhanced activity and durability toward oxygen reduction. Nano Lett 14(6):3570–3576
64. Yang P, Somorjai GA, Radmilovic V et al (2007) Shaping binary metal nanocrystals through epitaxial seeded growth. Nat Mater 6(9):692–697
65. Peng X (2003) Mechanisms for the shape-control and shape-evolution of colloidal semiconductor nanocrystals. Adv Mater 15(5):459–463
66. Choi S, Shao M, Lu N et al (2014) Synthesis and characterization of Pd@Pt-Ni core-shell octahedra with high activity toward oxygen reduction. ACS Nano 8(10):10363–10371
67. Niu Z, Wang D, Yu R et al (2012) Highly branched Pt-Ni nanocrystals enclosed by stepped surface for methanol oxidation. Chem Sci 3(6):1925
68. Van der Vliet DF, Wang C, Tripkovic D et al (2012) Mesostructured thin films as electrocatalysts with tunable composition and surface morphology. Nat Mater 11(12):1051–1058
69. Debe MK, Steinbach ZAJ, Vernstrom GD et al (2011) Extraordinary oxygen reduction activity of Pt_3Ni_7. J Electrochem Soc 158(8):B910–B918
70. Bang JH, Suslick KS (2010) Applications of ultrasound to the synthesis of nanostructured materials. Adv Mater 22(10):1039–1059
71. Nagao D, Shimazaki Y, Saeki S et al (2007) Effect of ultrasonic irradiation on carbon-supported Pt-Ru nanoparticles prepared at high metal concentration. Colloids Surf A 302(1–3):623–627
72. Guo Z, Chen Y, Li L et al (2010) Carbon nanotube-supported Pt-based bimetallic catalysts prepared by a microwave-assisted polyol reduction method and their catalytic applications in the selective hydrogenation. J Catal 276(2):314–326
73. Song S, Wang Y, Shen PK (2007) Pulse-microwave assisted polyol synthesis of highly dispersed high loading Pt/C electrocatalyst for oxygen reduction reaction. J Power Sources 170(1):46–49
74. Han B, Carlton CE, Kongkanand A et al (2015) Record activity and stability of dealloyed bimetallic catalysts for proton exchange membrane fuel cells. Energy Environ Sci 8(1):258–266
75. Zhao Z, Liu H, Gao W et al (2018) Surface-engineered PtNi-O nanostructure with record-high performance for electrocatalytic hydrogen evolution reaction. J Am Chem Soc 140(29):9046–9050
76. Wang Y, Long W, Wang L et al (2018) Unlocking the door to highly active ORR catalysts for PEMFC applications: polyhedron-engineered Pt-based nanocrystals. Energy Environ Sci 11(2):258–275
77. Ge J, Li Z, Hong X et al (2019) Surface atomic regulation of core-shell noble metal catalysts. Chem A Eur J 25(20):5113–5127
78. Zheng Y, Zeng J, Ruditskiy A et al (2013) Oxidative etching and its role in manipulating the nucleation and growth of noble-metal nanocrystals. Chem Mater 26(1):22–33
79. Long R, Zhou S, Wiley BJ et al (2014) Oxidative etching for controlled synthesis of metal nanocrystals: atomic addition and subtraction. Chem Soc Rev 43(17):6288–6310
80. Xiong Y, Chen J, Wiley B et al (2005) Understanding the role of oxidative etching in the polyol synthesis of Pd nanoparticles with uniform shape and size. J Am Chem Soc 127(20):7332–7333
81. Chen C, Kang Y, Huo Z et al (2014) Highly crystalline multimetallic nanoframes with three-dimensional electrocatalytic surfaces. Science 343(6177):1339–1343
82. Ruditskiy A, Xia Y (2017) The science and art of carving metal nanocrystals. ACS Nano 11(1):23–27
83. Wang Y, Chen Y, Nan C et al (2015) Phase-transfer interface promoted corrosion from PtNi10 nanoctahedra to Pt_4Ni nanoframes. Nano Res 8(1):140–155
84. Han S, Liu H, Chen P et al (2018) Porous trimetallic PtRhCu cubic nanoboxes for ethanol electrooxidation. Adv Energy Mater 8(24):1801326
85. Wu Y, Wang D, Niu Z et al (2012) A strategy for designing a concave Pt-Ni alloy through controllable chemical etching. Angew Chem Int Ed 51(50):12524–12528

86. Wang L, Yamauchi Y (2013) Metallic nanocages: synthesis of bimetallic Pt-Pd hollow nanoparticles with dendritic shells by selective chemical etching. J Am Chem Soc 135(45):16762–16765
87. Strasser P, Koh S, Anniyev T et al (2010) Lattice-strain control of the activity in dealloyed core-shell fuel cell catalysts. Nat Chem 2(6):454–460
88. Mani P, Srivastava R, Strasser P (2008) Dealloyed Pt−Cu core-shell nanoparticle electrocatalysts for use in PEM fuel cell cathodes. J Phys Chem C 112(7):2770–2778
89. Gan L, Heggen M, O Malley R et al (2013) Understanding and controlling nanoporosity formation for improving the stability of bimetallic fuel cell catalysts. Nano Lett 13(3):1131–1138
90. Koh S, Strasser P (2007) Electrocatalysis on bimetallic surfaces: modifying catalytic reactivity for oxygen reduction by voltammetric surface dealloying. J Am Chem Soc 129(42):12624–12625
91. Srivastava R, Mani P, Hahn N et al (2007) Efficient oxygen reduction fuel cell electrocatalysis on voltammetrically dealloyed Pt-Cu-Co nanoparticles. Angew Chem Int Ed 46(47):8988–8991
92. Yue J, Du Z, Shao M (2015) Mechanisms of enhanced electrocatalytic activity for oxygen reduction reaction on high-index platinumn(111)-(111) surfaces. J Phys Chem Lett 6(17):3346–3351
93. Su L, Jia W, Li C et al (2014) Mechanisms for enhanced performance of platinum-based electrocatalysts in proton exchange membrane fuel cells. Chemsuschem 7(2):361–378
94. Li Q, Wu L, Wu G et al (2015) New approach to fully ordered fct-FePt nanoparticles for much enhanced electrocatalysis in acid. Nano Lett 15(4):2468–2473
95. Li J, Xi Z, Pan Y et al (2018) Fe stabilization by intermetallic $L1_0$-FePt and Pt catalysis enhancement in $L1_0$-FePt/Pt nanoparticles for efficient oxygen reduction reaction in fuel cells. J Am Chem Soc 140(8):2926–2932
96. Li J, Sharma S, Liu X et al (2019) Hard-magnet $L1_0$-CoPt nanoparticles advance fuel cell catalysis. Joule 3(1):124–135
97. Chong L, Wen J, Kubal J et al (2018) Ultralow-loading platinum-cobalt fuel cell catalysts derived from imidazolate frameworks. Science 362(6420):1276–1281
98. Wang XX, Hwang S, Pan Y et al (2018) Ordered Pt_3Co intermetallic nanoparticles derived from metal-organic frameworks for oxygen reduction. Nano Lett 18(7):4163–4171
99. Liao H, Fisher A, Xu ZJ (2015) Surface segregation in bimetallic nanoparticles: acritical issue in electrocatalyst engineering. Small 11(27):3221–3246
100. Wu Y, Li Y (2015) New understanding of phase segregation of bimetallic nanoalloys. Sci China Mater 58(1):3–4
101. Cui C, Gan L, Heggen M et al (2013) Compositional segregation in shaped Pt alloy nanoparticles and their structural behaviour during electrocatalysis. Nat Mater 12(8):765–771
102. Shao M, Chang Q, Dodelet J et al (2016) Recent advances in electrocatalysts for oxygen reduction reaction. Chem Rev 116(6):3594–3657
103. Liu H, Nosheen F, Wang X (2015) Noble metal alloy complex nanostructures: controllable synthesis and their electrochemical property. Chem Soc Rev 44(1):356–378
104. Quan Z, Wang Y, Fang J (2012) High-index faceted noble metal nanocrystals. Acc Chem Res 46(2):191–202
105. Zhang H, Jin M, Xia Y (2012) Noble-metal nanocrystals with concave surfaces: synthesis and applications. Angew Chem Int Ed 51(31):7656–7673
106. Zhang P, Dai X, Zhang X et al (2015) One-pot synthesis of ternary Pt-Ni-Cu nanocrystals with high catalytic performance. Chem Mater 27(18):6402–6410
107. Yu X, Wang D, Peng Q et al (2011) High performance electrocatalyst: Pt-Cu hollow nanocrystals. Chem Commun 47(28):8094
108. Wang X, Feng J, Bai Y et al (2016) Synthesis, properties, and applications of hollow micro-/nanostructures. Chem Rev 116(18):10983–11060
109. Lim B, Xia Y (2011) Metal nanocrystals with highly branched morphologies. Angew Chem Int Ed 50(1):76–85

110. Williamson CB, Nevers DR, Hanrath T et al (2015) Prodigious effects of concentration intensification on nanoparticle synthesis: a high-quality, scalable approach. J Am Chem Soc 137(50):15843–15851
111. Skrabalak SE, Xia Y (2008) Pushing nanocrystal synthesis toward nanomanufacturing. ACS Nano 3(1):10–15
112. Skrabalak SE, Au L, Li X et al (2007) Facile synthesis of Ag nanocubes and Au nanocages. Nat Protoc 2(9):2182–2190
113. Niu G, Zhou M, Yang X et al (2016) Synthesis of Pt-Ni octahedra in continuous-flow droplet reactors for the scalable production of highly active catalysts toward oxygen reduction. Nano Lett 16(6):3850–3857
114. Wu F, Zhang D, Peng M et al (2016) Microfluidic synthesis enables dense and uniform loading of surfactant-free PtSn nanocrystals on carbon supports for enhanced ethanol oxidation. Angew Chem Int Ed 55(16):4952–4956
115. Sahoo HR, Kralj JG, Jensen KF (2007) Multistep continuous-flow microchemical synthesis involving multiple reactions and separations. Angew Chem Int Ed 46(30):5704–5708
116. Skrabalak SE, Brutchey RL (2016) Going with the flow: continuous flow routes to colloidal nanoparticles. Chem Mater 28(4):1003–1005
117. Kim YH, Zhang L, Yu T et al (2013) Droplet-based microreactors for continuous production of palladium nanocrystals with controlled sizes and shapes. Small 9(20):3462–3467
118. Van den Berg A, Craighead HG, Yang P (2010) From microfluidic application to nanofluidic phenomena. Chem Soc Rev 39(3):899–900
119. Polshettiwar V, Varma RS (2010) Green chemistry by nano-catalysis. Green Chem 12(5):743
120. Albrecht MA, Evans CW, Raston CL (2006) Green chemistry and the health implications of nanoparticles. Green Chem 8(5):417
121. Anastas P, Eghbali N (2010) Green chemistry: principles and practice. Chem Soc Rev 39(1):301–312
122. Gu Y, Jérôme F (2010) Glycerol as a sustainable solvent for green chemistry. Green Chem 12(7):1127

Chapter 6
Application of Oxygen Reduction Catalysts

Jinliang Zhu, Xiaolan Wei, Yongliang Li, and Pei Kang Shen

Abstract Oxygen reduction reaction (ORR) has been realized existing in many devices like low-temperature fuel cells, metal-air (oxygen) batteries, oxygen sensors and the production of hydrogen peroxide. Therefore, oxygen reduction catalyst has attracted much attention. This chapter will focus on key parameters of ORR performance, and the research progress of metal-air batteries and secondary lithium-air batteries.

Keywords Oxygen reduction reaction · Fuel cell · Metal-air battery · Secondary lithium-air battery

6.1 Application of fuel cells

Oxygen reduction reaction (ORR) is the cathode reaction of low-temperature fuel cell. The slow oxygen reduction kinetics seriously restricts the energy conversion efficiency of low-temperature fuel cell and which is the key of fuel cell. In the oxygen reduction test of fuel cell, the peak-starting potential, half-wave potential and limiting current obtained from the oxygen reduction curve can obviously reflect the catalytic performance of the oxygen reduction electrocatalytic material. In this section, peak potential, half-wave potential and limiting current are discussed.

J. Zhu · P. K. Shen (✉)
Collaborative Innovation Center of Sustainable Energy Materials, Guangxi Key Laboratory of Electrochemical Energy Materials, Guangxi University, Nanning, Guangxi, China
e-mail: pkshen@gxu.edu.cn

X. Wei
School of Chemistry and Chemical Engineering, South China University of Technology, Guangzhou, Guangdong, China

Y. Li
College of Chemistry and Environmental Engineering, Shenzhen University, Shenzhen, Guangdong, China

P. K. Shen, *Electrochemical Oxygen Reduction*,
https://doi.org/10.1007/978-981-33-6077-8_6

6.1.1 The Peak Potential

For a single fuel cell ($E = E_{cathode} - E_{anode}$), the higher the peak potential of oxygen reduction, the better. The peak potential of oxygen reduction mainly depends on the catalyst material itself (catalyst type).

In acidic media, although many nonplatinum catalysts, such as metal carbides, metal sulfides, metal selenides, M-N_x/C (M = Fe or Co) and heteroatom-doped carbon materials have been reported, their peak potentials are generally lower than platinum catalysts. In 2006, Huamin Zhang's group reported that Mo_2N catalyst demonstrated the oxygen reduction peak potential of 0.46 V versus SCE in 0.5 mol/L sulfuric acid solution [1]. In the study of Akimitsu Ishihara's group in 2012, the peak potential of oxygen reduction in 0.1 mol/L sulfuric acid solution was 0.5–0.6 V versus RHE. The oxygen reduction peak potential of Ta-CO obtained from TaC was 0.8 V versus RHE [2]. In 2010, Pei Kang Shen's and Shuhong Yu's group reported that the oxygen reduction peak potential of porous Co_9S_8 spheres in 0.5 mol/L sulfuric acid solution was 0.74 V versus RHE [3]. In 2008, Nicolas Alonso-Vante reported that the oxygen reduction peak potential of carbon-loaded Co_3S_4 in 0.5 mol/L sulfuric acid solution was 0.66 V versus RHE [4]. In 2011, Hongjie Dai's group at Stanford University studied the oxygen reduction performance of $Co_{1-x}S$/graphene and found that $Co_{1-x}S$ had the highest activity among the reported cobalt sulfide catalysts of oxygen reduction, showing the peak potential of 0.8 V versus RHE in 0.5 mol/L sulfuric acid solution [5].

Due to the combination of lone pair electrons of nitrogen atoms in nitrogen-doped carbon materials and π electron system on the surface of graphitized carbon materials, the reconfiguration of carbon atoms and the formation of local defects produce oxygen reduction activity [6], and it is one of the most promising materials in nonprecious metal catalysts. Nitrogen-doped carbon materials have the same peak potential of oxygen reduction as Pt in alkaline media. In 2009, the group of Liming Dai found that when nitrogen-doped carbon nanotube array was used as an oxygen reduction catalyst, it had almost the same peak potential of Pt/C catalyst in 0.1 mol /L KOH [7]. Afterward, a large number of experimental studies showed that the peak potential of oxygen reduction of nitrogen-doped carbon materials such as nitrogen-doped carbon nanotubes, nitrogen-doped graphene and nitrogen-doped graphite cage in alkaline media was equivalent to that of Pt/C catalyst. In 2010, Wolfgang Schuhmann's group in Germany [8] reported that nitrogen-doped carbon nanotubes (NCNT-800) obtained by heat treatment of carbon nanotubes at 800 °C under ammonia gas had a peak potential of 0.06 V (vs. Ag/AgCl/3 M KCl) and which was higher than that of commercial Pt/C in 1 mol/L sodium hydroxide solution. In 2011, Xueliang Sun's group in Canada [9] used ammonia gas at 900°C to heat treat graphene to obtain nitrogen-doped graphene N-graphene (900), the peak potential of oxygen reduction of in 0.1 mol/L potassium hydroxide solution was 0.308v (vs. SHE). It is more positive than the peak potential of oxygen reduction measured by commercial Pt/C (E-TEK) under the same experimental conditions. In 2012, Xizhang Wang research group of Nanjing University of China [10] used

pyridine as the precursor to prepare nitrogen-doped carbon nanocage by magnesium oxide template method. The peak potential of oxygen reduction of nitrogen-doped carbon nanocage in 0.1 mol/L potassium hydroxide solution was close to that of Pt/C catalyst under the same experimental conditions. However, in acidic media, the oxygen reduction peak potential of nitrogen-doped carbon catalyst is much lower than that of Pt under the same experimental conditions. In 2011, Xueliang Sun's research group in Canada prepared nitrogen-doped carbon nanotubes (CNx) with controllable nitrogen content by floating catalyst chemical vapor deposition [11], nitrogen-doped carbon nanotubes (CNx) with surface nitrogen content (atomic ratio) of 7.7 at.% have an oxygen reduction threshold potential of 0.705 V (vs. SHE) in 0.5 mol/L sulfuric acid solution saturated with oxygen. In 2014, Keiko Waki of Japan reported that nitrogen-doped carbon nanotubes only had a peak potential of about 0.73 vs RHE in acidic media [6]. The author further pointed out that the activity was caused by the reconstruction of carbon atoms and the formation of local defects. The nitrogen-doped carbon nanotubes and graphene composite (NT-G) catalyst prepared by professor Hongjie Dai of Stanford university in 2012 [12] showed a very positive peak potential in acidic media, and the peak potential of oxygen reduction was as high as 0.89 V (vs. SHE) in 0.1 mol/L perchloric acid solution. The oxygen reduction electrocatalytic activity of nitrogen-doped carbon materials has aroused great interest in recent years. Researchers used a lot of experiments and theoretical calculations to analyze the production of its catalytic activity. Some scholars believe that carbon atoms with high positive charge are formed by doping nitrogen atoms with strong electrophilic properties. This carbon atom can effectively bind O_2 [13, 14] through side adsorption of oxygen molecules, thus generating oxygen reduction activity. However, there is no strong evidence on the generation of oxygen reduction activity of nitrogen-doped carbon materials in the literature, and the real activity site and its causes of nitrogen-doped carbon materials still need to be further studied.

Another widely studied non-noble metal catalyst for high activity oxygen reduction is transition metal/nitrogen-carbon material M-N_x/C (M = Fe or Co). Early M-N_x/C catalysts were transition metal complexes of nitrogen-containing macromolecules such as phthalocyanine and porphyrin with coordination number of four [15, 16]. The metal ions coordinate with the four nitrogen atoms in these macromolecular heterocyclic compounds to form the planar MN_4 structure (M is the transition metal, N is the coordination nitrogen atom in the chelating heterocyclic compound), it is generally considered as the active point of oxygen reduction in catalysts [17, 18]. However, recent studies by J. P. Dodelet showed that FeN_2/C also has oxygen reduction activity, and MN_2 structure may also be an oxygen reduction activity point [17]. Therefore, the "general structural formula" of M-N_x/C electrocatalyst activity is often expressed as: M-N_x/C (M refers to transition metals such as Co, Fe, Ni, etc.; N is the nitrogen atom of the chelating agent; X = 2 or 4; C is generally sp^2 carbon).

In 1964, Jasinski [15] first discovered that phthalocyanine cobalt (CoPc) has electrocatalytic performance of oxygen reduction in alkaline solutions. In 1978, Bagotzky et al. [19] improved the electrocatalytic activity and stability of the original M-Nx/C catalyst in acidic solution by using high-temperature heat treatment in an inert atmosphere such as porfin and cobalt phthalocyanine. In 1989, Yeager et al. [20] prepared

oxygen reduction catalyst for the first time by heat treatment at 800°C with a mixture of nonmacrocyclic polyacrylonitrile, ferrous acetate (or cobalt acetate) and charcoal powder. The catalyst showed high oxygen reduction activity in acidic solutions, with a peak potential of about 0.90 V (vs RHE) in 0.05 mol/L sulfuric acid solution. In 2011, Gang Wu et al. [21] from Los Alamos National Laboratory obtained nitrogen-stable PANI-Fe–C and PANI-FeCo-C catalysts by heat-treating polyaniline and Fe-N_x (Co-N_x) complexes. The peak potential of oxygen reduction in perchloric acid solution at 0.1 mol/L reached 0.93 V (vs RHE), which was comparable to that of Pt/C (E-TEK) catalyst under the same conditions. M-Nx/C non-noble metal oxygen reduction catalysts have been extensively studied, and the oxygen reduction activity and peak potential of the catalysts have been optimized by adjusting different experimental conditions such as nitrogen source precursor, metal source and heat treatment process.

Palladium (Pd), in the same group as platinum, often exhibits similar chemical properties to platinum and has recently attracted great attention due to its obvious advantages in reserves and price over platinum [22]. After various structural modification and enhancement, the oxygen reduction activity of Pd-based electrocatalysts in acidic media has been significantly improved, showing a peak potential equivalent to platinum. In 2007, Mustain et al. successfully synthesized cobalt palladium ($CoPd_x$) bimetallic electrocatalyst [23], and $CoPd_3$ showed the highest oxygen reduction activity and peak potential of 0.9 V versus NHE in 0.5 mol/L acid sulfuric acid electrolyte. In $CoPd_3$, Co atom has played the role of adsorption of oxygen molecules and rapid electron transfer, so that $CoPd_3$ bimetallic electrocatalyst acid oxygen reduction performance improved, thus showing a higher peak potential. In the same year, Yang Hui et al., from Chinese academy of sciences, confirmed that CoPd of high temperature heat treatment has higher oxygen reduction activity and peak potential in 0.1 mol/L chloric acid solution [24]. In 2008, Solorza-Feria found that PdNi alloy also had good oxygen reduction performance in 0.5 mol/L sulfuric acid solution, and the introduction of Ni greatly reduced the oxygen reduction overpotential of Pd, making it 110 mV more positive than the peak potential of Pd [25]. In 2011, professor Shen Peikang's research group from Sun Yat-sen university reported that tungsten carbide (WC) enhanced PdFe bimetallic catalyst (PdFe-WC/C) had the same oxygen reduction peak potential as commercial Pt/C in 0.5 mol/L sulfuric acid solution, and the introduction of methanol in electrolyte had almost no impact on the oxygen reduction peak potential of PdFe-WC/C [26]. This work has attracted extensive attention to the oxygen reduction performance of Pd-based nonplatinum electrocatalysts in acidic environment. In 2014, professor Shen's group in Sun Yat-sen university once again reported that tungsten carbide cobalt (WC) enhanced Pd metal catalyst (Pd/Co_3W_3C) had the same oxygen reduction peak potential as commercial Pt/C in 0.1 mol/L chloric acid solution, reaching 0.98 V versus RHE.

Platinum, the most widely used oxygen reduction electrocatalyst for fuel cell, has the best electrocatalytic activity. The peak potential of oxygen reduction of platinum/carbon catalyst in acidic medium is generally considered to be around 1.0 V versus RHE [27, 28]. The oxygen reduction peak potential of platinum can be improved by carrier synergy and electron effect.

6.1.2 Half-Wave Potential ($E_{1/2}$)

The half-wave potential of oxygen reduction is the potential corresponding to the half of the limiting diffusion current. Half-wave potential is an important parameter of oxygen reduction performance of catalyst material, which can be directly obtained from oxygen reduction curve, and it is a direct reflection of electrocatalytic activity of oxygen reduction catalyst. From catalyst (Pt catalysts, for example), the calculation [formula (6.1) ~ (6.3)] of quality activity and specific activity can be seen that different catalyst with moderate thickness (the limiting current of oxygen reduction test will not change obviously due to the thickness of catalyst layer) and the same test conditions (such as the same temperature, the same electrolyte solution, the same speed and the same electrochemical scanning speed), when the quality of the catalyst active substances (Pt) and specific surface area are constant, and oxygen reduction limiting current phase is the same, the higher the half-wave potential of oxygen reduction, the better the mass activity and specific activity of the catalyst at the same potential.

$$\mathrm{i_k} = \mathrm{i_d i}/(\mathrm{i_d} - \mathrm{i}) \tag{6.1}$$

$$i_m\ (\mathrm{m}A\ mg_{Pt}^{-1}) = \frac{i_k\ (mA)}{Pt_{Loading}\ (\mathrm{m}g)} \tag{6.2}$$

$$i = nFD_0\frac{a_O^0 - a_O^{\mathrm{s}}}{\delta} \tag{6.3}$$

i_k is the kinetic current, and i_d is the limiting current; i is the measured current under any potential; i_m is the mass activity of catalyst; $i_s$is the specific activity of catalyst; $Q_{\text{H-adsorption}}$ is electricity of hydrogen adsorption, L_{Pt} is Pt loading mass.

The half-wave potential is mainly dependent on the oxygen reduction catalyst material, and it is also affected by the supporting electrolyte solution and the test temperature. The catalyst material, supporting electrolyte and test temperature are discussed.

It can be seen that the treatment of nanoporous pni alloy with ionic liquid ([MTBD][beti]) significantly improved the half-wave potential of oxygen reduction [about 0.4 V vs. (RHE)], mainly because the solubility and diffusion coefficient of oxygen in ionic liquid ([MTBD][beti]] were significantly improved in perchloric acid solution.

As shown in Fig. 6.1, the half-wave potential of oxygen reduction reaction polarization curve of commercial Pt/C catalyst (Japan TKK, 47.6%Pt) in various oxygen saturated electrolyte solutions (perchloric acid, sulfuric acid, nitric acid and hydrochloric acid) is also different, commercial Pt/C catalysts with the same amount showed the highest oxygen reduction half-wave potential in perchloric acid solution, and the second is in solutions of nitric and sulfuric acid, while in hydrochloric acid solution, the half-wave potential of oxygen reduction in catalyst oxygen reduction

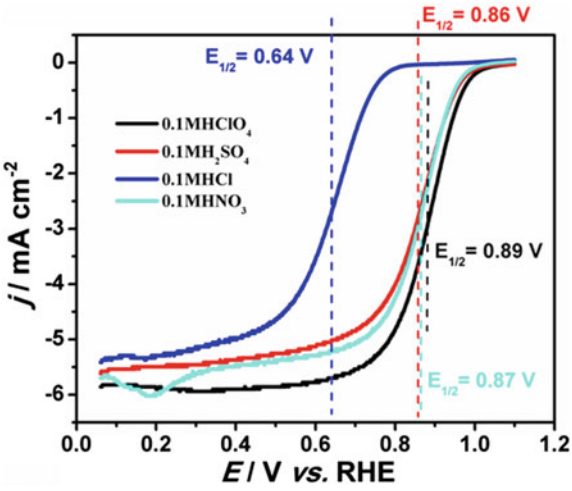

Fig. 6.1 Half-wave potential of oxygen reduction reaction polarization curve of commercial Pt/C catalyst (Japan TKK, 47.6%Pt) in different oxygen-saturated electrolyte solutions. Experimental conditions: electrode speed 1600 rpm, potential sweep 5 mV s^{-1}, temperature 25 °C, Pt load 40 μg cm^{-2}

was significantly reduced, only 0.64 V (vs. RHE). This is mainly due to the different solubility and diffusion coefficient of oxygen in different electrolyte solutions and the different adsorption effect of anions on electrocatalysts.

6.1.3 Limiting Current

Concentration polarization: if the reaction rate is determined by the mass transfer of the reactants or products, there may be polarization caused by the concentration difference in the electrolyte. If the cathode oxygen reduction reaction is expressed by the following equation:

$$O + e^{n-} \rightarrow R \tag{6.4}$$

When entering the steady state, according to Fick's First Law, the current density can be expressed as follows:

$$i = nFD_0 \frac{a_O^0 - a_O^8}{\delta} \tag{6.5}$$

$a_o{}^s$ is the activity of reactant oxygen on the electrode surface; $a_o{}^o$ is the activity of oxygen in solution.δ is the thickness of the diffusion layer; D_O is the diffusion coefficient of oxygen. From the above equation, it can be concluded that if the reaction is only controlled by mass transfer, the activity of oxygen on the electrode surface is almost zero, so the limiting current can also be expressed as follows:

$$i = nFD_0 \frac{a_O^0}{\delta} \tag{6.6}$$

In the oxygen reduction reaction, the limiting current can be expressed as:

$$i_d = \frac{nFD_0C_0}{\delta} \tag{6.7}$$

In the formula, D_O is the diffusion coefficient of oxygen, and C_o is the concentration of oxygen in solution. For rotating electrode, limited current can also be expressed by Levich's equation:

$$i_\mathrm{d} = 0.62nFD_0^{2/3}\omega^{1/2}\upsilon^{-1/6}C_0 \tag{6.8}$$

In the formula, n is the number of electrons transferred during oxygen reduction, F is Faraday constant, D_O is the diffusion coefficient of oxygen in electrolyte solution, ω is the angular velocity of electrode rotation, υ is the kinetic viscosity of electrolyte solution, Co is the concentration of oxygen in electrolyte solution.

From the above formula, we can get the factors that affect the oxygen reduction limiting current are the oxygen reduction test temperature, the electrolyte during the oxygen reduction test, the rotation rate of the working electrode and the thickness of the catalyst thin layer.

In Eq. (6.8), as the test temperature rises, the diffusion coefficient D_O of oxygen in the electrolyte solution will increase, but the oxygen concentration Co in the electrolyte solution will decrease, and the limiting current density will depend on their equilibrium value. In addition, too high temperature will lead to the change of the properties of Nafion membrane, thus affecting the limiting current density.

The solubility and diffusion coefficient of oxygen in different electrolyte solutions and the kinetic viscosity of electrolyte solutions vary with the types and concentrations of electrolyte solutions [32]. According to Eq. (6.8), the limiting current density of oxygen reduction in various electrolyte solutions of the same catalyst is also different. As shown in Fig. 6.2, in the same concentration of several kinds of common acid electrolyte solution (perchloric acid, sulfuric acid, nitric acid and hydrochloric acid), and the same loads of commercial Pt/C catalyst in perchlorate solution showed the biggest oxygen reduction limiting current density, the second is in the same concentration of nitric acid and sulfuric acid solution. In the same concentration of hydrochloric acid solution, the catalyst oxygen reduction limiting current density is the smallest. In different concentrations of the same kind of electrolyte, the limiting current density of catalyst oxygen reduction is also affected by the concentration of electrolyte solution. In the same type of electrolyte with different concentrations, as shown in Fig. 6.3, in sulfuric acid solution, the limiting current density of commercial Pt/C catalyst at the concentration of 0.1 mol/L is higher than that at the concentration of 0.5 mol/L. Figure 6.4 shows the effects of perchloric acid solutions of different concentrations on the limiting current density of commercial Pt/C oxygen reduction. Commercial Pt/C catalysts showed the maximum limiting

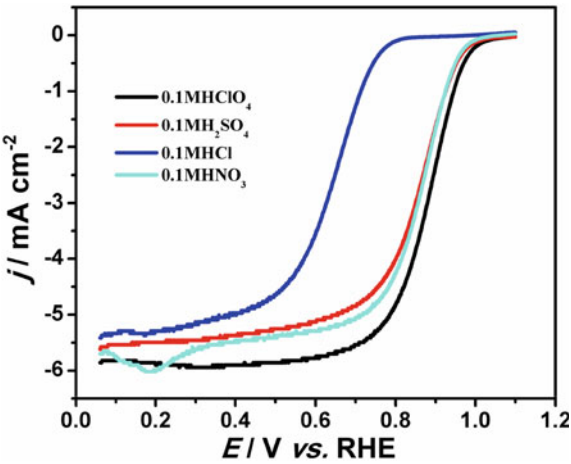

Fig. 6.2 Effect of different electrolyte solutions with the same concentration on the limiting current of oxygen reduction reaction of commercial Pt/C catalyst (Japan TKK, 47.6%Pt). (Oxygen saturated solution, electrode speed 1600 r min^{-1}, potential sweep 5 mV s^{-1}, temperature 25 °C, Pt load 40 ug cm^{-2}.)

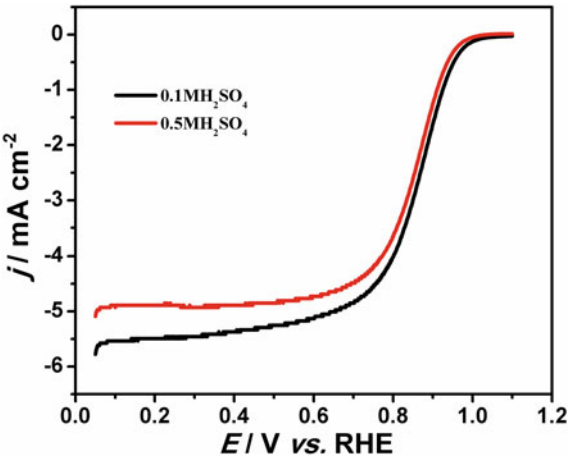

Fig. 6.3 Effect of the sulfuric acid solution with different concentrations on the limiting current of commercial Pt/C catalyst (Japan TKK, 47.6%Pt) oxygen reduction reaction. (Oxygen saturated solution, electrode speed 1600 r min^{-1}, potential sweep 5 mV s^{-1}, temperature 25 °C, Pt load 40 ug cm^{-2}.)

current density of oxygen reduction in perchloric acid solution at 0.1 mol/L, followed by 0.5 mol/L perchloric acid solution, and showed the minimum limiting current density of oxygen reduction in perchloric acid solution at 1.0 mol/L.

As the rotating speed of the working electrode increases, the thickness of diffusion layer will decrease, so the limiting current density of oxygen reduction will enhance. The relationship between the limiting current density of oxygen reduction and the rotation velocity of the working electrode (rotating disc electrode) can be further discussed according to Koutecky–Levich equation, which is as follows [33, 34]:

$$\frac{1}{j} = \frac{1}{j_k} + \frac{1}{B\omega^{1/2}} \tag{6.9}$$

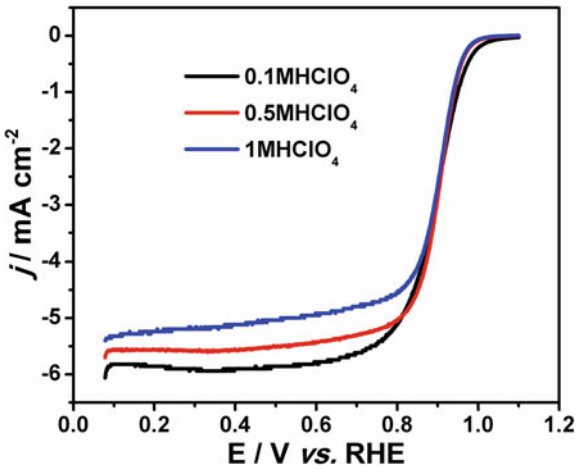

Fig. 6.4 Effects of perchloric acid electrolyte solutions with different concentrations on the limiting current of oxygen reduction reaction of commercial Pt/C catalyst (Japan TKK, 47.6%Pt). (Oxygen saturated solution, electrode speed 1600 rpm, potential sweep 5 mV s^{-1}, temperature 25 °C, Pt load 40 ug cm^{-2}.)

where j is the measured current density of oxygen reduction reaction, j_k is the kinetic current density of oxygen reduction reaction, and ω is the angular velocity of rotating disc electrode. It can be seen from the above equation that, in the diffusion region of low potential, the measured limiting current density of oxygen reduction is proportional to the inverse square root of angular velocity.

Figure 6.5 shows the oxygen reduction curve of platinum nanoparticles dispersed in carbon nanotube catalyst in 0.1 mol L^{-1} chloric acid solution. It can be seen from the figure that the limiting current density of oxygen reduction reaction displayed by catalyst boosts with the increase of rotating speed of working electrode. Between 0.3 V (vs. RHE) and 0.6 V (vs. RHE), the limiting current density of oxygen reduction measured by platinum nanoparticles dispersed in carbon nanotube catalyst in 0.1 mol L^{-1} chloric acid solution is proportional to the inverse square root of angular velocity of rotating disk electrode, resulting in Koutecky–Levich diagram (Fig. 6.6).

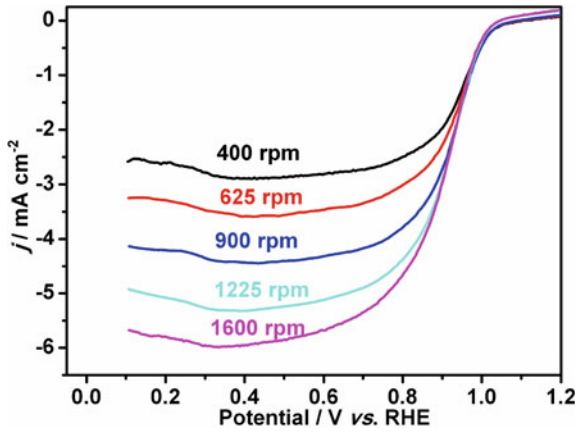

Fig. 6.5 The linear scanning curve of platinum nanoparticles dispersed at different rotation speeds in 0.1 mol L^{-1} perchloric acid solution. (Oxygen saturated solution, electrode speed 1600 r min^{-1}, potential sweep 5 mV s^{-1}, temperature 25 °C, Pt load 20.20 ug cm^{-2}.)

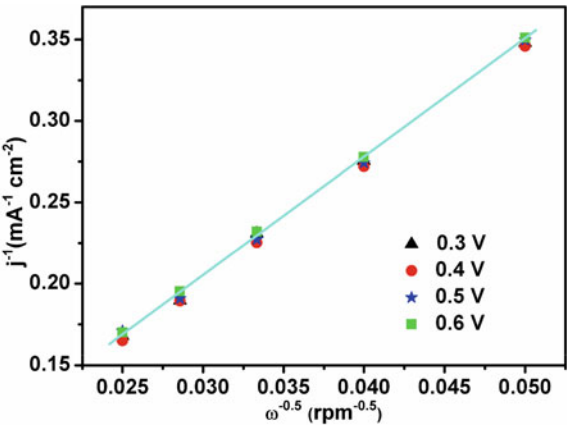

Fig. 6.6 Shows the Koutecky–Levich diagram of platinum nanoparticles dispersed in carbon nanotube catalyst at different potentials of 0.1 mol L^{-1} in chloric acid solution. (Oxygen saturated solution, electrode speed 1600 r min^{-1}, potential sweep 5 mV s^{-1}, temperature 25 °C, Pt load 20.20 ug cm^{-2}.)

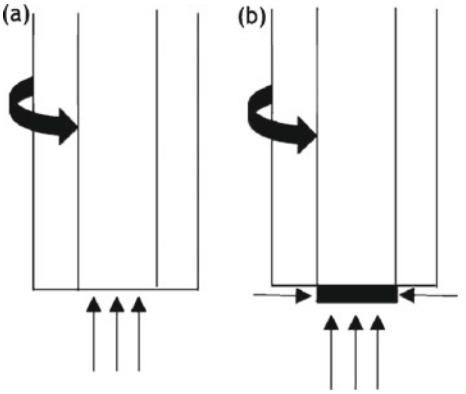

Fig. 6.7 Schematic diagram of mass transfer of catalyst film layer: **a** thin catalyst layer; **b** thick catalyst layer

Compared with the thinner catalyst layer, the mass transfer effect on the side of the thicker catalyst layer increases and cannot be ignored, so the limiting current density increases. However, with the increase of catalyst thickness, the oxygen reduction limiting current density deviates from the proportional relationship with the inverse square root of rotating disk electrode angular velocity. When the thin layer thickness of Pt/C catalyst increases to 8 μm, the measured limiting current density of oxygen reduction is no longer proportional to the inverse square root of angular velocity of rotating disk electrode.

The catalyst (Pt/C catalyst) layer is thin enough that mass transfer on the side of the catalyst layer can be ignored. The (rotating disk) electrode rotates at a speed of 1600 r min^{-1}, the limiting current density of the catalyst in an acid solution saturated with oxygen at 25 °C is 6 mA cm^{-2}. However, according to some reports, the limiting current of oxygen reduction electrocatalysis, especially for non-noble metal catalysts, is more than 6 mA cm^{-2}, this is mainly due to the mass transfer effect on the thick side of the catalyst layer cannot be ignored. Assuming that the

thickness of the catalyst layer is 50 μm and the geometric area of the electrode is 0.2475 cm^2 ($A_{geo} = 0.2475\ cm^2$), then the real area of the catalyst layer (A_{real}) is the sum of the geometric area of the electrode (A_{geo}) and the side area of the catalyst layer (A_{side}). At present, it is impossible to measure the thickness of catalyst thin layer accurately when measuring oxygen reduction with rotating disk electrode or ring disk electrode. When calculating the limiting current density of catalyst oxygen reduction reaction, it is still calculated according to the geometric area of electrode. Thus, the calculated limiting current density is greater than 6 mA cm^{-2} (as shown in Eqs. 6.2.3–6.7, 6.2.3–6.8 and 6.2.3–6.9).

$$A_{real} = A_{geo} + A_{side} = 0.2475 cm^2 + 0.005 * 3.14 * 0.56\ cm^2 = 0.2563\ cm^2 \tag{6.10}$$

$$i_d = 0.62nF\ D_0^{2/3}\omega^{1/2}v^{-1/6}C_0A_{real} = 6 * 0.2563 = 1.538\ mA \tag{6.11}$$

$$i_d / A_{geo} = 1.538\ mA\ /\ 0.2475\ cm^2 = 6.214\ mA\ cm^{-2} \tag{6.12}$$

6.2 Application in Metal-Air Battery

6.2.1 Overview of Metal-Air Batteries

The so-called metal-air battery refers to a kind of "semi-fuel cell" with the characteristics of both primary cell and fuel cell. The negative electrode of the battery is metal, the positive electrode of the battery is air electrode, and electrolyte is between the positive and negative electrodes of the battery [37–39].

Electrolytes can be divided into three types according to the reaction characteristics of metal negative electrodes: aqueous, nonaqueous and aqueous–nonaqueous mixed. Metal negative electrode of metal-air battery acts like fuel in fuel cell. Metal-air battery is also called metal fuel cell. The biggest difference with primary battery is that the positive active material of metal-air battery is air, the air electrode only accounts for a small part of the battery volume, and the vacant position can carry a large amount of active negative metal, so that the metal-air battery has a large energy density. The biggest difference with fuel cells is that the metal fuel is built-in and the negative electrode reaction is highly active, so expensive negative electrode catalyst is not needed and thus the price is low. In terms of high energy density of metal-air battery, Table 6.1 lists the comparison of actual performance parameters between two metal-air batteries and other kinds of vehicle power batteries.

Although the metal-air battery has obvious advantages, due to the high activity of the metal negative electrode, there are also some negative effects, for example, the self-discharge of metal contact electrolyte and the adhesion of discharge products on the metal surface reduce the discharge efficiency of the negative electrode, which

Table 6.1 Comparison of actual performance parameters between metal-air battery and other power batteries for electric vehicles

Battery type	Theoretical energy density (Wh/kg)	Actual energy density (Wh/kg)	Power density (W/kg)	Cycle life (n)	Cost (Yuan/Wh)
Lead acid battery	170	30–45	200–400	500	0.7
Nickel cadmium battery	214	40–60	200–400	1000	2.5
Ni-MH battery	275	70–80	400–1200	1000	4.0
Li-ion battery	444	150–250	400–1000	2000	4.0
Zinc-air battery	1350	180–230	100–200	>1000	0.7
Aluminum-air battery	8036	320–450	100–200	>1000	0.5

are the reasons why the efficiency of the metal-air battery is difficult to reach the theoretical value. Table 6.2 lists some advantages and disadvantages of metal-air battery.

Metal-air battery mainly considers the matching and economy with negative electrode in the selection of air positive electrode. In terms of metal electrode selection, the easy oxidation of metal, the contact stability between metal and electrolyte, and the complete oxidation degree of metal during discharge should be fully considered from the technical level. From the aspect of economy, the battery weight (or volume), cost and availability of negative electrode materials needed to release a certain amount of electric energy should be considered. Table 6.3 lists the theoretical energies of various metals when oxidized in electrochemical batteries. The weight of air can be ignored. The weight of battery includes electrolyte, battery case and current connector.

Table 6.2 Advantages and disadvantages of metal-air battery

Advantages	Disadvantages
High volume energy density	Dependence on environmental conditions:
The discharge voltage is stable	Once exposed to air, electrolyte dries up and shortens the service life of the electrode plate
In the dry storage state, the electrode plate has a long service life	If the electrode is submerged, the output power will be reduced
No ecological problems	Limited power output
Low cost (based on the cost of metal used)	Narrow operating temperature range
Within the operating range, the capacity and load are independent of temperature	Negative electrode corrosion generates hydrogen and alkaline electrolyte carbonation

Table 6.3 Theoretical energy density and potential characteristics of various metal-air batteries [37, 38]

Battery	Theoretical potential (V)	Theoretical energy density (Wh/kg)
Lithium-air	3.44	11,140
Aluminum-Air	2.71	8036
Magnesium-air	3.09	6812
Sodium-air	2.3	1600
Zinc-air	1.65	1350
Iron-air	1.28	1226
Cadmium-air	1.21	575
Lead-air	1.59	410

6.2.2 Classification of Metal-Air Batteries

There are many classification methods for metal-air batteries. According to the types of negative metal of the battery [38, 39], metal-air battery can be divided into lithium-air battery, sodium-air battery, magnesium-air battery, aluminum-air battery, zinc-air battery, iron-air battery, etc. According to the characteristics of battery electrolyte, it can be divided into aqueous, nonaqueous and aqueous–nonaqueous mixed electrolyte metal-air batteries. According to whether the battery is rechargeable, the metal-air battery can be divided into primary battery, secondary battery and mechanical rechargeable battery. The ideal primary metal-air battery should have the characteristics of large battery capacity, low price, long storage life, light weight, small size and portability. The ideal secondary metal-air battery should have the characteristics of good reversibility of electrode reaction (especially air electrode), low volatility of electrolyte and stable charging and discharging process. The ideal mechanical rechargeable battery should have the characteristics of large capacity, rapid replacement of negative electrode, and the electrolyte can be supplemented only by adding water. The discharged products of the battery can be sent to the central processing station for chemical or electrochemical reduction, and can be regenerated at low cost for repeated use.

Among several classification methods, the most common is the classification method according to different types of battery negative metal. Different kinds of metal-air batteries can be used for navigation marks, mine lighting, underwater power propulsion devices, electric vehicles, etc. depending on their discharge performance. Among them, metal-air power batteries for electric vehicles are one of the current research hotspots. Among several metal-air batteries, lithium-air, aluminum-air and zinc-air batteries are the most widely studied, among which aluminum-air batteries are the most promising commercial metal-air power batteries due to their low cost, use of aqueous electrolyte and relatively mature technology. The lithium-air battery is the metal-air battery with the most in-depth basic research under the promotion of the research on lithium ion battery and fuel cell.

6.2.2.1 Lithium-air Battery

Lithium-air battery has the highest theoretical energy density except H_2–O_2 fuel cell. Its theoretical energy density can reach 11,140 Wh/kg, which is close to the theoretical energy density of gasoline engine and is more than 10 times of the theoretical energy density of high-performance lithium-ion battery at present. Therefore, researchers have paid much attention to it. Compared with the existing lithium-ion battery, since the anode of the lithium-air battery does not use heavy metal oxides, the actual power storage capacity is four to five times that of the lithium-ion battery.

Lithium-air batteries can be divided into four categories according to the electrolyte used: nonaqueous solvent, aqueous solvent, nonaqueous/aqueous hybrid and all-solid-state electrolyte [40–42]. Among them, nonaqueous solvent type lithium-air battery is the research hotspot of lithium-air secondary battery.

(1) **Charging and discharging mechanism of lithium-air battery**

In nonaqueous organic electrolysis, the discharge reaction of lithium-air battery is [40, 41]:

$$4Li + O_2 \rightarrow 2Li_2O \ (E^{\ominus} = 2.9\ V).$$

$$2Li + O_2 \rightarrow Li_2O_2 \ (E^{\ominus} = 3.1\ V).$$

Theoretically, when the lithium-air battery discharges, the negative metal Li loses electrons to form Li^+ which enters the electrolyte and is transported to the positive electrode through the electrolyte. Positive oxygen is reduced under the catalysis of an air electrode catalyst to generate O^{2-} and $O_2{}^{2-}$. O^{2-} and $O_2{}^{2-}$ combine with Li^+ transported from the electrolyte to generate lithium oxide (Li_2O) or lithium peroxide (Li_2O_3). Due to the poor solubility of lithium oxide in organic electrolyte, it deposits on the positive electrode and gradually blocks the air channel to cover the catalyst. The final discharge is terminated. The discharge process is shown in Fig. 6.8.

During charging, Li^+ in the electrolyte obtains electron-generating metal Li deposition on the negative electrode and returns to the nondischarged metal state; O^{2-} and $O_2{}^{2-}$ in Li_2O or Li_2O_3 at one end of the positive electrode lose electrons to become O_2 and volatilize into the air, and the released Li^+ enters the electrolyte and is transmitted to one end of the negative electrode to supplement the reduction of Li^+ concentration caused by Li deposition in the electrolyte near the negative electrode until Li_2O or Li_2O_3 in the positive electrode is completely electrolyzed, and charging is completed at this time.

The actual charging and discharging situation is far from simple. When discharging, O_2 at one end of the positive electrode first obtains an electron under the action of an air electrode catalyst to form superoxide anion O^{2-}, and combines with Li^+ to form lithium superoxide LiO_2. LiO_2 either decomposes to release O_2 to generate Li_2O_3, or another electron is obtained and combined with Li^+ to form lithium peroxide Li_2O_3, and Li_2O_3 obtains another two electrons and combines with 2 Li^+ to form lithium oxide Li_2O.

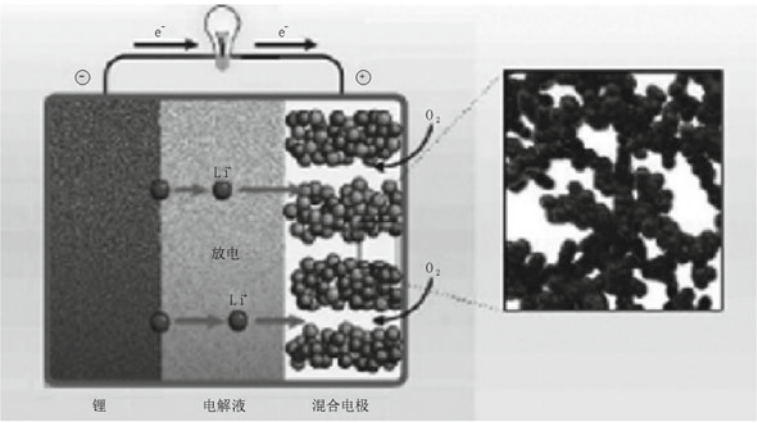

Fig. 6.8 schematic diagram of lithium-air battery discharge

$$O_2 + Li^+ + e^- = LiO_2.$$
$$2LiO_2 = Li_2O_2 + O_2.$$
$$LiO_2 + Li^+ + e^- = Li_2O_2.$$
$$Li_2O_2 + 2Li^+ + 2e^- = 2Li_2O.$$

Superoxide anion O^{2-} formed in the discharge process is extremely active, and besides the above-mentioned main discharge reaction, it may also attack the binder in electrolyte, air electrode, etc. For example, O^{2-} can decompose ester, ether and amide electrolytes to form Li_2CO_3 on the air electrode, affecting the stability of the electrolyte; O^{2-} can capture a proton in polyvinylidene fluoride (PVDF) as an air electrode binder, release F, convert C–C in PVDF into C = C, etc., and affect the service life of the air electrode. CO_2 in the air also reacts with the oxide of lithium deposited on the anode to generate Li_2CO_3. Since the positive electrode undergoes various reactions, the potential shown by the battery is actually a mixed potential. When the battery is charged, O_2 evolution reaction should theoretically occur at one end of the air electrode:

$$LiO_2 = O_2 + Li^+ + e^-$$
$$Li_2O_2 = O_2 + 2Li^+ + 2e^-$$
$$Li_2O = 1/2O_2 + 2Li^+ + 2e^-$$

However, the generated byproduct Li_2CO_3 is difficult to undergo reverse reaction to remain in the positive electrode, thus reducing the charging degree of the battery and further reducing the cycle life of the lithium-air battery. In recent years, when studying the reaction mechanism of lithium-oxygen/carbon dioxide batteries, Lim et al.[43] found that electrolytes with different dielectric constants would affect the formation of Li_2CO_3. The electrolyte with low dielectric constant can inhibit the reaction of generating Li_2CO_3, thus promoting the positive electrode to form Li_2O_2, while the electrolyte with high dielectric constant can activate carbon dioxide and further

promote the generation of Li_2CO_3. However, they discovered unexpectedly in the research process that high dielectric constant electrolyte such as dimethyl sulfoxide (DMSO) can make Li_2CO_3 reversibly react. This important discovery means that this kind of electrolyte can stabilize the cycle performance of the battery and reduce the influence of CO_2 in the air on the battery, because the formation of Li_2CO_3 in the lithium-air battery is inevitable.

(2) Electrolyte for lithium-air battery.

When discharging the positive electrode of the water-soluble electrolyte type lithium-air battery, O_2 is reduced at the three-phase interface of the air electrode, and the reduced product forms LiOH with Li^+, which can prevent the air electrode from blocking so as to reduce the overpotential of O_2. However, it is difficult to completely decompose and precipitate LiOH during charging, resulting in low energy density and poor cycle performance of the battery. In addition, N_2, CO_2, H_2O, etc. contained in the air will produce a series of side reactions on the electrodes, affecting the cycle performance of the battery. The metal lithium cathode of water-based lithium-air battery needs to be covered with a protective layer [44] with Li^+ conductivity to prevent self-discharge caused by reaction of metal lithium with H_2O. However, the limited service life of the protective layer is difficult to prevent the formation of lithium dendrites during long-term charging and discharging of the battery.

In the nonaqueous solvent electrolyte, O_2 is reduced by dissolving in the electrolyte and then diffusing to the air electrode during discharge. Secondary lithium-air batteries mostly use nonaqueous solvent electrolyte. Unlike nonaqueous solvent electrolyte for lithium ion batteries, nonaqueous solvent electrolyte for secondary lithium-air batteries must be resistant to oxidation of active intermediate ions such as O^{2-}, O_2^{2-}, etc. generated by reduction of air electrode O_2. In addition, the ionic conductivity and viscosity of electrolyte, the degree of dissolution of O_2, the compatibility of electrolyte solvent polarity with porous carbon carrier materials, and the partial solubility of discharge products Li_2O_3 and Li_2O have significant effects on the performance of lithium-air batteries [45–48]. The ideal electrolyte for secondary lithium-air batteries, first, should remain relatively stable in the process of battery charging and discharging, and the active intermediate O^{2-} or O_2^{2-} which is not easy to be reduced by oxygen is oxidized to form Li_2CO_3 on the air electrode. Second, the electrolyte should have large ionic conductivity and low viscosity to reduce the internal resistance of the battery. Third, the solubility of the electrolyte to O_2 is larger, and the diffusion rate of O_2 in the electrolyte is faster, thus reducing the concentration polarization of the electrode. Fourthly, the electrolyte solvent has good wettability to porous carbon materials and can reduce the mass transfer resistance in the O_2 reduction process. Fifth, the electrolyte has certain solubility to the discharge products Li_2O and Li_2O can reduce the blockage of air electrode channels, thus improving the air diffusivity and further prolonging the single discharge quantity. In addition, the volatility and water absorption of electrolyte are also problems that cannot be ignored in electrolyte selection. Low volatility and nonwater absorption electrolyte

can prolong the cycle life of battery. In order to meet the above requirements, lithium-air battery electrolyte is generally a multicomponent mixed solution. Adding some fluorine substituted solvents (methyl nonafluorobutyl ether and trifluoroethyl phosphonic acid) can improve the solubility of O_2, while adding tri (pentafluorophenyl) borane (TPFPB) and crown ether can enhance Li_2O and the solubility of Li_2O.

(3) Porous carbon material and oxygen permeable selective membrane for air electrode.

Research shows that the overpotential of the lithium cathode can be basically ignored during the charging and discharging process of the lithium-air battery, and the overpotential of the battery mainly comes from the air cathode. Unlike the air electrode of a fuel cell, the air electrode of a lithium-air battery not only catalytically reduces O_2 but also contains discharge products LiO_2, Li_2O_3, Li_2O and even byproduct Li_2CO_3. The preparation method and physical characteristics of air electrode deeply affect the specific discharge capacity, rate performance and cycle performance of the battery. Therefore, higher requirements are put forward for the specific surface area, porosity, pore size distribution, carbon loading and electrode thickness of carbon materials as catalyst carriers, with higher requirements for pore size distribution. During the battery discharge process, lithium oxide is deposited on the electrode surface, and smaller pores are easily blocked, thus affecting the transmission of electrolyte and air; On the contrary, mesoporous and macroporous materials can accommodate a certain amount of discharge products without affecting the diffusion of O_2. As the amount of discharge products tend to saturate in the pores, the battery stops discharging.

Water in the air permeates into the battery through the air electrode and will react with the negative electrode of lithium metal to corrode the negative electrode of lithium metal. Organic electrolyte in the battery volatilizes and absorbs water through the air electrode, which will affect the discharge capacity, cycle performance and service life of the battery. Therefore, it is necessary to choose a membrane material that can not only prevent or delay water infiltration and volatilization of organic electrolyte but also ensure O_2 diffusion into the battery in the air. Teflon-coated glass fiber membrane (TCFC) can effectively prevent the infiltration of water. The air environment test for 40 days shows that the volatilization rate of electrolyte is only 2%, the negative electrode of metal lithium is bright as new, and its overpotential increases by only 13 ~ 24 mV. In addition, the film prepared by adding polyaniline (PAn) with good conductivity also has good waterproof and air permeability.

6.2.2.2 Aluminum-Air Battery

Aluminum-air battery has always attracted people's attention because of its theoretical energy density second only to lithium-air battery, low price of negative electrode material and its ability to discharge in aqueous electrolyte. In the 1970s, the USA developed aluminum-air batteries for navigation beacon lights and mine lighting. In the 1980s, Canadian Aluminum Power Company developed battery

systems for portable power supplies, backup power supplies and underwater propulsion devices using alloyed aluminum anodes and effective air electrodes. At present, the research hotspots in various countries mainly focus on aluminum-air batteries for high-power electric vehicles or automobiles. In February 2014, at the advanced automotive battery conference held in Atlanta, USA, Alcoa and Israel's Phinergy Company signed a joint development agreement on the further development of Phinergy aluminum-air batteries. The purpose of this joint development is to promote the commercialization process of aluminum-air batteries as soon as possible. Earlier, Israel's Phinergy Company announced that it has developed an aluminum-air battery for electric vehicles. The battery consists of 50 aluminum plates and has an endurance of 1600 km. During this period, only water needs to be injected. The quality of the aluminum-air battery is only 70% of that of a standard battery, and rapid mechanical charging can be realized by replacing an aluminum plate. The battery uses aluminum alloy with high energy utilization rate as the negative electrode, Ag as the air catalyst, the electrolyte used can dissolve aluminum oxide on the surface layer of the aluminum negative electrode, the discharge product of the battery is $Al(OH)_3$, and the $Al(OH)_3$ can be processed and recycled by an aluminum factory to realize sustainable utilization. In July 2019, at the Shanghai International Aluminum Industry Exhibition, Chinalco Group introduced three aluminum-air battery products, namely, aluminum fuel emergency power supply, portable aluminum fuel emergency power supply and hydrothermal integrated aluminum fuel emergency support equipment. Aluminum fuel emergency power supply is mainly used as backup power for 5G communication base stations and other communication systems. Portable aluminum fuel emergency power supply, which mainly provides power for camping and rescue applications; water, electricity and heat integrated aluminum fuel emergency support equipment supplies power, water and heat to scenes such as field training, disaster-stricken resettlement sites or urban shelters.

(1) Working principle of aluminum-air battery [49]

Unlike lithium-air batteries, which use nonaqueous electrolytes, aluminum-air batteries generally use aqueous solutions, mainly neutral and alkaline. In neutral aqueous electrolyte, the discharge reaction of aluminum-air battery is:

$$2A1 + 3/2O_2 + 3H_2O = 2A1(OH)_3(E^v = 2.71V)$$

In alkaline aqueous electrolyte, the discharge reaction of aluminum-air battery is:

$$2A1 + 3/2O_2 + 2OH^- + 3H_2O = 2\,[A1(OH)_4]^-\,(E^v = 2.73\,V)$$

Theoretically, O_2 is reduced on the air electrode to generate OH^-, which is transferred to the negative electrode via electrolyte and combined with Al^{3+} to generate $Al(OH)_3$. When the electrolyte is neutral, part of the generated $Al(OH)_3$ is dispersed in the flowing electrolyte and taken away by circulation, and the other part is attached to the surface of the negative electrode, thus protecting the negative electrode from

hydrogen evolution reaction with the electrolyte. When the electrolyte is strongly alkaline, $Al(OH)_3$ attached to the surface of the aluminum cathode combines with OH^- in the electrolyte to generate soluble $[A1(OH)_4]^-$ so that the metal aluminum is continuously exposed to the electrolyte to ensure continuous and rapid discharge of the aluminum metal. When the negative electrode material of the battery is discharged to the limit, the purpose of fast charging can be achieved by renewing the negative electrode metal plate and electrolyte.

In fact, in the neutral electrolyte, due to the adhesion of $Al(OH)_3$ on the surface of the negative electrode, the discharge speed of metallic aluminum is slowed down, resulting in that the neutral aluminum-air battery cannot discharge at large current. However, in the strong alkaline electrolyte, the exposed metal aluminum will have a side reaction of hydrogen evolution with the alkaline electrolyte.

$$2Al + 6H_2O + 2OH^- = 2[A1(OH)_4]^- + 3H_2.$$

At the same time of high-power discharge, there is the problem of low energy utilization rate (also called battery efficiency) of aluminum cathode due to self-corrosion phenomenon. Therefore, it is necessary to solve the above problems from the aspects of aluminum negative electrode, electrolyte, etc.

(2) **Aluminum cathode of aluminum-air battery**

From the standard electrode potentials $E^e(Al(OH)_3/Al) = -2.31$ V and $E^e([Al(OH)_4]^-/Al) = -2.328$ V of aluminum, it can be seen that aluminum has a strong ability to lose electrons in neutral and alkaline solutions. However, when the aluminum electrode is actually discharged, the electrode potential will move forward. For example, even when it is discharged at a current density of 100 mA/cm^2 in strong alkaline electrolyte, the electrode potential will even move forward to about − 1.2 V, showing a serious polarization phenomenon, which is even more serious in neutral electrolyte [50–53]. The reasons for this are: (1) aluminum oxide passivation film exists on the surface of aluminum, which inhibits the electrochemical activity of aluminum; (2) in strong alkaline electrolyte, the amphoteric nature of aluminum will cause serious hydrogen evolution corrosion of aluminum, resulting in positive electrode potential shift and reduction of battery current efficiency. This corrosion will not stop even in nonworking state. (3) $Al(OH)_3$ colloid generated by corrosion reaction will reduce the conductivity of electrolyte. In order to solve the problems of aluminum surface passivation and hydrogen evolution corrosion, trace alloy elements are usually added to metal aluminum and the heat treatment process of aluminum alloy is improved at the same time [49, 53]. In order to solve the problem that the conductivity of electrolyte drops due to $Al(OH)_3$ colloid, electrolyte is usually filtered or other additives are added for improvement.

Trace alloying elements added to aluminum anodes can be divided into three categories according to their functions in aluminum anodes: (1) metals used to destroy passivation films and reduce oxide film resistance, such as Sn, Ga, In, etc. (2) metals

used to form low-temperature eutectic alloys, such as Ga, In, Sn, Bi, Tl, etc. The low-temperature comelt is liquid on the aluminum surface within the working temperature range of the battery, destroying the combination of the passivation film and the metal substrate, thus improving the electrochemical activity of the aluminum cathode. (3) metals used to activate aluminum, reduce self-corrosion rate and increase hydrogen evolution overpotential, such as Pb, Sn, Hg, Zn, etc.

Adding Sn element can play the above three roles. Sn can cause pores in the passivation film on the aluminum surface to accelerate ion transport, and holes formed after Al^{+3} element in the passivation film is replaced by trace Sn^{+4} can reduce the resistance of the passivation film. Sn has high hydrogen evolution overpotential, which can effectively inhibit hydrogen evolution corrosion of Sn-containing aluminum alloy. Sn can also form a low cosoluble mixture with Ga, In and the like, which damages the combination of the aluminum surface passivation film and the aluminum alloy substrate and produces the effect of activating the negative electrode. The addition of Ga element can also improve the electrochemical performance of aluminum alloy cathode. Ga, Bi, Pb and other elements form a low-temperature cosoluble mixture within the working temperature range of the electrode (60–100 °C) to prevent the formation of a passivation film on the aluminum surface; The existence of Ga can also change the anisotropy of pure grains in the dissolution process, thus making the corrosion of aluminum cathode uniform. In and Ga are more active metals than aluminum. Adding aluminum can greatly negative shift the potential of the alloy anode and reduce the polarization of the cathode. Zn, Sn, Pb, Hg, Bi and other elements in the alloy have high hydrogen evolution overpotential, which can inhibit hydrogen evolution corrosion of aluminum alloy cathode and improve its current efficiency and utilization rate of aluminum alloy electrode.

Heat treatment is mainly achieved by affecting the distribution of trace elements and the microstructure of aluminum alloy. The distribution of a small amount of added elements and impurity elements contained in aluminum is affected by heat treatment, especially for elements with small solid solubility in aluminum, the effect of heat treatment is more significant, such as Pb, Bi and other elements have very small solid solubility in aluminum, Pb and Bi will diffuse to the surface during heat treatment, thus activating and enhancing aluminum alloy. However, the solid solubility of In, Sn, Ga and other elements is slightly higher, and the effect of heat treatment is very small. For aluminum alloy with high Fe content, heat treatment can affect the distribution of Fe, thus affecting the overall properties of aluminum alloy. Among the four heat treatment methods (normalizing, annealing, quenching and tempering), normalizing treatment has the most negative potential and small polarization. After annealing, the potential slightly moves forward and the polarization is also very small. Quenching treatment increases polarization and uneven dissolution of surface anode. Normalized and annealed anodes have the highest efficiency (94–98%), because they avoid grain boundary corrosion and the surface corrosion is uniform, while quenched and tempered anodes have an efficiency of only about 69%, because quenched and tempered anodes contain microscopic defects and produce local dissolution corrosion.

(3) **Electrolyte for Aluminum-Air Battery**

As mentioned earlier, the electrolyte of aluminum-air battery mainly includes alkaline electrolyte and neutral electrolyte. The alkaline electrolyte is mainly NaOH or KOH aqueous solution, and the neutral salt electrolyte is mainly NaCl or NH_4Cl aqueous solution. In order to solve the defects of hydrogen evolution corrosion of aluminum negative electrode in alkaline electrolyte and slow discharge speed of aluminum negative electrode in neutral electrolyte, additives that inhibit hydrogen evolution corrosion of aluminum and can activate aluminum negative electrode are generally added to electrolyte [53–55]. The main additives are: (1) Inorganic ions, such as Cl^-, F^-, SO_4^{2-}, SnO_3^{2-}, Bi^{3+}, In^{3+} and Ga^{3+}, etc. Cl^- and F^- can activate the negative electrode of aluminum. Bi^{3+}, In^{3+} and Ga^{3+} plasma will be deposited on the surface of aluminum cathode, which will destroy the anode passivation film. SnO_3^{2-} can not only play the role of anode activation, but also be reduced to Sn, forming a porous precipitate on the aluminum surface to inhibit hydrogen evolution corrosion of the cathode, and $Sn(OH)_2$ generated by SnO_3^{2-} hydrolysis can be used as crystal nucleus of precipitated colloidal $Al(OH)_3$ to improve the conductivity of electrolyte; (2) Organic additives such as ethylenediaminetetraacetic acid can form coordination ions with aluminum ions to inhibit the formation of colloidal $Al(OH)_3$; Citrate can inhibit the hydrogen evolution corrosion of aluminum and the generation of $Al(OH)_3$, while ethanol can reduce the corrosion of aluminum cathode surface. (3) Composite additives, compared with pure inorganic ions or organic additives, the improvement mechanism of composite additives on electrolyte performance is relatively complex, and various influencing factors interact with each other, so further research is needed. Some scholars compound K_2MnO_4 with citrate and stannate as electrode additives, which improves the utilization rate of aluminum cathode from 28.5 to 81.0%, and reduces the corrosion current density from 123.8 mA/cm^2 to 17. 87 mA/cm^2.

The $Al(OH)_3$ accumulated in the electrolyte will be supersaturated, making the electrolyte pasty or even semisolid, resulting in a decrease in the conductivity of the electrolyte. Common solutions include replacing electrolyte regularly, circulating electrolyte or adding seed crystal to the electrolyte to precipitate $Al(OH)_3$. For example, one of the purposes of adding SnO_3^{2-} to the electrolyte is to serve as seed crystal. The corresponding battery design also includes precipitation and filtration devices, etc.

Some scholars believe that acidic H_2SO_4 electrolyte is better than NaCl (Cl^- ion is easy to induce pitting corrosion of aluminum alloy). Strengthening the research of electrolyte is expected to make the aluminum air battery have a wider application prospect. Other scholars try to replace aqueous solution with organic polymer solid electrolyte [56]. Research shows that solid polymer electrolyte (SPEM) is prepared by mixing (poly vinyl alcohol: PVA) and (polyacrylic acid: PAA) at a ratio of 10: 7.5 and compounding alkaline solution. When the solid electrolyte is used in aluminum-air battery, the utilization rate of aluminum cathode of aluminum-air battery can reach 90%.

Since the aluminum-air battery is mainly a mechanical rechargeable battery using aqueous electrolyte, the air electrode requirement is lower than that of the secondary

lithium-air battery, and the conventional air electrode can be satisfied, except that different catalysts can be used according to different battery uses. This type of air electrode has been discussed many times before and will not be described here.

6.2.2.3 Zinc-air Battery

Zinc-air battery has become another important metal-air battery besides lithium-air battery and aluminum-air battery due to its advantages of cheap and easily available cathode material, capability of charging and discharging cycle in aqueous solution system, stable working voltage, low pollution, safety and reliability, etc. Although the theoretical energy density of zinc-air battery is lower than that of lithium, aluminum and magnesium-air battery, it is still three times that of lithium ion battery. Unlike lithium-air and aluminum-air batteries, zinc-air batteries can be charged and discharged in aqueous electrolyte, that is, zinc-air batteries can be charged in aqueous electrolyte. This is because in neutral or alkaline electrolyte, the hydrogen evolution overpotential on the zinc surface is very large, Zn^{2+} near the negative electrode preferentially obtains electrons to form metal Zn than H^+ during charging, which makes it possible for the aqueous zinc-air battery to be used as a secondary battery, and it is precisely this characteristic that the discharge product ZnO of the zinc-air battery can also be regenerated by electrolysis. As secondary zinc-air uses aqueous electrolyte, the risk of fire or explosion caused by leakage of organic electrolyte can be reduced, making it safer than secondary lithium-air battery.

Since 1995, Israel Electric Fuel Co., Ltd. used zinc-gas battery for electric vehicles for the first time, bringing zinc-gas battery into practical stage. Since then, the USA, Germany, France, Sweden and other countries have also actively promoted the application of electric vehicles. The zinc-air batteries developed mainly include secondary batteries and mechanical rechargeable batteries. EOS Energy Storage Company claimed that the secondary zinc-air battery developed in the USA can realize 2700 cycles of charge and discharge [59]. The key points of its technology are as follows: (1) A new neutral electrolyte is used to overcome the problem of pore blockage caused by carbonate deposition on the air electrode due to absorption of CO_2 by alkaline electrolyte; (2) The horizontal cell structure design is adopted, and the electrolyte is separated from the electrode by gravity, thus overcoming the difficult problem that the zinc electrode is oxidized to form dendrites and the diaphragm is broken, thereby causing the cell to fail. The zinc-air battery for vehicles developed by Sweden and Israel is a mechanical rechargeable battery. This mechanical zinc refilling-air adopts the design of metal particle replacement and electrolyte circulation: automatically adding metal particles-discharging-pumping electrolyte, renewing electrolyte and discharging waste materials. The recovered zinc oxide can be regenerated into zinc particles by electrolysis for recycling. Figure 6.9 shows the structure of a metal particle replacement type single cell. The negative electrode is the matrix of zinc particles and is connected with the current collector. When the zinc particles are dissolved, the volume of the zinc particles in the battery shell is

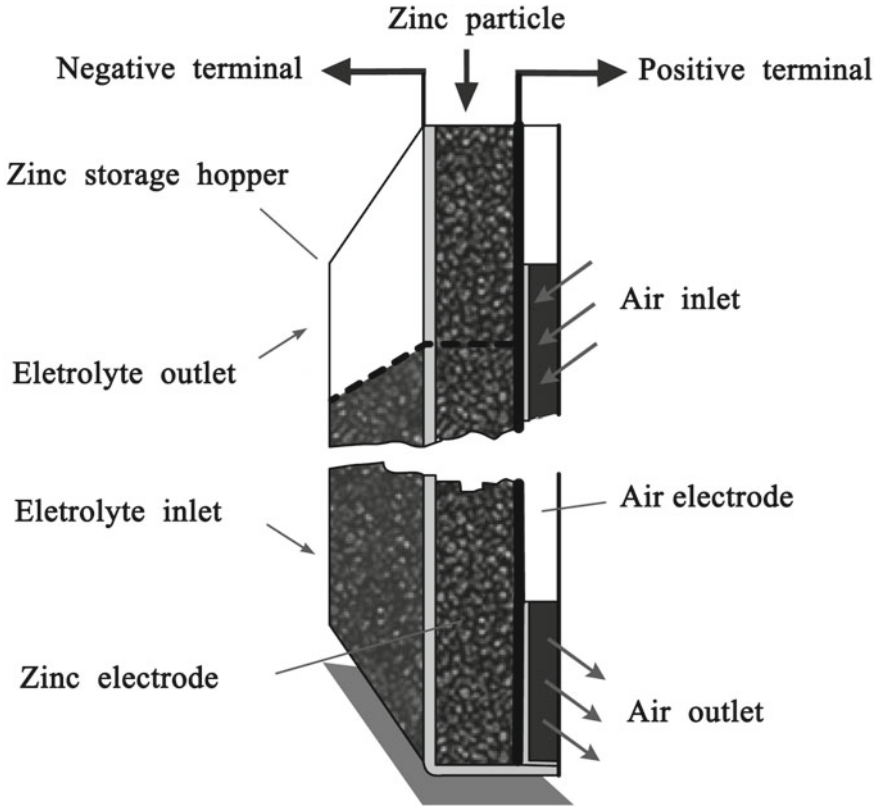

Fig. 6.9 Metal particle replacement single cell

continuously reduced, and unreacted zinc particles continuously enter the electrochemical reaction area of the battery from the zinc particle storage hopper on the upper part of the zinc electrode (each single cell has its own zinc particle storage hopper). During the discharge process, the zinc electrode is continuously washed and washed by flowing electrolyte, and the discharged zinc oxide is taken away by the electrolyte, thus ensuring the continuous and stable discharge of the battery.

(1) The working principle of zinc-air battery.

Similar to the aqueous electrolyte used in aluminum-air batteries, the electrolyte used in zinc-air batteries is also divided into neutral and alkaline. In neutral aqueous electrolyte, the discharge reaction of zinc-air battery is:

$$2Zn + O_2 + 2H_2O = 2Zn(OH)_2 \quad (E^\theta = 1.65\,V)$$

In alkaline aqueous electrolyte, the discharge reaction of zinc-air battery is:

$$2Zn + O_2 + 4OH^- + 2H_2O = 2[Zn(OH)_4]^{2-} \quad (E^\theta = 1.60\ V)$$

Theoretically, O_2 is reduced on the air electrode to generate OH^-. In neutral electrolyte, OH^- is transferred to the negative electrode and combines with Zn^{2+} to generate Zn $(OH)_2$; In alkaline electrolyte, OH^- combines with Zn^{2+} generated by negative electrode to generate $[Zn(OH)_4]^{2-}$. In fact, zinc-air battery has similar problems with aluminum-air battery: first, the working voltage and current density of neutral zinc-air battery are lower than those of strong alkaline battery; hydrogen evolution corrosion of strong alkaline batteries is serious. Second, the zinc electrode is easy to form "dendrites" after being corroded to damage the separator and make the battery ineffective. Third, when the battery is discharged for a long time, the contact of reaction products or alkaline electrolyte with external CO_2 will generate a large amount of carbonate to precipitate on the surface of the air electrode and block the air electrode gas channel, resulting in the performance and energy attenuation of the battery. The carbonation of electrolyte will also enhance the acidity of electrolyte and aggravate the hydrogen evolution corrosion of zinc electrode. Fourth, too high or too low humidity in the external environment will cause "flooding" or "drying up" of the semiopen air electrodes, and even "alkali climbing" or "liquid leakage" problems. Unlike aluminum-air batteries, which improve aluminum alloy composition and heat treatment process to solve hydrogen evolution, zinc-air batteries mainly achieve their goals by adding oxides in the negative reaction zone and improving electrolyte properties.

(2) Zinc cathode and electrolyte of zinc-air battery.

Metal oxides or hydroxides with high hydrogen overpotential are added to the reaction zone of the zinc electrode. The equilibrium potential of these metals in alkaline solution is generally higher than that of zinc, which is preferentially deposited when the electrode is charged and generally insoluble when the electrode is discharged. Due to the high hydrogen evolution overpotential of these added metals, hydrogen evolution corrosion reaction of Zn reducing H^+ in H_2O to generate H_2 can be inhibited while discharging metal zinc, and corrosion of zinc in electrolyte can be effectively slowed down. Some scholars have also increased hydrogen evolution overpotential by adding high concentration of zinc ions to alkaline electrolyte to inhibit H_2 evolution corrosion.

In order to overcome the problem of carbonation of electrolyte due to long-term use and absorption of CO_2, neutral and slightly acidic electrolyte is generally adopted. Although the working voltage and discharge current density of neutral or slightly acidic zinc-air batteries are not as high as those of alkaline zinc-air batteries, they can meet the discharge requirements of medium and small current densities and can replace alkaline zinc-air batteries in low-power discharge sites. Adding a complexing agent to the electrolyte to remove the dense zinc oxide layer will greatly improve

the cycle life of the secondary zinc-air battery. EOS Energy Storage Company in the USA has made progress in this regard.

To solve the problem of dendrite formation in zinc electrodes, quaternary ammonium salt is generally added to the electrolyte to adsorb organic macromolecular cations on the active center of zinc surface, thus inhibiting zinc deposition at these locations and generating dendrites. It is found that sulfate, polyvinyl alcohol, etc. also have the same effect as quaternary ammonium salt. In addition, the generation of zinc dendrites can be inhibited by changing the charging mode, or the diaphragm performance can be improved to reduce the influence of dendrites.

6.2.2.4 Other Metal-Air Batteries

(1) **Magnesium-air battery** [60]

The theoretical energy density of magnesium-air battery is second only to light metal lithium and aluminum. Magnesium-air batteries hold five times the energy of lithium batteries of the same size and can be mechanically charged with fast charging speed. Magnesium is an ideal electrode material for magnesium-air batteries because of its abundant reserves, low price and no pollution. The Korean Institute of Science and Technology has successfully completed the road test of a magnesium-air battery-powered vehicle, enabling the electric vehicle to travel 800 km under the drive of a complete battery.

Electrolytes used in magnesium-air batteries include aqueous solution and organic solution. Different electrolytes have different reaction mechanisms. In the aqueous solution system, the battery reaction is:

$$Mg + 1/2\ O_2 + H_2O\ =\ Mg(OH)_2$$

In the organic system, the battery reaction is:

$$Mg + 1/2\ O_2 =\ MgO$$

In practical applications, the response rate of the air cathode is slow due to the low reaction efficiency of the magnesium cathode. Although the energy density that the magnesium-air battery can store is large, the battery's ability to convert energy into actual power is very limited. Both types of batteries have technical bottlenecks that need to be overcome.

In organic magnesium-air batteries, the reactivity of metallic magnesium is very low, and the discharge current can only reach 0.1 mA cm^{-2}. Especially when the surface of magnesium electrode is oxidized to form a dense Mg $(OH)_2$ passivation film (the film cannot conduct Mg^{2+}), the electrode can hardly discharge normally. In the organic electrolyte, the discharge of O_2 in the air electrode can only depend on the solubility and diffusion rate of O_2 in the organic solution. MgO, the product of the discharge reaction, is insoluble in the organic solution and is easy to deposit on the

electrode, thus blocking the O_2 mass transfer channel of the air electrode. Moreover, the currently developed organic electrolyte (format reagent) suitable for magnesium electrode is a volatile substance, so volatilization on one side of the air electrode will be unavoidable. All these affect the performance of organic magnesium-air battery.

In the water-based magnesium-air battery, the main problems currently faced are the self-corrosion of Mg in aqueous solution, H_2 evolution, and the activation and passivation of magnesium alloy. Because it affects the stability, reactivity and energy utilization efficiency of magnesium anode in aqueous solution, and determines the performance of the battery. In order to solve these problems, Korean scientists have used a variety of substances to change the chemical composition of the magnesium anode, while improving the air cathode to improve the reaction efficiency and speed. Finally, the discharge specific energy of the team's magnesium-air battery was doubled compared with that of the traditional battery. Moreover, the battery only needed 10 min to charge and only needed mechanical replacement of the magnesium plate and brine electrolyte. However, there are still many difficulties to overcome before the commercialization of magnesium-air battery. At present, the fuel cost of magnesium-air battery cars is three times that of gasoline-powered cars. Once battery technology and $Mg(OH)_2$ recovery technology are developed, the later cost is expected to be greatly reduced, so commercialization of magnesium-air electric vehicles can still be expected.

(2) **Iron-air battery** [62]

The School of Arts and Sciences of the University of Southern California has developed an iron-air battery, which is low in cost, environmentally friendly and rechargeable, and can be used for energy storage of solar energy and wind power plants in rainy days. This iron-air battery uses iron as the negative electrode, air electrode as the positive electrode, and aqueous solution as the electrolyte. The discharging process of the battery is similar to iron rusting, and the battery developed at present has the capability of storing 8–24 h of energy. Iron-air battery faces a great problem in the research and development process: hydrogen evolution corrosion reaction of iron in the battery, which will lose about 50% of battery energy and greatly reduce battery efficiency. The research team managed to reduce the energy loss to 4% by adding a very small amount of bismuth sulfide to the battery. Bismuth can restrain the waste of energy in the process of hydrogen production. Very little bismuth sulfide will not affect the environmental protection characteristics of the battery, but it can improve the efficiency of the iron-air battery by about 10 times compared with the previous similar batteries.

(3) **Sodium-air battery** [62, 63]

The Karlsruhr Research Center of Giesen University in Germany and researchers from BASF Company cooperated to replace the most commonly used metallic lithium as electrode material with metallic sodium. A secondary sodium-air battery was designed and developed. The theoretical specific energy of the sodium-air battery can reach 1600 W/kg and the discharge voltage is 2.2 V. During the battery discharge

process, the metal sodium loses electrons to form Na^+, which is transmitted to the positive carbon material through the electrolyte and combines with the reduced oxygen element to generate stable Na_2O_2; during charging, Na^+ in the electrolyte near the negative electrode is reduced to metal Na, and Na_2O_2 on the positive electrode is reduced to Na^+ and O_2 and released into the air. The efficiency of the charging and discharging process can reach 80 ~ 90%. Compared with lithium materials, the electrochemical process of Na_2O_2 formed by the combination of sodium and oxygen is more stable. Therefore, this new sodium-air battery has the advantages of high stability and small voltage loss. The research results show that sodium materials also have the prospect of being used as electrode materials for future new battery systems.

6.3 Secondary Lithium-Air Battery Application

This section first introduces the working principle of secondary lithium-air batteries, then clarifies the process of oxygen reduction electrocatalysis during battery discharge, focuses on several commonly used oxygen reduction electrocatalysts, and discusses the electrocatalysts for this type of battery as well as the direction of development.

6.3.1 Secondary Lithium-air Batter

The secondary lithium-air battery is a new type of energy storage and conversion device. It converts the chemical energy in metallic lithium and oxygen into electrical energy when discharging, and stores electrical energy by decomposing the discharge products when charging. Lithium-air batteries differ from conventional batteries in that their cathode reactive material oxygen (air) is not stored in the battery, but is provided by the outside environment during discharge, so when it is working, the oxygen needs to be continuously inserted into the battery [64, 65].

The electrochemical reactions during charge and discharge are as follows:

The anode process is:

$$Li \leftrightarrow Li^+ + e^-$$

The cathode process is:

$$2Li^+ + 2e^- + O_2 \leftrightarrow Li_2O_2 \qquad (E_0 = 2.96\ V\ vs.\ Li/Li^+)$$

It can be seen that when the battery discharges, the cathode undergoes an oxygen reduction reaction to generate superoxide ions (O_2^{2-}), which are combined with lithium ions (Li^+) moving from the anode and electrons (e^-) transported from the

external circuit to generate a discharge product (Li_2O_2). The charge is the electrochemical decomposition process of the discharge products. An electrocatalyst is required during the electrode reactions, such as an oxygen reduction electrocatalyst during discharge and an oxygen evolution electrocatalyst during charging.

Lithium-air batteries have many advantages:

(1) Extremely high specific energy. As mentioned above, the battery does not store the cathode active material, so it has a very high specific energy, about 11,000 Wh kg^{-1};
(2) Environmentally friendly. Because the battery generates electricity in accordance with the electrochemical principle and does not go through the combustion process as the heat engine, it emits almost no nitrogen oxides and sulfur oxides, reducing the pollution to the atmosphere;
(3) Quiet operation. The battery works relatively quietly and with low noise.

However, there are still many problems in the field of lithium-air batteries that restrict its development.

(1) Lithium metal anode protection. When the battery is working in the air, the organic electrolyte easily absorbs moisture in the air and causes corrosion of the lithium metal negative electrode, resulting in a hidden safety hazard.
(2) Electrolyte stability. Intermediate products generated during the battery discharge process easily react with the organic electrolyte, which results in the formation of by-products, which in turn affects the battery's charging characteristics. Furthermore, with the progress of the electrode reaction, the electrolyte will be gradually consumed, which will affect the cycle stability of the battery. Finally, because the battery works in an open environment, the electrolyte is volatile, which also affects battery performance and even safety.
(3) Optimization of cathode materials. The discharge product of the battery is insoluble in the organic electrolyte and will be deposited in the porous positive electrode. When all the pores are blocked, the discharge of the battery is terminated. Therefore, the optimization of the structure of the cathode material is also a key issue.
(4) The electrode reaction kinetics is slow. More importantly, if no electrocatalyst is used, the charge and discharge reaction of the battery is slow, and the polarization phenomenon is very serious, which affects the cycle life of the battery. Because the cathode reaction determines the charge–discharge performance and cycle life of lithium-air batteries, the research on electrocatalysts can accelerate the practical application of such batteries.

6.3.2 *Electrocatalytic Process for Oxygen Reduction of Secondary Lithium-Air Batteries*

The oxygen reduction electrocatalysis process of secondary lithium-air batteries is more complicated, not only related to the electrocatalyst used but also to the electrolyte, especially the cations in the electrolyte have a great influence on the oxygen reduction process. In electrolytes containing tetraethylammonium (TEA^+) or tetrabutylammonium (TBA^+), oxygen (O_2) can be quickly reduced to superoxide ions (O_2^-), and the redox process shows good performance. During this oxygen reduction process, the equilibrium potentials of the redox pairs O_2/O_2^- are about 2.0 V on the surfaces of the precious metals, platinum, ruthenium, gold, and glassy carbon electrodes, showing insensitivity to the electrocatalyst (Fig. 6.10).

This nonselective performance of the electrocatalyst is explained from the following aspects: (1) Unlike the traditional slow oxygen reduction process, it is not necessary to break the oxygen–oxygen bond in the lithium-air battery reaction; (2) O_2^- is a free radical that is poorly adsorbed and easily soluble in the electrolyte, so the interface of the electrocatalyst may only play a role in transferring charge.

In contrast, if the electrolyte contains small metal cations such as Li^+, Na^+ or K^+, the oxygen reduction process becomes very different. First, the redox equilibrium potential is positively shifted from about 2.0 V to about 3.0 V. Second, the reversibility of the redox reaction becomes worse, as shown in Fig. 6.11.

The theory of soft and hard acid and base can well explain the mechanism of the cation's effect on the oxygen reduction process. According to the theory, TEA^+ is a soft acid that can effectively stabilize the soft base O_2^- and prevent its further reaction. However, for alkali metals, they are hard acids, which do not have a stable effect. Therefore, the reaction will continue to occur, resulting in producing O_2^{2-}. This is also the reason why intermediate products LiO_2 cannot be detected in the actual battery discharge products. However, the on-site surface-enhanced Raman technology can

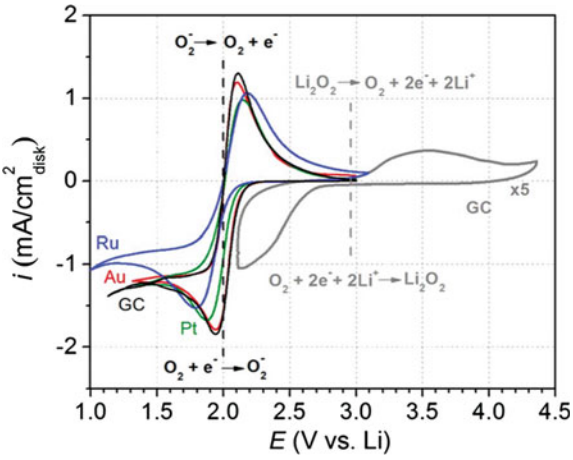

Fig. 6.10 Cyclic voltammetry curves for the oxygen reduction/oxygenation reactions on the surface of various electrodes. The electrolyte is 0.5 M $TBAClO_4$/Dimethoxyethane (DME) [66]

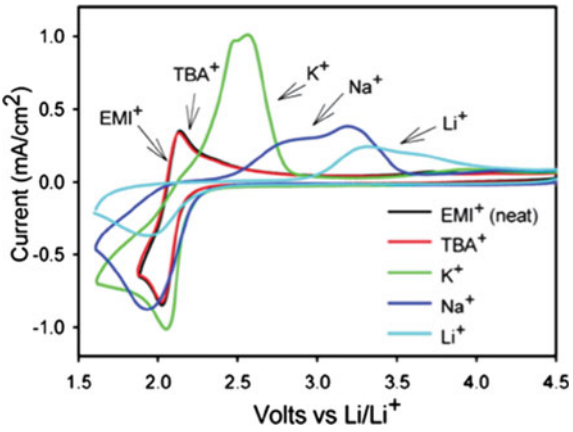

Fig. 6.11 Cyclic voltammetry curves of 1-methyl-3-ethylimidazolium bis (trifluoromethyl) (EMITFSI) solutions containing different salts, with a concentration of 0.025 M and a sweep speed of 100 mV s^{-1} [67]

clearly detect the oxygen-reduced intermediates in the organic electrolyte containing Li^+, and then form the bond with the surface of the metal catalyst (Fig. 6.12).

It can be seen that the oxygen reduction reaction process of secondary lithium-air batteries is very complicated: (1) the electrochemical process of the battery contains more than one elementary reaction; (2) the electrolyte, electrode materials, and oxygen partial pressure all affect the reaction process (3) the discharge product is a solid substance that is insoluble in the electrolyte, increasing the complexity of

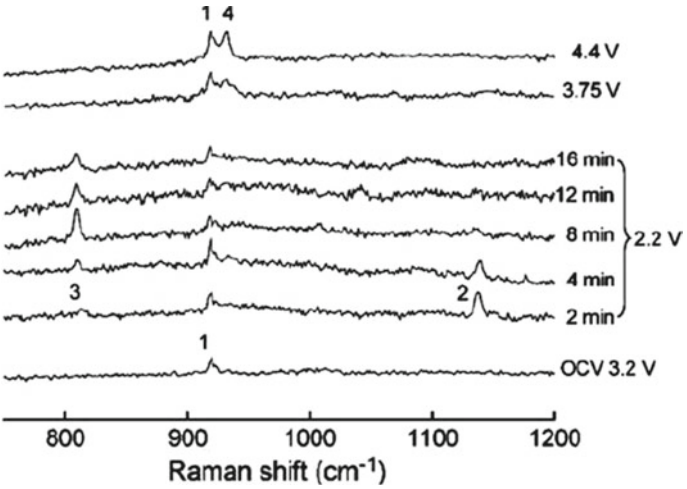

Fig. 6.12 In situ surface-enhanced Raman spectrum of the oxygen reduction/oxygen evolution reaction on the surface of the gold electrode [68]

its research. There are also some controversies on the role of electrocatalysts in the reaction. For example, the oxygen reduction reaction does not depend on electrocatalysts. However, there are reports that the size, morphology, and composition of discharge products can be changed by using electrocatalysts.

6.4 Introduction to Oxygen Reduction Electrocatalyst for Secondary Lithium-Air Battery

In general, the use of electrocatalysts can improve the energy density, capacity, and cycle performance of batteries. It has also been reported that the performance of secondary lithium-air batteries is mainly determined by the cathode material. Although the catalytic mechanism of the electrocatalyst to the electrode reaction is not clear, there have been many studies on it. Generally speaking, secondary lithium-air battery electrocatalysts are divided into four categories, as shown in Table 6.4.

Several commonly used electrocatalysts have their own advantages and disadvantages, and their research needs to be deepened, but in general, the requirements for the electrocatalyst should be that it can discharge the battery (oxygen reduction reaction) and charging process (oxygen evolution reaction) must have catalytic activity, that is, it can show "dual function" characteristics.

Table 6.4 Classification of electrocatalysts for lithium-air secondary batteries

Electrocatalysts	Pros	Cons
Carbon materials	Show a certain catalytic activity for the discharge process (oxygen reduction reaction)	Poor catalytic activity for the charging process (oxygen precipitation reaction)
Metal oxides	Inexpensive and stable in nature, and show excellent catalytic performance in electrode reactions	Electrical conductivity is generally low, and it is difficult to make particles with extremely high surface area, which greatly reduces the utilization of active surface area
Precious metals	Has extremely high reversibility to the electrode reaction, which greatly improves the energy efficiency and cycle performance of the battery	Limited resources and high prices limit its large-scale application
Nonprecious metals	Improve the performance of the battery to a certain extent	The preparation process is complex, the yield is low, and the stability needs to be improved

6.4.1 Carbon Material Electrocatalyst

Strictly speaking, a carbon material electrocatalyst is not an electrocatalyst in the traditional sense, but is used as an electrode material, a support of an electrocatalyst or a conductive additive of a battery. Because the carbon material can provide a very suitable porosity, the discharge products of the battery can be deposited in pores of various sizes, thereby affecting the discharge performance of the battery. The pores in the mesopore size range have the greatest impact on battery performance, because in this interval, oxygen and electrolyte can fully enter, thereby forming an effective reaction zone, and the insoluble electrolyte products formed by discharge can also be deposited into the mesopores, of which the filling rate is higher than that of the large pores, and more products can be accommodated than the small pores. In addition to the pore properties, the characteristics of the carbon material itself also affect the performance of the battery. For example, carbon powder doped with nitrogen is more catalytically active than undoped, thereby improving discharge performance.

One-dimensional nanocarbon materials, such as carbon nanotubes and carbon nanofibers, are also used for lithium-air battery electrodes. For example, carbon nanotubes also exhibit higher performance after doping, as shown in Fig. 6.13. Sun et al. found that the initial discharge capacity of nitrogen-doped carbon nanotubes is 866 mAh g^{-1}, which is about 1.5 times that of undoped samples. More importantly, the voltage platform for doped discharge also increased by about 0.1 V, indicating that the electrocatalytic activity of the oxygen reduction reaction is higher. This gives stronger evidence for increasing the activity of carbon materials by doping.

In the field of lithium-air batteries, graphene also shows very good performance. Sun et al. synthesized graphene nanosheet material and used it as an electrode material. It was found that the discharge capacity of the battery was several times higher than that of commercial carbon materials. This is because graphene has good pore properties, which improves the effective area of the battery and it can also improve the mass transfer effect and promote the deposition of discharge products, so the discharge capacity of the battery has been greatly improved. More importantly, after

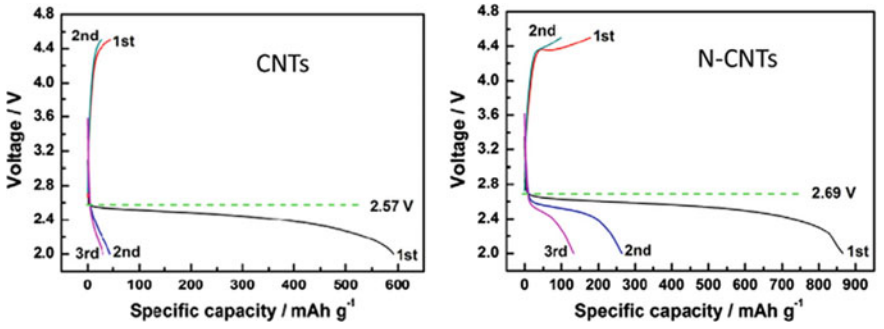

Fig. 6.13 Charge and discharge curves of carbon nanotube (left) and doped carbon nanotube (right) electrodes [69]

observing the electrode material after discharge, it was found that more products were deposited on the edges of graphene, because the carbon atoms on the edges have higher oxygen reduction activity due to the presence of unsaturated bonds. They also studied the performance of doped graphene, and found that after doping nitrogen, the number of defect sites and surface functional groups in graphene increased, which showed a certain electrocatalytic activity for the electrode reaction, further improving the performance of the battery (Fig. 6.14).

Xiao et al. used a surfactant to functionalize graphene, and then built it into a three-dimensional electrode with different pores. It was found that the mass transfer in the electrode was accelerated, and the electrochemically active area was also greatly increased, as shown in Fig. 6.15.

6.4.2 Metal Oxide Electrocatalyst

Manganese oxide is the most studied electrocatalyst material in the field of lithium-air batteries. Bruce et al. systematically compared manganese oxides with different morphologies, sizes, compositions, and crystal forms, and found that nanowires showed the best performance (Fig. 6.16).

In addition, a variety of other metal oxides such as Fe_2O_3, Fe_3O_4, NiO, CuO and Co_3O_4 are also used as electrocatalyst materials for lithium-air batteries. Because they have different catalytic activities, the batteries exhibit different charge and discharge properties. Among them, the Fe_2O_3 material shows the highest discharge capacity, and the Fe_3O_4 and CuO materials show a relatively high capacity retention rate, and the Co_3O_4 material has good performance on discharge capacity and cycle life. Wen et al. used an ammonia-induced evaporation growth method to synthesize directionally grown Co_3O_4 nanorods on the surface of nickel foam and directly used them as electrodes for lithium-air batteries (Fig. 6.17), which can be used both as an electrode for discharge products to be deposited and an electrocatalyst which promoted the electrode reaction.

6.4.3 Precious Metal Electrocatalyst

Shao-Horn et al. reported for the first time the use of PtAu/C electrocatalysts to show good "dual-function" catalytic activity in lithium-air batteries, that is, the electrocatalyst is active for both oxygen reduction and oxygen evolution, thereby enabling battery energy efficiency is greatly improved. As shown in Fig. 6.18, the use of alloy electrocatalysts reduces the polarization voltage, especially the charging voltage is reduced by about 900 mV compared to activated carbon.

Further research by the Shao-Horn group showed that among a variety of precious metal electrocatalysts, palladium showed the highest activity for oxygen reduction catalysis, and correspondingly it had the lowest overpotential during the discharge

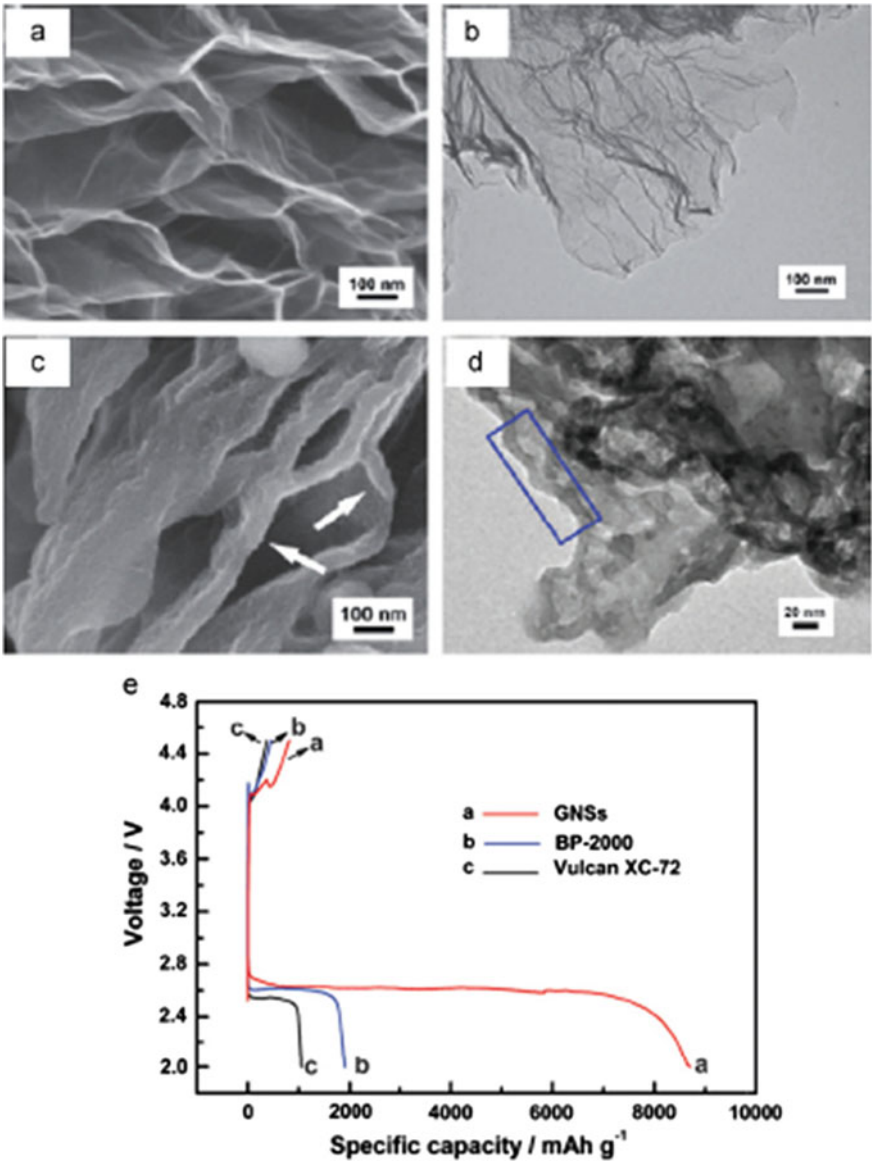

Fig. 6.14 Scanning electron micrograph (**a**) and projection electron micrograph (**b**) of the graphene electrode before (**c**) and after discharge (**d**), and their charge and discharge curves (**e**) [70]

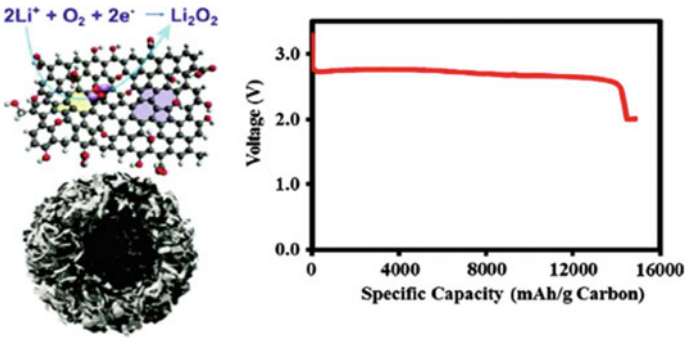

Fig. 6.15 Schematic diagram and discharge curve of a functionalized graphene three-dimensional electrode [71]

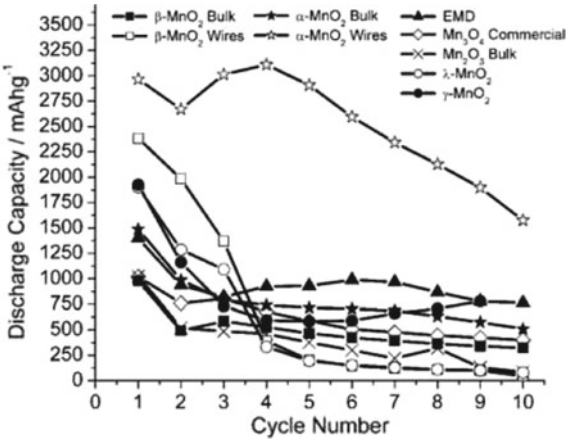

Fig. 6.16 Cycle performance of manganese oxide electrodes with different morphologies, sizes, compositions and crystal forms [72]

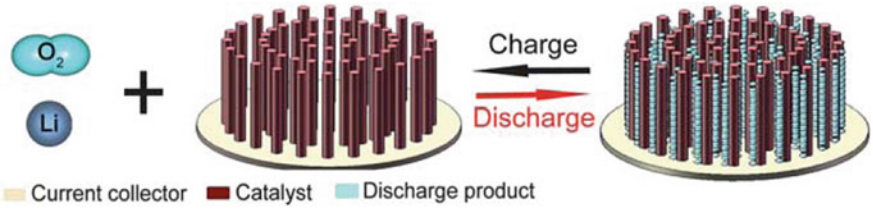

Fig. 6.17 Schematic diagram of self-supporting Co_3O_4 electrode charging and discharging [73]

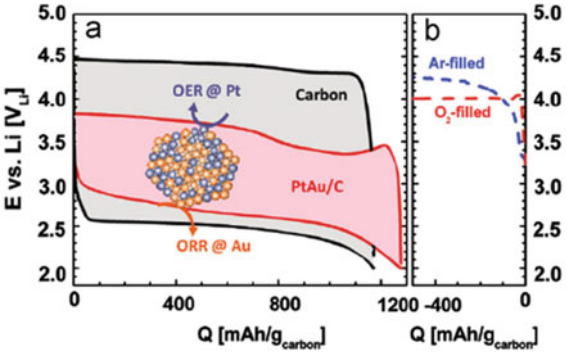

Fig. 6.18 Charge and discharge curves of carbon electrode and PtAu/C electrode [74]

of lithium-air batteries. Because the production of precious metals is scarce and expensive, it has limited their large-scale applications. New technologies that reduce the amount of use and improve performance should be sought. And more importantly, the catalytic properties of the noble metal in the oxygen reduction reaction of the organic electrolyte system are different from those of other electrolytes, and its catalytic mechanism is also worth studying.

6.4.4 Nonprecious Metal Electrocatalyst

Zhang et al. found that the use of carbon-supported iron–copper phthalocyanine complex electrocatalysts showed good discharge performance [75]. The discharge process is terminated when all active sites are covered by the discharge products. Some other research groups have also proposed similar hypotheses. After adding additives to the electrolyte, the solubility of the discharge products in the electrolyte can be increased, thereby extending the discharge time of the battery, but more evidence is needed to supporting this hypothesis, the application of field testing techniques may provide some ideas for the solution of this problem [76, 77].

6.4.5 Prospect of Oxygen Reduction Electrocatalyst for Secondary Lithium-Air Battery

The discharge capacity, cycle life, and energy efficiency of secondary lithium-air batteries are related to the use of electrocatalysts. Therefore, the nature of electrocatalysts should be strengthened to clarify the catalytic mechanism and the relationship between the performance of the battery and the performance of the battery. In addition, the choice of the actual electrocatalyst is also an important issue. For example, the charge and discharge currents of batteries today are in a very small range, from 0.1 to 1.0 mA cm^{-2}, which is far from meeting the needs of real products, by screening the

appropriate electrocatalyst to improve the rate performance of the battery. Furthermore, research on the stability of electrocatalysts should be strengthened. Finally, there are many places in the research of secondary lithium-air battery electrocatalysts that can be borrowed from the field of fuel cells, and this should be the starting point for faster development [78–81].

References

1. Zhong H, Zhang H, Liu G, Liang Y, Hu J, Yi B (2006) A novel non-noble electrocatalyst for PEM fuel cell based on molybdenum nitride. Electrochem Commun. 8:707–712
2. Ohgi Y, Ishihara A, Matsuzawa K, Mitsushima S, Ota K-i, Matsumoto M, et al. (2012) Oxygen reduction reaction on tantalum oxide-based catalysts prepared from TaC and TaN. Electrochim Acta 68:192–7
3. Zhou YX, Yao HB, Wang Y, Liu HL, Gao MR, Shen PK et al (2010) Hierarchical hollow Co9S8 microspheres: solvothermal synthesis, magnetic, electrochemical, and electrocatalytic properties. Chem-A Eur J 16:12000–12007
4. Feng Y, He T, Alonso-Vante N (2007) In situ free-surfactant synthesis and ORR-electrochemistry of carbon-supported Co3S4 and CoSe2 nanoparticles. Chem Mater 20:26–28
5. Wang H, Liang Y, Li Y, Dai H (2011) Co1− xS–Graphene hybrid: a high-performance metal chalcogenide electrocatalyst for oxygen reduction. Angew Chem Int Ed 50:10969–10972
6. Waki K, Wong RA, Oktaviano HS, Fujio T, Nagai T, Kimoto K et al (2014) Non-nitrogen doped and non-metal oxygen reduction electrocatalysts based on carbon nanotubes: mechanism and origin of ORR activity. Energ Environ Sci 7:1950–1958
7. Gong K, Du F, Xia Z, Durstock M, Dai L (2009) Nitrogen-doped carbon nanotube arrays with high electrocatalytic activity for oxygen reduction. Science 323:760–764
8. Nagaiah TC, Kundu S, Bron M, Muhler M, Schuhmann W (2010) Nitrogen-doped carbon nanotubes as a cathode catalyst for the oxygen reduction reaction in alkaline medium. Electrochem Commun 12:338–341
9. Geng D, Chen Y, Chen Y, Li Y, Li R, Sun X et al (2011) High oxygen-reduction activity and durability of nitrogen-doped graphene. Energy Environ Sci 4:760–764
10. Chen S, Bi J, Zhao Y, Yang L, Zhang C, Ma Y et al (2012) Nitrogen-doped carbon nanocages as efficient metal-free electrocatalysts for oxygen reduction reaction. Adv Mater 24:5593–5597
11. Geng D, Liu H, Chen Y, Li R, Sun X, Ye S et al (2011) Non-noble metal oxygen reduction electrocatalysts based on carbon nanotubes with controlled nitrogen contents. J Power Sources. 196:1795–1801
12. Li Y, Zhou W, Wang H, Xie L, Liang Y, Wei F et al (2012) An oxygen reduction electrocatalyst based on carbon nanotube-graphene complexes. Nat Nanotechnol 7:394–400
13. Wang S, Yu D, Dai L, Chang DW, Baek J-B (2011) Polyelectrolyte-functionalized graphene as metal-free electrocatalysts for oxygen reduction. ACS Nano 5:6202–6209
14. Wang S, Yu D, Dai L (2011) Polyelectrolyte functionalized carbon nanotubes as efficient metal-free electrocatalysts for oxygen reduction. J Am Chem Soc 133:5182–5185
15. Jasinski R (1964) A new fuel cell cathode catalyst
16. Bashyam R, Zelenay P (2006) A class of non-precious metal composite catalysts for fuel cells. Nature 443:63–66
17. Lefèvre M, Dodelet J, Bertrand P (2002) Molecular oxygen reduction in PEM fuel cells: evidence for the simultaneous presence of two active sites in Fe-based catalysts. J Phys Chem B 106:8705–8713
18. Xu G, Li Z, Wang S, Yu X (2010) Planar polyphthalocyanine cobalt absorbed on carbon black as stable electrocatalysts for direct methanol fuel cell. J Power Sourc 195:4731–4735

19. Bagotzky V, Tarasevich M, Radyushkina K, Levina O, Andrusyova S (1978) Electrocatalysis of the oxygen reduction process on metal chelates in acid electrolyte. J Power Sourc 2:233–240
20. Gupta S, Tryk D, Bae I, Aldred W, Yeager E (1989) Heat-treated polyacrylonitrile-based catalysts for oxygen electroreduction. J Appl Electrochem 19:19–27
21. Wu G, More KL, Johnston CM, Zelenay P (2011) High-performance electrocatalysts for oxygen reduction derived from polyaniline, iron, and cobalt. Science 332:443–447
22. Antolini E (2009) Palladium in fuel cell catalysis. Energ Environ Sci 2:915–931
23. Mustain WE, Prakash J (2007) Kinetics and mechanism for the oxygen reduction reaction on polycrystalline cobalt–palladium electrocatalysts in acid media. J Power Sourc 170:28–37
24. Wang W, Zheng D, Du C, Zou Z, Zhang X, Xia B et al (2007) Carbon-supported Pd-Co bimetallic nanoparticles as electrocatalysts for the oxygen reduction reaction. J Power Sourc 167:243–249
25. Ramos-Sánchez G, Yee-Madeira H, Solorza-Feria O (2008) PdNi electrocatalyst for oxygen reduction in acid media. Int J Hydrog Energ 33:3596–3600
26. Yin S, Cai M, Wang C, Shen PK (2011) Tungsten carbide promoted Pd–Fe as alcohol-tolerant electrocatalysts for oxygen reduction reactions. Energ Environ Sci 4:558–563
27. Zhu J, Shen PK (2013) Chelate resin self-assembled quaternary Co–N–P–C catalyst for oxygen reduction reaction. Rsc Adv 3:14686–14690
28. Zhu J, He G, Liang L, Wan Q, Shen PK. Direct anchoring of platinum nanoparticles on nitrogen and phosphorus-dual-doped carbon nanotube arrays for oxygen reduction reaction. Electrochim Acta
29. Snyder J, Fujita T, Chen M, Erlebacher J (2010) Oxygen reduction in nanoporous metal–ionic liquid composite electrocatalysts. Nat Mater 9:904–907
30. Elezović NR, Babić BM, Krstajić NV, Gojković SL, Vračar LM (2008) Temperature dependence of the kinetics of oxygen reduction on carbon-supported Pt nanoparticles. J Serb Chem Soc 73:641–654
31. Wong W, Daud W, Mohamad A, Kadhum A, Loh K, Majlan E et al (2014) The impact of loading and temperature on the oxygen reduction reaction at nitrogen-doped carbon nanotubes in alkaline medium. Electrochim Acta 129:47–54
32. Paulus U, Schmidt T, Gasteiger H, Behm R (2001) Oxygen reduction on a high-surface area Pt/Vulcan carbon catalyst: a thin-film rotating ring-disk electrode study. J Electroanal Chem 495:134–145
33. Zhu J, He C, Li Y, Kang S, Shen PK (2013) One-step synthesis of boron and nitrogen-dual-self-doped graphene sheets as non-metal catalysts for oxygen reduction reaction. J Mater Chem A 1:14700–14705
34. Jukk K, Kozlova J, Ritslaid P, Sammelselg V, Alexeyeva N, Tammeveski K (2013) Sputter-deposited Pt nanoparticle/multi-walled carbon nanotube composite catalyst for oxygen reduction reaction. J Electroanal Chem 708:31–38
35. Jiang J, Yi B (2005) Thickness effects of a carbon-supported platinum catalyst layer on the electrochemical reduction of oxygen in sulfuric acid solution. J Electroanal Chem 577:107–115
36. He C, Zhang JJ, Shen PK (2014) Nitrogen-self-doped graphene-based non-precious metal catalyst with superior performance to Pt/C catalyst toward oxygen reduction reaction. J Mater Chem A 2:3231–3236
37. Cheng F, Chen J (2012) Metal–air batteries: from oxygen reduction electrochemistry to cathode catalysts. Chem Soc Rev 41:2172–2192
38. Kim H, Jeong G, Kim YU et al. (2013) Metallic anodes for next generation secondary batteries. Chem Soc Rev 42:9011–9034
39. Li YG, Lu J (2017) Metal−Air Batteries: Will they be the future electrochemical energy storage device of choice. ACS Energy Lett 2:1370–1377
40. Song MK, Park S, Alamgir FM et al (2011) Nanostructured electrodes for lithium-ion and lithium-air batteries: the latest developments, challenges, and perspectives. Mater Sci Eng R 72:203–252
41. Jang-Soo Lee, Sun Tai Kim, Ruiguo Cao et al. (2011) Metal–air batteries with high energy density: Li–Air versus Zn–Air. Adv Energy Mater 1:34–50

42. Tan P, Chen B, Haoran Xu et al (2017) Flexible Zn– and Li–air batteries: recent advances, challenges, and future perspectives. Energy Environ Sci 10:2056–2080
43. Lim HK, Lim HD, Park KY et al (2013) Toward a lithium–"Air" battery: the effect of CO2 on the chemistry of a lithium-oxygen cell. J Am Chem Soc 135:9733–9742
44. Bruce PG, Freunberger SA, Hardwick LJ et al (2012) Li–O2 and Li–S batteries with high energy storage. Nat Mater 11:19–29
45. Read J, Mutolo K, Ervin M et al (2003) Oxygen transport properties of organic electrolytes and performance of lithium/oxygen battery. J Electrochem Soc 150:A1351–A1356
46. Lu YC, Xu ZC, Gasteiger HA et al (2010) Platinum-gold nanoparticles: A highly active bifunctional electrocatalyst for rechargeable lithium-air batteries. J Am Chem Soc 132:12170–12172
47. Read J (2002) Characterization of the lithium/oxygen organic electrolyte battery. J Electrochem Soc 149:A1190–A1195
48. Xu W, Xiao J, Zhang J et al (2009) Optimization of nonaqueous electrolytes for primary lithium/air batteries operated in ambient environment. J Electrochem Soc 156:A773–A779
49. Mokhtar M, Talib MZM, Majlan EH et al (2015) Recent developments in materials for aluminum–air batteries: a review. Ind Eng Chem Res 32:1–20
50. Zhuk AZ, Sheindlin AE, Kleymenov BV et al (2006) Use of low-cost aluminum in electric energy production. J Power Sourc 157:921–926
51. Zeng XX, Wang JM, Wang QL et al (2010) The effects of surface treatment and stannate as an electrolyte additive on the corrosion and electrochemical performances of pure aluminum in an alkaline methanol-water solution. Mater Chem Phys 121:459–464
52. Hu Y, Sun D, Luo B et al (2019) Recent progress and future trends of aluminum batteries. Energy Technol 7:86–106
53. Egan DR, de León CP, Wood RJK et al (2013) Developments in electrode materials and electrolytes for aluminum-air batteries. J Power Sourc 236:293–310
54. Macdonald DD, English C (1990) Development of anodes for aluminum/air batteries-solution phase inhibition of corrosion. J Appl Electrochem 20:405–417
55. Abdel-Gaber A, Khamis E, Abo-Eldahab H et al (2010) Novel package for inhibition of aluminium corrosion in alkaline solutions. Mater Chem Phys 124:773–779
56. Pino M, Chacón J, Fatás E et al (2015) Performance of commercial aluminium alloys as anodes in gelled electrolyte aluminium-air batteries. J. Power Sourc 299:195–201
57. Pan J, Xu YY, Yang H et al (2018) Advanced architectures and relatives of air electrodes in Zn–air batteries. Adv Sci 5:1700691–1700720
58. Li Y, Dai H (2014) Recent advances in zinc–air batteries. Chem Soc Rev 43:5257–5402
59. The editorial department of this newspaper (2012) The development of zinc-air battery in the United States can realize 2700 cycles of charge and discharge [J]. China Electric Power 45(10):41
60. Zhang T, Tao Z, Chen J (2014) Magnesium–air batteries: from principle to application. Mater Horiz 1:196–206
61. Saha P, Datta MK, Velikokhatnyi OI et al (2014) Rechargeable magnesium battery: current status and key challenges for the future. Prog Mater Sci 66:1–86
62. Liu C (2014) Research progress of metal-air batteries abroad. Power Supply Technol 138(2):199–200
63. Das SK, Lau S, Archer LA (2014) Sodium–oxygen batteries: a new class of metal–air batteries. J Mater Chem A 2:12623–12629
64. Shao YY (2012) Electrocatalysts for nonaqueous lithium-air batteries: status, challenges, and perspective. ACS Catal 2:844–857
65. Abraham K (1996) A polymer electrolyte-based rechargeable lithium/oxygen battery. J Electrochem Soc 143:1–5
66. Lu Y (2011) Catalytic activity trends of oxygen reduction reaction for nonaqueous Li-air batteries. J Am Chem Soc 133:19048–19051
67. Allen C (2012) Elucidating the mechanism of oxygen reduction for lithium-air battery applications. J Phys Chem C 116:20755–20764

68. Peng Z (2011) Oxygen reactions in a non-aqueous Li+ electrolyte. Angew Chem Int Ed 50:6351–6355
69. Li Y (2011) Nitrogen-doped carbon nanotubes as cathode for lithium–air batteries. Electrochem Commun 13:668–672
70. Li Y (2011) Superior energy capacity of graphene nanosheets for a nonaqueous lithium-oxygen battery. Chem Commun 47:9438–9440
71. Xiao J (2011) Hierarchically porous graphene as a lithium-air battery electrode. Nano Lett 11:5071–5078
72. Debart A (2008) α-MnO2 nanowires: a catalyst for the O2 electrode in rechargeable lithium batteries. Angew Chem Int Ed 47:4521–4524
73. Lu Y (2011) A free-standing-type design for cathodes of rechargeable Li–O2 batteries. Energy Environ Sci 4:4727–4734
74. Lu Y (2010) Platinum−gold nanoparticles: A highly active bifunctional electrocatalyst for rechargeable lithium−air batteries. J Am Chem Soc 132:12170–12171
75. Zhang S (2011) Heat-treated metal phthalocyanine complex as an oxygen reduction catalyst for non-aqueous electrolyte Li/air batteries. Electrochim Acta 56:4544–4548
76. Lee S (2010) The influence of catalysts on discharge and charge voltages of rechargeable Li-oxygen batteries. Electrochem Solid-State Lett 13:A162–A164
77. Grande L (2015) The lithium/air battery: Still an emerging system or a practical reality? Adv Mater 27:784–800
78. Balaish M (2014) A critical review on lithium-air battery electrolytes. Phys Chem Chem Phys 16:2801–2822
79. Gallagher K (2014) Quantifying the promise of lithium-air batteries for electric vehicles. Energy Environ Sci. 7:1555–1563
80. Geng D (2016) From lithium-oxygen to lithium-air batteries: Challenges and opportunities. Adv Energy Mater. 6:1502164
81. Imanishi N (2014) Rechargeable lithium-air batteries: characteristics and prospects. Mater Today 17:24–30